

Radar Performance Modelling

A study of radar performance assessment accuracy
sensitivity to the resolution of atmospheric input data

Case studies of North Sea environments

LTZ2 (TD) Joris Derksen

Master of Science Thesis



Radar Performance Modelling

**A study of radar performance assessment accuracy sensitivity to
the resolution of atmospheric input data
Case studies of North Sea environments**

MASTER OF SCIENCE THESIS

For the degree of Master of Science in Telecommunications and Sensing
Systems at Delft University of Technology

LTZ2 (TD) Joris Derksen

March 16, 2016

Faculty of Electrical Engineering, Mathematics and Computer Science (EEMCS)
Delft University of Technology

Cover: the Air Defence and Command Frigate HNLN Tromp (F803) of the Royal Netherlands Navy (RNLN) patrolling waters off the coast of Croatia during NATO Responce Force (NRF) exercise Noble Midas 07. The Air Defence Command Frigates of the RNLN are equipped with a highly advanced radar suite. The photo was taken by the author of this thesis on October 10, 2007.



Royal Netherlands
Meteorological Institute
*Ministry of Infrastructure and the
Environment*



Support Command
Ministry of Defence

The work in this thesis was supported by the Space and Naval Warfare Systems Command (SPAWAR), the Knowledge, Innovation, eXperimentation and Simulation (KIXS) centre of the Dutch Armed Forces, the Royal Netherlands Meteorological Institute (KNMI), and the Netherlands Defence Academy (NLDA). Their cooperation is hereby gratefully acknowledged.



Copyright © Microwave Sensing, Signals and Systems (MS³)
All rights reserved.

DELFT UNIVERSITY OF TECHNOLOGY
DEPARTMENT OF
MICROWAVE SENSING, SIGNALS AND SYSTEMS (MS³)

The undersigned hereby certify that they have read and recommend to the Faculty of
Electrical Engineering, Mathematics and Computer Science (EEMCS) for acceptance
a thesis entitled

RADAR PERFORMANCE MODELLING

by

LTZ2 (TD) JORIS DERKSEN

in partial fulfillment of the requirements for the degree of
MASTER OF SCIENCE TELECOMMUNICATIONS AND SENSING SYSTEMS

Dated: March 16, 2016

Supervisor(s):

prof. dr. A. Yarovoy

dr. A.V. van Leijen

dr. ir. F. Bolderheij

Reader(s):

dr. O.A. Krasnov

Abstract

Within navies, radio detection and ranging systems (radars) are the primary sensors for the detection, tracking and sometimes classification of friendly and hostile targets. They are essential for creating an operational picture of the surroundings and situational awareness. The performance of radars can be significantly influenced by the environment in which the systems are deployed. Under certain atmospheric condition refractive effects result in electromagnetic ducts, radar holes, skipping zones and/or increased shadow zones. These phenomena can lead to tactical advantages and disadvantages. For example, an advantage is that ducts lead to extended detection ranges thereby providing more response time to act against incoming hostile targets. A disadvantage is that hostile targets can remain undetected in radar holes and skipping zones that generally coexist with the developed duct.

As the environment can significantly affect the performance of radars, it is highly desirable to be able to assess radar performance under prevailing conditions. The ability to assess radar performance allows navies to fully benefit from the tactical advantages and to minimise the effects of the disadvantages that accompany certain atmospheric conditions. It also helps avoid false situational awareness.

Over the years models for modelling radar propagation¹ and performance have matured to the extent that they produce sufficiently accurate results provided that the environmental data input is also sufficiently accurate. With the successful development of these models attention shifted to methods for obtaining this environmental data. In large air masses over fast bodies of water away from the coast a single vertical refractivity profile suffices for accurate radar performance assessment. Such a profile can easily be obtained by means of a single radiosonde balloon measurement. Near coastlines however three dimensional (3D) refractivity data is required in many cases. Using a single profile in these cases may result in erroneous assessments.

Obtaining 3D atmospheric data for radar assessment purposes does not come without challenges. Because of this, it is important to get a sense of the required accuracy and resolution

¹As in many literary sources, "radar propagation" stands for the propagation of radio/microwaves (300 MHz - 300 GHz) through the atmosphere; it does not portray an actual radar system propagating over the earth's surface.

of input data, depending on atmospheric conditions, to assess radar performance sufficiently accurate. In cases where 3D data is obtained by numerical weather prediction (NWP) systems, assessment of the minimal 3D data resolution requirement allows the reduction of data file size. Currently NWP data file sizes are too big to send to navy ships by satellite communication (SATCOM) on a regular basis. This makes the use of NWP data, to a certain extent, unsuitable for operational use.

This thesis studies the performance assessment accuracy sensitivity to horizontal and temporal data resolution for different cases of North Sea weather conditions. This is done by comparing "ground truth" radar performance assessments with "spoiled" assessment². For this thesis, the ground truths are defined as the assessments computed by the radar propagation model AREPS³ (version 3.6) on the basis of high resolution NWP HARMONIE⁴ data. These truths are then compared to assessments based on sets of the same HARMONIE data which are reduced in horizontal or temporal resolution. Comparisons are made using several measures of accuracy. The ground truths are also compared to the assessments based on a single vertical profile and a standard atmosphere profile. In total 41 different cases are analysed. Case scenarios differed in ship position, radar deployment azimuths and weather conditions. In the available data from the KNMI, weather conditions varied between cold weather fronts (8x), warm weather fronts (8x), a warm sector (1x), advection of relatively warm air over water, high pressure systems and calm conditions, which is a fairly representative data set for the conditions over the North Sea throughout the year.

The actual radar performance assessments are obtained using AREPS. AREPS is an advanced propagation model that computes, for example, propagation losses versus range and height and detection probabilities (coverage) versus range and height for any specific radar, environment and target combination. The radar used was for all scenarios a 3300 MHz medium range surveillance radar and the target was a small fighter with a radar cross section of 2 m². The radar system and target were modelled using the integrated radar and target model in AREPS.

In order to acquiring the results that are summarised below, raw HARMONIE NWP data needed to be fed into AREPS. For this a new environmental model was developed that adapts HARMONIE NWP data so that it is suitable for radar performance assessment and can be used by AREPS⁵. Using NWP input data the model subsequently: integrates vertical NWP profiles to vertical profiles along the propagation path; computes the refractivity profile of the surface layer using Monin-Obukhov similarity theory (MOST); and blends the lower and upper profiles together. The model provides realistic refractivity profiles along the propagation path. Whilst it is suitable for the purpose of this thesis, it is has not yet been validated for operational use.

Converting the required atmospheric data into data suitable for radar performance assessment, obtaining the ground truth assessments and the spoiled assessments of the different examined

²The word "spoiled" in "spoiled assessments" indicates that these assessments are based on artificially reduced resolution data, as is often done in similar studies (e.g. [4]).

³Advanced Refractive Effects Prediction System (AREPS).

⁴Hirlam Aladin research on mesoscale operational NWP in Euromed (HARMONIE) is a NWP system developed by a cooperation between a number of European meteorological institutes.

⁵Note that this study is the first to use HARMONIE NWP data as input for radar performance assessment by AREPS.

scenarios and comparing these, allowed the assessment accuracy sensitivity to data input resolution to be studied.

Results show that in the reviewed cases near a cold or warm weather front or in a warm sector, assessments based on a single profile compared well with the ground truth. Hence, in these cases a single profile measured by, for example, a radiosonde will suffice for radar performance assessment.

In scenarios where warm dry air advected over cooler water the accuracy of the performance assessment decreases significantly at coarser resolutions. In only one of the nine scenarios a single profile sufficed. Using a single profile in the other eight scenarios resulted in erroneous assessment, which may have dramatic consequences if relied upon. For example, detection range prediction errors of over 150 km occurred. It is clear that in these cases acquiring 3D atmospheric data is a must.

Results for assessments in the vicinity of high pressure systems were similar to that of the scenarios where warm dry advected over cooler water. In these cases only two out of the eight scenarios allowed the use of a single profile for accurate radar assessment.

Seven scenarios were analysed in which it was expected that no anomalous propagation would occur. This expectation was based on the evaluation of the weather charts. In the absence of propagation anomalies, it was also expected that in these cases a single profile would suffice. This was true for only five out of the seven cases. Hence, one cannot dependably predict if a single profile will suffice merely by looking at weather charts.

Comparing assessments based on a single profile to the assessments based on a standard profile showed that, in general, a single profile provides more accurate radar performance assessments than the standard profile. This said, when 3D data is a must, both assessments will be significantly in error.

Investigating the sensitivity of assessment accuracy to temporal resolution was done by comparing the ground truth to assessments based on atmospheric data with the same spatial resolution but of a different time. The results show that a single measurement every 24 hours is not sufficient in many cases. Current practice in the RNLN, however, is to carry out atmospheric measurements only once every 24 hours. In many of the viewed cases a temporal resolution of no less than 1 hour is required. This said, in cases where a single profile suffices the required temporal resolution can be reduced, and in some cases to 24 hours.

In this thesis no actual minimum required resolutions are established. To do so many more scenarios should be evaluated. These scenarios should differ in radar parameters, target parameters and/or weather conditions. Also the minimum required resolution depends on the required accuracy which may vary with application.

Besides the research described above, other goals of this thesis were to provide clear and understandable documentation on radar propagation through an inhomogeneous atmosphere and to give recommendations to the Royal Netherlands Navy (RNLN) concerning radar performance assessment. This thesis can be used as a general overview on radar propagation, for educational purposes and as an introduction to further research. For the RNLN, the most important recommendation is to start using NWP data for radar performance assessment. The use of a single measured refractivity profile, which is current practice, can lead to erroneous assessments and potentially to dramatic operational consequences. As no minimum

required resolution is yet defined, it is recommended, although logistically challenging, that the maximum resolution of available atmospheric (NWP) data is used and that the data is updated every hour.

Preface

For my Bachelor Thesis, done at the Netherlands Defence Academy (NLDA), I developed the ray tracing program MIRAT (microwave ray tracing). This program allows radar operators to model electromagnetic propagation in simple environments in which the refractivity changes with height. MIRAT intuitively displays in which direction the radar's energy propagates. This helps the radar operator a great deal to get a sense of the radar's performance under the given conditions. Whilst developing MIRAT it became clear to me that the ability to assess radar performance under prevailing conditions is highly beneficial, if not essential, for the effective deployment of naval radar systems and for achieving accurate situational awareness. As a technical officer in the Royal Netherlands Navy (RNLN), I was immediately hooked on the topic of modelling and assessing radar performance.

After I finished my bachelor, the RNLN allowed me to continue my studies at the Technical University of Delft in the Netherlands. When the time came to start my Master Thesis my bachelor supervisors inquired me whether I was interested to elaborate on my Bachelor Thesis topic: radar propagation. They also mentioned that if I should choose to do so I would be working with SPAWAR, the developers of AREPS⁶, and leading scientists in the field of radar propagation. Who would not get excited?

After some initial research I discovered that much was still to be learned on the required resolutions of atmospheric input data for accurate radar propagation modelling. And, the use of three dimensional atmospheric data, such as numerical weather prediction data, was completely new to the RNLN. With this in mind, I decided, in consultation with my supervisors and graduation professor, that I should research resolution requirements of atmospheric input data for radar propagation models.

During my thesis I got to work with the RNLN and leading scholars in the field of radar propagation on a large scale field experiment with the goal of partially validating the AREPS model for active phased array radars. What I learned from the scientists I worked with was invaluable for my own work on my thesis. For more information on the field experiment contact one of my supervisors: dr. A.V. van Leijen from the KIXS⁷ centre of the Dutch Armed

⁶Advanced Refractive Effects Prediction System (AREPS) is an advanced propagation model.

⁷Knowledge, Innovation, eXperimentation and Simulation (KIXS).

Forces or KTZ (TD) dr. ir. F. Bolderheij of the Netherlands Defence Academy (NLDA).

Now that the work on this thesis nears completion and I can look back on my research over the course of a year along with my participation in the field experiment and the many interesting discussion that came with it, I am on the one hand sad that this great adventure is coming to an end. On the other hand I am happy that this will free up a great deal of time, and I look forward to new challenges and adventures that lie ahead.

I sincerely hope that you enjoy reading my work!

Joris Derksen

Acknowledgements

I thank all who have supported me during my research in one-way or an other. I especially thank the following people.

Dr. Sander Tijm from the Royal Netherlands Meteorological Institute (KNMI) for answering all my questions concerning numerical weather prediction (NWP) systems and for providing me with NWP data.

LTZ1 Tjarda Wilbrink from the Royal Netherlands Navy (RNLN) for helping with the meteorological aspects of my studies.

Dr. Amalia E. Barrios from the Space and Naval Warfare Systems Command (SPAWAR), Katherine Horgan from the Naval Surface Warfare Center, Dahlgren Division (NSWCDD) and dr. Robert E. Marschall also from NSWCDD for their invaluable support concerning parabolic equations, AREPS, radar assessments based on NWP data and blending algorithms.

My father Peter Derksen for proof reading my work, and my mother Maria Derksen for standing by my side.

Sara Voûte for sharing her own thesis experiences, for taking my mind off of thesis problems when I needed a break and for pushing me to continue and finish this work.

Professor dr. Alexander Yarovoy for his evaluation of my thesis and for his guidance throughout. I also thank dr. Oleg A. Krasnov for evaluating my work.

Finally I thank my supervisors dr. A. Vincent van Leijen from the Knowledge, Innovation, eXperimentation and Simulation (KIXS) centre of the Dutch Armed Forces and KTZ (TD) dr. ir. Fok Bolderheij of the Netherlands Defence Academy (NLDA) for assisting me during my entire thesis period. Hopefully our paths will cross again.

Joris Derksen

“If you know the enemy and know yourself, your victory will not stand in doubt;
if you know Heaven and know Earth, you may make your victory complete.”

— *Sun Tzu, The Art of War (Chapter 10, section 31)*

Table of contents

List of figures	xv
List of tables	xxi
List of abbreviations and acronyms	xxiii
1 Introduction	1
1-1 Problem background	1
1-2 Problem definition	4
1-3 Related research	6
1-4 Thesis goals and approach	7
1-5 Thesis structure	9
2 Propagation mechanisms	11
2-1 Spherical spreading	11
2-2 Refraction	12
2-3 Specular and diffuse reflection	14
2-3-1 Specular reflection	14
2-3-2 Diffuse reflection	16
2-4 Divergence	17
2-5 Interference	18
2-6 Diffraction	20
2-6-1 Diffraction by the spherical earth	20
2-6-2 Knife-edging	22
2-7 Troposcattering	23
2-8 Attenuation	25

3	Tropospheric propagation	29
3-1	Normal propagation	29
3-1-1	Standard atmosphere	29
3-1-2	Standard propagation	30
3-2	Anomalous propagation	31
3-2-1	Anomalous refraction	31
3-2-2	Sub-refraction	32
3-2-3	Super-refraction	33
3-2-4	Trapping and ducting	33
3-2-5	Lateral inhomogeneity	41
3-2-6	Terrain effects	45
3-3	Tactical consequences	48
3-3-1	Detection range effects	48
3-3-2	Radar holes, skipping zones and shadow zones	50
3-3-3	Altitude and range errors	51
4	Methods for modelling radar propagation	55
4-1	The geometrical optics method	56
4-2	The mode theory method	57
4-3	The parabolic equation method	58
4-4	Hybrid methods	61
4-5	Tactical decision aids	63
5	Modelling the environment	65
5-1	The tropospheric refractivity	66
5-2	Acquiring the vertical refractivity profile	68
5-2-1	Upper-air profiles	68
5-2-2	Lower-air profiles and Monin-Obukhov similarity theory	72
5-2-3	Blending upper- and lower-air profiles	79
5-3	Horizontal interpolation of vertical profiles	89
5-4	The environment model	90
6	Approach to assessing accuracy sensitivity to resolution	93
6-1	General approach	93
6-1-1	Ground truth	93
6-1-2	Sensitivity study of horizontal grid resolution	94
6-1-3	Sensitivity study of temporal resolution	96
6-2	Measures of accuracy	97
6-2-1	Propagation loss errors	97
6-2-2	Coverage errors	97

6-2-3	Maximum detection range errors	99
6-2-4	Other possible measures	99
6-3	Scenarios	100
6-3-1	Radar system parameters	100
6-3-2	Target parameters	100
6-3-3	Weather conditions	100
7	Accuracy sensitivity to resolution: results, analysis and discussion	103
7-1	Horizontal resolution	104
7-1-1	Cold weather fronts	104
7-1-2	Warm weather fronts	107
7-1-3	Warm sectors	111
7-1-4	Warm dry air advection	112
7-1-5	High pressure systems	116
7-1-6	Calm standard conditions	121
7-1-7	General conclusions	122
7-2	Temporal resolution	125
7-3	General discussion	130
8	Conclusions and recommendations	133
8-1	Conclusions	135
8-1-1	Goal 1 - reaching an understanding and providing documentation	135
8-1-2	Goal 2 - accuracy sensitivity to input data resolution	137
8-1-3	Goal 3 - providing recommendations	139
8-1-4	Minimum resolution requirements	140
8-1-5	Summary	141
8-2	Recommendations	141
8-2-1	Recommended further research	141
8-2-2	Recommendations for the Royal Netherlands Navy	142
9	Operational advice for the Royal Netherlands Navy	145
A	Radar assessment projections	147
B	Similarity functions	151
B-1	The LKB similarity functions	151
B-2	The NWA similarity functions	152
B-3	The NRL similarity functions	152
B-4	The BYC similarity functions	152
B-5	The NPS similarity functions	153
C	Implementation of MOST in MATLAB	155
D	Scenarios	171
	References	219

List of figures

1-1 Radar performance depends on the radar system itself, the propagation environment and the target, as well as radar operator experience. 1

1-2 Environmental effects can result in tactical advantages and disadvantages. The propagation mechanism refraction may lead to ducting, resulting in extended detection ranges skipping zones and radar holes. The radar coverage assessment is computed by the TDA AREPS. 3

1-3 Radar coverage assessments illustrating the error that may occur when assuming a horizontally stratified atmosphere. Image (a) shows the coverage assessment that is obtained by using atmospheric data with a horizontal grid resolution, R_{hor} , of 2.5 km. Image (b) shows the coverage assessment that is obtained by using a single profile. 5

2-1 An (hypothetical) isotropic transmitter radiates uniformly in all directions. The propagation loss is inversely proportional to the square of the distance. 12

2-2 Illustration of the propagation mechanism refraction. 13

2-3 Electromagnetic waves, propagating through an atmospheric layer in which the refractivity varies linear with height, propagate along a curved path with a curvature radius of R_c (see Eq. 2-6). 14

2-4 Ray trace pattern of rays propagating through a standard atmosphere over a smooth surface from a radar with a 20 m height above the surface. The figure was generated by MIRAT (microwave ray tracing). MIRAT is a ray tracing program developed by the author of this thesis. 15

2-5 The law of reflection. 15

2-6 The magnitude (a) and argument (b) of the reflection coefficient at different grazing angles for a electromagnetic wave with a frequency of 3 GHz, reflecting off of smooth sea water with a temperature of 20°C and average salinity. 16

2-7 Illustration of specular (left) to diffuse reflection (right) transition with increasing roughness. 17

2-8 Illustration of divergence due to reflection off a spherical surface. 18

2-9 Geometry for determining the resultant electrical field strength due to two-ray interference. 19

2-10	A radar coverage diagram illustrating the vertical lobe pattern caused by the propagation mechanism interference.	20
2-11	Diffraction, or knife-edging, is electromagnetic waves curving around the edge of an object and penetrating its geometric shadow region, which may result in small detection probabilities behind the object or in counter detection by enemy targets. b is the curvature radius of the object.	22
2-12	The troposcattering geometry. Troposcattering enables electromagnetic energy to propagate beyond the diffraction zone.	24
2-13	Propagation loss as function of range in a standard atmosphere above sea surface. The transmitter and receiver have a height of 20 m, the operating frequency is 3.3 GHz. Notice the different propagation regions. The radar horizon lies at approximately 37 km. Propagation losses are determined by AREPS.	25
2-14	The specific attenuation due to gases as function of frequency for a standard and dry atmosphere.	26
2-15	The specific attenuation due to rain as function of rain rate, polarisation (horizontal and vertical) and frequency (1, 3, 10, 30, 100 GHz).	27
3-1	Propagation losses in a standard atmosphere (b) with the associated refractivity profile ($dN/dh = -39$ N-units/km) (a). The propagation losses are computed using AREPS.	31
3-2	Refractive conditions	32
3-3	Propagation losses in an evaporation duct with a duct height of $z_{ED} = 25$ m (b) and associated modified refractivity profile (a). The propagation losses and ray traces in (b) are computed using respectively AREPS and the ray tracing program MIRAT. MIRAT is developed by the author of this thesis. The profile is obtained using the equation $M(z) = M_0 + 0.13(z - z_d \ln((z + z_0)/z_0))$, where M_0 is the modified refractivity at the surface, z_d the aerodynamic roughness parameter equal to 1.5×10^{-4} m, and z the height above sea level.	35
3-4	Propagation losses in a standard surface duct (b) with associated modified refractivity profile (a). The propagation losses and ray traces in (b) are computed using respectively AREPS and the ray tracing program MIRAT.	38
3-5	Propagation losses in a surface-based duct (b) with associated M -profile (a). The propagation losses and ray traces in (b) are computed using respectively AREPS and the ray tracing program MIRAT.	39
3-6	Propagation losses in an elevated duct (b) with associated M -profile (a). The propagation losses and ray traces in (b) are computed using respectively AREPS and the ray tracing program MIRAT.	40
3-7	Conditions above the North Sea on 12-05-2014 at 12:00 Z (a - d) and on 09-03-2014 at 15:00 Z (e - h): two dimensional refractivity data (a & e); modified refractivity gradient (b & f); ground truth radar assessment (c & g); radar assessment based on a single profile (d & h).	42
3-8	Maximum relative detection ranges (relative to standard conditions) for a small fighter at an altitude of 10 m on 09-03-2014 at 15:00 Z (a) and on 13-03-2014 at 18:00 Z (b) ($P_D = 0.95$, $P_{FA} = 10^{-6}$). Assessments are based on a single profile.	44
3-9	The effects of diffraction (a & b) and reflection (b) due to irregular terrain. Propagation losses are computed using PETOOL.	46
3-10	The effects of refraction, reflection and diffraction in elevated (a & b) and surface-based (c & d) ducting conditions over irregular terrain. Propagation losses are computed using PETOOL.	47

3-11	Tactical consequences as a result of anomalous refraction.	48
3-12	Radar coverage under different atmospheric conditions: sub-, standard- and super-refractive conditions (a), evaporation duct (b), standard surface duct (c), surface-based duct (d) and elevated duct (e). The corresponding modified refractivity profiles are given in the corresponding sections.	49
3-13	Optimum fly altitude for penetrating enemy radar.	50
3-14	Position error due to refraction.	52
3-15	Altitude error as a result of a surface based duct (b). The associated modified refractivity profile is given in (a). Errors are computed using AREPS.	53
4-1	Output of the ray trace model MIRAT (b), tracing rays in surface-based duct conditions (a).	56
4-2	The four regions of the Advanced Propagation Model: flat earth (FE), ray optics (RO), parabolic equation (PE) and extended optics (XO).	62
4-3	Detection probabilities computed by CARPET (a) and AREPS (b) under the same conditions: a surface-based duct rising into an elevated duct at 100 km.	64
5-1	Numerical weather prediction (NWP) models compute vertical profiles of wind velocity, pressure, temperature and humidity on a horizontal grid from the surface to the stratosphere; the results are comparable to launching multiple balloon radiosondes.	70
5-2	Evaporation duct profiles computed using different similarity functions under various conditions: unstable conditions (a-c) and stable conditions (d-f).	76
5-3	Evaporation duct models are highly sensitive to air-sea temperature difference. This sensitivity can result in the computation of unrealistic profiles with extremely high evaporation duct heights.	77
5-4	Radar performance predictions illustrating the importance of blending. From left to right the figure shows the modified refractivity profiles, the propagation loss assessments and the radar coverage assessments. From top to bottom the figure shows assessments for a surface-based duct environment (a), an evaporation duct environment (b) and a combined surface based and evaporation duct environment (c).	78
5-5	Blending by simply appending the lower profile (M_{Low}) to the lowest value of the upper profile (M_{Upp}) above the surface generally results in the distortion of salient profile features such as the evaporation duct height.	80
5-6	The cosine based α -filter.	81
5-7	Three methods for blending the lower- and upper-air refractivity profiles into a single profile: Method 1 (a), Method 2 (b) and Method 3 (c).	82
5-8	Criteria parameters used in choosing the appropriate blending method and interval.	84
5-9	Selection of the best blending method for the considered conditions: Method 1 (a), Method 2 (b) and Method 3 (c).	86
5-10	Blending lower and upper refractivity profiles with a evaporation duct height greater than z_{20} : $z_{20} < z_{ED} \leq z_2$ (a), $z_{20} < z_{ED} \leq z_2$ (b) and $z_2 < 50 \text{ m} \leq z_{ED}$ (c).	87
5-11	Two simple approaches for obtaining the refractivity profile along the propagation path from the NWP model grid.	88
5-12	Interpolating vertical modified refractivity profiles between grid points by NWP model levels (a) and by duct attributes (b).	88

5-13	Illustration of how vertical profiles on the NWP model grid are interpolated.	90
5-14	Interpolation of modified refractivity profiles in the physical domain.	91
6-1	Possible offsets for a grid resolution equal to 1/3 of the initial NWP grid resolution.	95
6-2	Illustration of the three measures of accuracy used in this thesis: propagation loss ground truth (a), propagation loss spoiled assessment (b), propagation loss error (c), coverage ground truth (d), coverage spoiled assessment (e) and coverage error (f).	98
7-1	Modified refractivity gradients (a) for a ship positioned behind a cold front deploying its radar towards the warm air mass (Scenario 6) and the corresponding radar coverage error when using a single (b) and standard (c) vertical profile.	105
7-2	Measures of accuracy for Scenario 6 (cold weather front): propagation loss error (a), coverage error (b) detection range error (c). Propagation loss errors are in decibel.	106
7-3	Mean and maximum radar coverage error near cold weather fronts (Scenarios 1-8).	107
7-4	Modified refractivity gradients for a ship positioned in front (Scenario 11)(a) and behind (Scenario 16)(b) a warm weather front deploying its radar toward the warm and cold air mass respectively.	108
7-5	Measures of accuracy for Scenario 16 (warm weather front): propagation loss error (a), coverage error (b) detection range error (c). Propagation loss errors are in decibel.	109
7-6	Mean and maximum radar coverage error near warm weather fronts (Scenarios 9-16).	110
7-7	Modified refractivity gradients for a ship positioned far into a warm sector (Scenario 17).	111
7-8	Measures of accuracy for Scenario 17 (warm weather sector): propagation loss error (a), coverage error (b) detection range error (c). Propagation loss errors are in decibel.	112
7-9	Modified refractivity gradients (a) for a ship positioned in weather conditions with warm dry air advecting over relatively cold water (Scenario 18) and the corresponding radar coverage error when using a single (b) and standard (c) vertical profile.	113
7-10	Measures of accuracy for Scenario 18 (warm dry air advection): propagation loss error (a), coverage error (b) detection range error (c). Propagation loss errors are in decibel.	114
7-11	Coverage error for Scenarios 19 (a) and 20 (b) (warm dry air advection).	115
7-12	Measures of accuracy for Scenario 17 (warm dry air advection): propagation loss error (a), coverage error (b) detection range error (c). Propagation loss errors are in decibel.	116
7-13	Modified refractivity gradients (a) for a ship positioned near a high pressure system (Scenario 29) and the corresponding radar coverage error when using a single (b) and standard (c) vertical profile.	117
7-14	Measures of accuracy for Scenario 29 (high pressure system): propagation loss error (a), coverage error (b) detection range error (c). Propagation loss errors are in decibel.	118

7-15	Measures of accuracy for Scenario 30 (high pressure system): propagation loss error (a), coverage error (b) detection range error (c). Propagation loss errors are in decibel.	119
7-16	Measures of accuracy for Scenario 31 (high pressure system): propagation loss error (a), coverage error (b) detection range error (c). Propagation loss errors are in decibel.	120
7-17	Measures of accuracy for Scenario 40 (calm conditions): propagation loss error (a), coverage error (b) detection range error (c). Propagation loss errors are in decibel.	121
7-18	Measures of accuracy for Scenario 38 (calm conditions): propagation loss error (a), coverage error (b) detection range error (c). Propagation loss errors are in decibel.	122
7-19	Averages of the different measures of accuracy: for scenarios in which a single profile suffices (a-c), for scenarios in which 3D atmospheric input data is required (d-f) and for all scenarios (g-i).	124
7-20	Measures of accuracy for Scenario 8 (cold weather front): propagation loss error (a), coverage error (b) and detection range error (c). Measures of accuracy for Scenario 41 (calm conditions): propagation loss error (a), coverage error (b) and detection range error (c). Propagation loss errors are in decibel.	126
7-21	Measures of accuracy for Scenario 6 (cold weather front): propagation loss error (a), coverage error (b) and detection range error (c). Measures of accuracy for Scenario 16 (warm weather front): propagation loss error (a), coverage error (b) and detection range error (c). Propagation loss errors are in decibel.	128
7-22	Measures of accuracy for Scenario 18 (warm dry air advection): propagation loss error (a), coverage error (b) and detection range error (c). Measures of accuracy for Scenario 29 (high pressure system): propagation loss error (a), coverage error (b) and detection range error (c). Propagation loss errors are in decibel.	129
A-1	Radar performance assessments for a standard atmosphere projected above a flat earth (a - c) and a spherical earth (d - e). The ray traces (a & d) are computed using MIRAT. The propagation loss assessment (b & e) and the coverage assessment (c & f) are computed using AREPS.	149
A-2	Radar performance assessments for a surface-based duct projected above a flat earth (a - c) and a spherical earth (d - e). The ray traces (a & d) are computed using MIRAT. The propagation loss assessment (b & e) and the coverage assessment (c & f) are computed using AREPS.	150

List of tables

3-1	Refractive conditions	32
3-2	Annual averages of evaporation duct heights.	36
3-3	Annual averages of surface duct heights and percentages of annual occurrence.	37
5-1	Table used for blending method selection.	85
6-1	Radar parameters used for modelling the radar in AREPS.	101
6-2	Target parameters used for modelling the target in AREPS.	101
7-1	Overview of scenarios where a single profile and/or the standard atmosphere profile suffices for accurate radar performance assessment.	123

List of abbreviations and acronyms

2D	two dimensional
3D	three dimensional
AIS	automatic identification system
APM	Advanced Propagation Model
AREPS	Advanced Refractive Effects Predictions System
ASTD	air-sea temperature difference
BYC	Babin, Young and Carton
CARPET	Computer-Aided Radar Performance Evaluation Tool
CIC	combat information centre
CMS	combat management system
COAMPS	Coupled Ocean/Atmosphere Mesoscale Prediction Systems
COARE	Centre for Oceanic Awareness, Research and Education
DMO	Defence Materiel Organisation
ECMWF	European Centre for Medium-Range Weather Forecasts
EMCON	emission control
EREPS	Engineer's Refractive Effects Prediction System
ESM	electronic support measures
EWA	early warning aircraft
FE	flat earth

FFT	Fast Fourier Transform
FSS	Fourier split-step
HARMONIE	Hirlam Aladin research on mesoscale operational NWP in Euromed
HNLM	His Netherlands Majesty's
ICA	International Commission of Aeronavigation
ITU-R	International Telecommunication Union Radiocommunication sector
KIXS	Knowledge, Innovation, eXperimentation and Simulation
KNMI	Royal Netherlands Meteorological Institute
lidar	light detection and ranging
LKB	Liu, Katsaros and Businger
MATLAB	Matrix Laboratory
MIRAT	Microwave Ray Tracing Program
MOST	Monin-Obukhov similarity theory
MTI	Moving Target Indication
NLDA	Netherlands Defence Academy
NPS	Naval Postgraduate School
NRL	Naval Research Lab
NRL-MRY	Naval Research Laboratory - Monterey Marine Meteorology Division
NSWCDD	Naval Surface Warfare Center, Dahlgren Division
NWA	Naval Warfare Assessment station in Corona
NWP	numerical weather prediction
PE	parabolic equation
radar	radio detection and ranging
RCS	radar cross section
RNLN	Royal Netherlands Navy
RO	ray optics
RPO	Radio Physical Optics
RSHMU	Russian State Hydrometeorological University
SA	situational awareness

SATCOM	satellite communications
SPAWAR	Space and Naval Warfare Systems Command
SPE	standard parabolic equation
TDA	tactical decision aid
TNO	Applied Scientific Research
TPEM	Terrain Parabolic Equation Model
VHF	very high frequency
XO	extended optics

Chapter 1

Introduction

1-1 Problem background

Within navies, radio detection and ranging systems (radars) are the primary sensors for the detection, tracking and sometimes classification of friendly and hostile targets. Radar is essential for creating an operational picture of the surroundings and situational awareness (SA). It can aid in collision avoidance and provide early warning of targets such as hostile fighters and incoming missiles. Radar is also used for missile guidance.

The performance of radar systems depends on the system itself, the propagation environment and the target, as well as on radar operator experience (see Fig. 1-1). How the performance depends on the system itself and the target is generally well understood. For example: increasing the transmission power of the radar system will increase the maximum detection range, whilst giving the target stealth capabilities will decrease the maximum detection range.

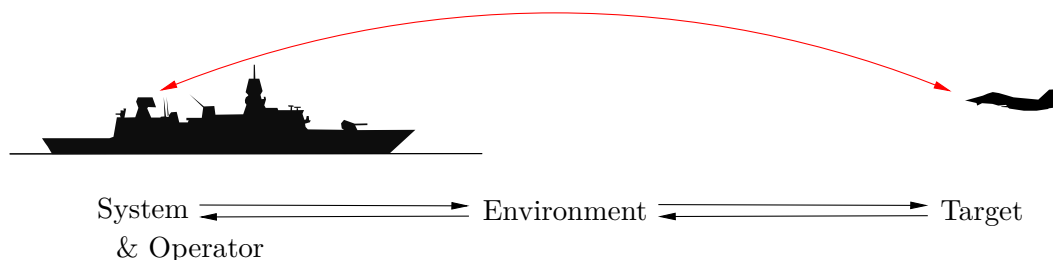


Figure 1-1: Radar performance depends on the radar system itself, the propagation environment and the target, as well as radar operator experience.

On the other hand, how the environment affects propagation and thereby the total radar

performance¹ is less intuitive. Radar signals propagating² through the earth's atmosphere are affected by multiple propagation mechanisms³. Along the propagation path the waves reflect, diverge, refract, diffract, scatter, are attenuated and interfere [1]. These mechanisms can, under certain environmental conditions, result in propagation anomalies which significantly alter radar performance. Propagation anomalies can cause tactical advantages as well as disadvantages.

For example, severe refraction can trap the radar's electromagnetic energy in a so called duct, resulting in a significant increase of the maximum detection range, far beyond the radar horizon [2]. The increased maximum detection range is a tactical advantage as it helps to detect enemy targets at further distances, giving more response time to act against incoming hostile threats. A disadvantage of an increased detection range is the possibility of counter detection at further distances by enemy targets using electronic support measures (ESM) [2].

Radar holes are another example. Due to refraction, electromagnetic energy can bend away from areas, resulting in low detection probability of targets within the energy depleted areas [2]. Radar holes can help to remain covert from enemy radar, but they hinder the detection of enemy targets.

Both effects are shown in Fig. 1-2. Figure 1-2 shows⁴ radar coverage for a typical S-band acquisition radar searching for a small fighter. Radar coverage is defined as the area where the probability of detection is 0.95 or higher with a false alarm probability of 10^{-6} . The radar holes shown is known as a skipping zone that accompanies a duct known as a surface-based duct.

Unawareness of these propagation effects may lead to uncertainty and confusion, decreasing the overall SA. For example: during the Vietnam War, in the Gulf of Tonkin, radar operators on the USS Maddox (DD-731) and the USS Turney Joy (DD-951) reported radar contacts that were classified as attacking torpedo boats. General quarters was set for both destroyers. Combat information centre (CIC) personnel reported "1500 yards and closing" then "1000 yards and closing" and next the contacts disappeared abruptly off radar [3].

The situation above can easily be explained by a duct. The increased detection range allowed the torpedo boats to be detected far beyond the radar horizon, but due to range ambiguity the targets were displayed by the radar at just a few hundred metres away. This effect is known as a second trace echo or a ghost target. The sudden disappearance of the targets can be explained by a skipping zone.⁵

¹In this thesis radar performance is a combination of radar coverage and accuracy. Radar coverage is defined as the area where the probability of detection is 0.95 or higher with a false alarm probability of 10^{-6} . Radar accuracy is related to the precision with which the radar determines the target's position. This thesis focuses primarily on coverage.

²In many studies radar signal propagation is referred to simply as radar propagation. This thesis follows that convention also.

³The word mechanism as used in this thesis can be interchanged with the words phenomenon or effect. The word mechanism was chosen as it is used in many similar studies (e.g [1]). The word phenomenon is in this thesis generally associated with the weather.

⁴Interpreting two dimensional radar assessments that are projected above a flat earth might lead to some confusion in the beginning for those who are new to the field of radar propagation modelling. Appendix A gives a brief explanation on how to interpret these figures.

⁵The disappearance of the targets can also be described by the radar repetitive blind zone due to the finite pulse length of the radar.

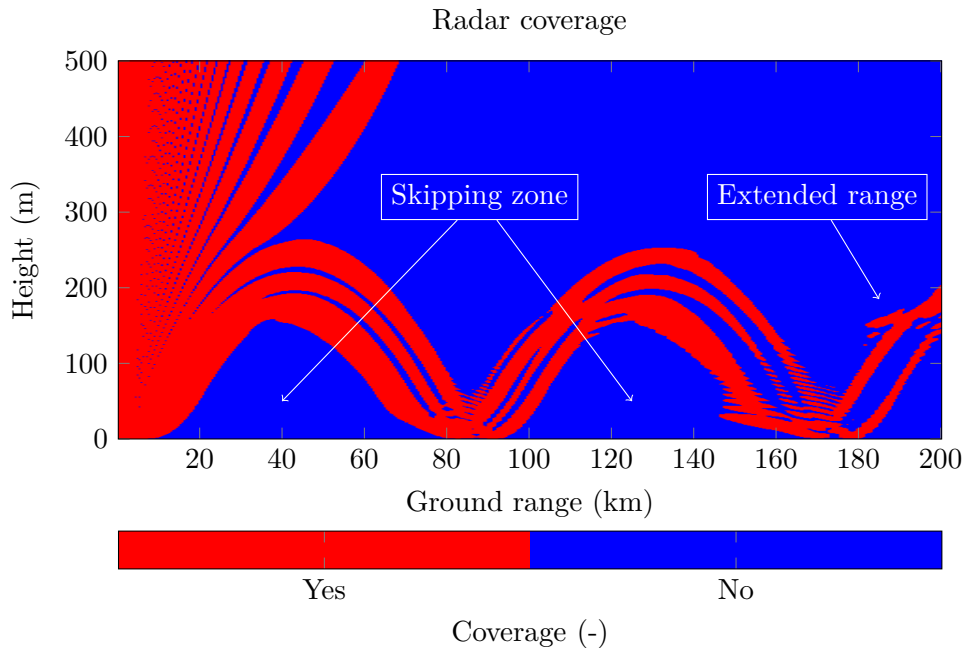


Figure 1-2: Environmental effects can result in tactical advantages and disadvantages. The propagation mechanism refraction may lead to ducting, resulting in extended detection ranges skipping zones and radar holes. The radar coverage assessment is computed by the TDA AREPS.

Operator awareness and understanding of the effects of prevailing environmental conditions on propagation and coverage can avoid confusion such as described above. It can also help operators to reduce the number of missed detections, improve emission control (EMCON) plans and exploit propagation effects to tactical advantage e.g. by using trapping to achieve an over the horizon detection capability. Additionally, understanding of the propagation effects allows correction for range and azimuth errors caused by propagation anomalies [2].

To help increase operator awareness and understanding of the effects of prevailing environmental conditions on propagation and radar performance, navies deploy different tactical decision aids (TDAs) based on a variety of radar propagation models, that allow radar performance assessment for specific radar-target combinations. The Royal Netherlands Navy (RNLN) uses two different propagation models as TDAs to assess radar performance: the Computer-Aided Radar Performance Evaluation Tool (CARPET) which is developed by the Netherlands Organisation for Applied Scientific Research (TNO) and the Advanced Refractive Effects Predictions System (AREPS) developed by the US Navy's Space and Naval Warfare Systems Command (SPAWAR). The TDAs are based on two different modelling methods, which both have advantages and disadvantages and will be covered in Chapter 4. Currently CARPET is integrated into the combat management systems (CMSs) of His Netherlands Majesty's (HNLN) naval ships. AREPS is yet to be integrated. Figure 1-2 shows radar coverage computed by AREPS⁶.

⁶All figures, unless stated otherwise, in this thesis similar to Figure 1-2 are generated using computations of AREPS.

1-2 Problem definition

Over the years models for modelling radar propagation and performance have matured to the extent that they produce sufficiently accurate results, provided that the environmental data input is also sufficiently accurate [4]. Especially the parabolic equation (PE) modelling method has demonstrated to provide results which are in excellent agreement with measured signal levels [4-8]. With the successful development of propagation models, the attention has shifted to methods for obtaining in situ atmospheric data⁷ that suffices in resolution and accuracy to feed the propagation model [4].

The importance of atmospheric data increased when the naval arena shifted from oceans to atmospherically more complex and dynamic coastal environments. Research shows that over the ocean the atmosphere varies little horizontally, therefore in the majority of cases the atmosphere can be assumed horizontally stratified [9]. This justifies the use of a single atmospheric vertical profile to model radar coverage accurately. A single vertical profile is easily obtained e.g. by deploying a radiosonde [10]. In coastal regions and near air mass boundaries, however, a single profile may not be sufficient as the atmospheric conditions may vary substantially with range and azimuth [4, 9]. To accurately model radar performance in a range- and azimuth-dependent environment, profiles at multiple ranges and azimuths are required. Assessments based on a single vertical profile in such environments may be wildly inaccurate. To rely on such assessments in operational scenarios may have dramatic consequences [11].

Figure 1-3 clearly illustrates the error which may occur when a single profile is used to assess radar coverage. The left image, Fig. 1-3(a), shows a radar coverage assessment that is obtained by using atmospheric data with a horizontal resolution⁸, R_{hor} , of 2.5 km whilst the right image, (b), shows radar coverage assessment that is obtained by using a single vertical profile with the assumption that the atmosphere is horizontally stratified. The atmospheric conditions were the conditions just north of the English Channel at 15:00 Z on 9 March 2014.

Methods for obtaining sets of range- and azimuth-dependent vertical profiles include frequent flights by manned or unmanned aircraft equipped with atmospheric sensors or dropsondes, and three dimensional remote sensing techniques (e.g. radar or light detection and ranging systems (lidars)) from ships, aircraft or satellites [4, 10]. These methods are currently still challenged by logistic or technological limitations.

Another method to obtain sufficient atmospheric data is through mesoscale numerical weather prediction (NWP) models. Mesoscale NWP is a rapid maturing technology that can provide sets of vertical profiles with a horizontal resolution of 1-10 km and forecast up to 48 hours into the future [12]. Hence, NWP models allow radar performance assessment for own as well as remote friendly or hostile systems up to 48 hours in advance; which can be a huge tactical advantage. NWP systems are currently used for radar performance assessment by several navies around the world, including those of the U.S., the U.K., Canada and New Zealand [13].

⁷Atmospheric data used for propagation modelling and radar assessment consists of the variation (vertical and horizontal) of the refractive index n . How a change in the refractive index affects radar propagation is explained in Chapter 2. How the refractive index depends on the atmospheric pressure, temperature and water vapour content is discussed in Section 5-1.

⁸Using atmospheric data with a horizontal resolution of 2.5 km is as measuring a vertical profile by radiosonde every 2.5 km along the propagation path.

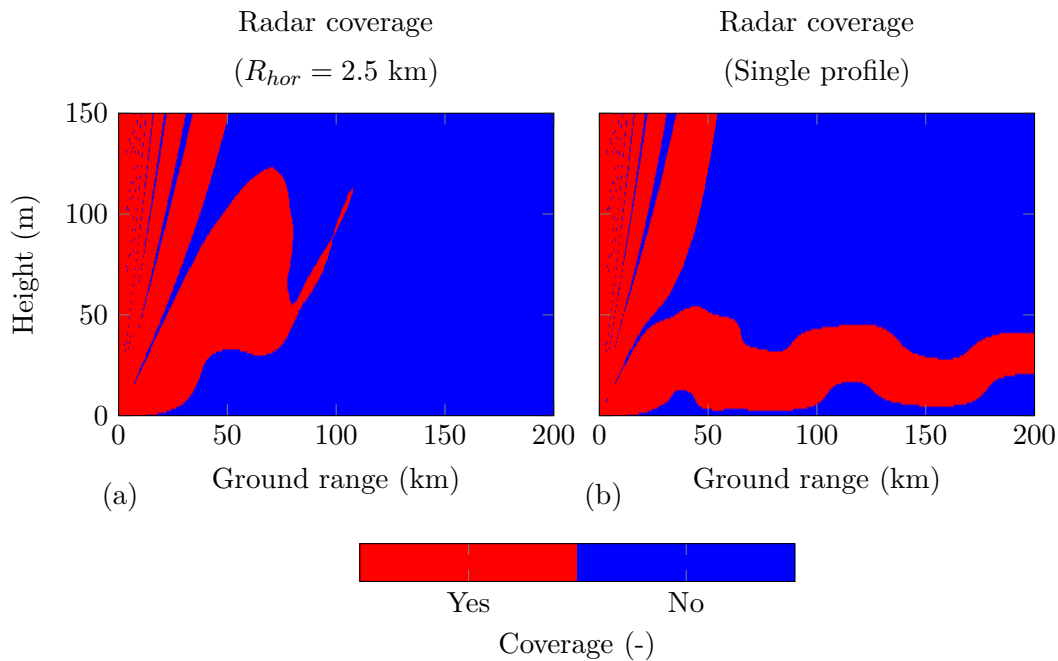


Figure 1-3: Radar coverage assessments illustrating the error that may occur when assuming a horizontally stratified atmosphere. Image (a) shows the coverage assessment that is obtained by using atmospheric data with a horizontal grid resolution, R_{hor} , of 2.5 km. Image (b) shows the coverage assessment that is obtained by using a single profile.

A problem is that the size and cost of the super computers on which NWP systems operate preclude their tactical deployment on board navy vessels. Also, the atmospheric data sets generated by NWP are currently too large for general distribution by satellite communications (SATCOM).

The US Navy currently solves these problems by distributing atmospheric NWP data sets, generated at shore facilities, to only major command platforms such as aircraft carriers. These platforms model performance for own and other platform sensors within the battle group based on the received NWP data [14].

All other platforms therefore receive just the performance assessments, without the underlying NWP data. The lack of supporting atmospheric data on board these other platforms precludes the use of ships own TDAs for further analysis, to assess radar performance in alternate scenarios, i.e. for other ship positions, or targets, or for different radar system settings. Any changes to the original scenario require further shore or major command vessel support. The dependence on shore based facilities and availability of secure data communication channels for the exchange of assessments requests and results is disadvantageous from an operational perspective.

Another approach to tackle the data distribution problem could be to reduce the atmospheric data set to a size that lends itself to general distribution, by reducing the horizontal grid and temporal resolution of the NWP data. For this it is important to assess the minimal horizontal grid and temporal resolution requirement for sufficiently accurate radar performance

assessment⁹.

The assessment of a minimal resolution requirement is also helpful in the general case, where atmospheric data is obtained through other means, e.g. by manned or unmanned aircraft, or remote sensing techniques. This yields the following question.

What is the minimal required horizontal grid and temporal atmospheric data resolution to assess radar performance with sufficient accuracy, under specific environmental conditions?

1-3 Related research

At present, notwithstanding the apparent importance of propagation modelling to the military, knowledge and research on minimal resolution requirements for spatial and temporal atmospheric data is sparse; for three reasons.

First, until recently research focused primarily - or even solely - on propagation modelling, given the required atmospheric data; generally as a single vertical profile assuming a horizontally and temporal homogeneous atmosphere. Only since propagation models have reached a level of maturity, the attention begins to shift toward the underlying atmospheric data [4].

The second reason is that resolution requirements for atmospheric data are use case specific, while the number of use cases is large. Different operational scenarios require different levels of propagation modelling accuracy [4]: a target engagement scenario, for instance, requires higher accuracy than determining a maximum detection range. Furthermore, given an assessment accuracy requirement, the resolution requirement for the underlying atmospheric data depends on characteristics of the atmosphere itself [4]: for a given propagation assessment accuracy, a surface-based duct formed by warm dry continental air advecting over cold water requires a different minimal resolution than does an evaporation duct found in the presence of a cold weather front. Given a propagation assessment accuracy requirement as well as specific atmospheric conditions, the required atmospheric data resolution still depends on the radar frequency as well as sensor and target positions (inside a duct, for instance, or above or below it and how far above or below). The possibilities are endless [4] ...

And finally: radar propagation experiments are hard and expensive. It is difficult and therefore expensive to obtain atmospheric data with a high spatial resolution as well as a high temporal resolution; the assets with which to conduct the experiments (ships, aircraft, radar systems, target drones) are expensive; the environment in which to conduct experiments is beyond control.

The research that is nonetheless available consistently indicates that spatial and temporal resolution of atmospheric data determine to a significant degree the radar performance modelling accuracy.

In the study of Dockery and Goldhirsh [4], which is based on two high resolution atmospheric data sets which were collected of the coast of San Nicolas Island and of Wallops Island¹⁰,

⁹Reducing file size can also be achieved by data compression techniques. However, till now there has been no success in developing techniques for reducing NWP file size such that it can be generally distributed by SATCOM whilst remaining sufficient for accurate radar assessment. In the near future the RNLN will start investigating the development of such techniques.

¹⁰The San Nicolas Island data collection experiment off the coast of Southern California on 19 March 1988 and the Wallops Island data collection experiment off the coast of Norfolk, Virginia on 26 April 1994.

the authors show that to assess propagation loss for low-altitudes with an accuracy of 5 dB, the minimal spatial resolution requirements are 6 m vertically and 17 km horizontally for the atmospheric conditions during the San Nicholas experiment. Under the conditions of the Wallops Island experiment, minimal resolutions of 10 m and 17 km were required for the same assessment accuracy. In both cases the prevailing atmospheric conditions resulted in a surface-based duct with considerable lateral inhomogeneity. The above results are based on the performance assessment of a 10 GHz radar at a height of 20 m. The same study also concludes that while the effects of varying resolution on propagation modelling accuracy are significant, they are not at all intuitively clear.

Whereas the study of Dockery and Goldhirsh, [4], considers resolution in the direction along the propagation path only, the study of Haack et al., [13], looks into three dimensional grid resolutions. Haack et al. states that for mesoscale NWP systems to provide sufficient input data to assess radar performance in duct environments horizontal grid spacing of at least 5 km and average vertical spacing of at least 60 m is required in the bottom 1 km of the atmosphere.

Findings of above studies and others are discussed in more detail in Section 3-2-5. None of the studies to date have yielded a general method to relate performance modelling accuracy requirements to the spatial and temporal resolution with which atmospheric conditions are to be modelled to support the required accuracy.

1-4 Thesis goals and approach

Within the Royal Netherlands Navy, the understanding of the effects of environmental conditions on radar performance is limited, as is the understanding of radar performance modelling in general. Currently the RNLN assumes a horizontally stratified, but otherwise homogeneous, atmosphere for the assessment of radar performance. As mentioned before, this assumption may yield inaccurate assessments and can potentially have dramatic consequences.

Besides increasing the understanding of radar performance modelling within the RNLN, there is, as explained above, in general a lot of research yet to be done in order to assess how accurate input atmospheric data needs to be exactly to accurately assess radar performance. For this, three thesis goals are set.

1. The first goal is to reach a better understanding of the mechanisms by which microwaves propagate through the (inhomogeneous) troposphere¹¹, of how these mechanisms determine radar performance/coverage, of electromagnetic propagation models and of the atmospheric data that is required for radar performance assessment. This goal includes providing clear and understandable documentation on the above listed topics and on the findings of this study.
2. The second and main goal of this thesis is to examine the sensitivity of radar performance assessment accuracy to the horizontal and temporal resolution of input data for different weather conditions over the North Sea, as well as the error as a result of assuming the

¹¹In this thesis only propagation through the troposphere is discussed. The troposphere has the most impact on microwave propagation (frequency band: 300 MHz - 300 GHz).

atmosphere to be laterally homogeneous and using a single refractivity profile for radar performance assessment. Note that vertical resolution is not investigated as obtaining data with sufficient vertical resolution is less problematic.

3. The third goal is to advise the RNLN on the use of radar propagation models which are facilitated by NWP systems for the assessment of radar performance in an inhomogeneous atmosphere, and on further research.

This first goal will be achieved through an extensive literature study, summarising the available literature and documenting each step, assumption and discovery made during this research. The produced documentation can be used as an introduction to radar propagation and performance modelling in inhomogeneous atmospheres, as a source for further research, et cetera.

The second goal will be achieved by comparing "ground truth" radar performance assessments to "spoiled" assessments¹². The ground truth resembles the true propagation and is in this thesis equal to the radar assessment based on high resolution NWP HARMONIE¹³ data. Note that the ground truth is not truly the propagation as obtained by measurements; however it will suffice for the purpose of this thesis since the assessment as well as the corresponding NWP data are realistic and in accordance with the North Sea weather scenarios that are investigated in this thesis. The spoiled assessments are based on the same NWP data set but then reduced in horizontal or temporal resolution. The radar assessments will be provided by AREPS.

The spoiled assessments will be compared to the ground truths using three different measures of accuracy specifically defined for this thesis. The measures will consider propagation losses, radar coverage and maximum detection ranges. In total 41 scenarios will be examined. The scenarios will differ in ship position, radar azimuth and weather conditions. The weather conditions to be considered are: cold and warm weather fronts, a warm sector, relative warm dry air advecting from land over water, high pressure systems and calm weather scenarios where standard propagation is expected. For all scenarios a 3.3 GHz radar that is similar to a naval medium range surveillance radar will be considered, with a small fighter as a target. The complete method for achieving this goal will be more elaborated upon in Chapter 6.

It is important to realise that achieving the second goal does not answer the general question concerning the minimal resolution requirements for accurate radar performance assessment presented in Section 1-2; as the results in this thesis apply only to the examined scenarios. This general question will not be answered as it lies beyond the scope of this thesis. To answer this question additional research, covering substantially more scenarios, would be required.

The third goal will be achieved by presenting this thesis and multiple presentations on this topic to the RNLN. As mentioned, for the assessment of radar performance, the RNLN currently assumes the atmosphere to be horizontally stratified. This thesis will clearly show

¹²The word "spoiled" in "spoiled assessments" indicates that these assessments are based on artificially reduced resolution data, as is often done in similar studies (e.g. [4]).

¹³Hirlam Aladin research on mesoscale operational NWP in Euromed (HARMONIE) is a NWP system developed by a cooperation between a number of European meteorological institutes. It provides accurate vertical atmospheric profiles for the prevailing conditions with a horizontal resolution of circa 2.5 km and a temporal resolution of 1 hour up to 48 hours ahead.

that this assumption is not always valid and should be made carefully as it may have dramatic consequences. There will be a lot to discuss.

Within this thesis the following step-by-step approach will be followed to achieve all three goals:

1. find and study relevant literature;
2. obtain realistic atmospheric NWP data for different weather conditions over the North Sea;
3. generate an environment model that is based on NWP data which is suitable for radar performance modelling;
4. define measure of goodness functions, in this thesis referred to as measures of accuracy, to compare spoiled radar assessments to ground truth;
5. define scenarios;
6. determine the ground truth radar assessments;
7. compare spoiled radar assessments to their corresponding ground truth;
8. analyse comparisons and connect results to the prevailing weather conditions;
9. draw conclusions.

At the end all results and findings will be documented and presented.

1-5 Thesis structure

This thesis is larger than master theses generally are. This is because this document provides, besides documentation on the research done for this thesis, a thorough introduction to radar propagation through inhomogeneous atmospheres, radar propagation models and the use of NWP systems for radar performance modelling. This thesis can therefore be used as an introduction to radar propagation in general or for educational purposes.

Chapters 2 through 4 and part of Chapter 5, provide an overview of relevant theory and literature. These chapters are a good introduction for those who are new to the field of radar propagation through inhomogeneous atmospheres and radar performance modelling. Readers who are already familiar with the underlying theory can scan or skip these chapters and start from Chapter 5.

The structure of this thesis broadly follows the step-by-step approach listed above. Chapter 2 presents a general overview of the different propagation mechanisms that affect electromagnetic waves propagating through the troposphere.

The combined effect of these mechanisms under varying circumstances is discussed in Chapter 3, along with a discussion of tactical implications. The main focus of this chapter lies on refractive phenomena such as: ducting, radar holes and lateral inhomogeneity.

In Chapter 4 the most common methods used to model radar propagation are discussed: the geometric optics method, the mode theory method, the parabolic equation method and a hybrid method known as the advanced propagation model (APM). This chapter will also look into the integration of propagation models in TDAs.

Chapter 5 provides an overview of consulted literature and introduces a new environmental model, based on NWP input data, for accurate radar assessment. Topics such as Debye's formula, obtaining upper and lower air profiles, profile blending and horizontal grid (profile) interpolation will be examined. The environmental model described in Chapter 5 is the model that was developed to obtain the results of this thesis.

In Chapter 6 the approach used to assess the accuracy sensitivity to the horizontal and temporal resolution of input data is presented. The method is explained and discussed, the measures of accuracy are motivated and the examined scenarios are defined.

The results of the sensitivity study are analysed and discussed in Chapter 7, and conclusions are drawn.

Chapter 8 reviews and discusses the three goals set above and summarises the conclusions based on the results of Chapter 7. Recommendations for further research and for the RNLN are also stated in this Chapter.

The last chapter, Chapter 9, is an additional chapter specifically of interest to the RNLN from an operational perspective. This chapter provides a short discussion on how the RNLN currently operates with regard to radar performance assessment and what, in the opinion of the author, should be changed to improve the overall accuracy of performance assessment on board HNLM naval ships. Governed by current disclosure policies, this chapter is excluded from the general publication of this thesis.

Propagation mechanisms

The ability to model the prevalent and forthcoming radar performance, under the prevailing atmospheric conditions, is operationally highly beneficial for a number of reasons, e.g. it increases the overall situational awareness (SA). To be able to model radar performance, the different mechanisms¹ that affect electromagnetic propagation should be known thoroughly. Electromagnetic waves propagating through the atmosphere near the earth's surface (i.e. through the troposphere) spread, refract, reflect, diverge, interfere, diffract, scatter and are attenuated. This chapter provides a concise introduction into these propagation mechanisms which play a role in the modelling of radar performance². The models/equations given in this chapter describe how the individual mechanisms affect radar propagation. The models can be combined to model electromagnetic propagation in non-complex atmospheric conditions.

2-1 Spherical spreading

Spherical spreading of electromagnetic energy is the most fundamental propagation mechanism [1]. In free-space, which is an isotropic and homogeneous loss-free environment, power that radiates outward from an isotropic antenna³ spreads uniformly in all directions over an increasing spherical surface (see Fig. 2-1). Hence, the one way propagation loss due to spherical spreading is inversely proportional to the square of the distance, d , between the transmitter and receiver. In decibels the spherical spreading loss, L_f , is given by:

$$L_f = 32.45 + 20 \log(f_{MHz}) + 20 \log(d_{km}), \quad (2-1)$$

¹The word mechanism as used in this thesis can be interchanged with the words phenomenon or effect. The word mechanism was chosen as it is used in many similar studies (e.g [1]). The word phenomenon is in this thesis generally associated with the weather.

²Radar frequencies, or microwave frequencies, lie between 300 MHz and 300 GHz. These frequencies are generally only affected by the atmosphere's troposphere. Therefore only mechanisms that occur in the troposphere will be discussed in this thesis.

³Isotropic antenna: a theoretical point source that transmits and receives electromagnetic energy equally in all directions [15].

where f_{MHz} is the operating frequency in MHz, and d_{km} the distance in km.

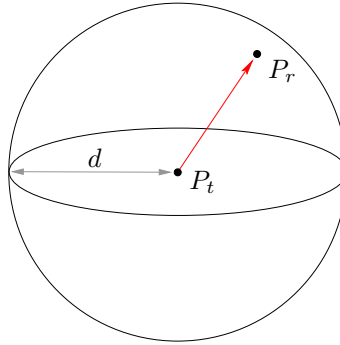


Figure 2-1: An (hypothetical) isotropic transmitter radiates uniformly in all directions. The propagation loss is inversely proportional to the square of the distance.

Far removed from the earth, where free-space spherical spreading is the only acting propagation mechanism, the power received⁴ in decibel, P_r , at a propagation distance d can be determined by:

$$P_r = 10 \log (P_t) + 10 \log (G_t) + 10 \log (G_r) - L_f, \quad (2-2)$$

where P_t is the transmitted power and G_t and G_r are the gains, a measure of antenna directivity, of respectively the transmit and receive antenna. For an isotropic antenna the gain is equal to 1.

2-2 Refraction

In a free-space environment, where the refractive index is constant, electromagnetic waves propagate in straight lines. In the troposphere however, electromagnetic waves refract due to the variation of the refractive index. When the refractive index changes along the wave's propagation path, or when the wave enters a different medium, the wave will curve towards the region with the highest refractive index, as illustrated in Fig. 2-2. The degree of refraction can be determined using Snell's law [16]:

$$n_1 \cos (\beta_1) = n_2 \cos (\beta_2) = \text{constant}, \quad (2-3)$$

where β_1 and β_2 are the grazing angles of the incident and refracted wave respectively, and n_1 and n_2 are the refractive index of medium 1 and 2 (see Fig. 2-2). The refraction index n is an electrical property of the propagation medium and is defined as the ratio between the speed of light in a vacuum, c_0 , and the speed of the wave through the medium, v (see Eq. 2-4).

⁴The received power density ($P_a = 10 \log (P_t) + 10 \log (G_t) - L_f$) is related to the free-space electric field strength at the receiver, E_0 , as follows: $P_a = E_0^2/120\pi$. The free-space electric field strength at the receiver will be used more frequent later on.

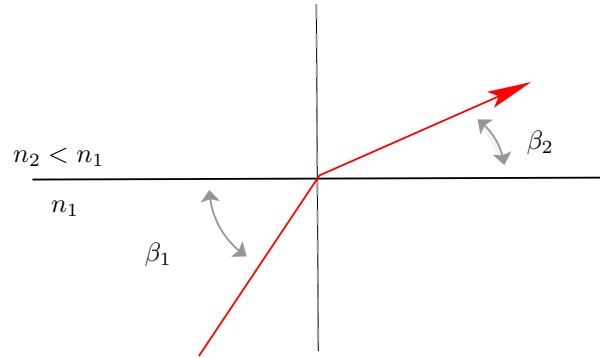


Figure 2-2: Illustration of the propagation mechanism refraction.

The refractive index varies in the troposphere due to the variation of pressure, temperature and water vapour content. For radio waves the refractive index of the troposphere is given by the empirical formula of Debye:

$$n = \frac{c_0}{v} = 1 + \frac{77.6}{T} \left[p + \frac{4810e}{T} \right] \times 10^{-6}, \quad (2-4)$$

where p is the atmosphere's barometric pressure in millibars, T is the temperature in degrees Kelvin, and e the partial water vapour pressure in millibars [17,18]. Debye's formula will be discussed in more detail in Section 5-1.

In the troposphere, the refractive index varies between 1.000250 and 1.000400 n-units [2]. Even though the variations of the refractive index are small, the mechanism refraction can have a significant, if not the most, impact on radar performance [1]. For example, refraction may result in a substantial increase or decrease of maximum detection ranges (see Section 3-3). This being said, the variations of the refractive index are not strong enough to significantly affect waves with a frequency below 100 MHz [19].

For studies of radio wave propagation the refractive index is not a convenient number. Therefore, in most studies, the refractivity N is used. The refractivity N is simply a conveniently scaled version of the refractive index n and is given by Eq. 2-5. In the troposphere the refractivity varies between 250 and 400 N-units and is given by:

$$N = (n - 1) \times 10^6 = \frac{77.6}{T} \left[p + \frac{4810e}{T} \right]. \quad (2-5)$$

Assuming that in an atmospheric layer the refractivity varies linear with height, and with height only, the propagation path of electromagnetic rays can be derived quite easily using Snell's law (Eq. 2-3). As illustrated in Fig. 2-3 the individual rays propagating under these conditions will propagate along a curved path with a curvature radius R_c . Derived, among others, in [20] and [16] the curvature radius of the ray's propagation path can be determined using:

$$R_c = \frac{-n}{\frac{dn}{dh} \cos(\beta)}, \quad (2-6)$$

where n is the refractive index at any point along the propagation path in the atmospheric layer, β is the grazing angle relative to the local horizontal at that point and dn/dh is the refractive index gradient of the atmospheric layer in which the wave is propagating. Depending on the sign of R_c the ray will curve away or towards the earth. With a positive R_c the ray will curve towards the earth. This occurs when the refractivity decrease with height ($dn/dh < 0$).

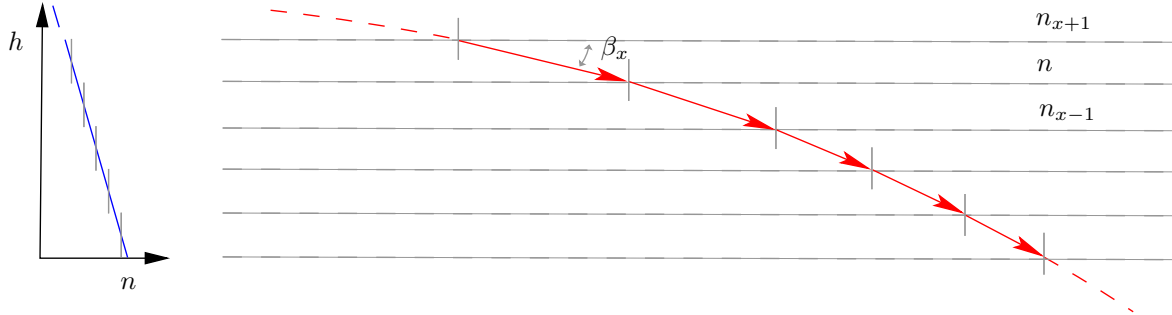


Figure 2-3: Electromagnetic waves, propagating through an atmospheric layer in which the refractivity varies linear with height, propagate along a curved path with a curvature radius of R_c (see Eq. 2-6).

For an example, Fig. 2-4 shows a set of electromagnetic rays (in red) traced through the standard atmosphere⁵ in which the refractivity decreases linear with 39 N-units/km ($dN/dh = -39$ N-units/km). Because the earth is projected flat in Fig.2-4 it seems that the rays are propagating away from the earth. This however is not the case⁶. To make this clear the black dashed ray shows the propagation path of a ray which travels in a straight line ($dN/dh = 0$). See how this ray curves away faster from the earth than the other solid black ray where as with the red rays $dN/dh = -39$ N-units/km. Both black rays have an initial departure angle of 0 relative to the local horizontal. Hence, the red rays must be curving towards the earth. The radar in Fig. 2-4 has a height of 20 m above the earths surface. More ray trace examples are provided in the propagation loss figures of Section 3-2-4.

2-3 Specular and diffuse reflection

2-3-1 Specular reflection

When an electromagnetic wave strikes a surface such as the earth, al or part of its energy will reflect from the surface and continue propagating along a new path [1]. When the reflected surface is smooth⁷, as for example a calm body of water, the grazing angle of the reflected wave, β_r , is equal to the grazing angle of the incident wave, β_i (see Eq. 2-7). This type of reflection is known as specular reflection and is illustrated in Fig. 2-5.

⁵The standard atmosphere is defined by the International Commission of Aeronavigation (ICA) as the atmosphere in which the refractivity decreases linearly with 39 N-units/km. The standard atmosphere will be discussed in more detail in Section 3-1-1.

⁶Appendix A provides a more detailed explanation on how to interpreted radar propagation assessment figures projected above a flat earth.

⁷A surface can be assumed smooth when the standard deviation, σ_h , is relatively small to the wavelength, λ , of the propagating wave.

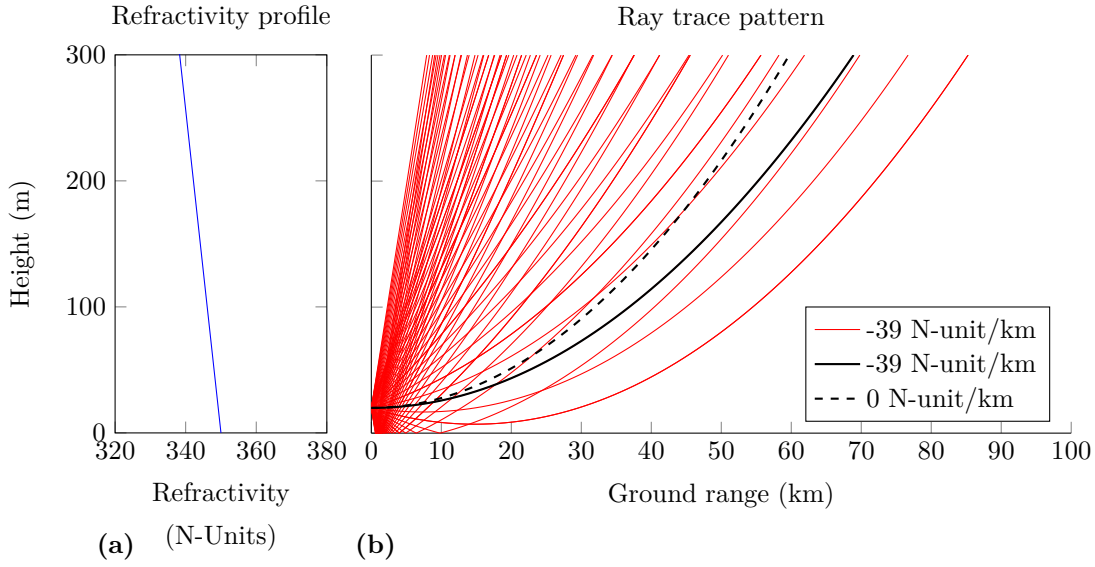


Figure 2-4: Ray trace pattern of rays propagating through a standard atmosphere over a smooth surface from a radar with a 20 m height above the surface. The figure was generated by MIRAT (microwave ray tracing). MIRAT is a ray tracing program developed by the author of this thesis [20].

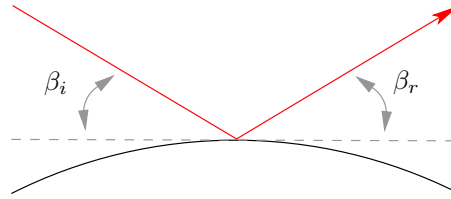


Figure 2-5: The law of reflection.

$$\beta_i = \beta_r \quad (2-7)$$

In general, a wave undergoing reflection, will experience a reduction in strength and a change in phase. Both effects can be described using the reflection coefficients of Fresnell, which gives the ratio of the reflected, E_r , and incident, E_i , complex electric field [21]. The magnitude of the coefficient is equal to the ratio of the reflected field strength to the incident field strength. The argument of the reflection coefficient is equal to the phase change of the wave at the reflecting surface. Fresnell's coefficients for horizontal, R_S^H , and vertical, R_S^V , polarisation are respectively:

$$R_S^H = \frac{E_r}{E_i} = \frac{\sin(\beta_i) - \sqrt{n_s^2 - \cos^2(\beta_i)}}{\sin(\beta_i) + \sqrt{n_s^2 - \cos^2(\beta_i)}}, \quad (2-8)$$

and

$$R_S^V = \frac{E_r}{E_i} = \frac{n_s^2 \sin(\beta_i) - \sqrt{n_s^2 - \cos^2(\beta_i)}}{n_s^2 \sin(\beta_i) + \sqrt{n_s^2 - \cos^2(\beta_i)}}, \quad (2-9)$$

where n_s is the refractive index of the reflecting surface and is given by:

$$n_s = \sqrt{\epsilon_r - i60\sigma\lambda}, \quad (2-10)$$

in which ϵ_r is the relative permittivity of the surface, σ the conductivity of the surface and λ the wavelength of the electromagnetic wave [1,21]. The electrical properties ϵ_r and σ are functions of frequency and type of surface, and can be determined from multiple sources, under which [22].

Figure 2-6 displays the magnitude and argument of the reflection coefficient at different grazing angles for an electromagnetic wave with a frequency of 3 GHz, reflecting off smooth sea water with a temperature of 20 °C and average salinity, resulting in a relative permittivity of $\epsilon_r = 70$ and a conductivity of $\sigma = 7$ S/m.

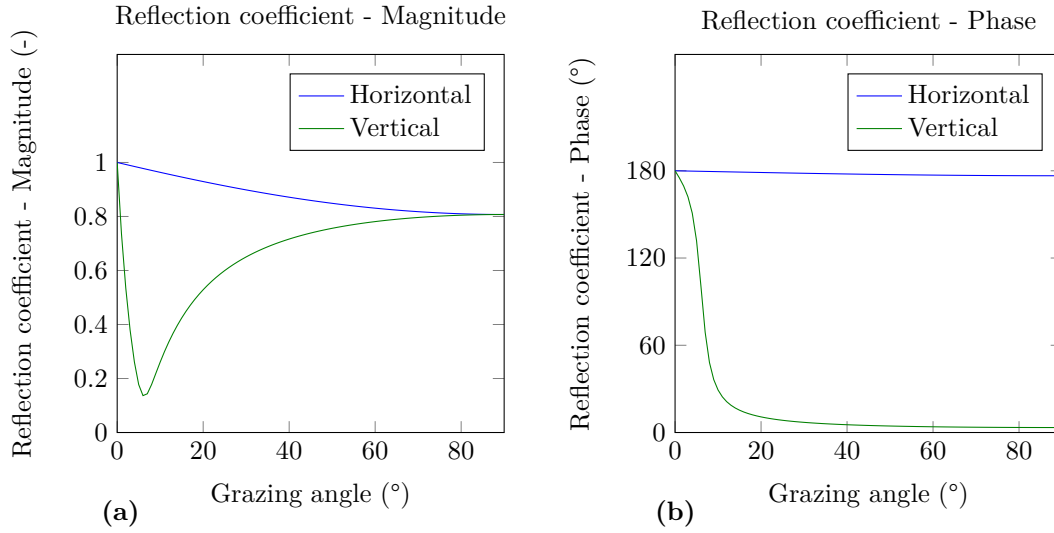


Figure 2-6: The magnitude (a) and argument (b) of the reflection coefficient at different grazing angles for a electromagnetic wave with a frequency of 3 GHz, reflecting off of smooth sea water with a temperature of 20°C and average salinity.

2-3-2 Diffuse reflection

When an electromagnetic wave reflects off a rough surface, e.g. a wind-roughened sea, only part of the reflected energy will reflect coherently in the specular direction [1]. The rest will scatter in different directions as shown in Fig. 2-7. For determining the field strength of the specular reflected wave the complex reflection coefficients of Fresnel must be modified for the effects of surface roughness [6]. According to the Miller-Brown surface roughness model the complex (coherent) reflection coefficient for rough surfaces in the specular directions, R_R , is:

$$R_R = R_S \exp \left[-2 (2\pi g)^2 \right] I_0 \left[2 (2\pi g)^2 \right], \quad (2-11)$$

where R_S is the Fresnel reflection coefficient given by Eq. 2-8 or 2-9, g the apparent ocean roughness and I_0 the modified Bessel function [6,23]. The apparent ocean roughness is given by:

$$g = \frac{\sigma_h \sin(\beta_i)}{\lambda}, \quad (2-12)$$

where σ_h is the standard deviation of the sea-surface elevation and can be estimated from the wind speed, u , by using the Phillips' saturation curve give by:

$$\sigma_h = 0.0051u^2. \quad (2-13)$$

To avoid the Bessel function in the Miller-Brown surface roughness model the complex (coherent) reflection coefficient for rough surfaces can be approximated by the International Telecommunication Union Radiocommunication sector (ITU-R) approximation [1]:

$$R_R = \frac{1}{\sqrt{1.6g^2 - 2 + \sqrt{(1.6g^2)^2 - 3.5g^2 + 9}}}. \quad (2-14)$$

Besides reflection from a surface, such as the surface of the earth, electromagnetic waves can also reflect off an atmospheric layer. This happens when there is a quick significant change in the refractive index, due to, for example, a quick variation of humidity within the atmosphere. However, significant reflection occurs mainly within the very high frequency (VHF) band and seldom at higher frequencies [24]. This because the change in the refractive index is not significant enough compared to the wavelength.

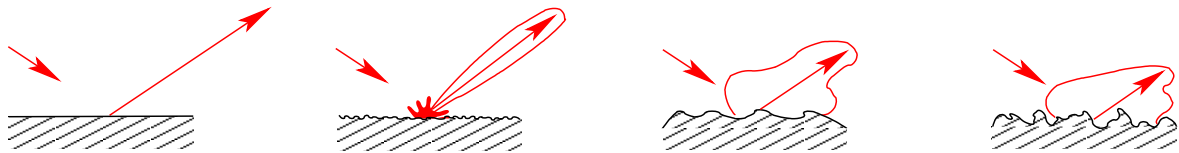


Figure 2-7: Illustration of specular (left) to diffuse reflection (right) transition with increasing roughness.

2-4 Divergence

When a divergent electromagnetic beam reflects of a plane surface the propagation direction of the beam alters but the angle of divergence remains the same. This however is not the case when a divergent beam reflects of a spherical surface such as the earth. A divergent beam will diverge at a greater rate after reflection from a spherical surface, as illustrated in Fig. 2-8 [1]. In other words, the beam suffers a spreading loss in addition to the normal spherical spreading.

The degree of divergence is given by the divergence factor, which is defined as the ratio of the field strength obtained after reflection off a spherical surface to that obtained after reflection off a plane surface [21]. For small grazing angles ($\beta_i < 5^\circ$), and by considering only the divergence in elevation⁸, the divergence factor is given by:

⁸Divergence in azimuth is negligibly small [21].

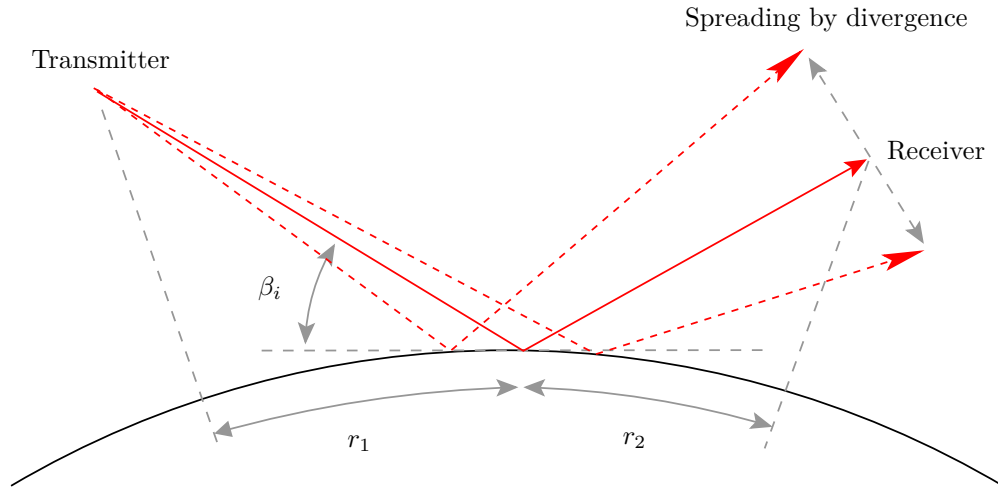


Figure 2-8: Illustration of divergence due to reflection off a spherical surface.

$$D = \left[1 + \frac{2r_1r_2}{kR_e(r_1 + r_2) \tan(\beta_i)} \right], \quad (2-15)$$

where r_1 is the ground range between the transmitter and the reflection point, r_2 the ground range between the receiver/target and the reflection point, k the effective-earth-radius factor⁹ and R_e the earth's radius. For extreme small angles ($\tan(\beta_i) = (\lambda/2\pi kR_e)^{1/3}$) the divergence factor is in substantial error. For greater grazing angles the divergence factor is close to unity. The derivation of the divergence factor is given in [21].

2-5 Interference

Interference is a phenomenon in which two or more electromagnetic waves superimpose to form a resultant wave with a greater or lower amplitude. In other words, when multiple rays intersect constructive or destructive interference will take place. Constructive and destructive interference will result in regions with an increased or decreased electric field strength and in some cases complete cancellation creating a null, also known as a blind spot.

Assume two electromagnetic rays, a direct ray (AC) and an indirect reflected ray (ABC), transmitted from a transmitter in point A and intersecting at the receiver/target in point C (see Fig. 2-9). Due to the different paths taken and the reflection of the indirect ray the two rays will differ at the point of intersection in electric field strength and phase. To determine

⁹Under normal refractive conditions, a radio wave curves downward with a curvature radius larger than the earth's surface. The ray's curvature makes modelling mechanisms such as divergence difficult. The effective-earth radius concept replaces the earth's true radius with a larger radius such that the relative curvature between ray and the earth's surface is maintained and the electromagnetic wave's propagation path becomes straight, thereby simplifying many computations [6]. The effective-earth-radius factor is equal to: $k = 1/[R_e(dn/dh)]$, where R_e is the earth's radius and dn/dh is the refractive index gradient. A simple solution such as the effective-earth-radius factor does not help in modelling the anomalous propagation discussed in Section 3-2.

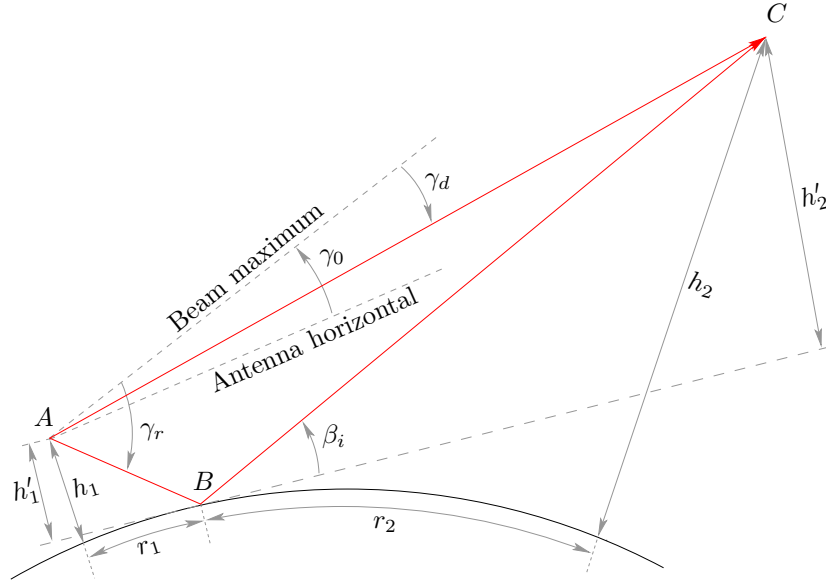


Figure 2-9: Geometry for determining the resultant electrical field strength due to two-ray interference.

the total electric field strength at the receiver the electric field strengths of the direct and indirect must be totaled, whilst taken the phase difference into account. For a two-ray scenario as shown in Fig. 2-9, and assuming a smooth earth, the ratio of the resultant electric field at the receiver to the free space field at the receiver is given by:

$$\frac{E}{E_0} = \sqrt{f_d^2 + [f_r D R_R]^2 + 2 f_d f_r D R_R \cos(\Omega)}, \quad (2-16)$$

where f_d and f_r are the direct and reflected antenna pattern factors corresponding to the angles γ_d and γ_r relative to the main beam pointing angle γ_0 above the local horizontal, D is the divergence factor given by Eq. 2-15, R_R is the reflection coefficient for rough surfaces given by Eq. 2-11, and Ω the total phase lag between the two intersecting rays. The total phase lag Ω is the sum of the phase lag due to reflection and the phase lag due to the difference in propagation path lengths. The phase lag due to reflection is the argument of the reflection coefficient given by Eq. 2-11. The phase lag due to the difference in path length is given by:

$$\delta = \frac{2\pi}{\lambda} \frac{2h'_t h'_r}{r_1 + r_2}, \quad (2-17)$$

where h'_t and h'_r are the effective transmitter and receiver/target heights given by respectively $h'_t = h_t - r_1^2/2kR_e$ and $h'_r = h_r - r_2^2/2kR_e$, where h_t and h_r are respectively the transmitter and receiver height. The model presented by Eq. 2-16 assumes that the transmitter height is always less or equal to the receiver height. If this is not the case, the transmitter and receiver height can be simply reversed and the calculation in Eq. 2-16 remains correct according to the Lorentz reciprocity theorem [6].

Equation 2-16 is only valid for grazing angles¹⁰ greater than $\tan(\beta_i) = (\lambda/2\pi kR_e)^{1/3}$, due

¹⁰The grazing angle can be computed using: $\beta_i = h'_t/r_1 = h'_r/r_2$.

to substantial errors in the divergence factor, and smaller than $\beta_i < 5^\circ$, due to small angle approximations. Also Eq. 2-16 is only valid for conditions in which only two waves interfere and the electrical path length difference is greater or equal to $\pi/2$. The region in which the mechanism interference is dominant is known as the interference region and lies before the radar horizon. For more information on interference see [1, 21, 23, 25]. The net effect of interference is illustrated in Fig. 2-10. The coverage diagram in Figure 2-10 shows the lobing pattern created by constructive and destructive interference (see also Fig. 3-1).

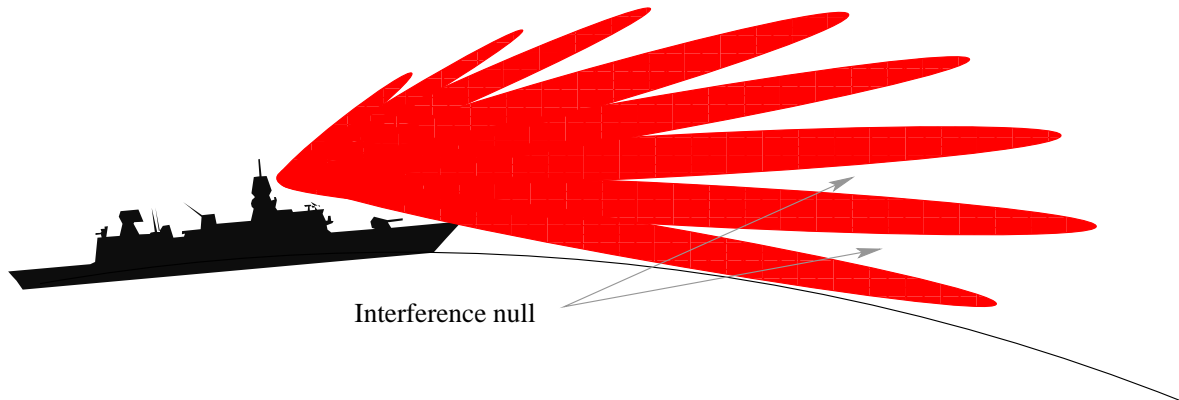


Figure 2-10: A radar coverage diagram illustrating the vertical lobe pattern caused by the propagation mechanism interference.

2-6 Diffraction

Diffraction is a mechanism by which waves curve around the edges of an opaque object and penetrate its geometric shadow region [26]. This allows detection of targets within the earth's shadow or behind obstacles (e.g. mountains) as shown in Fig. 2-11. In this section diffraction by the spherical earth and a single isolated obstacle is described. For diffraction by more complex surfaces refer to [16, 27–29].

2-6-1 Diffraction by the spherical earth

From just before to somewhat after the radar horizon, under normal atmospheric conditions, the dominant propagation mechanism is diffraction by the spherical earth [1, 2]. Due to diffraction, electromagnetic energy is able to propagate into the shadow zone created by the earth, resulting in small detection probabilities behind the radar horizon. In the diffraction region the electromagnetic field can be described by an infinite series of modes [23]. To obtain the electromagnetic field near the horizon a large amount of modes must be summed to accurately determine field strengths. However, at distance well beyond the horizon, the electric field strength can be described quite accurately using a single mode [6, 23, 27]. The minimum distance r_d by which a single mode solution is adequate is given by [6, 21]:

$$r_d = r_h + 230.2 \left(\frac{k^2}{f_{MHZ}} \right)^{1/3}, \quad (2-18)$$

where r_h is the radar horizon range and equal to $r_h = 3.572[\sqrt{kh_t} + \sqrt{kh_r}]$, where h_t and h_r are respectively the height of the transmitter and receiver/target.

A model based on a single mode residue solution, and which includes normal refraction effects, is given by the ITU-R [27]. Even though this model can strictly only be used at distance well beyond the horizon, it can approximate field strengths at the horizon with a maximum error of about 2 dB, in most cases. An outline of the model is given below. For more information refer to [6, 23, 27]. The diffracted electric field strength E , relative to the free space field strength E_0 , is given by:

$$20 \log \left(\frac{E}{E_0} \right) = F(\hat{R}) + G(\hat{H}_t) + G(\hat{H}_r), \quad (2-19)$$

where $F(\hat{R})$ is the distance gain term with \hat{R} as the normalised range over ground, and $G(\hat{H})$ the height gain term with \hat{H}_t and \hat{H}_r as the transmitter and receiver/target normalised height respectively. Normalised range and height are given by respectively:

$$\hat{R} = \beta \left(\frac{\pi}{\lambda (kR_e)^2} \right)^{1/3} r \quad (2-20)$$

and

$$\hat{H}_{t/r} = 2\beta \left(\frac{\pi^2}{\lambda^2 kR_e} \right)^{1/3} h_{t/r}, \quad (2-21)$$

where r is the ground range between the transmitter and receiver and $h_{t/r}$ the height of the appropriate terminal. The parameter β allows for the type of ground and polarisation to be taken into consideration, and is given by the semi empirical formula:

$$\beta = \frac{1 + 1.6K^2 + 0.67K^4}{1 + 4.5K^2 + 1.53K^4}, \quad (2-22)$$

where K is for horizontal, K_H , and vertical, K_V , polarisation:

$$K_H = \left(\frac{2\pi kR_e}{\lambda} \right)^{-1/3} [(\epsilon_r - 1)^2 + (60\lambda\sigma)^2]^{-1/4}, \quad (2-23)$$

and

$$K_V = K_H \left[\epsilon_r^2 + (60\lambda\sigma)^2 \right]^{1/2}. \quad (2-24)$$

For horizontal polarisation at all frequencies, and for vertical polarisation above 20 MHz over land or 300 MHz over sea, β may be taken as 1. This because at these frequencies electrical properties of the earth are not important. The distance gain term is given by:

$$F(\hat{R}) = \begin{cases} 11 + 10 \log(\hat{R}) - 17.6\hat{R} & \text{for } \hat{R} \geq 1.6, \\ -20 \log(\hat{R}) - 5.6488\hat{R}^{1.425} & \text{for } \hat{R} < 1.6. \end{cases} \quad (2-25)$$

The height gain term is given by:

$$G(\hat{H}) \cong \begin{cases} 17.6(B - 1.1)^{1/2} - 5 \log(B - 1.1) - 8 & \text{for } B > 2, \\ 20 \log(B + 0.1B^3) & \text{for } B \leq 2, \end{cases} \quad (2-26)$$

where B is equal to $B = \beta\hat{H}$. If $G(\hat{H}) < 2 + 20 \log(K)$, $G(\hat{H})$ can be set to $G(\hat{H}) = 2 + 20 \log(K)$ [27].

From the above it can be shown that propagation in the diffraction region is characterised by an exponential decay of signal strength, or with other words a linear increase of propagation loss in decibel with range [1]. Typical values for a standard atmosphere are 1 dB/km and 10 dB/km at respectively 1 and 10 GHz. The intermediate region between the interference region and the diffraction region where the single mode solution is valid, field strengths are frequently determined by bold interpolation with range. This technique gives remarkably good results for standard conditions [6].

2-6-2 Knife-edging

Another form of diffraction is knife-edging, which allows electromagnetic energy to penetrate in the shadow region of, for example, a mountain. Targets hiding behind these objects can therefore still be detected as shown in Fig. 2-11. And of course, counter detection by enemy targets using electronic support measures (ESM) within this regions will therefore also be possible.

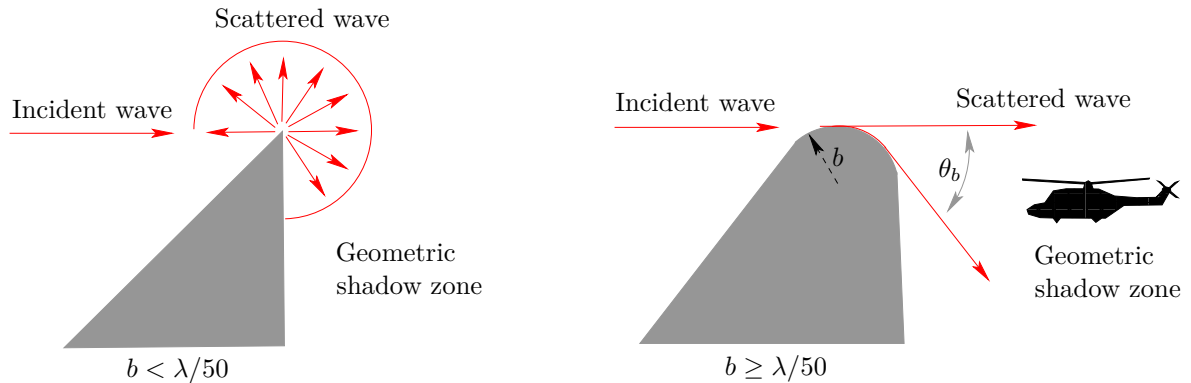


Figure 2-11: Diffraction, or knife-edging, is electromagnetic waves curving around the edge of an object and penetrating its geometric shadow region, which may result in small detection probabilities behind the object or in counter detection by enemy targets. b is the curvature radius of the object.

The knife-edge effect can be explained by the Huygens-Fresnel principle, which states that a well defined obstruction to an electromagnetic wave can act as a secondary source, and

creates a new wavefront which propagates into the geometric shadow region of the obstacle (see left image of Fig. 2-11). One method of determining the propagation loss, $J(\nu)$, due to knife-edging is by Fresnel surface integrals [27]:

$$J(\nu) = -20 \log \left(\frac{\sqrt{[1 - C(\nu) - S(\nu)]^2 + [C(\nu) + S(\nu)]^2}}{2} \right), \quad (2-27)$$

where $J(\nu)$ is given in decibel and $C(\nu)$ and $S(\nu)$ are the real and imaginary parts respectively of the complex Fresnel integral given by:

$$F_c(\nu) = C(\nu) + jS(\nu) = \int_0^\nu \exp \left(j \frac{\pi s^2}{2} \right) ds, \quad (2-28)$$

where ν is a dimensionless parameter describing the geometry of the knife-edge diffraction problem (see [27]). For more information on this method see [16, 27–29].

A more simplified method is once again based on a single mode residue solution. Two types of obstacles are considered: an isolated object with a sharp edge ($b < \lambda/50$, where b is the curvature radius of the object) as shown left in Fig. 2-11 and an isolated object with a curved edge ($b \geq \lambda/50$) as shown right in Fig 2-11. For the sharp edge the diffracted electric field strength, E , relative to the field strength when there is no obstacle (free-space), E_0 , is given by Sommerfield as:

$$\left(\frac{E}{E_0} \right)^2 = \frac{1}{2\sqrt{2\pi}} \left[\sec \frac{1}{2} (\theta_b + \pi) + \csc \frac{1}{2} (\theta_b + \pi) \right] \quad (2-29)$$

where θ_b is the shadow angle as shown in Fig. 2-11. For large edges ($b \geq \lambda/50$) a more general solution is given by Keller:

$$\left(\frac{E}{E_0} \right)^2 = \left(\frac{2\pi b}{\lambda} \right)^{1/3} \frac{C_0}{\sqrt{2}} \exp \left[-\tau_0 \left(\frac{2\pi b}{\lambda} \right)^{\theta_b/3} \right] \sin \left(\frac{\pi}{3} \right) \sqrt{\frac{\lambda}{2\pi}}, \quad (2-30)$$

where for a real dielectric surface the mode coefficients are $C_0 = 0.910719$ and $\tau_0 = 1.8557 \exp(\pi/3)$. For more information on the models of Sommerfield and Keller see [26].

Last but not least, it must be mentioned that diffraction due to both the spherical earth or an obstacle is frequency sensitive. The lower the frequency the stronger the diffraction.

2-7 Troposcattering

At ranges far beyond the horizon the electric field strength starts to decrease less rapidly than the diffraction model discussed in Section 2-6-1 would permit [21]. Hence, another propagation mechanism must contribute to the propagation of electromagnetic energy beyond the horizon.

According to Booker and Gordon, the major source of electromagnetic energy in the region beyond the diffraction region is due to energy scattering off of refractive index inhomogeneities

just before the horizon and propagating beyond the horizon (see Fig 2-12) [21]. This phenomenon is known as troposcattering and is the most dominant propagation mechanism beyond the diffraction region. Even though troposcattering mostly affects communication systems rather than radar systems, it is, for integrity reasons, discussed shortly.

There are various empirical models for determining propagation losses in the troposcattering region. The model given by Yeh is quite good and easy to implement [6]. According to Yeh the propagation loss (including free-space loss) in the troposcattering region is equal to:

$$L_s = 57 + 10\theta_s + 20 \log(d) + 30 \log(f_{MHz}) - 0.2(N_s - 310), \quad (2-31)$$

where L_s is the propagation loss given in dB, θ_s is the scattering angle in degrees, d is the ground range between the transmitter and receiver and N_s the surface refractivity [30]. The scattering angle depends on the geometry of the problem and is, for a smooth earth as shown in Fig. 2-12, equal to:

$$\theta_s = \frac{180}{\pi} \frac{d - d_1 - d_2}{kR_e}, \quad (2-32)$$

where d_1 is equal to $d_1 = \sqrt{2kR_e h_t}$ with h_t being the transmitter height, where d_2 is equal to $d_2 = \sqrt{2kR_e h_r}$ with h_r being the receiver height and d the ground distance between the transmitter and receiver (see Fig. 2-12). Scattering angles for other geometries, including over land, are given by [30].

Besides the propagation loss determined by Eq. 2-31, an aperture-to-medium coupling loss must be added to the total loss. There are several expressions for the coupling loss, but one relatively simple version is given by the ITU-R:

$$L_c = 0.07 \exp [0.055 (G_t + G_r)], \quad (2-33)$$

where G_t and G_r are the antenna gains of respectively the transmitter and receiver [31]. For more information on troposcattering see [16, 30].

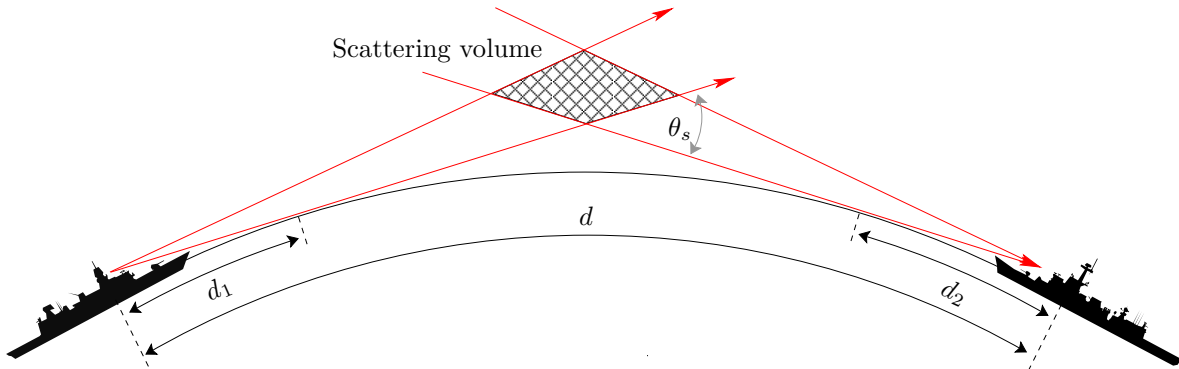


Figure 2-12: The troposcattering geometry. Troposcattering enables electromagnetic energy to propagate beyond the diffraction zone.

Figure 2-13 shows the one-way propagation loss as function of distance over the interference, diffraction and tropospheric scatterer region. The radar had an operating frequency of 3.3 GHz

and a height of 20 m. The target had a height of 20 m. Notice the interference nulls in the interference region before the radar horizon, which lies approximately at a distance of 37 km. See how the propagation loss increases linear between approximately 20 and 60 km. The linear increase of propagation loss is typical for the diffraction region. Also notice the decrease in rate at which the propagation loss increases. As mentioned this is due to troposcattering.

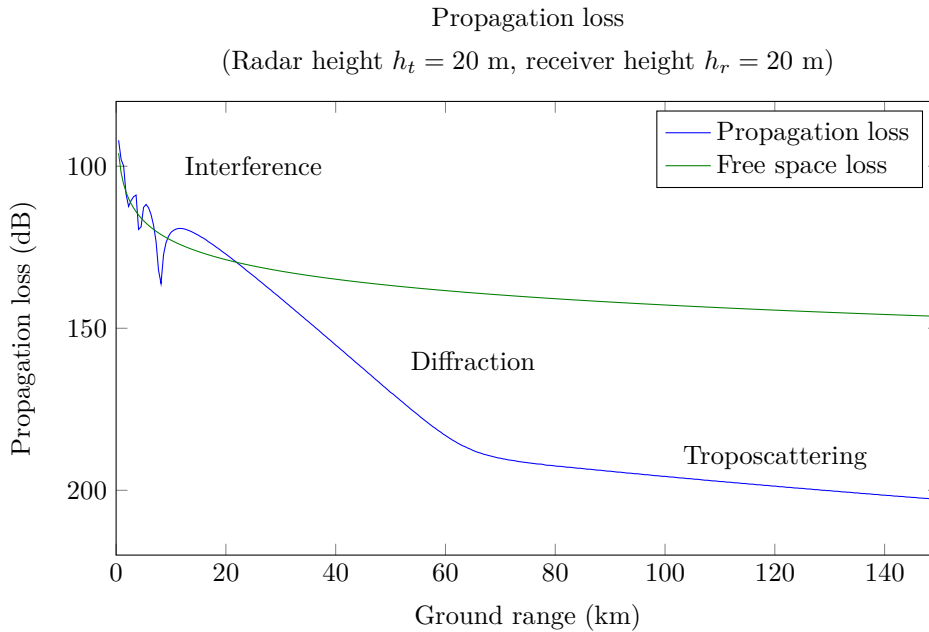


Figure 2-13: Propagation loss as function of range in a standard atmosphere above sea surface. The transmitter and receiver have a height of 20 m, the operating frequency is 3.3 GHz. Notice the different propagation regions. The radar horizon lies at approximately 37 km. Propagation losses are determined by AREPS.

2-8 Attenuation

The last propagation mechanism to consider is attenuation by atmospheric gases and meteorological phenomena such as rain, fog, snow and hail [26]. Attenuation of electromagnetic energy by gases is due to the interaction between the electromagnetic wave and the molecular dipole moments of the atmospheric gases [23]. The gases that are primarily responsible for attenuation are water vapour and oxygen¹¹ [1,23]. In general the effects of attenuation due to gases are small, especially for frequencies below 20 GHz and relative to the other propagation mechanisms, but should still be considered when waves propagate over large distances [1]. The degree of attenuation is given by the specific attenuation coefficient, α .

The specific attenuation at frequencies up to 1000 GHz due to dry air and water vapour, can be evaluated most accurately at any value of pressure and humidity by means of a summation of the individual resonance lines from oxygen and water vapour, together with small additional factors for the non-resonant Debye spectrum of oxygen below 10 GHz, pressure-induced

¹¹Above 100 GHz the attenuation due to Nitrogen also becomes significant [23,32]

nitrogen attenuation above 100 GHz and a wet continuum to account for the excess water vapour-attenuation found experimentally [32]. Figure 2-14 shows the specific attenuation due to gases, α_g , as function of frequency, for a standard atmosphere with a pressure of 1013 hPa, a temperature of 15°C, for the cases of a dry atmosphere and a water vapour density of 7.5 g/m³. The model used to generate Fig. 2-14 is given in [32].

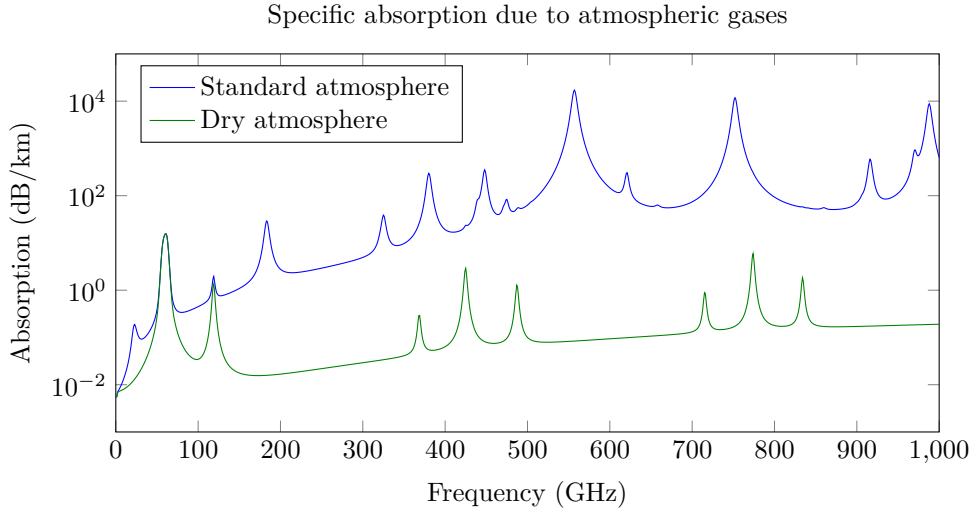


Figure 2-14: The specific attenuation due to gases as function of frequency for a standard and dry atmosphere.

Attenuation due to rain is generally characterised by the rain rate, R , and the drop size distribution [26]. A general model to estimate attenuation due to rain is given by:

$$\alpha_r = kR^\alpha, \quad (2-34)$$

where k and α are coefficients based on drop-size distributions, temperature, frequency and polarisation [26]. Figure 2-15 shows the specific attenuation due to rain as function of rain-rate, frequency and polarisation. The coefficients k and α are obtained from [32].

As mentioned, attenuation can also be caused by fog, snow and hail. Information on attenuation due to fog, snow and hail can be found in [26, 33]. To determine the total experienced attenuation the sum of all significant attenuation coefficient must be integrated along the entire propagation path [1].

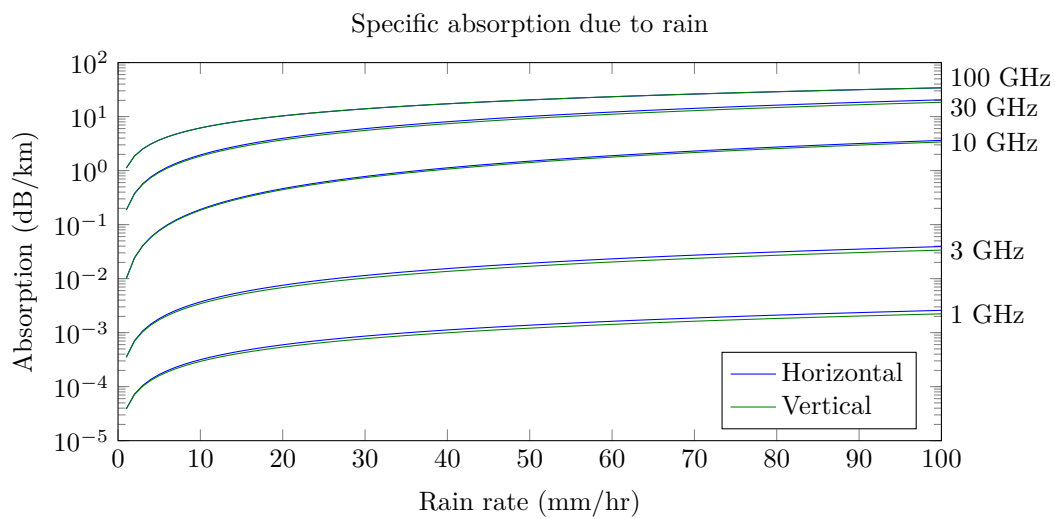


Figure 2-15: The specific attenuation due to rain as function of rain rate, polarisation (horizontal and vertical) and frequency (1, 3, 10, 30, 100 GHz).

Tropospheric propagation

In combination the mechanisms discussed in Chapter 2 determine how electromagnetic waves propagate through the troposphere under given atmospheric conditions. This chapter discusses the combined effect of the propagation mechanisms and the associated tactical consequences. It hereby shows the importance of having the ability to assess radar performance under prevailing atmospheric conditions.

Based on whether the atmospheric conditions conform to what is generally considered as normal conditions, the resulting propagation is referred to as normal or anomalous propagation. The first and second section of this chapter describe normal and anomalous propagation respectively. The third section discusses some of the tactical consequences anomalous propagation may lead to. Because refraction is the propagation mechanism which is most likely to substantially alter the radar performance [1], the focus primarily lies on refractive effects.

3-1 Normal propagation

3-1-1 Standard atmosphere

The earth's atmosphere is a collection of gases, under which nitrogen, oxygen, argon, carbon, together with suspended particles of liquids and solids. The lowest portion of the atmosphere is the troposphere and extends from the earth surface to an altitude of 8 to 10 km at polar latitudes and up to 18 km at the equator [2].

According to Debye's formula (Eq. 2-5) the refractivity of the troposphere depends on atmospheric pressure, temperature and water vapour content. Due to differential heating of the earth's surface, sporadic evaporation of water from oceans, lakes, rivers and other water reservoirs and horizontal and vertical winds, the atmospheric pressure, temperature and water vapour content varies horizontally and vertically throughout the troposphere, resulting in a variation of refractivity [2].

On global scale the troposphere can be assumed to be stratified in horizontal layers, meaning that pressure, temperature and water vapour content varies only with height and not with

range [19]. In an atmosphere at rest, it can be shown that the pressure decreases exponentially with height, dropping to a fraction $1/e$ of its value at the surface at a height of approximately 8 km [19]. The troposphere is characterised by an average linear temperature decrease of 6.5°C per kilometre [2, 34]. The concentration of water vapour in the troposphere decreases rapidly with height. At an altitude of 1.5 km, the water vapour content is approximately half of that at the surface [2].

Since the barometric pressure and water vapor content¹ of the atmosphere decreases rapidly with height, while temperature decreases relatively slow, the refractivity (normally) decreases with altitude [2]. More specifically the net average effect of the variations in pressure, temperature and water vapour results in a refractivity which decreases exponentially with increasing height in such a manner that at low altitudes, up to 1 km, the decrease is almost linear with an average gradient of $dN/dh = -39$ N-units/km [2, 9, 17, 19]. The gradient of -39 N-units/km is based on long term averages of the mid-latitude atmosphere [19]. In 1925 the International Commission of Aeronavigation (ICA) defined an atmosphere with a refractivity gradient of -39 N-units/km as the standard atmosphere [23].

Before continuing, it should also be mentioned, that generally under standard atmospheric conditions it is assumed that the earth's surface is smooth; and that thereby effects due to terrain, e.g. knife edging, are not considered. Effects due to reflections from a rough ocean surface are generally taken into account.

3-1-2 Standard propagation

The standard propagation defined above is used excessively in radar measurements, modelling and other radar applications. The combined effect of the propagation mechanisms discussed in Chapter 2 under standard conditions is shown in Fig. 3-1. Figures 3-1(a) and (b) show respectively the refractivity profile of the standard atmosphere and the two-way propagation loss². The radar has a height of 20 m above the sea surface.

In Fig. 3-1 (b) the effects of different propagation mechanisms are clearly visible. First notice that the propagation loss increases with distance from the radar. This is due to the propagation mechanisms spherical spreading and attenuation. The lobing pattern due to interference between the direct and surface reflected wave is also clearly visible. The mechanism refraction is illustrated by the dashed black ray. The black dashed line is the straight propagation path of a ray propagating through a free space environment ($dN/dh = 0$) with an initial grazing angle of 0. Notice how the dashed black ray propagates faster away from the earth than the interference lobes. Hence, in a standard atmosphere, refraction curves the electromagnetic energy towards the earth (see also Appendix A). Last but not least, diffraction by the earth is shown by the linear increase of propagation loss along the last interference lobe with increasing ground range. The mechanism troposcatter is not visible due to the chosen color map interval. Looking only at the propagation loss at a height of 20 m will give the results shown in Fig. 2-13.

¹It is the humidity gradient that mostly dominates the refractivity [10] (see also Eq. 2-5).

²The ratio, expressed in decibels, of the effective radiated power transmitted in the direction of maximum radiation of the antenna pattern to the power received at any point by an omnidirectional antenna.

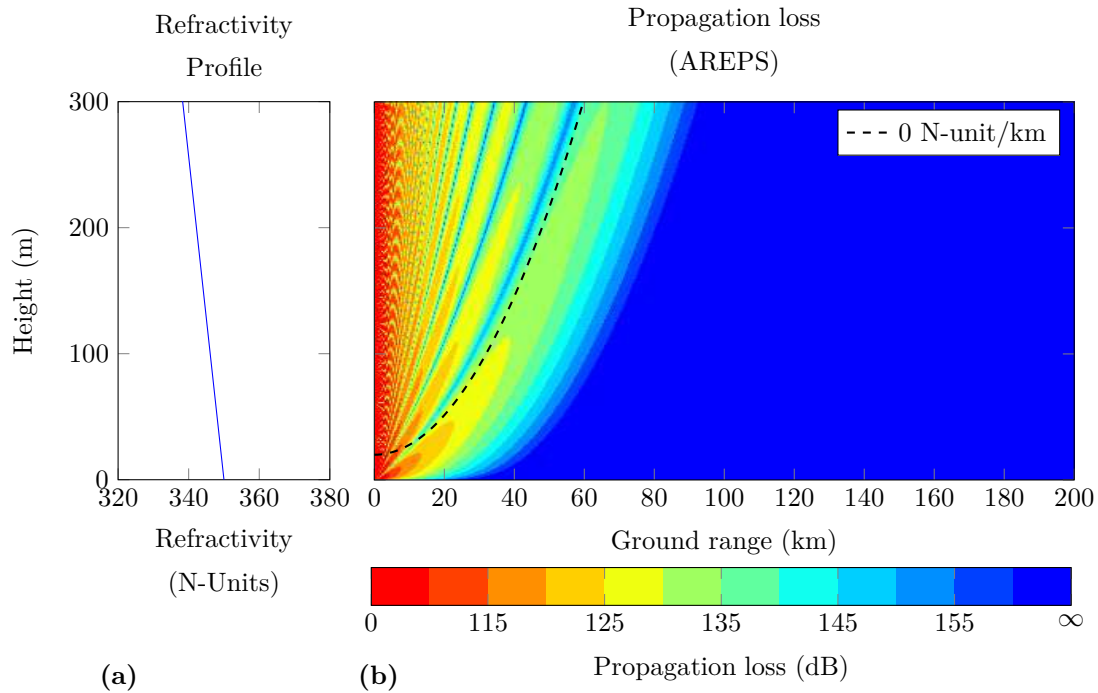


Figure 3-1: Propagation losses in a standard atmosphere (b) with the associated refractivity profile ($dN/dh = -39$ N-units/km) (a). The propagation losses are computed using AREPS [2].

The resulting radar coverage, with a detection probability of $P_D = 0.95$ and a false alarm probability of $P_{FA} = 10^{-6}$, is illustrated in Fig. 3-12(a) using the colour grey. Many navy radar operators who are unaware of the underlying physics of radar propagation, assume to have this radar coverage. Even though this is true for the average case, depending on the local prevailing weather conditions, it should not be assumed automatically.

Atmospheric conditions that cause similar propagation as under standard conditions are known as normal conditions. Normal propagation occurs when the refractivity gradient varies between 0 and -79 N-units/km [1, 2].

3-2 Anomalous propagation

The combined effect of the propagation mechanisms under non standard atmospheric conditions can result in anomalous propagation that significantly differs from normal propagation. Anomalous propagation is characterised by vertical profiles that are substantially different from the standard atmosphere profile, or by propagation paths that are located over variable terrain [1].

3-2-1 Anomalous refraction

Anomalous refraction is characterised by how the refractivity varies with height. Defined by the refractivity gradient the following anomalous propagation conditions are distinguished:

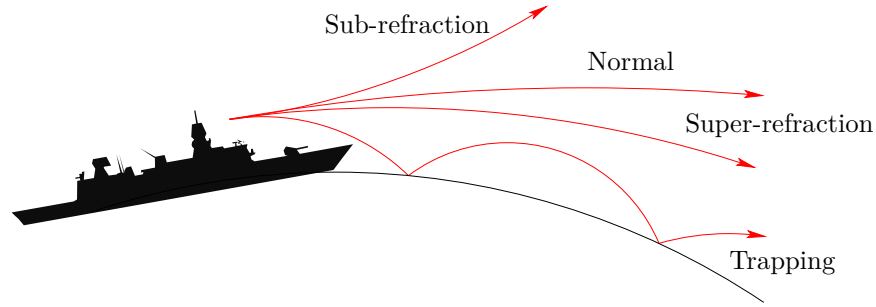


Figure 3-2: Refractive conditions

Table 3-1: Refractive conditions [2].

Condition	dN/dz (N-unit/km)	dM/dz (M-unit/km)
Sub-refractive	$0 < dN/dz$	$157 < dM/dH$
Normal	$-79 < dN/dz \leq 0$	$79 < dM/dH \leq 157$
Super-refractive	$-157 < dN/dz \leq -79$	$0 < dM/dH \leq 79$
Trapping	$dN/dz \leq -157$	$dM/dH \leq 0$

sub-refractive, super-refractive and trapping [1, 2]. The different conditions are discussed in more detail below. The conditions and their refractivity gradients are summarised in Table 3-1 and Fig. 3-2.

Table 3-1 also gives the modified refractivity gradient, dM/dh . The modified refractivity is an other conveniently scaled version of the refractive index, n , which takes the earth's curvature into account [1, 4, 16]. Hereby, trapping conditions, which are the most significant, are easily identified in the modified refractivity profile by their negative gradient. The modified refractivity profile is defined as:

$$M = N + h/R_e \times 10^3 = N + 0.157h, \quad (3-1)$$

where N is the refractivity and given by Eq. 2-5, h is the height above the earth's surface and R_e is the radius of the earth and equal to 6370×10^3 m [1, 4, 16].

3-2-2 Sub-refraction

Under certain conditions the distribution of water vapour and temperature may result in an increase of refractivity with height ($dN/dh > 0$ N-units/km and $dM/dh > 157$ M-units/km) [2]. Under these conditions the electromagnetic energy will bent upwards away from the earth rather than bend downwards towards the earth as under normal atmospheric conditions. The bending of electromagnetic waves away from the earth is termed sub-refraction and results in a decrease of the maximum detection range (see Fig. 3-12(a)). Even though sub-refractive conditions occur infrequently, it still must be taken into account when assessing radar performance [2].

As seen in Eq. 2-5 the refractive index may decrease with height when there is an increase of water vapour content. An increase of water vapor content is generally caused by the advection of warm moist air over a relative cold surface or air mass [2]. Due to the fact that cold air can hold less water vapour than warm air, the moist warm air directly adjacent to the colder surface or air mass will lose water vapour due to condensation, resulting in an increase of water vapour with height and hence an increase of the refractivity. These conditions occur in areas where surface temperatures reach between 10 and 30°C and have relative humidities of above 60%, for example: off the coast of the Western Mediterranean, the Red Sea and the Indonesian Southwest Pacific [2]. The accompanying temperature inversion is generally too weak to counter the increase of water vapour with height [34]. Similar atmospheric conditions occur near warm weather fronts and in warm sectors [2, 34].

According to Eq. 2-5 a strong decrease of temperature with height will also lead to a sub-refractive layer. However, the strong decrease of temperature is generally always countered by a decrease of water vapour which has a more significant impact on the refractivity. If this is the case the sub-refractive layer will not develop.

3-2-3 Super-refraction

In conditions where water vapour content decreases faster with height than under normal atmospheric conditions, and/or a temperature inversion is present, the refractive index will decrease more rapidly than under normal conditions. Under these conditions electromagnetic waves will curve stronger towards the earth, resulting in an increase of the maximum detection range (see Fig. 3-12(a)).

Super-refraction occurs when the curvature radius of the electromagnetic wave's propagation path is smaller than under normal conditions and larger than the curvature radius of the earth. These conditions are characterised by a refractivity gradient between -157 and -79 N-units/km or a modified refractivity gradient between 0 and 79 M-units/km [1, 2].

Super-refractive layers adjacent to the surface may develop when dry air advects over water or a moist surface, resulting in a rapid decrease of water vapour content; or when warm air advects over a relatively cold surface, resulting in a temperature inversion [2, 34]. When the advected air is dry and relatively warm a very strong super-refractive layer will develop, however it could also become a trapping layer (see Section 3-2-4). Super-refractive layers adjacent to the surface generally occur above coastal waters [34].

Super-refractive layers aloft may develop within high pressure systems where subsidence of air causes heating as the air undergoes compression. The subsidence leads to a layer of warm dry air overlaying a cool moist layer of air [2]. Hence the rapid decrease of water vapour and the temperature inversion. As above, if the water vapour decrease and/or the temperature inversion are too extreme, a trapping layer may develop rather than a super-refractive layer.

3-2-4 Trapping and ducting

Under similar circumstances as super-refraction, but where the temperature inversion and/or the decreases of humidity is more extreme, the electromagnetic waves will propagate with a curvature radius smaller or equal to the earth's radius [1, 34]. The electromagnetic waves

will strongly curve towards the earth and will either strike the earth's surface and undergo surface reflection, as illustrated in Fig. 3-2, or enter a region of sub, normal or super-refractive conditions and propagate away from the earth, only to re-enter the area of trapping conditions and refract back down [2]. In other words the electromagnetic energy is trapped within an atmospheric layer. A trapping layer is defined as an atmospheric layer in which the refractive gradient is below $dN/dh \leq -157$ N-units/km or the modified refractivity gradient is negative, $dM/dh \leq 0$.

The layer in which the electromagnetic energy is trapped is called a duct, and can be compared to a waveguide which follows the curvature of the earth (see for example Fig. 1-2) [2]. Ducting is the most notable effect of the propagation mechanism refraction, and can significantly affect radar performance. For example, ducting can alter the normal lobe pattern and lead to a significant increase of detection range, as will be shown below [2]. The frequencies above about 1 GHz up to 20 GHz are most affected by ducting [7]. For higher frequencies other propagation mechanisms play a predominant role (e.g. attenuation).

A ducting layer will only trap radiowaves if certain geometrical constraints apply. In particular the angle of incidence of electromagnetic energy at the layer must be very small. A simple rule of thumb, derived from the total-internal-reflection condition of geometric optics is that the maximum angle of incidence θ_{max} , in degrees, is related to the change in refractivity ΔN across the layer by $\theta_{max} = 0.081\sqrt{|\Delta N|}$ [19].

In a marine environment there are three distinct types of ducts: the evaporation duct, the surface duct and the elevated duct [1]. The surface duct can further be categorised into two sorts of ducts: the standard surface duct and the surface-based duct.

Evaporation ducts

The evaporation duct is a very persistent phenomenon and is found nearly everywhere over large bodies of water [1, 2]. Due to its influence on radar performance and its persistency much effort has gone into understanding the evaporation duct.

For continuity reasons, the air immediately adjacent to the water is (nearly) saturated and thus has a relative humidity of nearly 100%. However, this high humidity generally decreases rapidly with height until an ambient humidity value is reached, resulting in a rapid decrease of the refractive index and thereby creating a trapping layer adjacent to the surface [1]. The rapid decrease of humidity results in a modified refractivity profile as shown in Fig. 3-3(a). The trapping layer is indicated by the red dashed line. For an evaporation duct to develop a temperature inversion is not required.

The effect of the evaporation duct is shown in the propagation loss figure Fig. 3-3(b). See how the energy of the lowest optical interference lobe bends towards the earth resulting in low propagation loss beyond the radar horizon relative to the normal atmosphere. For clarity, individual rays are traced and shown in black. Note how the rays strongly refract towards the earth, followed by reflection off the earth surface only to be refracted back down. In other words the rays are trapped. The propagation losses and ray propagation paths are computed by respectively AREPS and the Microwave Ray Tracing Program (MIRAT)³.

³MIRAT is a ray trace program developed by the author of this thesis in [20].

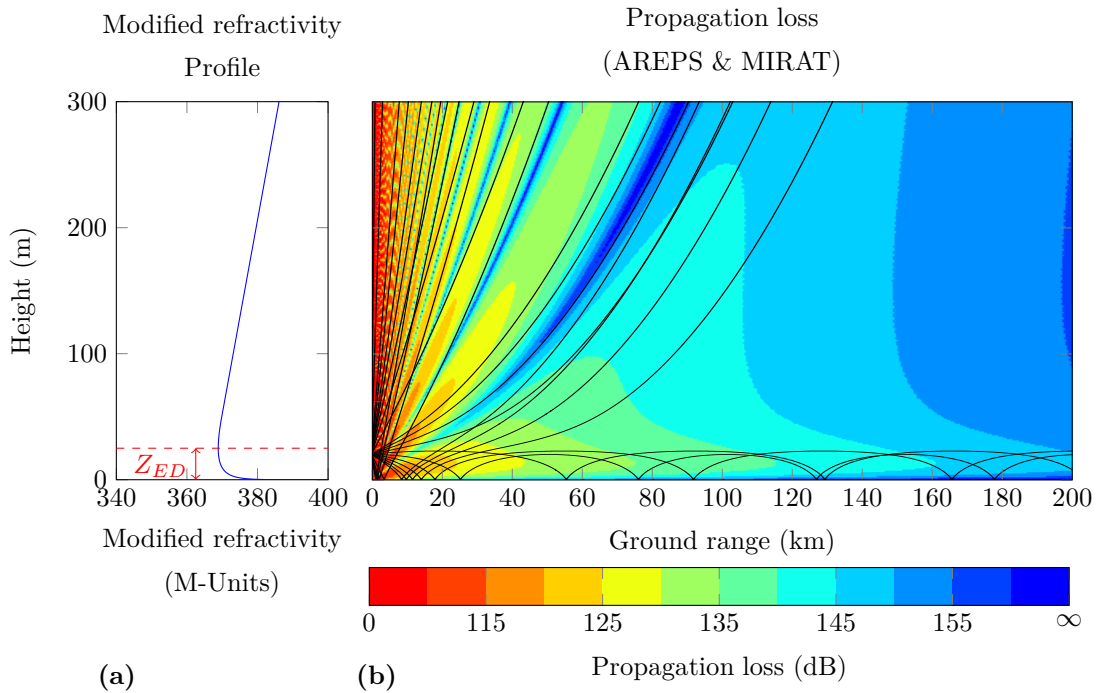


Figure 3-3: Propagation losses in an evaporation duct with a duct height of $z_{ED} = 25$ m (b) and associated modified refractivity profile (a). The propagation losses and ray traces in (b) are computed using respectively AREPS and the ray tracing program MIRAT. MIRAT is developed by the author of this thesis [20]. The profile is obtained using the equation $M(z) = M_0 + 0.13(z - z_d \ln((z + z_0)/z_0))$, where M_0 is the modified refractivity at the surface, z_d the aerodynamic roughness parameter equal to 1.5×10^{-4} m, and z the height above sea level [7].

The height where the modified refractivity reaches its minimum is known as the evaporation duct height, z_{ED} , which is a measure of the duct's strength or in other words its capability to trap electromagnetic energy. The evaporation duct height varies between a metre or two at northern latitudes during winter nights and 40 m at tropical latitudes during summer days, with a long term world wide average of 13 m [2]. Table 3-2 gives annual averages of the evaporation duct height for different regions world wide. The evaporation duct profile shown in Fig. 3-3(a) has an evaporation duct height, z_{ED} , of 25 m.

The duct's strength is besides a function of the water vapour gradient also a function of atmospheric stability and wind velocity. In unstable windy conditions the evaporation duct will be stronger developed than in stable calm conditions [2]. This being said, too much wind will result in the dissemination of water vapour and thereby the dissipation of the evaporation duct [34]. Generally in cold dry air masses behind cold weather fronts the evaporation duct is developed strongly. In the proximity of warm weather fronts or in the warm sector the evaporation duct is mostly weak.

The capability of the evaporation duct to trap electromagnetic energy is also frequency dependent [1]. The lower the frequency the stronger/higher the duct must be to trap energy. A rough approximation of the minimum frequency, also known as the cut-off frequency, CoF , which is trapped, is given by Eq. 3-2, where z_{ED} is the evaporation duct height in metres

Table 3-2: Annual averages of evaporation duct heights [1].

Region	Average duct height (m)
Labrador Sea	3.5
North Sea	6.4
Norwegian Sea	6.7
Bay of Biscay	8.2
Adriatic Sea	10.9
Aegean Sea	13.1
Arabian Sea	14.8
Gulf of Mexico	16.6
Caribbean Sea	17.6
World wide	13.0

[35]. For most practical applications, the lower frequency limit at which the electromagnetic energy is trapped by an evaporation duct is 3 GHz. The most affected frequency seems to be around 18 GHz [1]. Even though higher frequencies are affected by the evaporation duct, its effect is limited due to other propagation mechanisms such as attenuation and scattering from rough surfaces.

$$CoF = 3.6 \times 10^{11} \times z_{ED}^{-3/2} \quad (3-2)$$

In open sea conditions where sea temperature and meteorological conditions vary little, the evaporation duct will extend for hundreds of kilometres with almost the same duct height. In coastal areas however, the duct height may vary significant with range.

Surface ducts

Surface ducts are globally less common than evaporation ducts, but affect radar propagation much more dramatic. The surface duct develops mainly over coastal waters such as the North Sea (especially in the English Channel), or over enclosed seas surrounded by warm dry land such as the Mediterranean and the Gulf Area [19]. In some regions surface ducts can occur with an annual frequency of up to 58% (see also Table 3-3). Unlike the evaporaton duct the surface duct is not particular sensitive to frequency. Effects may already be noticeable at frequencies as low as 20 Mhz. Surface ducts are responsible for most reports of extreme long over the horizon detection and communication ranges [9].

The surface duct is characterised by a temperature inversion [4]. The temperature inversion directly results in a more rapid decrease of refractivity. Further more, the temperature inversion suppresses the unstable vertical airflow, allowing sharp humidity gradients to form [17]. The result is a strong trapping layer near the earth's surface. Surface ducts develop under the following conditions.

Surface ducts are mostly formed due to advection, caused by the interaction between low and high pressure systems, of warm dry air from land over relatively cold water. The interaction of the continental air with the underlying cooler and moister air results in the formation of

Table 3-3: Annual averages of surface duct heights and percentages of annual occurrence [1, 7, 36].

Region	Average duct height (m)	Occurrence (%)
Northern Atlantic	42	1.3
Eastern Atlantic	64	2.8
Canadian Atlantic	86	4.1
Western Atlantic	118	9.8
Mediterranean	125	13.4
Persian Gulf	202	58.0
Indian Ocean	110	13.4
Tropics	99	13.6
Northern pacific	74	6.2
World wide	85	14.0

a temperature inversion and a rapid decrease of water vapour content, producing a strong trapping layer [19]. These types of surface ducts are typically less than 200 m thick and can exist persistently for several days being the strongest in the early evening [2, 19]. Depending on the land-sea temperature difference these ducts may persist well offshore to distances as far as 500 km, becoming weaker further out of the coast. The distance can be roughly determined using:

$$d \approx 5625u \times 10^4 \left(\frac{\Delta T_p}{T_{ps}} \right), \quad (3-3)$$

where u is the wind speed in m/s, ΔT_p is the land-sea potential temperature difference in degrees Kelvin and T_{ps} is the sea surface potential temperature in degrees Kelvin [12].

Surface ducts also develop due to large scale subsidence in the vicinity of high pressure systems. The relatively dry descending air heats up during its descend as it undergoes adiabatic compression and forms a strong temperature inversion with the cooler surface layer. The temperature inversion, accompanied with a rapid decrease of humidity, forms a trapping layer close to the surface of the earth. A duct due to subsidence can be relatively homogeneous but tends to slope down from the centre to the edge of the high pressure system. Generally subsidence results in stronger ducts than advection [19].

Other conditions that may result in the formation of surface ducts are sea and land breezes [17]. During the day when the land is generally warmer than the sea, the warm dry air above land rises and is replaced by air from the sea, thereby creating a circulation from sea to land, called a sea breeze. At night the circulation can set up in the opposite direction. Air rises above the relatively warm sea and is replaced by air from land. Such circulation is known as a land breeze. By a sea breeze a duct may develop due to the subsidence (see explanation above) of dry air over the water. During a land breeze the surface duct is also generated by subsidence but now above land. After formation the trapping layer is carried out to sea by the land breeze. In general the ducts due to sea and land breezes decrease in height and increases in strength towards the shore [12]. Sea breezes are quite common and may last for several days.

Generally surface ducts are associated with fair weather. However, a surface duct may develop due to the relative divergence of relatively cool air under a thunderstorm. Even though this is less likely to result in a surface duct, it may still affect radar propagation (e.g. increased detection ranges) for a few hours during thunderstorms [2].

Last but not least surface ducts may form due to nocturnal radiation [19]. During clear nights the earth's surface will cool due to the radiation of heat. The air adjacent to the surface will become cold relative to the air higher up. Hence the temperature inversion and the formation of a trapping layer. This said, these conditions generally only result in the formation of a duct above dry land. Above water the radiative heat loss is minimum and the temperature inversion is most likely to be accompanied with an increase of humidity with height. This due to the fact that the cold air will condense near the surface. In these conditions it is more likely that a sub-refractive layer is formed rather than a surface duct.

As mentioned earlier, surface ducts are categorised into two types of ducts: the standard surface duct and the surface-based duct.

Standard surface duct A standard surface duct is mainly formed by advection and is characterised by a trapping layer adjacent to the surface. Figure 3-4(a) gives a modified refractivity profile typical for a standard surface duct. The trapping layer lies between the red dashed line and the surface. The height of the duct which corresponds with the height of the trapping layer is a measure of duct strength. Standard surface ducts are typically less than 200 m high.

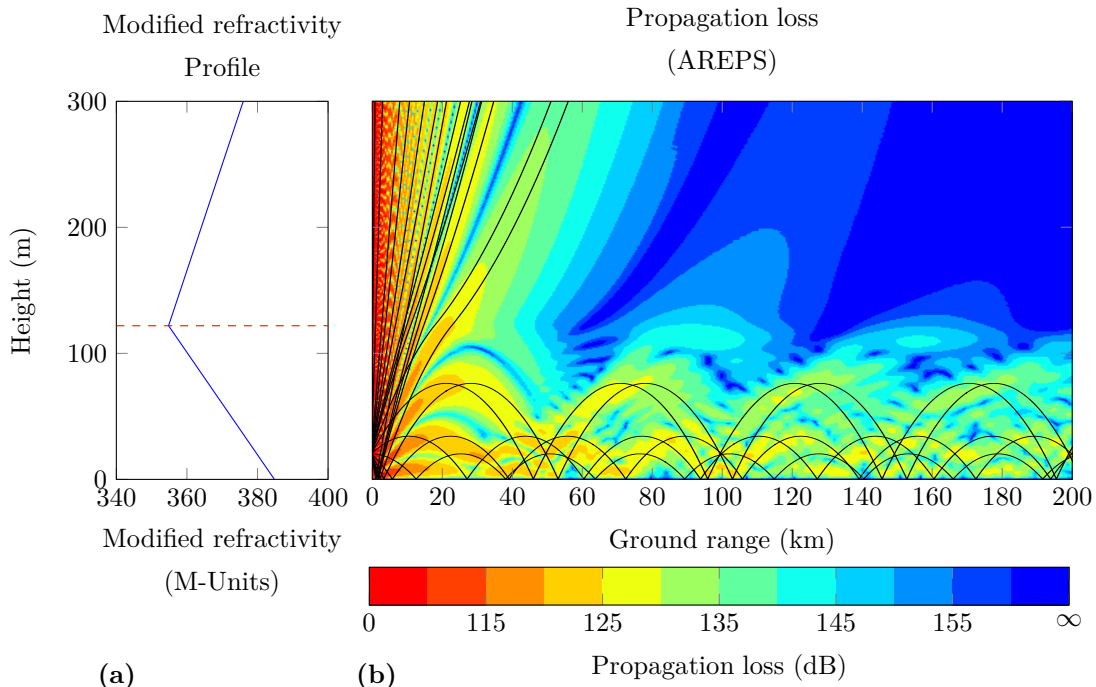


Figure 3-4: Propagation losses in a standard surface duct (b) with associated modified refractivity profile (a). The propagation losses and ray traces in (b) are computed using respectively AREPS and the ray tracing program MIRAT [20].

The effects of the standard surface duct are illustrated in Fig. 3-4. See how the electromagnetic energy propagates strongly along the earth's surface, more so than in an evaporation duct. For clarity of how electromagnetic waves propagate, individual rays are also shown in Fig. 3-4.

Surface-based duct The surface-based duct is characterised by an elevated trapping layer which may lie several hundred metres above the surface. In Fig. 3-5(a), which shows the modified refractivity profile of a surface-based duct, the elevated trapping layer lies between the red dashed lines. Even though the trapping layer is elevated, the bottom of the duct still reaches the earth. This because the modified refractivity at the top of the trapping layer is less than the surface value. The effect of a surface-based duct on radar propagation is shown in Fig. 3-5(b). See how the energy is trapped between the top of the trapping layer and the earth's surface. Surface based ducts can have heights up to 1000 m but generally have an average height of 300 m [34].

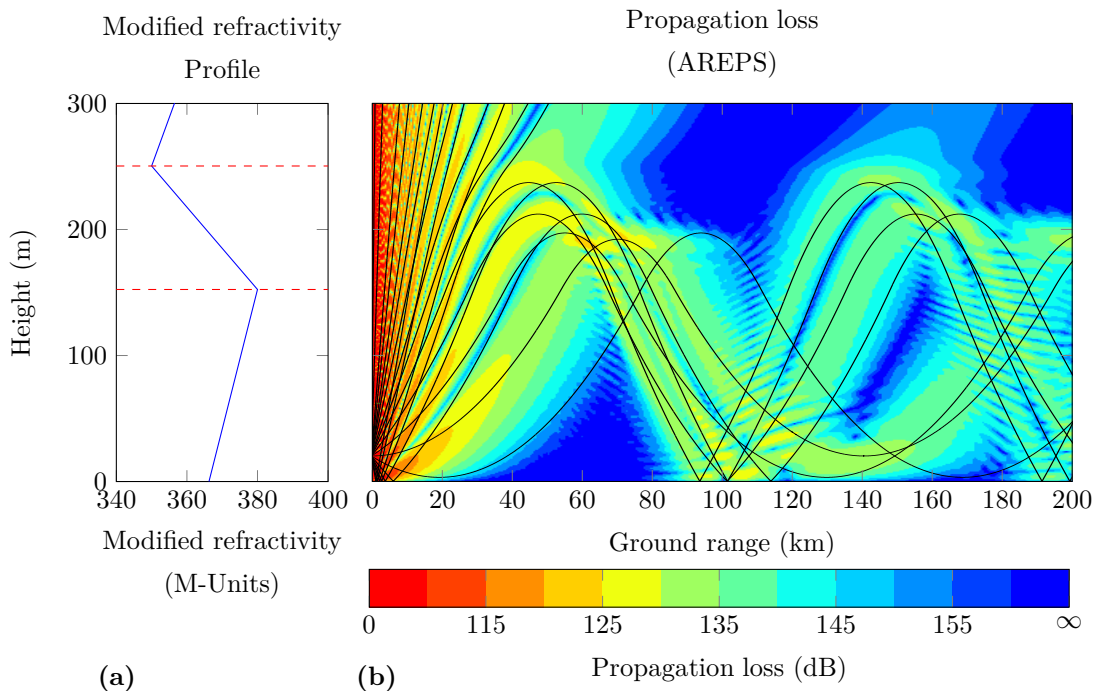


Figure 3-5: Propagation losses in a surface-based duct (b) with associated *M*-profile (a). The propagation losses and ray traces in (b) are computed using respectively AREPS and the ray tracing program MIRAT [20].

Surface based ducts are generally formed by subsidence near a high pressure systems or during sea and land breezes and are generally stronger than standard surface ducts [12,19]. A surface based duct can also form when the trapping layer of a standard surface duct rises from the surface due to a vertical motion of air further out at sea [2].

A significant difference with the standard surface duct is that a surface-based duct is accompanied with a skipping zone. A skipping zone is an energy depleted region which occurs near the normal radar horizon [2]. A skipping zone, as shown between the ranges 40 and 80 km

in Fig. 3-5(b), can have significant tactical consequences, which will be discussed in Section 3-3.

Elevated ducts

The last duct type is the elevated duct. As with a surface-based duct the trapping layer is elevated. Electromagnetic waves propagating in an elevated duct are, as in any trapping layer, strongly refracted towards the earth; however, as in other ducts the waves do not reflect off the earth's surface but rather enter a region of sub, normal or super-refractive conditions only to refract again when they re-enter the elevated trapping layer. Hence, the duct does not reach the surface as is clearly shown in Fig. 3-6(b). An example of a typical modified refractivity profile for an elevated duct is given in Fig. 3-6(a). For an elevated duct to form it is necessary that the modified refractivity value at the top of the trapping layer is greater than the modified refractivity value at some height below the elevated trapping layer [1]. The duct extends from the top of the trapping layer down to the highest value at which the modified refractivity value below the trapping layer equals the modified refractivity value at the top of the trapping layer. The trapping layer in Fig. 3-6(a) lies between the two top red dashed lines, the duct between the top and bottom red dashed lines.

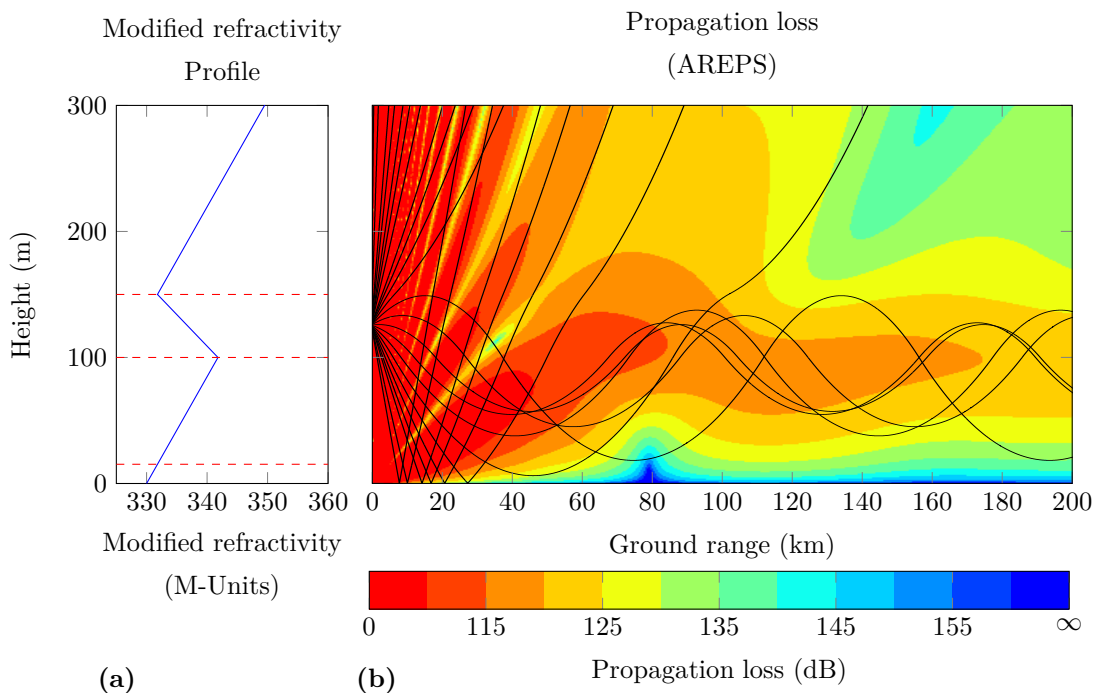


Figure 3-6: Propagation losses in an elevated duct (b) with associated *M*-profile (a). The propagation losses and ray traces in (b) are computed using respectively AREPS and the ray tracing program MIRAT [20].

The thickness of the duct, a measure of strength, can range from zero to several hundred metres and may have an altitude as high as 6 km, but are most common below 3 km [9]. As by surface ducts, the elevated duct is not particularly sensitive to frequencies and can affect propagation for frequencies above 100 MHz [1]. This being said, only transmitters

and receivers/targets inside, just above or below the elevated duct experiences increase in signal strength or detection range. An elevated duct, however, can cause radar holes (energy depleted regions) to form above the duct for radars below the duct and vice versa [1, 2].

Elevated ducts occur under similar conditions as surface-based ducts. Mostly elevated ducts are formed due to subsidence in semi-permanent high pressure systems as discussed above [1, 2, 17, 34]. Also as, by surface-based ducts, elevated ducts can form by a trapping layer rising over a cooler moist air mass [2].

3-2-5 Lateral inhomogeneity

Today's propagation and radar performance assessment models provide accurate estimates of propagation losses and coverage when the models are provided with sufficient refractivity data [4]. In the past, and for many navies still today (including the Royal Netherlands Navy (RNLN)), radar performance assessment was usually based on a single slant refractivity profile obtained by a radio sonde measurement in the vicinity of the propagation path at the time of interest. By using a single profile, it is assumed that the atmosphere is homogeneous stratified [9]. Because the refractivity varies much more vertical than horizontal⁴, especially over open oceans where sea temperature and meteorology changes little with range [17, 19], the assumption of a homogeneous stratified atmosphere is in most cases valid [9], and hence a single refractivity profile suffices for accurate radar assessment. If the assumption is valid, the same stratification may persist over a horizontal region tens or hundreds of kilometres in extent [19].

Figures 3-7(a-d) give an example when homogeneous stratification can be assumed. Figure 3-7(a) provides two dimensional refractivity data with a horizontal resolution of 2.5 km for a ship positioned just North outside the English Channel at 12:00 Z on the 12th of May 2014 and looking in the direction North. The atmosphere was well mixed and weather conditions were calm. Notice that the refractivity varies little, especially horizontally. The corresponding modified refractivity gradient is given in Fig. 3-7(b). Under these conditions it is clear that a single profile will provide similar results as when using the full two dimensional refractivity data for radar assessment. Figures 3-7(c-d) show that this is indeed the case. The propagation loss assessment based on a single vertical profile (Fig. 3-7(d)) agrees extremely well with the "ground truth" (Fig. 3-7(c)). In this thesis the ground truth is defined as the radar performance assessment based on two dimensional refractivity data with the highest resolution available, which in this case is an average vertical resolution of 65.4 m in the first kilometre and a horizontal resolution of 2.5 km (HARMONIE resolution). Hence, under these conditions, the assumption of a homogeneous stratified atmosphere is valid. Research shows that from a radar assessment point of view, a single profile is sufficient to provide accurate results for about 86% of the time [9].

This being said, the vertical refractivity profile may vary substantially with range, azimuth and time, especially in ducting environments, such as coastal waters, and near meteorological weather fronts [4, 9]. As mentioned in Section 3-2-4 a duct may change with range. For example, a duct do to subsidence at a high pressure system tends to slope down from the system's centre to the edge. Or how a trapping layer of a standard surface duct may rise from the surface to form a surface-based duct or even an elevated duct further out at sea. Ducts

⁴About two orders of magnitude more [19].

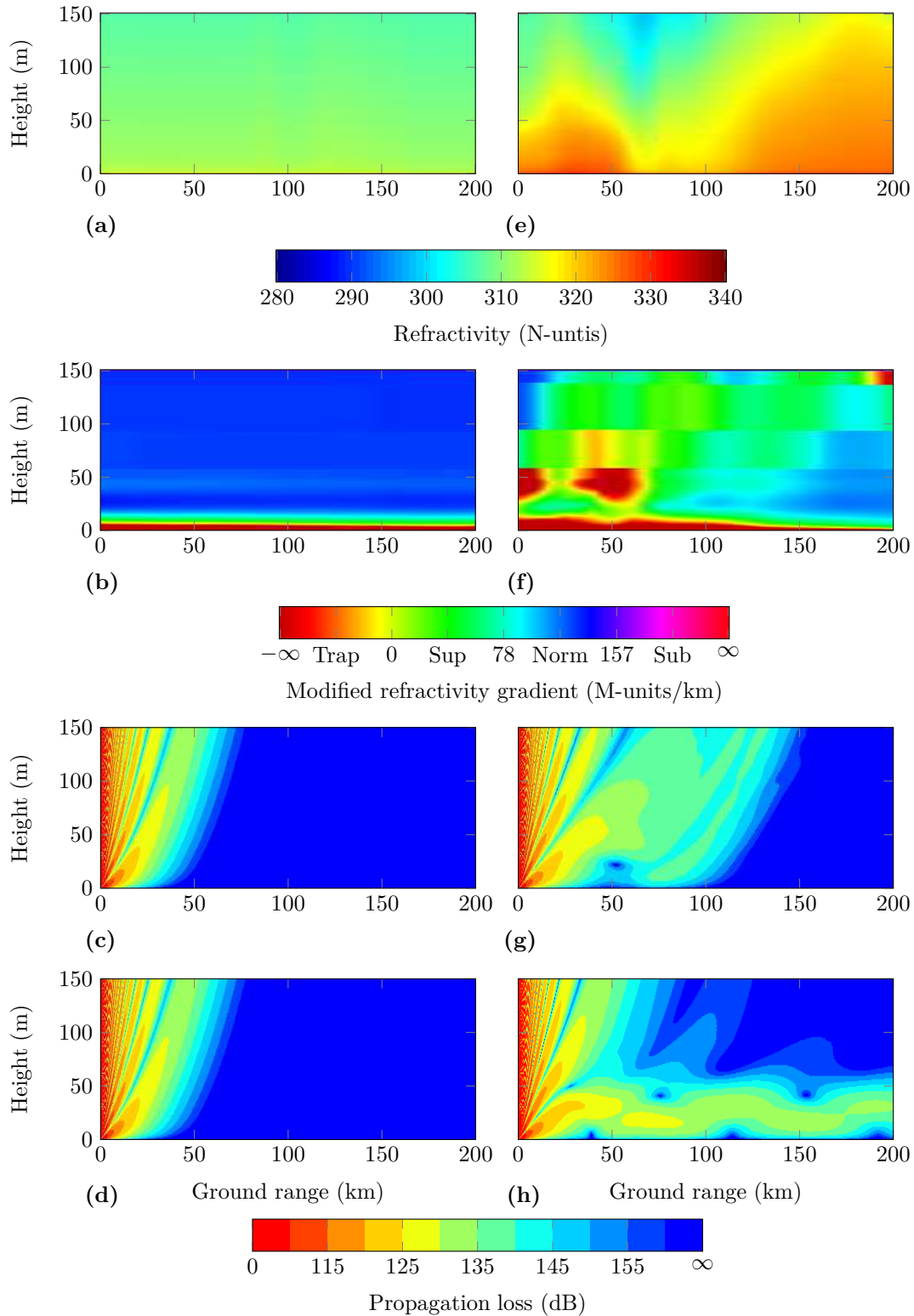


Figure 3-7: Conditions above the North Sea on 12-05-2014 at 12:00 Z (a - d) and on 09-03-2014 at 15:00 Z (e - h): two dimensional refractivity data (a & e); modified refractivity gradient (b & f); ground truth radar assessment (c & g); radar assessment based on a single profile (d & h).

due to advection, sea or land breezes tend to become thicker but weaker further out of the coast. In some cases the duct can even dissipate abruptly.

Weather fronts may also result in significant changes in the refractivity profile, depending on the fronts strength and slope. For example, during the passage of a cold front the temperature will drop, the pressure will also drop but is followed by an increase of pressure, and the humidity will decrease. Hence, the refractivity profile will change. During the passage of a cold front temperature can drop 15 degrees Celsius within the first hour [37]. By a passage of a warm front, the opposite occurs. This being said, refractivity variations are generally more significant in ducting conditions near the coast than near meteorological weather fronts.

In the above conditions, where the refractivity profile is range, azimuth and/or time dependent, radar assessments based on a single vertical refractivity profile can result in significant errors, and may have dramatic consequences. Figures 3-7(e-h) give an example when a single profile should not be used. The refractivity is shown in Fig. 3-7(e), which is data for the same location as in Fig. 3-7(a), but at 15:00 Z on the 9th of March 2014. See that the refractivity varies notably more compared to the refractivity in Fig. 3-7(a). The corresponding modified refractivity gradient is shown in Fig. 3-7(f). A surface-based duct (due to advection) and an evaporation duct are clearly present between the ranges of 0 and 60 km. However, the surface-based duct dissipates abruptly at approximately 60 km and the evaporation duct height decreases with range. By looking at Fig. 3-7(f) it is already clear that the assumption of a homogeneous stratified atmosphere is invalid. Figures 3-7(g) and 3-7(h), showing the propagation loss assessments obtained when using respectively the two dimensional refractivity data (ground truth) and a single profile, confirm this. Notice the significant difference. In Fig. 3-7(h), which is based on a single profile, the duct is consistent, allowing the electromagnetic energy to follow the earth's surface the entire range, whilst, in Fig. 3-7(g), the ground truth, the electromagnetic energy follows the earth's surface only for a small distance, before it propagates away from the surface when the duct dissipates. The corresponding coverages are shown in Fig. 1-3. See how the coverage assessment based on a single profile predicts detection ranges beyond 200 km at low altitudes, whilst this is clearly not the case according to the ground truth.

In the study of Goldhirsh and Dockery [38], the resulting error due to the assumption of a homogeneous stratified atmosphere is studied. Two dimensional high resolution⁵ refractivity data was collected by a helicopter equipped with sensors and flying a vertical "sawtooth" pattern of the coast off the Wallops Island. Previous studies have shown that obtaining refractivity data in such a manner resulted in accurate radar assessments. Data was collected over 30 independent days. Comparison between propagation loss assessments using a single profile and the ground truth showed that significant errors can occur when a single profile is used. On average for a 3 GHz radar, 16% of the predicted area at short⁶ ranges is in error greater than 5 dB. At extended ranges 45% of the predicted area is in error greater than 5 dB. In many radar assessment studies a 5 dB error is found to be acceptable. The same study compared the ground truth with a standard atmosphere. This showed even more significant errors. Hence, the assumption of a homogeneous stratified atmosphere gives better results

⁵Refractivity data obtained during the Wallops Island experiment had a vertical and horizontal resolution of 0.6 m and 6.5 km respectively.

⁶In this study short ranges were defined as an area with a range interval of 10-30 km from the source and a height interval of 5-30 m from the surface. Extended ranges were defined as an area with a range interval of 30-90 km from the source and a height interval of 5-300 m from the surface.

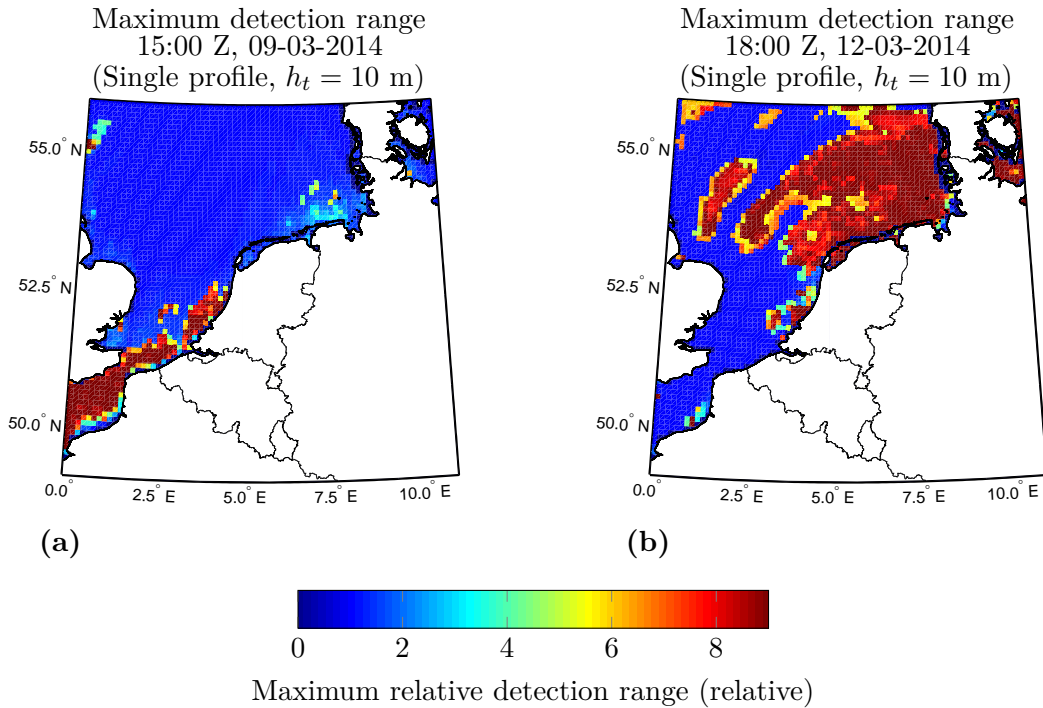


Figure 3-8: Maximum relative detection ranges (relative to standard conditions) for a small fighter at an altitude of 10 m on 09-03-2014 at 15:00 Z (a) and on 13-03-2014 at 18:00 Z (b) ($P_D = 0.95$, $P_{FA} = 10^{-6}$). Assessments are based on a single profile.

than using no in situ data. The study concluded with stating that at smaller ranges (< 30 km) the atmosphere can in most cases be assumed homogeneous stratified but that at larger ranges multiple profile measurements can be a necessity for avoiding significant errors.

Another study, by the same authors [4], gave a starting effort in determining the refractivity resolution requirements for accurate radar assessment. The study focused on surface-based duct environments, because surface-based ducts tend to have severe refractivity resolution requirements. Based on two high resolution data sets obtained by helicopter off the coast of San Nicolas Island⁷ and of Wallops Island⁸, the authors show that to assess 10 GHz propagation loss for low-altitudes with an accuracy of 5 dB, the minimal vertical and horizontal resolution requirements were respectively 6 m and 17 km for the atmospheric conditions during the San Nicholas experiments. Under the conditions of the Wallops Island experiment, minimal resolutions of 10 m and 17 km were required for the same assessment accuracy. At 3 GHz the resolution requirements were less. The conclusions were drawn by comparing the ground truth with radar assessments based on degraded in resolution refractivity data. Comparisons were made at heights 30 and 100 m and at ranges 30 and 50 km. As in [38], the study also concluded that assessments based on a single profile can have dramatic consequences. Based on the same San Nicolas data set, [11] stated similar results but compared assessment areas

⁷Refractivity data obtained during the San Nicolas Island experiment had a vertical and horizontal resolution of 0.6 m and 8.5 km respectively.

⁸Refractivity data obtained during the Wallops Island experiment had a vertical and horizontal resolution of 0.6 m and 12 km respectively.

of 350 m in height and 90 km in range with the ground truth rather than specific heights and ranges. [11] also concluded that radar assessments, at 3 GHz, based on 73 minutes old refractivity data leads to 40% of the assessed area having an error exceeding 5 dB. The area is reduced to 10% when using 34 minutes old data.

It should be mentioned that the above findings are case specific. For determining general resolution requirements many more independent scenarios must be examined. This thesis can be seen as an addition to the above, which examines a multiple of scenarios on the North Sea and in the English Channel. Figure 3-8 gives already a rough idea on the horizontal refractivity variation above the North Sea and how this will affect radar performance. The figure gives maximum detection ranges based on a single refractivity profile and relative to the detection range at standard conditions for a small fighter at an altitude of 10 m. The detection range under standard conditions is 21.8 km. The used 3.3 GHz radar has an height of 20 m; the probability of detection and false alarm are $P_D = 0.95$ and $P_{FA} = 10^{-6}$ respectively. Because the relative detection ranges are based on a single profile they are most likely incorrect. However, the relative ranges can be seen as a measure of ducting at the corresponding location. Hence, at locations with small relative detection ranges (but greater than one) normal or super refraction takes place, whereas locations with large relative detection ranges ducting takes place. Sub-refraction takes place where the relative detection range is smaller than one. See how the maximum relative detection range can vary significantly on the North Sea. Hence, in these conditions it is not recommended to use only a single refractivity profile for radar assessment.

3-2-6 Terrain effects

In the previous sections propagation of electromagnetic waves through an inhomogeneous troposphere above a relatively smooth surface has been discussed extensive. The operational shift in battle space from open oceans to coastal environments, however, resulted in a need of understanding how electromagnetic waves propagate over irregular coastlines and how it affects radar coverage. Even though this thesis does not focus on propagation over irregular terrain, for integrity reasons, this section illustrates how anomalous propagation due to irregular terrain affects radar performance.

When at least part of the propagation path is over irregular terrain, terrain obstacles will obstruct or interfere with the electromagnetic wave [1]. To assess radar performance over terrain, the mechanisms reflection, refraction and diffraction must all be properly incorporated in a single model [8, 39].

As discussed in Section 2-6-2 the diffraction mechanism knife-edging allows electromagnetic waves to curve around the edge of the obstacle and penetrate into the obstacle's shadow region which may result in small detection probabilities. Figure 3-9(a) shows how electromagnetic energy bends around a coastal cliff. Notice that the field strength does not abruptly go to zero in the obstacle's shadow region but decreases gradually with increase of the shadow angle. Hence the possibility of detection and/or counter detection⁹ within the shadow region. The propagation losses in Fig. 3-9(a) are computed using the parabolic equation model PETOOL [39]. The radar used in Fig. 3-9(a) has an operating frequency of 3.3 GHz and a height

⁹Counter detection is the detection of deployed radar systems by (passive) electronic support measures (ESM).

of 20 m. Remember that by decreasing the frequency the effect of diffraction/knife-edging significantly increases.

Besides diffraction, reflection off of irregular terrain also results in anomalous propagation. Reflection re-directing the waves in multiple directions makes propagation somewhat unpredictable [39]. It can even result in a wave propagating back to the radar, leading to complex interference. Figure 3-9(b) shows how reflection of the cliff results in complex interference between the forward and backward propagating wave. See how the backward propagating wave changes the vertical lobe pattern.

The atmospheric conditions in Fig. 3-9(a) and (b) are standard. Figures 3-10(b) and (d) give an example of anomalous propagation due to both refraction and irregular terrain. In Fig. 3-10(b) and (d) atmospheric conditions result in the formation of respectively a elevated and surface-based duct. The corresponding modified refractivity profiles are given in Fig 3-10(a) and (c) respectively.

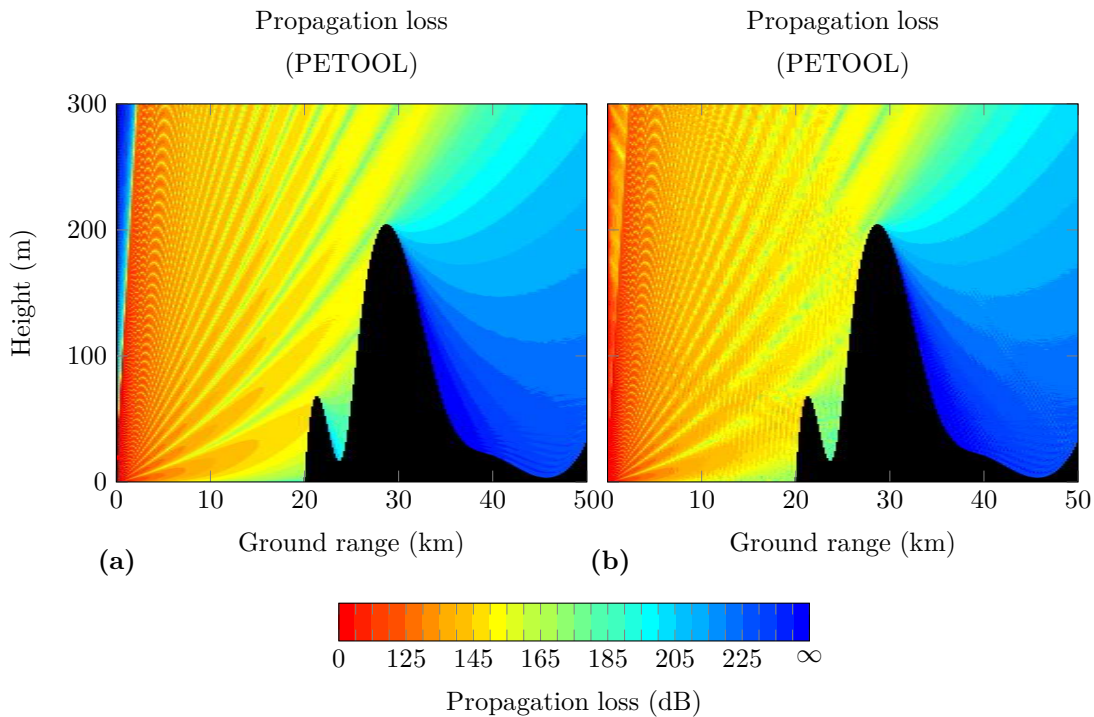


Figure 3-9: The effects of diffraction (a & b) and reflection (b) due to irregular terrain. Propagation losses are computed using PETOOL [39].

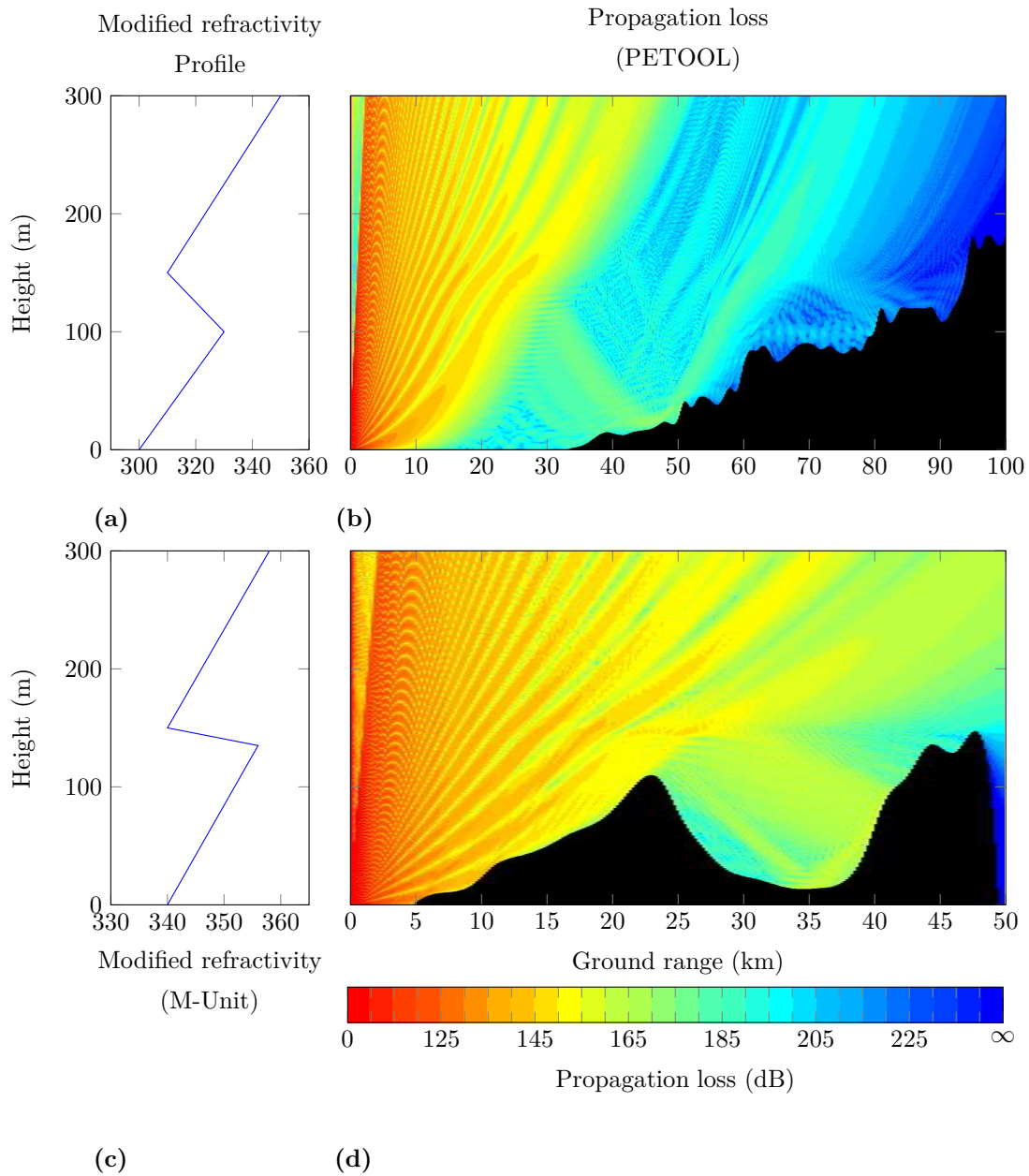


Figure 3-10: The effects of refraction, reflection and diffraction in elevated (a & b) and surface-based (c & d) ducting conditions over irregular terrain. Propagation losses are computed using PETOOL [39].

3-3 Tactical consequences

As shown above the troposphere can have a significant impact on how electromagnetic waves propagate and thereby the overall performance of radar systems. This section discusses a couple of tactical consequences as a result of anomalous propagation. Depending on the scenario these consequences can be seen as an advantage or disadvantage. The consequences discussed will also shed light on the importance of having the ability to assess radar performance and coverage under the prevailing atmospheric conditions.

Figure 3-11 illustrates several consequences of anomalous refraction: detection range effects, radar holes, skipping zones and position errors. Each of these are addressed in some detail below. The ability, due to diffraction, to detect or counter detect targets in shadow zones will also be discussed.

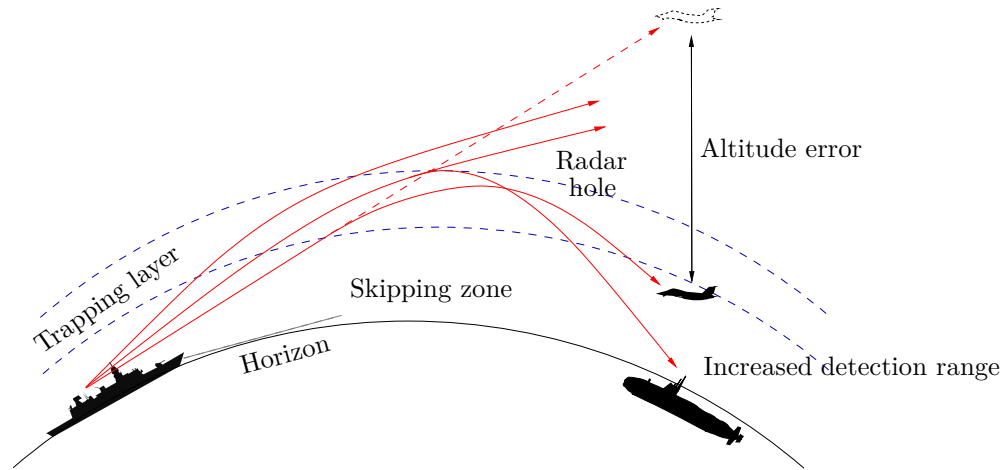


Figure 3-11: Tactical consequences as a result of anomalous refraction.

3-3-1 Detection range effects

As a result of anomalous propagation, detection ranges may increase significantly, as well as decrease. Figure 3-12 shows radar coverage for a 3.3 GHz radar searching for a small fighter under the atmospheric conditions discussed above. The radar has a height of 20 m above the surface and coverage is defined as the area where the probability of detection is 0.95 or higher with a false alarm probability of 10^{-6} . Notice how in Fig. 3-12(a), relative to standard conditions, subrefractive conditions decrease detection ranges while superrefractive conditions yield an increase. Figures 3-12(b-e) show how ducting may dramatically alter detection ranges; notice that the detection ranges may extend well beyond the radar horizon. A well known example of a detection range effect is the detection of targets in Arabia with a 200 MHz radar based in Bombay India, 1700 miles away [9]. As a natural consequence of range extension, second or even third trace echo's, also known as ghost targets, are likely to occur [40]. Such echo's led to the confusion on board the USS Maddox and the USS Turner Joy as described in the Introduction (Section 1-1).

Another aspect of range effects is that with increased detection ranges, jamming will also be effective over a greater distance. A jammer flying within a duct will be effective over a great distance whilst its standoff range will well clear the effective interception range of the combatant being jammed [2].

Finally, range extension also results in more energy being reflected off the sea surface over the extended range. As a consequence sea-clutter may significantly increase, especially in surface-based duct conditions [12, 34].

3-3-2 Radar holes, skipping zones and shadow zones

It should be noted that in general, while the capture of electromagnetic energy within a duct may dramatically improve the detection range within the duct, the trapping at the same time reduces coverage outside the duct: the extended ranges inside the duct comes at the expense of reduced ranges, radar holes and/or skipping zones elsewhere. A target outside a duct may therefore go undetected by a radar within that duct while it would have been detected under normal conditions, or if the radar had been outside the duct itself [40]. Radar holes and skipping zones are energy depleted regions with low or no probability of detection.

Under normal conditions a tactic employed by an attack aircraft in penetrating an enemy's target defences is to fly as low as possible to remain "beneath" the radar coverage¹⁰. In ducting conditions however, this is not advised, as can be seen in Fig. 3-13. Under ducting conditions the optimum strike altitude for an attack aircraft is in the radar hole just above the duct [2].

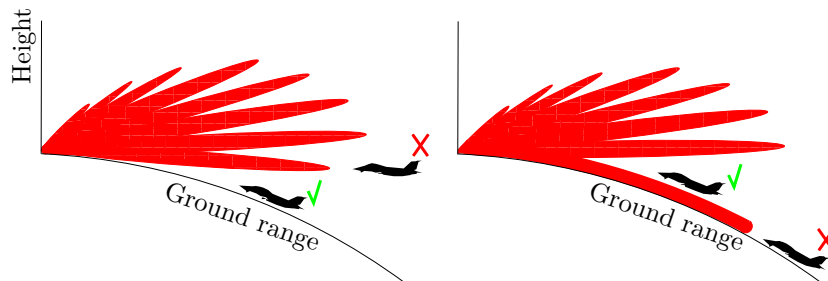


Figure 3-13: Optimum fly altitude for penetrating enemy radar.

The above tactic was used against an American Aircraft Carrier strike group conducting flight operations in the Arabian Gulf [3]. Enemy forces deployed a reconnaissance aircraft to observe the activity. None of the radars in the strike group detected the enemy reconnaissance aircraft; the first to see the contact was a lookout on board the aircraft carrier. The reconnaissance aircraft approached in a radar hole. Even though the ability to assess radar coverage would most likely not have prevented the covert approach, it would have been less of a surprise if the strike group would have had the ability to assess the prevailing coverage.

However, it is important to know that some electromagnetic energy will penetrate into the radar hole. Although the duct can be compared to a waveguide, a duct does not have rigid and impenetrable boundaries, with exception of the earth's surface. Therefore, electromagnetic

¹⁰Another tactic is to fly down an interference null but the possibility of remaining undetected are slim because of the ships movement and the use of multiple (or broadband) radars on different frequencies [2].

energy is continually leaking from the duct. While the energy level within the radar hole may be insufficient for radar detection of an incoming target, it may be sufficient for the target to intercept the radar by ESM [2].

The flying altitude of an early warning aircraft (EWA) must be considered when deployed. Under normal conditions flying as high as possible will lead to maximum detection ranges. However, under ducting conditions, depending on the flying altitude, an elevated duct can significantly effect the EWA's coverage. An aircraft flying in an elevated duct for the benefit of extended coverage within the duct, will at the same time experience greatly reduced coverage, due to radar holes, in the larger volume outside the duct. In general, flying within a duct is therefore tactically undesirable, as any targets cannot be counted on to also fly in the duct. To minimise the effect of an elevated duct the EWA must fly as high above the elevated duct as possible [2]. This being said, flying in the duct is good for increasing communication ranges between aircraft [1].

Surface-based ducts are accompanied with so called skipping zones which are energy depleted areas as result of the electromagnetic energy repeatedly "skipping" over the earth's surface. The first skipping zone occurs near the geometrical horizon [41] and is clearly visible in Fig. 3-12(d). Skipping zones are important features to bear in mind, as detected surface targets or sea-skimming aircraft/missiles can abruptly disappear off radar as it enters the energy depleted area, and reappear close to the detecting ship. A skipping zone is one of the explanations that can explain the repeated disappearance of the torpedo boats "attacking" the USS Maddox and USS Turney Joy as described in the Introduction.

Last but not least, knife-edging, a type of diffraction, allows electromagnetic energy to curve around the edge of obstacles and penetrate into the obstacle's shadow region (see Fig. 3-10(d)). In many cases the penetrated energy is insufficient for radar detection but it may be sufficient for ESM intercept of radar. Thus, a ship positioned covertly behind a coastal mountain range might be detected by enemy troops using ESM inland on the otherside of the mountain [2].

3-3-3 Altitude and range errors

Besides that refractive effects alter the radar's coverage, refraction can also lead to incorrect target positioning¹¹. A target's position is determined by the azimuth and elevation angle of the return radar pulse and the time between transmitting and receiving the pulse.

Figure 3-14 shows how aircraft C will erroneously be positioned by the detecting radar at height C' , while ship B will be positioned at a range that equals the total path length of the propagating ray AB rather than at the actual, much shorter, range. Figure 3-15 shows that altitude error can be substantial, especially at long ranges. For example, a ship at a range of 120 km will be detected with an altitude error of over 500 m and therefore projected as an aircraft flying at an altitude of over 500 m.

Whilst position errors can have significant consequences, such as erroneous identification of enemy targets and missed engagements, little research has yet been done to minimise these errors "real-time" by the use of propagation models. It is therefore recommended that the RNLN look into the use of propagation models for minimising position errors as a result of

¹¹Incorrect target positions due to reasons other than (range) ambiguity.

propagation effects. Note that the question on the required atmospheric data resolution (see Section 1-2) is relevant in this respect also and that resolution requirements for sufficiently accurate positioning may differ from the requirements for adequate coverage and maximum detection range assessment.

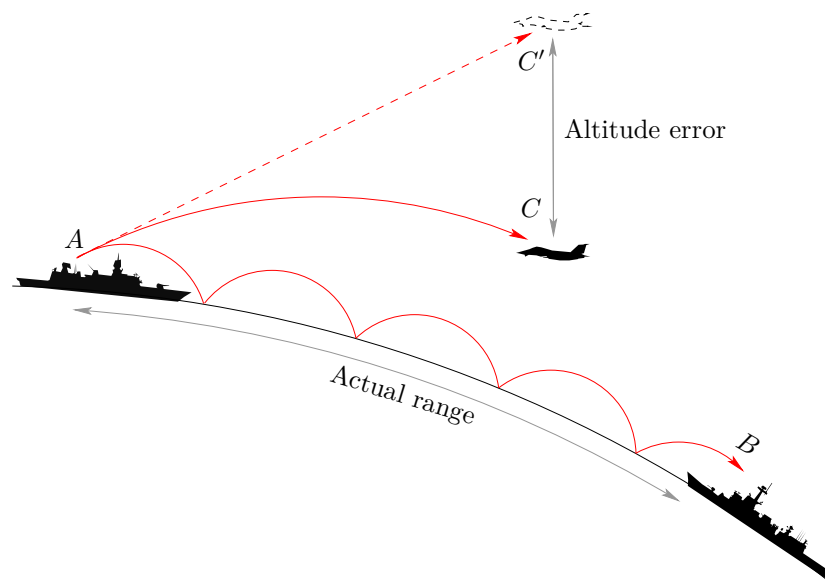


Figure 3-14: Position error due to refraction.

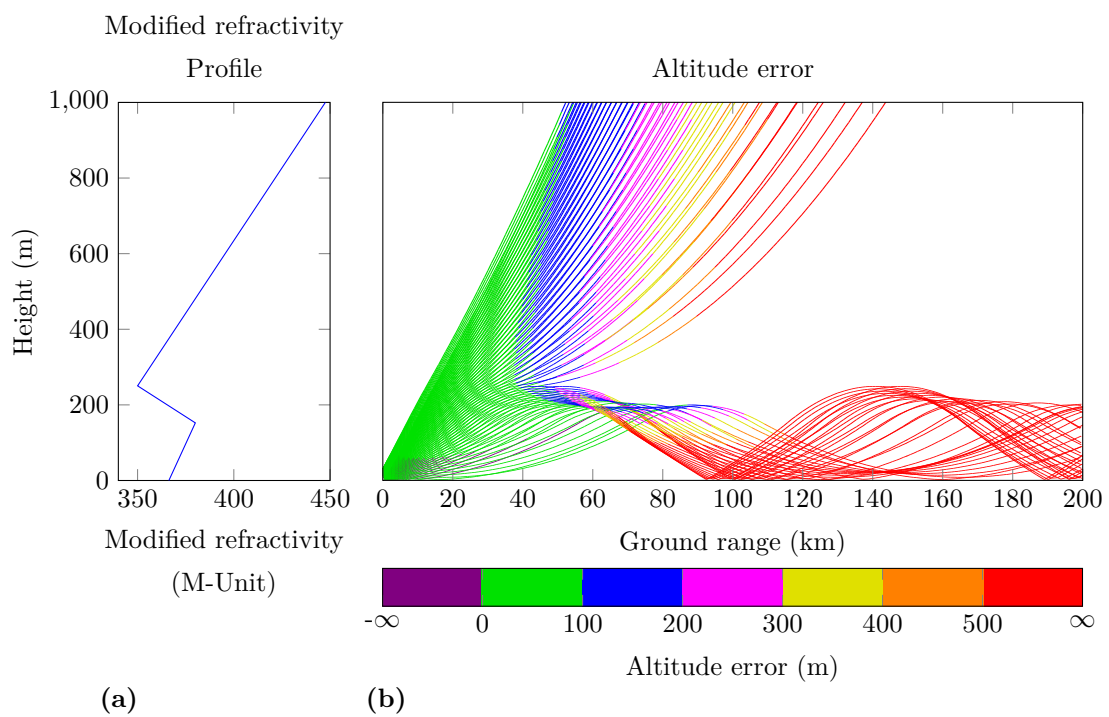


Figure 3-15: Altitude errors as a result of a surface based duct (b). The associated modified refractivity profile is given in (a). Errors are computed using AREPS [2].

Chapter 4

Methods for modelling radar propagation

In the previous chapter it became clear that the troposphere can have a significant effect on the performance of radar. Because of the resulting tactical consequences, the ability to model and assess radar performance and coverage under prevailing weather conditions is highly beneficial for naval operations. To model anomalous propagation as discussed in Section 3-2 one, or a combination, of three methods are generally used: geometric optics, mode theory and parabolic equation [19]; each having their advantages and disadvantages.

For many years radar assessments were based mainly on geometric optics and mode theory methods [42]. These methods for modelling propagation will be discussed in Sections 4-1 and 4-2 respectively. Nowadays, the parabolic equation method is the most advanced and widely used method for radar/propagation assessment [7, 42], and will be discussed in Section 4-3. To increase computational speeds different methods are combined to form hybrid models [6]. A well established hybrid model which combines the geometric optics and parabolic equation method is known as the Advanced Propagation Model (APM) [2, 43] and will be discussed in Section 4-4.

At the end of this chapter the TDAs CARPET and AREPS will be discussed briefly, both these TDAs are in use by the RNLN. The TDA CARPET is based on geometric optics whilst AREPS is based on APM, which combines the geometric optics and parabolic equation method.

It should be noted that for accurate radar assessment the radar itself as well as the target must also be modelled accurately. This however will not be discussed within this thesis. For information on modelling the radar and target see [2, 23] or any radar principle book such as [25, 44].

4-1 The geometrical optics method

The geometric optics model, also known as ray tracing, is a relatively simple yet very effective method to model anomalous propagation [9,19]. The method is based on repeated use of Snell's law to trace the path of individual rays characterised with different initial elevation angles propagating outwards from the transmitter through a horizontally stratified atmosphere [19]. As shown in Section 2-2, rays propagating through a layer where refractivity varies linearly with height propagate along a curved path which curvature radius is dependent on the layer's refractivity gradient. Besides curving, rays reflect from the earth surface.

Plotting the propagation paths of multiple rays as determined by the way they curve through the various layers of the atmosphere and reflect off the earth, yields excellent qualitative pictures of the propagating conditions [42]. Figure 4-1(b) gives an output example of the ray tracing program MIRAT (MICrowave RAY Tracing) developed by the author of this thesis [20]. See how intuitively the figure shows how the surface-based duct and its skipping zones develop under the atmospheric conditions that are represented by the modified refractivity profile given in Fig. 4-1(a). Note that the picture does not show field strength: where rays are packed close together the field strength may or may not be high, depending on the coherent.

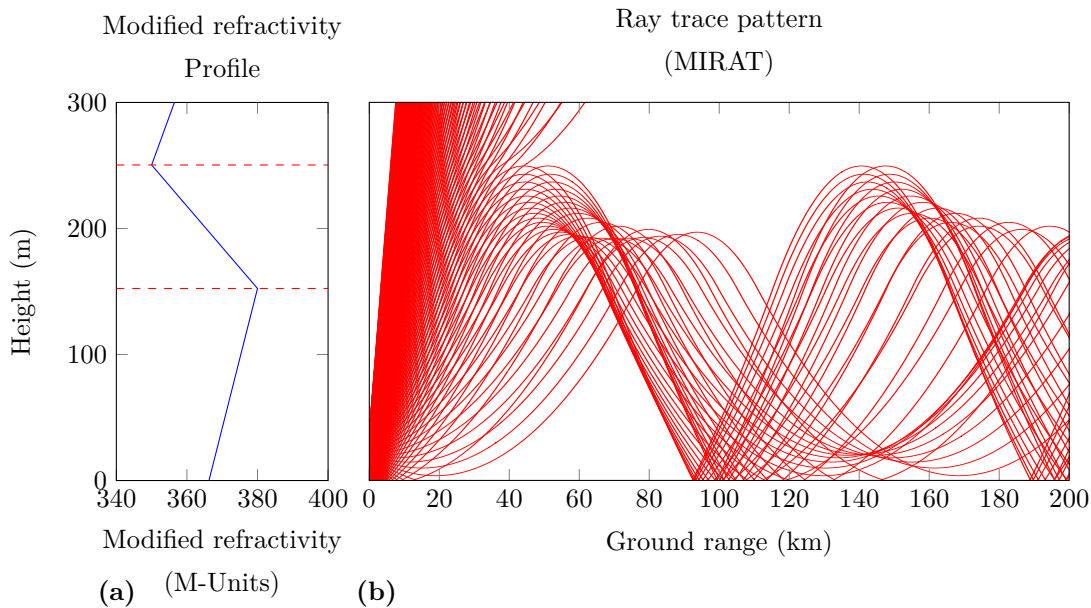


Figure 4-1: Output of the ray trace model MIRAT (b), tracing rays in surface-based duct conditions (a).

Besides simplicity and intuitive results, advantages of models based on the geometric optics method include fast code execution [19] and straightforward modelling of propagation through an inhomogeneous atmosphere in which the vertical refractivity profile varies with range.

Due to its simplicity, the geometric optics method does have several limitations. Whilst the field strength can be determined quite accurate under simple condition, the first limitation lies in the difficulty of determining field strength in ducting conditions. Field strength determination is complicated in the first place because a single ray does not carry amplitude information [19]. To overcome this, rays must be categorised into separate families or ray tubes, each of

which contains rays that have followed similar propagation paths. Note that characterising rays into tubes is already quite difficult to do automatically [19]. Within a single tube and in simple cases the energy at a certain point may be calculated by the intensity law of geometric optics which is based on the fact that the energy flux along a ray tube is constant and that the field intensity therefore must be proportional to the inverse of the tube's cross-section [42]. To subsequently determine total field strength at any point, the contribution from all ray tubes passing through that point must be added together: coherently [19]. For this, all ray tubes that intersect at that point must be determined, along with the phase with which the rays belonging to each of these tubes arrive at the point considered. Phase determination is particularly tricky as this requires determination of path lengths with high accuracy, well within the wave length of the considered frequency [19]. Field strength determination is most difficult, and as a consequence generally does not yield dependable results, at ray caustics, where a large number of ray tubes intersect [19]. In Fig 4-1 a caustic occurs at a range of approximately 140 km and a height of 20 m. Because of the difficulties described above field strength determination based on geometric optics is hard.

A second limitation is that while the method provides accurate results within the line-of-sight region, results, especially field strength results, in trans-horizon regions are inaccurate [6,19]. This because the geometric optics method does not model diffraction along the earth surface.

Thirdly, in geometric optics, when a ray encounters a layer, it either penetrates or is turned around by it: there is no concept of ray splitting into two components [19]. Geometric optics therefore cannot accurately model leakage that occurs at the boundaries of trapping regions (see Section 3-2 and 3-3) due to ray splitting. Ray splitting is a frequency dependent phenomenon, and the geometric optics method is frequency independent [19].

Because of its weaknesses ray tracing is, besides providing intuitive figures such as Fig 4-1, generally not used as a radar assessment model all on itself. Because of its computational speed is it often used in hybrid models, where ray tracing is used in regions where it yields dependable results while other methods are employed elsewhere.

4-2 The mode theory method

The mode theory method is primarily appropriate for modelling propagation in an atmospheric duct. Propagation in a duct is similar to propagation in a normal wave guide in that the same mechanisms apply. Similar to waveguides supporting multiple propagation modes depending on waveguide dimensions relative to the wave's wavelength, ducts support propagation modes depending on duct height [19]. The total field strength within the duct can be estimated quite accurate at a point by summing the contribution of all significant propagation modes.

The contribution of each mode to the combined resulting field strength can be computed using Maxwell's equations. The computation becomes numerically difficult, but not impossible, in the presence of a large number of modes, which increases with frequency [19]. Therefore mode theory is generally not well suited for propagation prediction for high frequencies at short ranges. At greater ranges, the number of contributing modes is reduced as the energy of higher modes leaks across the soft boundaries of the duct¹; this eases calculation [19].

¹Unlike ducts, metallic waveguides have sharp defined boundaries. For surface ducts the earth surface

Therefore the mode theory method is particularly useful near or beyond the radar horizon under ducting conditions. The overall performance depends on the ability of the model to determine the significant propagation modes [6]. A method for finding the modes is based on an algorithm described by Morfitt and Shellman [9].

Even though mode theory has proven to be very effective, especially at ranges near and beyond the horizon, it does have several limitations. The first limitation is that mode theory is generally only accurate in lateral homogeneous atmospheres. In conditions where the refractivity varies with range, the field strengths are mostly overestimated [19]. This being said, in the case of lateral inhomogeneity the field strength can be estimated accurately by breaking the "waveguide" up into sections and using a technique known as mode conversion [6]. However, this method is much less efficient than the parabolic equation method and therefore has not been developed further [6].

Another limitation is that models based on mode theory tend to underestimate field strengths when the radar and/or the target is positioned outside the duct. The main cause of this is that ducts are generally leaky, which the mode theory method does not take into account [25]. Also mode theory has no easy way to incorporate the effects of terrain diffraction [6].

Because of the limitations of the mode theory method, models based on mode theory are being replaced by the more effective and practical models based on parabolic equations. Nonetheless, the wave guide method is still widely used for validation purposes [42].

4-3 The parabolic equation method

Ideally propagation problems are solved by solving Maxwell's equations exactly. However, because the propagation environment in naval radar applications is very large relative to the wavelength, solving Maxwell's equations exactly is too complex and too demanding on computational resources for practical applications [45]. For many years, propagation problems were therefore solved by geometric optics and/or mode theory as discussed above, regardless of their limitations [42]. In 1946 Leontovich and Fock introduced the parabolic equation as an alternative method for solving propagation problems, but practical solutions were possible only for very simple atmospheric and boundary conditions [5]. The approach did not become particularly attractive until Hardin and Tappert introduced the Fourier split-step (FSS) technique in 1973, which numerically solves the parabolic equation using the Fourier transform [46]. However, whilst the split-step parabolic equation method became rapidly popular for solving acoustic propagation problems underwater [47], it was not until 1983 when Ko et al. introduced it for solving tropospheric electromagnetic propagation problems [5].

The parabolic equation is an approximation of the Helmholtz wave equation, which models energy propagating in a cone centred on a preferred direction, the paraxial direction [42]. The most simple but widely used narrow-angle parabolic equation (also known as the standard parabolic equation (SPE)) is derived in a few steps below. For a more comprehensive derivation, or for the derivation of other parabolic equations methods, see [42]. Assuming the field is independent of y the scalar Helmholtz wave equation is given by:

provides a sharp lower boundary whereas the upper atmospheric layer provides a soft boundary. Elevated duct have two soft boundaries

$$\frac{\delta^2 \psi}{\delta x^2} + \frac{\delta^2 \psi}{\delta z^2} + k_0^2 n^2 \psi = 0, \quad (4-1)$$

where $k_0 = 2\pi/\lambda$ is the free-space wavenumber (λ is the wavelength), $n(x, z)$ is the refraction index², and ψ denotes the electric or magnetic field in horizontal or vertical polarisation respectively. Here x and z represent respectively the range and height coordinates. Next the reduced function associated with the paraxial direction x is introduced:

$$u(x, z) = \exp(-jk_0 x) \psi(x, z). \quad (4-2)$$

The point of using the reduced function is that it is slowly varying in range for energy propagating at angles close to the paraxial direction, which gives it convenient numerical properties [42]. Substituting the reduced function in the Helmholtz wave equation (Eq. 4-1) results in:

$$\frac{\partial^2 u}{\partial x^2} + \frac{\partial^2 u}{\partial z^2} + 2jk_0 \frac{\partial u}{\partial x} + k_0^2 (n^2 - 1)u = 0, \quad (4-3)$$

which can be split into two psuedo-differential equations³ of the first order in x , or in other words a forward and backward propagating wave component:

$$\frac{\delta u}{\delta x} = \begin{cases} -jk_0(1 - Q)u & \text{forward,} \\ -jk_0(1 + Q)u & \text{backward,} \end{cases} \quad (4-4)$$

where the operator $Q = \sqrt{\frac{i}{k^2} \frac{\partial}{\partial z^2} + n^2}$. To simplify the implementation of solving the standard parabolic equation and to reduce the demand on computational resources, most propagation assessment models/programs (e.g. AREPS) neglect the backward propagating wave. Considering only the forward propagating wave, propagation can be modelled accurately (at small elevation angles from the paraxial direction) by finding the formal solution of the forward propagating wave component in Eq. 4-4. The solution can be expressed as:

$$u(x + \Delta x, z) = e^{ik\Delta x(-1+Q)} u(x, z), \quad (4-5)$$

where Δx is a range step size. From Eq. (4-5) it can be seen that the forward propagating field at a given range is obtained from the field at the previous range, whilst applying appropriate boundary conditions at the top and bottom of the domain [42]. In other words, the field at any range is determined through a marching technique. Using the first-order Taylor expansion (i.e. $\sqrt{1+q} \approx 1 + q/2$) to approximate the operator Q yields the SPE [42]:

$$\frac{du}{dx} = \frac{1}{2jk} \left(\frac{\delta^2 u}{\delta z^2} + k^2 (n^2 - 1) \right), \quad (4-6)$$

²By replacing the refraction index with the modified refraction index, m , the earth's curvature is taken into account.

³Hence the terminology "parabolic".

Three main numerical techniques to solve the parabolic equation have become popular: Fourier split-step (FSS) based algorithms, finite difference based algorithms and finite element based algorithms [7]. Whilst each technique has its advantages and disadvantages and whilst the choice of the preferred technique depends on the specific problem, the FSS technique has become the preferred method for solving long-range tropospheric radarwave propagation problems. This is because the FSS method has been proven to be the most stable and efficient method for marching the field to further ranges [7]. The FSS solution of the SPE is given by:

$$u(x + \Delta x, z) = \exp \left[jk(n^2 - 1) \frac{\Delta x}{2} \right] F^{-1} \left\{ \exp \left[-ip^2 \frac{\Delta x}{2k} \right] F \{u(x, z)\} \right\}, \quad (4-7)$$

where p is the transform variable and equal to $p = k \sin \theta$ (θ being the elevation angle from the paraxial direction) and F the Fourier transform [39]. From Eq. 4-7 the total (one way) propagation loss can be computed using [39]:

$$PL = -20 \log |u| + 20 \log(4\pi) + 10 \log x - 30 \log \lambda. \quad (4-8)$$

There are several advantages to the split-step PE method. First, and probably most important, is that it models all propagation mechanisms discussed; it even allows relatively simple and efficient modelling of environments where the refractivity varies both vertically as horizontally [6, 42].

Second is that the parabolic equation is valid and efficient at all ranges (within, near and beyond the horizon) unlike the more traditional methods. Hence, a single method can be used to determine the field in all regions of interest. This being said the SPE provides accurate results only within elevation angles of less than 10° – 15° [39]. The error is a result of neglecting terms in the Taylor expansion when approximating the operator Q . The error developed is proportional to the first neglected term of the expansion, $\sin^4 \theta$ [39, 42]. Hence, the SPE is a narrow-angle approximation of the parabolic equation. Even though elevation angles encountered in long-range propagation problems are usually less than a few degrees, wide-angle parabolic equation methods can be developed by approximating the operator Q more accurately. Wide-angle parabolic equation methods are generally used for high altitude radars or for modelling propagation over irregular terrain with high slopes. For more information on wide-angle methods see [42].

Another advantage of the parabolic equation method is that it is proven to be very robust in the sense that it works well for any practical environment [6]. Modifying the FSS standard parabolic equation even allows accurate propagation modelling above complex terrain [8].

The main disadvantage is that the parabolic equation method demands large computational resources, both in terms of memory and executions times, for applications involving combinations of high frequencies, high elevation angles, high terminals and long maximum ranges [6]. A solution to this is the use of Hybrid methods, which combines fast geometric optics with the advanced robust parabolic equation method to assess radar propagation in large domains. Hybrid methods will be discussed in the next section.

Another disadvantage is that the implementation of the backward propagating wave is complicated. The backwards propagating wave is therefore often neglected in propagation models,

for example in AREPS. PETOOL is an example of a model that does account for both the forward and backward propagating wave [39] (see also Section 3-2-6).

Due to the above characteristics, the parabolic equation method has become the preferred method for complex tropospheric radar assessment problems [7]. Examples of parabolic equation model results are given throughout the text. All figures displaying propagation losses or coverage are computed using parabolic equation based models.

4-4 Hybrid methods

In some cases the strengths and capabilities of the above methods are combined in a single hybrid model. One of the most advanced propagation models today, actually named the Advanced Propagation Model (APM), combines the parabolic equation method with geometric optics. The reason for combining these methods is to benefit from the advantages of the parabolic equation method at small elevation angles whilst using the relatively fast geometric optics method to reduce execution times and to determine field strengths at high elevation angles where the parabolic equation method becomes inaccurate [42]. The reduction of execution times is especially important for naval operations where time is of the essence.

APM is based on the well documented Radio Physical Optics (RPO) propagation model developed by Hitney in 1992; which uses different "submodels" based on either the geometric optics or the parabolic equation method in defined regions: flat earth (FE), ray optics (RO), parabolic equation (PE) and extended optics (XO) (see Fig. 4-2) [43, 48]. The RPO model is proven to be 25 to 100 times faster than pure parabolic equation models in determining field strengths for large domains at high frequencies, whilst remaining accurate [48]. The main difference between the RPO model and APM lies in the used parabolic equation model. APM uses the more advanced Terrain Parabolic Equation Model (TPEM) which allows radar assessment above variable terrain [43], whilst RPO was developed for surface-based radar assessment only over water [48].

The FE submodel is used at ranges up to 2.5 km from the source and for all elevation angles above 5°. The FE model uses a simple geometric optics model similar to the model discussed in Section 2-5. Such a model suffices because refraction effects are significantly small at elevation angles above 5°. Although this model assumes a flat earth, the earth curvature and refractive effects are still accounted for by using the effective-earth-radius k_e . The use of the effective-earth-radius ensures a smooth transition between the FE- and RO-region of 0.1 dB or less.

The region in which the RO submodel is used is determined by the limiting reflected ray R_0 (see Fig. 4-2) characterised with the grazing angle β at the surface. The limiting ray ensures that the field strength can be computed accurately at any point in the RO region by the geometric optics method discussed in Section 4-1. The field can be determined accurately by geometric optics because the chosen grazing angle is large enough to avoid diffraction problems by the earth's surface and any ducting effects within the RO-region. In a homogeneous stratified atmosphere the limiting grazing angle is 2.5 times the limit given by Reed and Russel, limited to values above 0.002 radians, and includes an extra term to account for ducting:

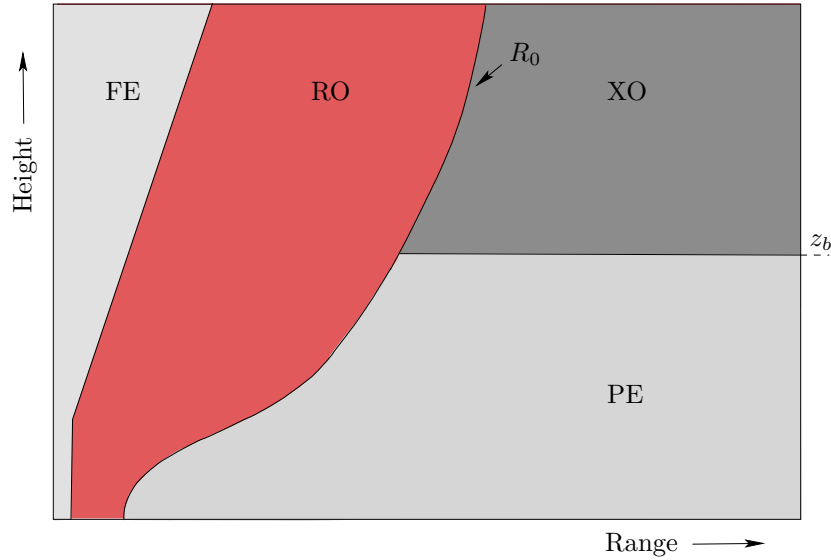


Figure 4-2: The four regions of the Advanced Propagation Model: flat earth (FE), ray optics (RO), parabolic equation (PE) and extended optics (XO).

$$\beta = \beta_0 + \delta\beta,$$

$$\beta_0 = \max \left(0.002, 2.5 \times \left[\frac{0.01772}{f_{MHz}^{1/3}} \right] \right), \quad (4-9)$$

$$\delta\beta = \sqrt{2 \times 10^{-6} \Delta M},$$

where f_{MHz} is the frequency in MHz and ΔM is the M-unit difference in the modified refractivity profile between the minimum value and that at the surface. The factor 2.5 is chosen to ensure a smooth transition between the RO- and PE-region of 0.1 dB or less. For an inhomogeneous atmosphere β_0 in Eq. 4-9 is doubled.

Beyond the RO-region and below the altitude z_b the field strength is computed by a wide angle parabolic equation model. By minimising the altitude z_b , the size of the Fast Fourier Transform (FFT) is minimised resulting in faster computation times. However, z_b must be chosen such that it encompasses all significant refractive effects and the majority of terrain effects. In general z_b is chosen at 120% of the maximum terrain height along the propagation path, or the height of the highest trapping layer specified in the refractivity profile(s), whichever is greater.

Beyond the RO-region and at altitudes above z_b lies the XO-region (see Fig. 4-2). Within the XO region the field computed by the parabolic equation model at height z_b is extended to higher altitudes using geometric optics (ray tracing). The idea is that if z_b is chosen sufficiently large, the rays above z_b will propagate almost parallel⁴ to each other and therefore, to good

⁴Hence there are no severe refraction effects above z_b .

approximation, the electric field amplitude relative to free space can be assumed constant to that computed with the PE model at height z_b . Using geometric optics, the constant ratio is traced into the XO-region.

Whilst many assumptions are made within APM, comparison with pure parabolic equation models and mode theory models has shown that results are virtually identical, whilst decreasing execution times significantly. It should be stated that the model described above is applicable only for surface-based emitters below 100 m in cases where the terrain is flat for the first 2.5 km. When the terrain is not flat within the first 2.5 km APM uses the PE and XO models only. For airborne applications only the PE model is used. For more information on APM, the RPO model or hybrid models in general see [42, 43, 48].

4-5 Tactical decision aids

Since the 1980's propagation models have been embedded in tactical decision aids (TDAs) giving the operational user the ability to assess radar performance in (near) real time and to mitigate and exploit atmospheric effects [9]. Embedded in TDAs, propagation models are typically required to execute rapidly over large domains and for the full range of radar parameters, often at the expense of accuracy. Furthermore, these models must be very robust in the sense that the operation by inexperienced users will not result in errors or other numerical problems [5]. The RNLN uses two different propagation models as TDAs for radar assessment: CARPET [23] and AREPS [2]. Currently CARPET is integrated into the combat management systems (CMSs) of His Netherlands Majesty's (HNLN) naval ships. AREPS is yet to be integrated, which is highly recommended.

The Computer-Aided Radar Performance Evaluation Tool (CARPET) developed by the Netherlands Organisation for Applied Scientific Research (TNO) is a fast and easy tool for (near) real-time evaluation and the design of surface-based radar systems, i.e. maritime and land-based. It focuses on the entire radar system and its environment, including transmitter/receiver characteristics, clutter, jamming, antenna and propagation. CARPET meticulously maps the effects of radar parameters and environmental conditions on the detection probability as a function of target range, velocity or altitude. Besides detection probabilities CARPET can provide a variety of graphs such as: Moving Target Indication (MTI) improvement factor and blind zone diagrams. It therefore is a great tool for scientific research.

Although CARPET does consider basic environmental effects it lacks the ability to model anomalous propagation. This is because the used propagation model is primarily based on the geometric optics method, which as discussed has difficulties in determining field strengths in ducting conditions. CARPET solves this by approximating the effects of ducting by a mode theory based model known as the Engineer's Refractive Effects Prediction System (EREPS). Whilst this improves results significantly, it is still shortcoming compared to other, generally parabolic equation based, radar assessment programs. This because CARPET is only capable of modelling the evaporation duct and the surface-based duct; and thereby uses only the duct height rather than a whole vertical refractivity profile; let alone it models lateral inhomogeneity. Also, CARPET is currently insufficient in modelling terrain effects. In spite of its limitations, CARPET is excellent in modelling radar systems and target characteristics and to a certain extent gives fast insight on radar performance and can thereby, for example,

increase situational awareness. For more information on how CARPET models propagation see [23].

The more advanced propagation assessment model Advanced Refractive Effects Predictions System (AREPS) developed by the US Navy's Space and Naval Warfare Systems Command (SPAWAR) is unlike CARPET a TDA designed especially for naval operations. Among other things AREPS displays: propagation losses, radar coverage, electronic support measures (ESM) vulnerability and UHF/VHF communications; all as function of height, range and bearing. AREPS is based on the APM model discussed above and can therefore accurately model anomalous propagation, including propagation through lateral inhomogeneous atmospheres and terrain effects. As environmental input, AREPS is able to use full vertical refractivity profiles. Hence, AREPS is an excellent model for radar assessment in prevailing environmental conditions. For more information on how AREPS models propagation see [2, 43].

Output examples of both CARPET and AREPS under the same conditions are given in Fig. 4-3(a) and (b) respectively. Both figures display detection probabilities of a 3.3 GHz radar at a height of 20 m searching for a small fighter with a radar cross section (RCS) of 2 m^2 and the probability of false alarm being $P_{FA} = 10^{-6}$. Notice that CARPET is capable of modelling the surface duct (including ONLY the first skipping zone) but not the transition from a surface duct to an elevated duct at 100 km (as shown in the AREPS results). This being said, whilst AREPS is better in considering environmental effects, CARPET is generally faster and models radar systems and target characteristics more elaborate.

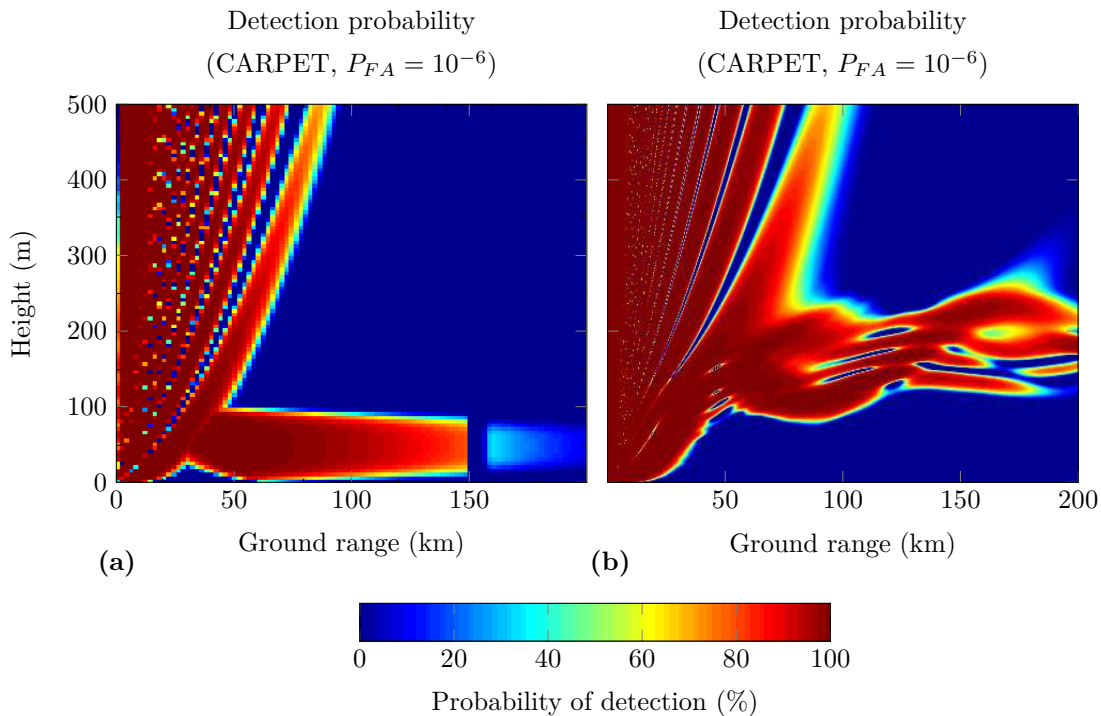


Figure 4-3: Detection probabilities computed by CARPET (a) and AREPS (b) under the same conditions: a surface-based duct rising into an elevated duct at 100 km.

Modelling the environment

In Chapter 4 three methods¹ for modelling anomalous propagation and assessing radar performance were examined; of which the parabolic equation method is currently the most advanced and preferred method [7]. The parabolic equation method has demonstrated to provide results that are in excellent agreement with measurements [4]. This said, the results are only accurate when the model is provided with sufficient environmental input data, both in accuracy and resolution.

This chapter discusses ways of modelling the environment for radar propagation assessment and how the required environmental data may be obtained. A new environmental model will be developed, which is later used within this thesis (in Chapter 7) to examine the radar performance assessment accuracy sensitivity to the required horizontal and temporal resolution of atmospheric data, and the error as a result of assuming a homogeneous stratified atmosphere. To examine this, the new environmental model needs to produce realistic modified refractivity profiles. The proposed model does this and is therefore suitable for the purpose of this thesis. While the model may also be suitable for operational radar performance assessment, it is by no means certain that it is, and it is not presented as such. Prior to operational use, the model should at least be validated. Such validation is beyond the scope of this thesis.

In the first section the refractivity of the troposphere and its dependence on pressure, temperature and water vapour will be discussed. The next section looks into acquiring the vertical refractivity profiles, which can be obtained through measurements, numerical modelling or both [10]. Because measuring the refractivity in the lower metres of the troposphere is problematic it requires a different technique than that which is used for acquiring refractivity elsewhere. For that reason, this section is split up into three subsections. Acquiring the upper- and lower-air profiles will be examined in the first two subsections. The third subsection looks into methods for blending the upper and lower-air profiles together. Also, within this subsection, a completely new blending algorithm is developed. Next, the interpolation between multiple vertical profiles will be discussed. At the end of this chapter all concepts will be integrated into an environmental model.

¹Excluding hybrid methods.

When considering the effect of the environment on radar performance it is generally important to also consider effects due to the earth's surface: is the ocean smooth or rough, is there propagation over variable terrain? Whilst the effects of the earth's surface were discussed in Chapter 2 and 3, this thesis will not examine the required input data for describing the surface. Existing terrain databases hold sufficient information for modelling terrain effects on radar propagation [7]. For information on surface modelling see Barrios [8].

For the purpose of this thesis it is assumed that all propagation paths occur over smooth sea water, which can be modelled as a perfectly conducting surface. This simplification is allowable because sea roughness has little effect on the required horizontal refractivity resolution.

5-1 The tropospheric refractivity

As seen in Section 2-2 and Chapter 3 electromagnetic energy propagating through an inhomogeneous medium does not travel in a straight line but refracts. According to Snell's law the propagation path of electromagnetic energy is governed by the refractive index n (see Eq. 2-3 and 2-6). Hence, the value and variation of the refractive index n are fundamental to understanding the way in which electromagnetic waves propagate through the atmosphere [19]. The refractive index is defined as the ratio of the propagation speed of energy in a vacuum, c_0 to the speed in a specified medium, v :

$$n = \frac{c_0}{v}. \quad (5-1)$$

The refractive index of the troposphere depends on the molecular composition of the air: nitrogen, oxygen, argon, carbon-dioxide and water vapour. It deviates from unity because of the polarisation of molecules in the presence of electromagnetic fields and because of quantum mechanical molecular resonances [19]. Neglecting the effects of molecular resonance, which causes attenuation of electromagnetic energy rather than refraction, the refractive index of the troposphere, at microwave frequencies, is equal to the additive combination of three terms [18]. The first and second term are respectively the sum of the distortion of electronic charges of the dry gas molecules (nitrogen, oxygen, argon and carbon dioxide) and of water vapour under the influence of an applied electromagnetic field. The third term is the effect of the orientation of the electric dipoles of water vapour under the influence of a field. The refractive index can be expressed by the refractivity as:

$$N = (n - 1) \times 10^6 = K_1 \frac{p_d}{T} + K_2 \frac{e}{T} + K_3 \frac{e}{T^2}, \quad (5-2)$$

where p_d is the partial pressure of the dry gases in millibar (mb), e is the partial pressure of water vapour in millibar, T the temperature in degrees Kelvin and where K_1 , K_2 and K_3 are constants. The constants have been determined empirically multiple times with different outcomes by various organisations. In 1953 Smith and Weintraub [18] proposed a reliable set of constants based on the mean of previous independent determinations. Today the proposed set of constants is used widely in the radar propagation community [17]. The first term K_1 ,

determined by multiple independent laboratory measurements on dry air and by correcting for carbon-dioxide content², is equal to:

$$K_1 = 77.607 \pm 0.013 \frac{^{\circ}\text{K}}{\text{mb}}. \quad (5-3)$$

The constants K_2 and K_3 were evaluated from a survey of water vapor Debye constants by Birnbaum and Chatterjee. K_2 and K_3 are equal to:

$$K_2 = 71.6 \pm 8.5 \frac{^{\circ}\text{K}}{\text{mb}}, \quad (5-4)$$

and

$$K_3 = (3.747 \pm 0.031) \times 10^5 \frac{^{\circ}\text{K}^2}{\text{mb}}. \quad (5-5)$$

Substituting the constants K_1 , K_2 and K_3 in Eq. 5-2, reducing the constant values to three figures significant and utilizing the total pressure $p = p_d + e$ yields:

$$N = 77.6 \frac{p}{T} - 6 \frac{e}{T} + 3.75 \times 10^5 \frac{e}{T^2}, \quad (5-6)$$

where p is the atmospheric barometric pressure in millibar. Introducing a negligible, error Eq. 5-6 can be simplified through lumping the second and third term together (see [18]), resulting in the widely used tropospheric refractivity expression:

$$N = (n - 1) \times 10^{-6} = \frac{77.6}{T} \left[p + \frac{4810e}{T} \right]. \quad (5-7)$$

Notice that the expression is independent of frequency. The derived empirical expression is considered to be accurate to 0.5% for frequencies up to 30 GHz for temperature ranges between -50 and 40 °C, atmospheric pressures ranges between 200 and 1100 millibar and water vapour pressure ranges between 0 and 30 millibar [18]. Beware, the 0.5% accuracy does not consider the errors in measuring temperature, pressure and humidity. This being said, with today's standard meteorological measuring equipment the refractive index is determined with a high enough accuracy for radar assessment [10]. Note that for radar assessment the accuracy of determined vertical refractivity gradient is of more importance than the accuracy of the actual value of the refractivity, this because the refractive index of the troposphere deviates little from unity (see Eq. 2-6).

For integrity reasons, it was pointed out that molecular resonance causes attenuation of electromagnetic energy rather than refraction. Attenuation of electromagnetic energy is limited to certain narrow frequency bands as shown in Fig. 2-14 (e.g. 22 GHz and 60 GHz bands); and can be modelled by adding a complex term to the refractivity [19]. In this thesis however, the refractivity is kept real and the effects of attenuation are neglected. Neglecting the effect

²Laboratory measurements are usually done in carbon-dioxide free air because of the variable concentrations of carbon-dioxide in laboratories. Smith and Weintraub therefore corrected the original value of K_1 to correspond to dry air with a carbon-dioxide content of 0.03%.

of attenuation is valid within this study because they are small and vary little at the used operating frequencies (see Fig. 2-14 at 3.3 GHz) and therefore has a minimal affect on the required resolution.

5-2 Acquiring the vertical refractivity profile

The vertical refractivity profiles for radar assessment can be obtained through different measuring techniques, modelling techniques or both. Because different heights require different approaches for obtaining the refractivity the vertical profile is split up into an upper profile, which extends from approximately 10 m and upwards, and the lower profile also named the evaporation duct profile, which extends from the surface to approximately 50 m.

5-2-1 Upper-air profiles

The upper-air refractivity profile is needed to assess the effects of surface and elevated ducts on radar performance. The upper profile can be obtained by measuring the refractivity indirectly or directly and from numerical weather prediction models [19]. Compared to the lower-air profile, the upper profile is relatively easy to measure. This because there is less temporal fluctuations in the upper troposphere.

Measuring refractivity

Upper vertical refrativity profiles are aquired most frequently through the use of radiosondes. A sonde, attached to a helium filled balloon measures pressure, temperature and humidity along its ascent and transmits its measurements back to a base station [19]. Typical accuracies of sonde measurements are 0.5 hPa for pressure, 0.2 degrees Kelvin for temperature and 2% for relative humidity [10]. From the received data height and refractivity can be derived that are sufficiently accurate for operational radar assessment. Currently radiosondes are the only technique used in the RNLN³ to obtain upper atmospheric refractivity data for radar performance assessment.

Advantages of radiosonde balloon measurement include that balloons are easily launched from operational platforms, and that sondes need not be recovered as they are inexpensive [19]. A major disadvantage of radiosonde measurements is that a single launch provides only a single vertical profile. While a single profile suffices in a homogeneous stratified atmosphere, multiple profiles are required where the atmosphere is inhomogeneous. To cover an extended inhomogeneous area by radiosonde balloon measurements is nearly impossible under operational conditions.

Radiosondes can also be used as parachute suspended dropsondes, which are jettisoned from aircraft (manned or unmanned) and transmit measurements during their descent. Unlike

³It is not always possible for a ship to acquire a vertical profile by launching a radiosonde balloon. The main reason for this is that they simply do not posses over the required equipment on board. If this is the case, it is common to use radiosonde measurements from a nearby weather station, which can be acquired through the world wide web. Using a remote sonde measurement from a nearby weather station must be done with care as the air at the station might differ from the air near the ship and the sonde measurement is most likely taken above land which may introduce significant errors in the radar performance assessment.

balloon carried sondes, dropsondes are practical for the measurement of multiple profiles [4]. For measuring an extended area, dropsonde measurement soon becomes time consuming and cost prohibitive.

Refractometers are an alternative to radiosondes. Unlike sondes, refractometers measure refractivity directly. They are also more accurate, typically an order of magnitude better than sondes, and have a higher resolution [17]. Because refractometers are complex, bulky and expensive [10] they are however unsuited for operational use. Refractometers are generally carried by aircraft. Typical applications include detailed measurements of larger areas for specific experiments such as those described in Section 3-2-5 [19].

Remote sensing techniques which are currently being developed include radar, lidar⁴ and radiometric⁵ techniques [10]. Sensors may be carried by ships, aircraft and satellites. A major advantage of remote sensing techniques is that by their applications larger 3D areas can be covered quickly. While remote sensing techniques to date have shown promising qualitative results, the techniques are still plagued by logistic and technical limitations [4, 10, 19]. Resolution and accuracy of current remote sensors fall short for accurate propagation assessment. This said, remote sensing techniques will continue to develop because of its relative ease and speed in obtaining 3D refractivity data and thereby making it the preferred measuring technique, especially for naval operations [10].

Radio propagation techniques which are also under development aim to establish refractivity profiles by passive monitoring of fixed (e.g. cellular mast near the coast) or satellite borne transmitters with a exact known location [10]. Active radiopropagation techniques aim to extract refractivity information from monitoring seaclutter effects due to ducting [10]. For example, sea clutter rings can be a result of the skipping zone accompanied by a surface-based duct. The range of these rings depend on the height and thickness of the trapping layer.

Whilst there are a number of measuring techniques, some still under development, obtaining 3D refractivity data is still difficult and impractical, especially in naval operations. Most navies that measure refractivity only, including the RNLN, therefore, rely on balloon radiosonde measurements and assume a stratified homogeneous atmosphere.

Numerical weather prediction models

Another method for acquiring upper vertical refractivity profiles is provided by numerical weather prediction (NWP) models. NWP models numerically compute vertical profiles of wind speed, pressure, temperature and humidity on a horizontal grid from the surface upwards into the stratosphere by using the primitive equations for the conservation of momentum and mass, Newton's second law of motion, the first law of thermodynamics and the ideal gas law [12, 49]. With the computed grid profiles and equation 5-7, the associated vertical refractivity profiles can be determined. The result is as if multiple radiosondes had been deployed from the grid points throughout the battle space, as illustrated in Fig. 5-1.

The initial NWP field conditions are obtained from a combination of local short term NWP forecast fields and new standardised world wide observations of meteorological data from

⁴Light detection and ranging (lidar) system.

⁵Radiometric techniques are especially attractive for naval operations. This because they are a passive remote sensing technique and are therefore ideally suited for where active emissions are undesirable [10].



Figure 5-1: Numerical weather prediction (NWP) models compute vertical profiles of wind velocity, pressure, temperature and humidity on a horizontal grid from the surface to the stratosphere; the results are comparable to launching multiple balloon radiosondes. (Photo taken by Mass Communication Specialist Seaman Brian G. Reynolds (March 24, 2012) [50].)

radiosondes, ships, buoys, land-stations airplanes and satellites. Grid boundary conditions are provided by (coarser in resolution) global NWP models. After all data is assimilated on a three dimensional grid, the primitive equations are used to numerically determine conditions in the future [12, 49].

Current mesoscale NWP models have an 1 to 10 km horizontal resolution which is sufficient for the modelling of mesoscale weather phenomena⁶, as for example sea breezes which have a significant impact on radar performance [12]. For radar assessment NWP models should have a horizontal model resolution of at least 5 km and an average vertical resolution of at least 60 m in the first kilometre of the troposphere [13]. Note that the horizontal resolution requirement of 5 km is the required model resolution to accurately model mesoscale weather phenomena which can have a significant impact on radar performance. Depending on the prevailing weather conditions this resolution can be reduced to a coarser resolution whilst remaining sufficient for accurate radar performance assessment.

Although NWP data is not perfect and does not account for fine scale atmospheric fluctuations and temporal variability, NWP output is sufficiently detailed to provide a useful indication of radar performance under prevailing weather conditions [12], and thereby can significantly increase the insight in radar performance and the situational awareness on board. In as far as NWP data is not entirely accurate, in the presence of significant horizontal inhomogeneity NWP based performance prediction still outperforms prediction that is based on a single profile as derived from a single radiosonde launch. Radar assessment based on a single profile

⁶Mesoscale meteorological phenomena are phenomena with dimensions that generally range from around five kilometres to several hundred kilometres.

can have significant consequences [11]. Other advantages of NWP models include the possibility of 48 hour forecasts with a one hour resolution [12], and the option to predict radar performance from other vantage points, including those of opposing forces.

To improve radar assessment in inhomogeneous atmospheres and the ability of forecasting radar performance, effort is taken into improving NWP models. Improvements include the increase of spatial and temporal resolution and the ability to include local in situ meteorological measurements as discussed above in addition to world wide standard measurements [12].

Currently the US, Canadian, New Zealand and Royal Navies use NWP models for radar assessment [13]. Contrary to the RNLN that uses radiosonde measurements to obtain refractivity profiles for radar assessment, the US Navy uses NWP generated profiles only and abandoned in situ radiosonde measurements entirely. The US Navy's NWP model COAMPS (Coupled Ocean/Atmosphere Mesoscale Prediction Systems), developed by the Naval Research Laboratory - Monterey Marine Meteorology Division (NRL-MRY), has a horizontal resolution of 3 km and an average vertical resolution of 47 m in the first kilometre of the troposphere and a temporal resolution of 1 hour. COAMPS can forecast up to 48 hours. The US Navy's TDA AREPS, which is used within this thesis, is designed such that it interfaces directly with COAMPS data [2].

The RNLN is currently investigating, by means of this thesis, the use of the NWP model HARMONIE (Hirlam Aladin research on mesoscale operational NWP in Euromed). HARMONIE, developed by a cooperation between a number of European meteorological institutes⁷, is a non-hydrostatic NWP model with a standard horizontal resolution of 2.5 km, an average vertical resolution of 65.6 m in the first kilometre of the troposphere and a temporal resolution of 1 hour. HARMONIE can forecast up to 48 hours. Within this thesis HARMONIE data is used to assess resolution requirements for accurate radar assessment. Even though, according to [13] the average vertical resolution is (just) not sufficient for accurate radar assessment, HARMONIE is still sufficient for assessing horizontal resolution requirements. For this it is required that the NWP data has a high horizontal resolution (e.g. 2.5 km) and that it is realistic for the prevailing weather conditions. HARMONIE provides such data.

Note that NWP data can also be used for naval applications other than radar performance assessment. For weather prediction, for example, but also for performance assessment of electrical optical and infra-red systems or for improving weapon accuracy. Weapon accuracy can be improved by using prevailing atmospheric data to estimate, for example, the ballistic trajectory of naval gun fire⁸. It is recommended that the RNLN look further into other operational applications of NWP data.

⁷Danish Meteorological Institute (DMI) (Denmark), Estonian Meteorological and Hydrological Institute (EMHI) (Estonia), Finnish Meteorological Institute (FMI) (Finland), Icelandic Meteorological Office (IMO) (Iceland), Lithuanian Hydrological and Meteorological Service (LHMS) (Lithuania), Met Éireann (ME) (Ireland), Norwegian Meteorological Institute (MET) (Norway), Royal Netherlands Meteorological Institute (KNMI) (The Netherlands), Agencia Estatal de Meteorología (AEMET) (Spain), Swedish Meteorological and Hydrological Institute (SMHI) (Sweden), Météo-France (France).

⁸Weapon accuracy can be improved also by determining the target's position more accurately as discussed in Section 3-3-3.

5-2-2 Lower-air profiles and Monin-Obukhov similarity theory

The evaporation duct is a persistent phenomenon found nearly everywhere over water; and as shown in Section 3-2-4, the evaporation duct can have a significant effect on the propagation of electromagnetic energy [1]. Hence, the evaporation duct must be considered when assessing radar performance. However, contrary to measuring the vertical refractivity profile of the upper atmosphere, the refractivity profile near the earth's surface, also known as the evaporation duct profile, cannot be measured easily.

Measuring the refractivity near the water surface is challenging for a number of reasons [10]. First, measuring the vertical humidity profile is difficult because humidity decreases rapidly from (nearly) saturated at the surface to its ambient value within the first few centimetres. Second, determining the measuring height above the water surface is burdensome due to waves continuously changing the surface height. Hence, a surface height must be defined by averaging multiple surface height measurements over time. The third and probably the biggest problem is that individual measured profiles are characterised by temporal fluctuations due to turbulence, which are of the same order as the vertical changes of interest. Individual measured profiles are therefore not meaningful for radar assessment. Averaging individual profile measurements over time (in the order of one minute) is a solution, however, this is impractical, especially in naval operations.

Because the evaporation duct profile is difficult to measure, especially on a routine basis, different empirical surface layer models have been developed to compute the average refractivity profile near the earth's surface using four bulk measurements: the pressure, temperature, humidity at a single height (e.g. the ship's bridge) and sea-surface temperature; all of which can be measured using standard measuring equipment [10, 51].

The needed bulk measurements can also be obtained from the lowest model level (at approximately 10 m) of a NWP model. Mesoscale NWP models themselves are incapable of computing the lower refractivity profile because they are based on less sophisticated equations than surface layer models and make numerous assumptions in order to save computational time in the lowest levels of the atmosphere [52].

Monin-Obukhov similarity theory

Almost all modern surface layer models are based on the semi empirical Monin-Obukhov similarity theory (MOST) [51]. The vertical refractivity profile is determined by numerically modelling the vertical profiles of pressure, temperature and humidity. The refractivity profile is then determined using Eq. 5-7. MOST is valid within the surface layer which is defined as that part of the boundary layer in which turbulent fluxes vary by less than 10% with altitude. The surface layer extends from the surface to circa 50-300 m (depending on the atmospheric stability) [53].

First, the pressure profile can be approximated by considering that pressure decreases exponentially with height [51, 54]:

$$p(z) = p_r \exp\left(-\frac{z - z_r}{H}\right), \quad (5-8)$$

where p is the pressure at height z , p_r is the measured reference pressure at height z_r . H is the scale height which is defined as the distance over which the pressure decreases by a factor of e and can be approximated using $H = k_B T_v / \bar{M} g$, where k_B is the Boltzmann constant, T_v is the virtual temperature, \bar{M} the molecular mass of dry air and g the acceleration due to gravity. The more complicated temperature and humidity profiles are computed using MOST which states that the time averages of the vertical gradients of wind velocity u , potential virtual temperature⁹ Θ , and specific humidity¹⁰ q can be represented by similarity functions (ψ_u and ψ_h) of the dimensionless stability parameter $\zeta = z/L$:

$$\frac{\delta u}{\delta z} = \frac{u_*}{kz} \psi_u(\zeta), \quad (5-9)$$

$$\frac{\delta \Theta}{\delta z} = \frac{\Theta_*}{kz} \psi_h(\zeta), \quad (5-10)$$

$$\frac{\delta q}{\delta z} = \frac{q_*}{kz} \psi_h(\zeta), \quad (5-11)$$

where $k \approx 0.4$ is the von Karman constant, L is the Monin-Oboukhov length, ψ_u is the wind similarity function, ψ_h is the temperature-specific humidity similarity function and u_* , Θ_* and q_* are the scaling parameters of wind velocity, temperature and humidity respectively [51]. The Monin-Oboukhov length is a characteristic height scale of the surface layer and gives a relation between parameters characterising dynamic, thermal, and buoyant processes. The Monin-Oboukhov length also acts as a criterion for the stability of the surface layer: in unstable conditions $L < 0$ and in stable conditions $L > 0$. Unstable and stable conditions occur when the air-sea temperature difference (ASTD)¹¹ is respectively negative and positive. The degree of stability increase with an increase of the absolute ASTD and decreasing wind speeds. The conditions are neutral when the absolute value of the Moni-Oboukhov length is large [51]. The length L is defined as:

$$L = \frac{u_*^2 \Theta}{kg \Theta_*}. \quad (5-12)$$

By integrating Eq. 5-9, 5-10 and 5-11 from the roughness height (z_{0u} , $z_{0\Theta}$ and z_{0q}) to height z the vertical wind velocity, potential virtual temperature and the specific humidity profile are given by:

$$u(z) - u(z_{0u}) = \frac{u_*}{k} \left[\ln \frac{z}{z_{0u}} - \Psi_u(\zeta) \right], \quad (5-13)$$

⁹The potential virtual temperature is the temperature of an air parcel in which all moisture is converted into dry air and brought to a pressure of 1000 hPa. The potential virtual temperature is equal to $\Theta = T(1 + 0.608q)(1000/p)^{0.286}$, where T is the temperature in degrees Kelvin, q the specific humidity and p the atmospheric pressure [54].

¹⁰The specific humidity is the ratio of the mass of water vapour in an air parcel to the total mass of the parcel. The specific humidity is equal to $q = \frac{\varepsilon e}{p - (1 - \varepsilon)e}$, where e is the water vapour pressure, p the atmospheric pressure and $\varepsilon = 0.62197$ [53].

¹¹ASTD is air temperature minus sea temperature.

$$\Theta(z) - \Theta(z_{0\Theta}) = \frac{\Theta_*}{k} \left[\ln \frac{z}{z_{0\Theta}} - \Psi_h(\zeta) \right], \quad (5-14)$$

$$q(z) - q(z_{0q}) = \frac{q_*}{k} \left[\ln \frac{z}{z_{0q}} - \Psi_h(\zeta) \right], \quad (5-15)$$

where the integrated similarity functions Ψ_u and Ψ_h are defined as:

$$\Psi(z) = \int_{z_0}^z [1 - \psi(z)] \frac{dz}{z}. \quad (5-16)$$

The roughness heights z_{0u} , $z_{0\Theta}$ and z_{0q} are very low heights at which the wind speed, potential virtual temperature and specific humidity become theoretically equal to their surface values $u(0)$, $\Theta(0)$ and $q(0)$. Hence, in Eq. 5-13, 5-14 and 5-15 the values $u(z_{0u})$, $\Theta(z_{0\Theta})$ and $q(z_{0q})$ can be replaced with their surface values [51, 54]. At sea level the wind velocity $u(0)$ is equal to zero, the potential virtual temperature $\Theta(0)$ coincides with the sea surface temperature and the specific humidity $q(0)$ is the humidity at a relative humidity of 98-100%, depending on the salinity of the water. The roughness heights z_{0u} , $z_{0\Theta}$ and z_{0q} are specified as empirical functions of the wind velocity scale u_* and the integral functions $\Psi_u(\zeta)$ and $\Psi_h(\zeta)$ are determined empirically; the roughness heights and the integral functions will be discussed below. Hence, the only unknowns are u_* , Θ_* and q_* , which can be determined by solving the system consisting of Eq. 5-12, 5-13, 5-14 and 5-15. The system can be solved by successive iterations [51].

Roughness heights

Different implementations of MOST use different values for the roughness heights. Whilst all are a function of u_* , they differ because they are based on different independent experiments held under different atmospheric conditions. For the wind velocity height most implementations use the common expression given by:

$$z_{0u} = \frac{\alpha_{ch} u_*^2}{g} + \frac{0.11\nu}{u_*}, \quad (5-17)$$

where α_{ch} is the Charnock constant and $\nu \approx 1.5 \times 10^{-5} \text{m}^2/\text{s}$ is the dynamic viscosity [51]. Different definitions are used for the Charnock constant; some researches even state that the constant is dependent on wind speed. A good overall approximation of the Charnock constant is $\alpha_{ch} = 0.018$ [51]. This value will be used within this thesis to model the evaporation duct.

A relatively simple yet accurate approximation of the temperature and humidity roughness heights can be obtained by specifying these as the product of ν/u_* and a certain function of the Reynolds roughness number for velocity R_{Re} [51]:

$$z_0 = f(R_{Re}) \frac{\nu}{u_*}. \quad (5-18)$$

The European Centre for Medium-Range Weather Forecasts (ECMWF) reduces the Reynolds roughness function to constants [51] and defines the temperature and humidity roughness heights as:

$$z_{0\Theta} = 0.40 \frac{\nu}{u_*}, \quad (5-19)$$

and

$$z_{0q} = 0.62 \frac{\nu}{u_*}. \quad (5-20)$$

There are more sophisticated approaches in which, instead of constants, empirically derived functions of the Reynolds roughness number are used (see [51]). For this thesis the ECMWF approach is adopted.

Similarity functions

At first similarity functions were derived from experiments made over land, which, as can be expected, resulted in erroneous lower vertical profiles for wind, temperature and humidity when applied over water. In 1979, Liu, Katsaros and Businger (LKB) derived the first set of similarity functions for estimating profiles over water [53]. Since then, different researches have derived sets of similarity functions $\psi_{u/h}(\zeta)$, and/or their integral representation $\Psi_{u/h}(\zeta)$, based on specifically organised experiments [51]. The similarity functions of LKB in integral form and four other sets of functions which are used in other evaporation duct models, and which are also based on the LKB functions, are provided in Appendix B:

- The LKB model (1979) [51],
- The Naval Warfare Assessment station in Corona (NWA) model developed by Liu and Blanc (1984) [53],
- The Naval Research Lab (NRL) model developed by Cook (1991) [53],
- The model developed by Babin, Young and Carton (BYC) (1996) [53],
- The Naval Postgraduate School (NPS) model developed by Frederickson, Davidson and Gorocho (2000) [53],

All of the above models use separate similarity equations for stable and unstable conditions.

Implementation of MOST in an evaporation duct model

Because the five sets of similarity functions mentioned above are based on different data sets obtained from independent experiments, it is expected that they, to some extent, yield different results. To get an impression of how much the results differ, the similarity functions described in Appendix B have been implemented into an evaporation duct model using Matrix Laboratory (MATLAB). The used roughness heights are given by Eqs. 5-17, 5-19 and 5-20.

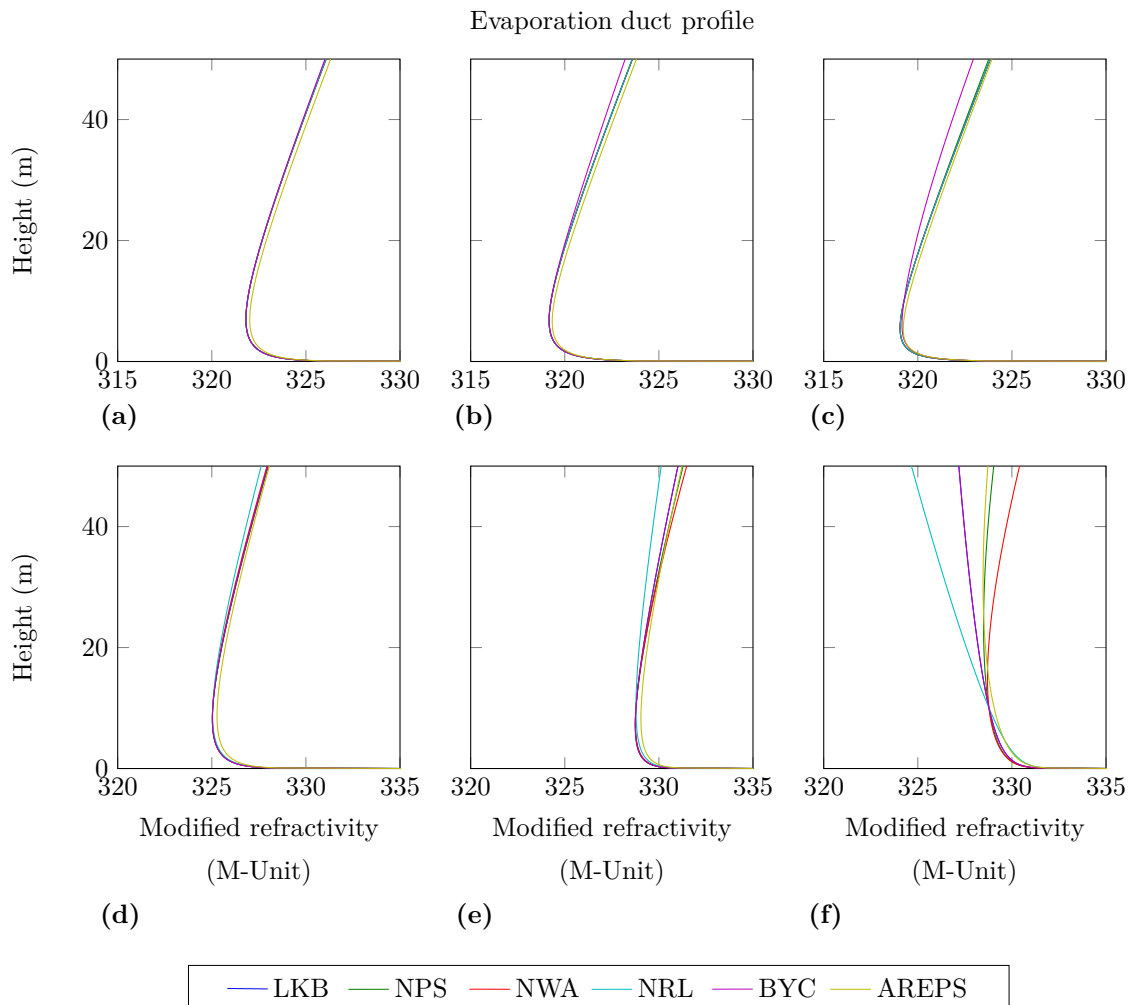


Figure 5-2: Evaporation duct profiles computed using different similarity functions under various conditions: unstable conditions (a-c) and stable conditions (d-f).

The implementation is an adaptation of the evaporation duct model developed and used¹² by the RNLN. The developed model uses the similarity functions of the NPS model. In reviewing the model of the RNLN a number of implementation errors were discovered. These errors were pointed out to the Defence Materiel Organisation (DMO) of the Dutch Armed Forces. The implementation made in this thesis can be found in Appendix C.

For comparison, Fig. 5-2 shows how different similarity functions yield different profiles under various conditions. For validation of these implementations, the profiles computed by the validated NPS model, which is integrated in AREPS, are also shown [2,55]. The difference between the output of the validated NPS model and that of the NPS model implemented here is most likely due to the use of different sets of roughness heights, and to small implementation differences. Overall, the results compare well, especially in unstable conditions. For this

¹²The evaporation duct model developed by the RNLN is integrated into the combat management systems (CMSs) of His Netherlands Majesty's (HNLN) naval ships and is the navy's primary model used to acquire the lower refractivity profile for radar performance assessment.

reason, the implemented NPS based model is the evaporation duct model used for the final proposed environmental model that is described in Section 5-4.

The top row of Fig 5-2 shows results for unstable conditions ($z/L < 0$ and $ASTD < 0$) where from left to right the conditions become more unstable due to a decrease in ASTD and/or wind speed. Notice that the profiles start to diverge when the conditions become increasingly unstable. However, for all three unstable cases the results are still similar. From left to right the evaporation duct heights computed by the used of similarity functions differ no more then: 0.1 m, 0.4 m and 0.9 m.

The bottom row shows results for stable conditions ($z/L > 0$ and $ASTD > 0$) where from left to right the conditions become increasingly stable due to an increase of ASTD and/or a decrease of wind speed. Compared to the results obtained in unstable conditions the profiles in stable conditions diverge more, especially under strong stable conditions. While the reason for this is beyond the scope of this thesis, the pronounced divergence may partly be explained by the high ASTD-sensitivity under stable conditions that is a common trait of MOST based evaporation duct models. Due to this high sensitivity, MOST based models are known to be prone to generating erroneous profiles with extremely high evaporation ducts [55]. See in Fig. 5-2 how for three of the six profiles (LKB, NRL and BYC) the evaporation duct height is unrealistically high¹³. The ASTD-sensitivity of the implemented NPS model is also shown by the duct height graphs of Fig. 5-3.

A conclusion as to which of the above MOST based models best suits the RNLN's purposes, lies beyond the scope of this thesis. Note, however, that the performance of each model is location dependent. The models will work best in locations where the similarity functions are empirically deduced. It is recommended that the RNLN further research which model is best suited for naval operations world wide and/or develop their own model.

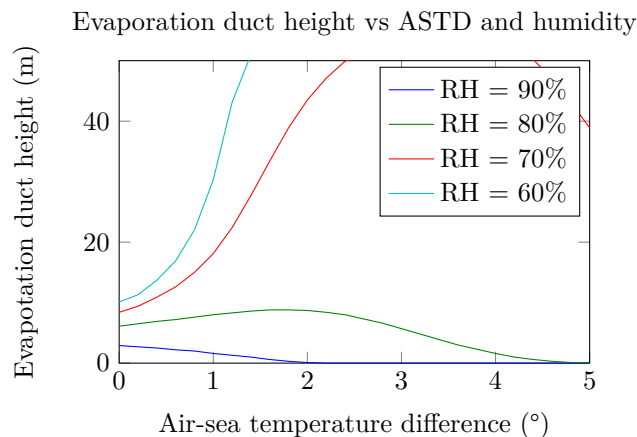


Figure 5-3: Evaporation duct models are highly sensitive to air-sea temperature difference. This sensitivity can result in the computation of unrealistic profiles with extremely high evaporation duct heights.

¹³The evaporation duct height varies between a metre or two at northern latitudes during winter nights and 40 m at tropical latitudes during summer days [2].

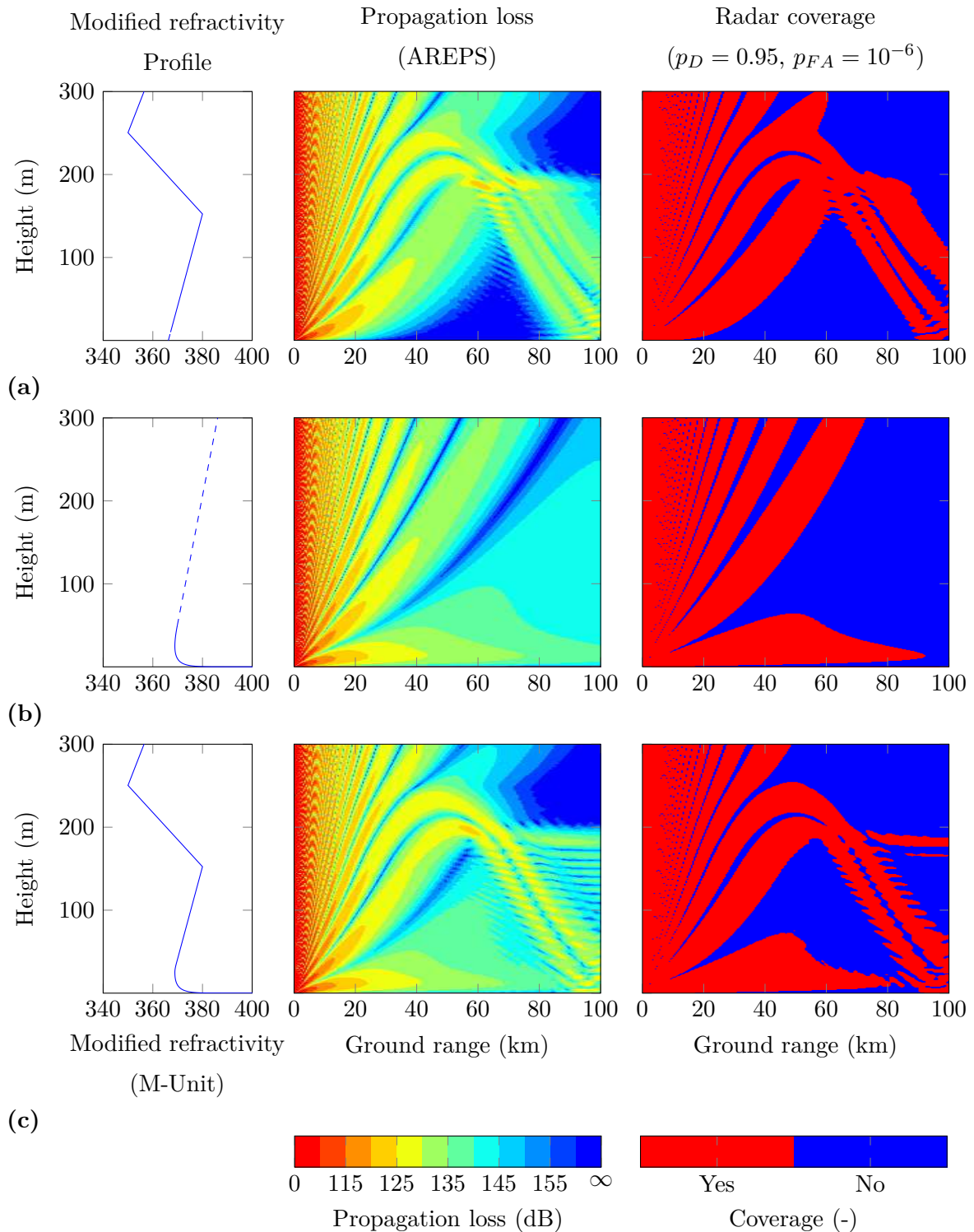


Figure 5-4: Radar performance predictions illustrating the importance of blending. From left to right the figure shows the modified refractivity profiles, the propagation loss assessments and the radar coverage assessments. From top to bottom the figure shows assessments for a surface-based duct environment (a), an evaporation duct environment (b) and a combined surface based and evaporation duct environment (c).

5-2-3 Blending upper- and lower-air profiles

As discussed above, methods for obtaining the vertical refractivity profile differ for higher and lower altitudes. The upper refractivity profile, which extends approximately from 10 m and upwards, is obtained with sufficient accuracy for radar assessment by measurements and/or NWP models, whilst the lower profile, which extends from the surface to approximately 50 m, is generally obtained by evaporation duct models based on MOST.

However, because refractivity structures (e.g. a surface-based duct) in the upper air also influence propagation near the surface (Fig. 5-4(a)) and because the evaporation duct near the surface also influences propagation at higher altitudes (see Fig. 5-4(b)), the effects of both profiles must be combined to accurately assess radar performance (see Fig. 5-4(c)). This subsection proposes a blending technique in the modified refractivity domain, and will be used in the final environmental model. At the end of this section a blending technique in the physical domain will also be discussed.

Obviously, for accurate electromagnetic propagation prediction, the combining or blending of propagation effects in the upper and lower layers must yield realistic results. At the level of propagation effects it is not at all obvious how the propagation loss diagrams in Fig. 5-4(a) and (b) could be combined into the blended result of Fig. 5-4(c). The same goes for the coverage diagrams of Fig. 5-4(a-c). At the underlying level of refractivity, how to go about realistically blending the upper and lower profiles of Fig. 5-4(a) and (b) into the combined profile of Fig. 5-4(c) seems, on the face of it, more obvious. In the first place, the combined profile should be continuous.

In early versions of AREPS¹⁴, for instance, the lower profile is simply appended to the lowest value of the upper profile above the surface. While this straightforward approach does provide a single continuous profile, it generally results in an unrealistic kink in the blended profile [55]. Also, this approach may significantly alter the evaporation duct height and thereby impairing the accuracy of the radar assessment [55]. See how in Fig. 5-5 the duct height of approximately 20 m of the originally computed profile M_{Low} is reduced to approximately 10 m after blending the upper-air profile M_{Upp} with the lower-air profile into a single profile $M(z)$.

More realistic blending of the profiles is necessary to avoid blending artifacts and consequent erroneous radar assessment results. The goal is to blend the lower profile obtained by MOST and the upper air profile obtained by e.g. NWP in such a way that:

1. the transition is continuous;
2. the transition is smooth, i.e. the derivative of the profile is continuous;
3. no blending artifacts, such as extreme gradients, are introduced;
4. no salient features of the upper and lower profile, such as the evaporation duct height, are distorted [52, 55].

The challenge lies in defining suitable blending methods for varying combinations of profiles, deciding which methods are appropriate for which cases, choosing appropriate blend intervals and automating all of these processes [55].

¹⁴Including the version (3.6) used in this thesis.

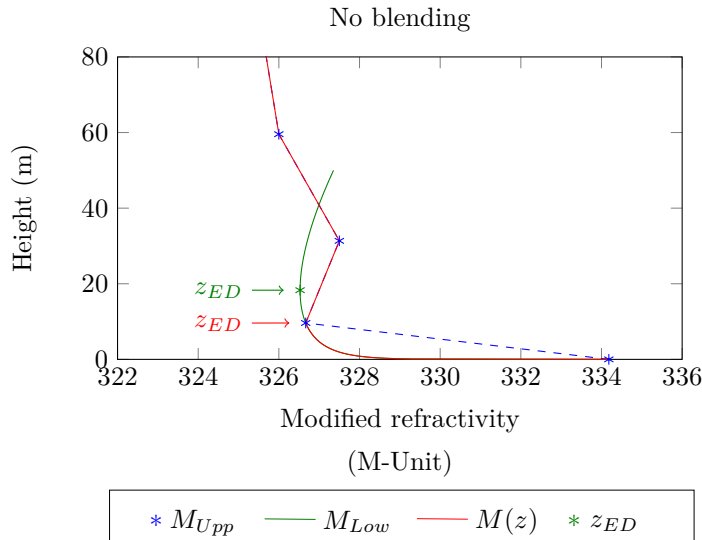


Figure 5-5: Blending by simply appending the lower profile (M_{Low}) to the lowest value of the upper profile (M_{Upp}) above the surface generally results in the distortion of salient profile features such as the evaporation duct height.

In this thesis a blending algorithm is proposed for blending the upper refractivity profile obtained from a NWP model with the lower refractivity profile that is obtained from a MOST based evaporation duct model. The lowest three NWP model levels should have heights of approximately 10, 30 and 60 m. The bulk parameters (air temperature, pressure and humidity) used for determining the lower profile are those given by the lowest data point of the NWP produced temperature, pressure and humidity profiles. The sea surface temperature is also taken from the NWP model. The blending technique is optimised for regions where the evaporation duct height does not exceed 20 m (e.g. the North Sea).

The proposed blending algorithm follows an approach that is similar to the approach that was adopted by Frederickson [55] in the development of the blending technique for the latest version of AREPS. As in his approach, blending is performed in the modified refractivity domain and the blending method as well as the blending interval depend on the structures of the profiles. Unlike Frederickson's approach, the blending proposed here does not negate the NWP model's data points: the algorithm is devised to blend in the lower profile in such a way that the resulting combined profile passes through all of the NWP points.

The resulting refractivity profile $M(z)$ is divided into three sections (see Eq. 5-21). In the lowest section, which extends from the surface to the lower boundary of the blending interval at height z_{BL} , the resulting profile is equal to the lower refractivity profile, M_{Low} , obtained from the evaporation duct model. In the highest section, which extends upwards from the upper boundary of the blending interval at height z_{BU} , the resulting profile is equal to the upper refractivity profile, M_{Upp} , obtained from the NWP model. In the middle section, the blending interval, the blended profile smoothly transitions from the lower profile into the upper profile. This section of the resulting profile profile, M_{Blend} is obtained by one of the three methods described below. The height of the upper boundary of the blending interval depends only on the method used, whereas the lower boundary of the blending interval depends on the structure of the upper and lower refractivity profiles. The method for determining the

lower boundary is discussed following the description of the blending methods.

$$M(z) = \begin{cases} M_{Low}(z) & \text{for } 0 \leq z \leq z_{BL}, \\ M_{Blend}(z) & \text{for } z_{BL} \leq z \leq z_{BU}, \\ M_{Upp}(z) & \text{for } z_{BU} \leq z, \end{cases} \quad (5-21)$$

Method 1

Method 1 divides the blending section into two subsection. In the lower subsection, which extends from z_{BL} to the third data point of the upper profile at height z_2 , the lower profile is blended into the gradient line M_{g2} using the cosine based filter α (see Eq. 5-22, Fig. 5-6 and 5-7(a)). The gradient line M_{g2} is defined as the line that passes through the second and third data point of the upper profile, as shown in Fig. 5-7(a). In the upper subsection, which extends from the third data point to the upper bound Z_{BU} , blends the lower results into the upper profile also using the α -filter (see Eq. 5-22). The upper bound of the blending interval is always at a height of $z_{BU} = 50$ m. An example of this method is shown in Fig. 5-7(a). Notice how the lower profile is blended smoothly with the upper profile.

$$M_{Blend}(z) = \begin{cases} \alpha(z)M_{Low}(z) + (1 - \alpha(z))M_{g2}(z) & \text{for } z_{BL} \leq z \leq z_2 \\ \alpha(z)M_{g2}(z) + (1 - \alpha(z))M_{Upp}(z) & \text{for } z_2 \leq z \leq z_{BU} \end{cases} \quad (5-22)$$

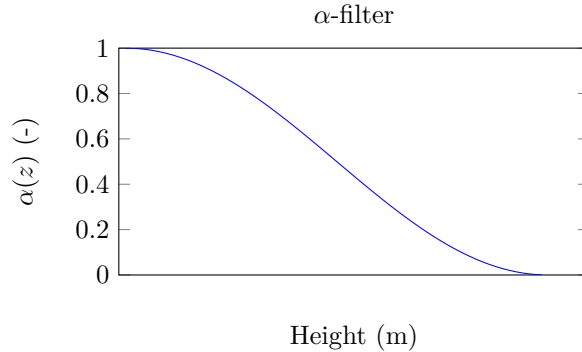


Figure 5-6: The cosine based α -filter.

Method 2

The second method blends the upper and lower modified refractivity profile by means of a third degree polynomial in such a way that, like in the first method, the blend is smooth. That is to say that the gradient of the resulting profile is equal to the gradient of the lower profile at the lower boundary of the blending interval; and that the gradient of the resulting profile is equal to the gradient of the upper profile at the upper boundary of the interval which, in this method, has a height equal to $z_{BU} = z_2$. The resulting profile is given by:

$$M_{Blend}(z) = a_2z^3 + b_2z^2 + c_2z + d_2 \quad \text{for } z_{BL} \leq z \leq z_{BU}, \quad (5-23)$$

where the polynomial coefficients a_2 , b_2 , c_2 and d_2 are chosen such that:

$$M_{Blend}(z) = \begin{cases} M_{Low}(z) & \text{for } z = z_{BL}, \\ M_{Upp}(z) & \text{for } z = z_{BU}, \end{cases} \quad (5-24)$$

and,

$$\frac{M_{Blend}}{dz} = \begin{cases} \frac{M_{Low}}{dz} & \text{for } z = z_{BL}, \\ \frac{M_{Upp}}{dz} & \text{for } z = z_{BU}. \end{cases} \quad (5-25)$$

An example of this method is shown in Fig. 5-7(b). Notice how the lower profile is blended into the upper profile more rapidly than in the case of Method 1.

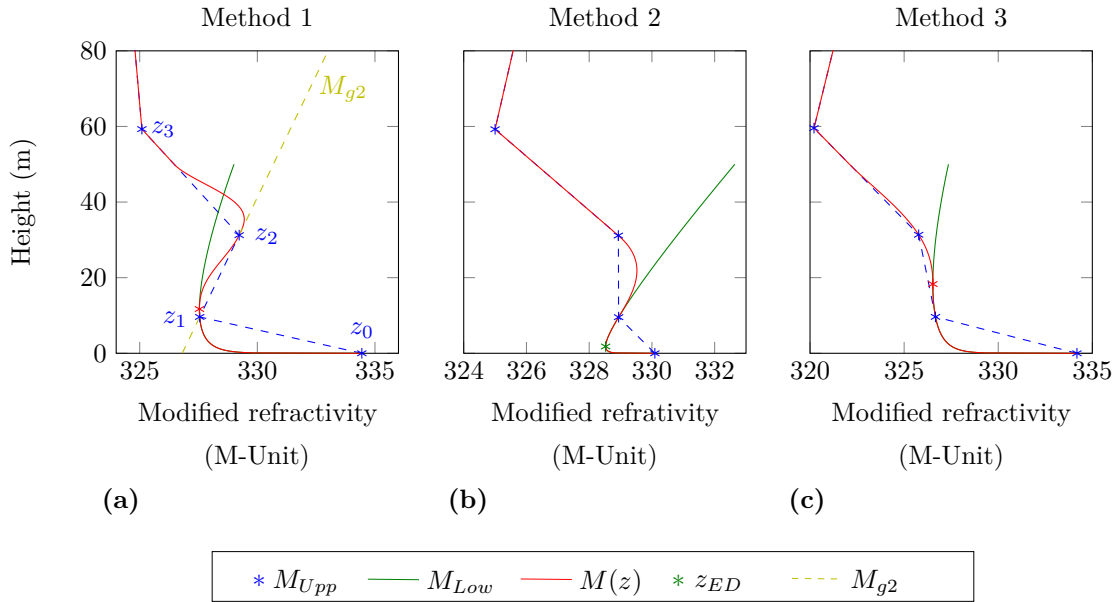


Figure 5-7: Three methods for blending the lower- and upper-air refractivity profiles into a single profile: Method 1 (a), Method 2 (b) and Method 3 (c).

Method 3

The third method uses a fourth degree polynomial for blending the lower and upper profiles together. The difference between Methods 2 and 3 is that the blending interval of Method 3 is larger as it extends as Method 1 to $z_{UB} = 50$ m. Because the blending interval is larger the profiles blend slower than in Method 2 and thereby avoiding unrealistic sharp gradients. The modified refractivity profile within the blending interval is defined as:

$$M_{Blend}(z) = a_3z^4 + b_3z^3 + c_3z^2 + d_3z + e_3 \quad \text{for } z_{BL} \leq z \leq z_{BU}, \quad (5-26)$$

where the polynomial coefficients a_3 , b_3 , c_3 , d_3 and e_3 are chosen such that:

$$M_{Blend}(z) = \begin{cases} M_{Low}(z) & \text{for } z = z_{BL}, \\ M_{Low}(z) & \text{for } z = z_2, \\ M_{Upp}(z) & \text{for } z = z_{BU}, \end{cases} \quad (5-27)$$

and

$$\frac{M_{Blend}}{dz} = \begin{cases} \frac{M_{Low}}{dz} & \text{for } z = z_{BL}, \\ \frac{M_{Upp}}{dz} & \text{for } z = z_{BU}, \end{cases} \quad (5-28)$$

An example of how the lower and upper profile are blended is shown in Fig. 5-7(c).

Method and lower boundary selection

An algorithm for method selection was developed by considering a large number of combinations of upper and lower profiles that jointly cover the range of possible conditions. Based on evaporation duct height (z_{ED}), the relative values of the upper and lower modified refractivity profile (M_{U2} and M_{L2}) at the height z_2 and the modified refractivity gradients (g_2 and g_3) of the upper profile (see Fig. 5-8), each of these cases was assigned to one of forty blending categories which are characterised by a specific combination of a blending method, M_{th} , and the lower boundary of the blending interval z_{BL} . Table 5-1 shows the criteria defining each category. As an example, for the upper and lower profiles shown in Fig. 5-8 the following is true:

- $z_1 < z_{ED} < z_{20}$.
- $M_{L2} > M_{U2}$,
- $g_2 \leq 0$,
- $g_3 > g_2 \cap g_3 < 0$,

where $z_{20} = 0.5(z_{U1} + z_{U2}) \approx 20$ m, $g_2 = (z_{U2} - z_{U1})/(M_{U2} - M_{U1})$ and $g_3 = (z_{U3} - z_{U2})/(M_{U3} - M_{U2})$ (see also Fig. 5-8). The red entries in Table 5-1 show that under these conditions Method 3 is used for blending the upper and lower profiles together and that the blending starts at height $z_{BL} = z_{ED}$.

Besides the blending methods described above, a Method 0 is also incorporated in the final proposed blending algorithm. Method 0 is used when the evaporation duct profile does not have the expected log-linear form shown in Fig. 5-2. It is unclear why the evaporation duct model sometimes computes a non log-linear evaporation duct profile. However, if this is the case it is assumed that there is no evaporation duct and the blending algorithm only returns the full upper modified refractivity profile.

Table 5-1 is constructed by determining for all of the cases that were assigned to a particular category, which method over all yields the best blending result, considering the blending goals described above. An example of this process is shown in Fig. 5-9. For this case, Method 3 shows the best blending result as it follows the lower profile closely until it blends smoothly

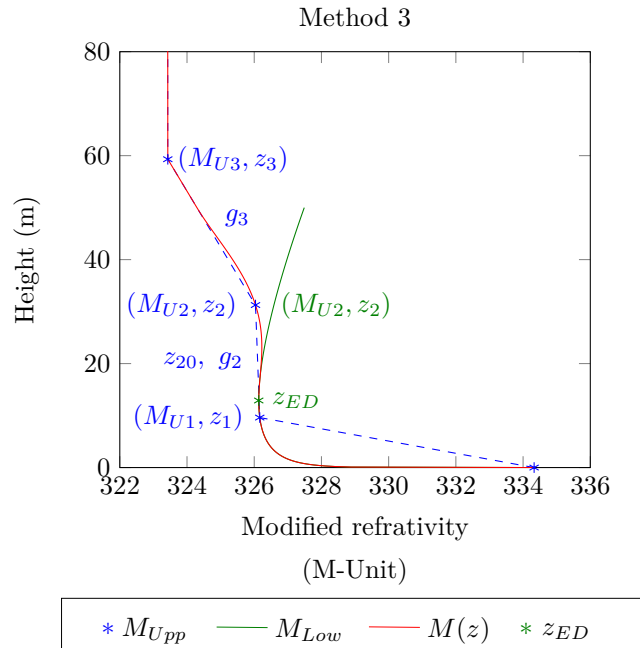


Figure 5-8: Criteria parameters used in choosing the appropriate blending method and interval.

without any extreme gradients into the upper profile. It should be noted that while the blending goals discussed above have a solid and objective basis, the selection process for the method that best achieves the blending goals is at this time rather subjective as the selection is based solely on visual inspection. While a more rigorous and deterministic selection process seems certainly feasible, the definition of such process is beyond the scope of this thesis. Nonetheless, the blending process as proposed shows realistic blending results.

For the lower boundary of the blending interval, there are three options. Start blending:

1. above the evaporation duct height,
2. at the evaporation duct height,
3. below the evaporation duct height.

The first and second options are preferred, because for these options the evaporation duct height, which is a salient refractivity feature of the lower profile, is incorporated into the blended profile unchanged. However, for reasons explained in Subsection 5-2-2, under certain conditions the evaporation duct height of the modelled lower profile is unrealistically high. In these cases the lower boundary is chosen to lie below the evaporation duct height, which will generally result in lowering the evaporation duct height to a more realistic value. Over the North Sea, for which this blending algorithm is designed, evaporation duct heights above $z_{20} \approx 20$ m are considered high, as for this area the evaporation duct has an annual average duct height of 6.4 m [1] while duct heights over 20 m¹⁵ are rare.

When the evaporation duct height lies below the lowest NWP model level ($z_{ED} \leq z_1$), the blending interval starts at $z_{LB} = z_1$. In these cases blending is relatively easy as the upper

¹⁵That duct heights over 20 m are rare can be found in the surface climatology of AREPS [2].

Table 5-1: Table used for blending method selection.

		$g_2 \leq 0$		$g_2 > 0$	
		$g_3 \leq g_2,$ $\cup g_3 > 0$	$g_3 > g_2,$ $\cap g_3 < 0$	$g_3 \geq g_2,$ $\cup g_3 \leq 0$	$g_3 < g_2,$ $\cap g_3 > 0$
$0 < z_{ED} \leq z_1$	$M_{L2} \leq M_{U2},$	N.A. N.A.	N.A. N.A.	$M_{th} = 1,$ $z_{BL} = z_1$	$M_{th} = 3,$ $z_{BL} = z_1$
	$M_{L2} > M_{U2}$	$M_{th} = 1,$ $z_{BL} = z_1$	$M_{th} = 2,$ $z_{BL} = z_1$	$M_{th} = 3,$ $z_{BL} = z_1$	$M_{th} = 1,$ $z_{BL} = z_1$
$z_1 < z_{ED} \leq z_{20}$	$M_{L2} \leq M_{U2},$	$M_{th} = 3,$ $z_{BL} = z_{ED}$	$M_{th} = 1,$ $z_{BL} = z_{ED}$	$M_{th} = 1,$ $z_{BL} = z_{ED}$	$M_{th} = 3,$ $z_{BL} = z_{ED}$
	$M_{L2} > M_{U2}$	$M_{th} = 2,$ $z_{BL} = z_{ED}$	$M_{th} = 3,$ $z_{BL} = z_{ED}$	$M_{th} = 3,$ $z_{BL} = z_{ED}$	$M_{th} = 1,$ $z_{BL} = z_{ED}$
$z_{20} < z_{ED} \leq z_2$	$M_{L2} \leq M_{U2},$	$M_{th} = 1,$ $z_{BL} = z_{20}$	$M_{th} = 1,$ $z_{BL} = z_{20}$	$M_{th} = 1,$ $z_{BL} = z_1$	$M_{th} = 3,$ $z_{BL} = z_1$
	$M_{L2} > M_{U2}$	$M_{th} = 2,$ $z_{BL} = z_1$	$M_{th} = 3,$ $z_{BL} = z_{20}$	$M_{th} = 3,$ $z_{BL} = z_{20}$	$M_{th} = 1,$ $z_{BL} = z_{ED}$
$z_2 < z_{ED} < 50 \text{ m}$	$M_{L2} \leq M_{U2},$	$M_{th} = 2,$ $z_{BL} = z_1$	$M_{th} = 3,$ $z_{BL} = z_1$	$M_{th} = 3,$ $z_{BL} = z_1$	$M_{th} = 3,$ $z_{BL} = z_1$
	$M_{L2} > M_{U2}$	$M_{th} = 3,$ $z_{BL} = z_1$	$M_{th} = 3,$ $z_{BL} = z_1$	N.A. N.A.	N.A. N.A.
$50 \text{ m} \leq z_{ED}$	$M_{L2} \leq M_{U2},$	$M_{th} = 3,$ $z_{BL} = z_1$	$M_{th} = 1,$ $z_{BL} = z_1$	$M_{th} = 3,$ $z_{BL} = z_1$	$M_{th} = 2,$ $z_{BL} = z_1$
	$M_{L2} > M_{U2}$	$M_{th} = 3,$ $z_{BL} = z_1$	$M_{th} = 1,$ $z_{BL} = z_1$	$M_{th} = 0,$ N.A.	$M_{th} = 0,$ N.A.

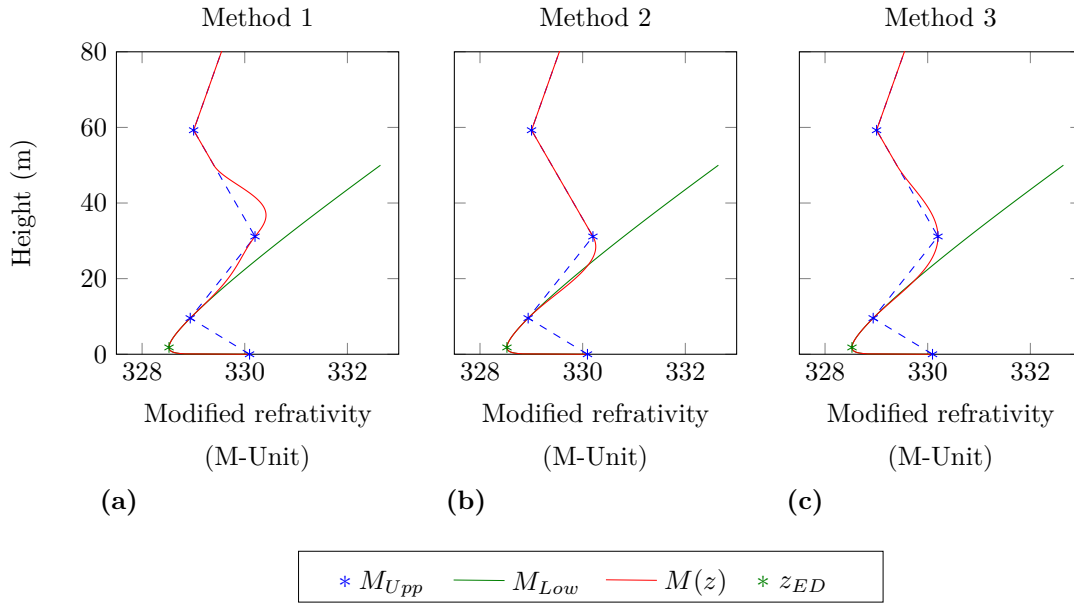


Figure 5-9: Selection of the best blending method for the considered conditions: Method 1 (a), Method 2 (b) and Method 3 (c).

and lower profile will always intersect at z_1 . A blending example of when $z_{ED} \leq z_1$ is shown in Fig. 5-9(c).

When the evaporation duct height lies between $z_1 < z_{ED} \leq z_{20} \approx 20$ m, the blending interval starts at the evaporation duct height $Z_{LB} = z_{ED}$. In this case it is assumed that the evaporation duct model still provides realistic lower profiles and therefore, as in the case above, the evaporation duct height is preserved. Examples of when $z_1 < z_{ED} \leq z_{20}$ are given in Fig. 5-7(a) and (c).

If the evaporation duct is higher than z_{20} , the blending interval will start below the evaporation duct height, which results in a reduction of the duct height. For cases where $z_{20} < z_{ED} \leq z_2$ the lower boundary of the blending interval lies at $z_{LB} = z_1$, $z_{LB} = z_{20}$ or $z_{LB} = z_{ED}$ depending on the structural differences of the upper and lower profile. As for the blending method selection process described above, multiple cases were visually inspected to see which lower boundary height resulted in the most realistic blended profile. Examples of when $z_{LB} = z_{20}$ and $z_{LB} = z_1$ are given in Fig. 5-10(a) and (b) respectively.

Lastly, when the evaporation duct extends above z_2 ($z_2 < z_{ED}$), the lower boundary of the blending interval will automatically be set to z_1 , as the lower profile is clearly unrealistic for the North Sea. An example of this is given in Fig. 5-10(c).

Blending in the physical domain

An alternative approach to blending the upper and lower profiles in the modified refractivity domain, as presented above, is to blend the upper and lower temperature, humidity and pressure profiles. Blending in the physical domain has certain advantages over blending in the modified refractivity domain. In the first place the underlying physics of temperature and

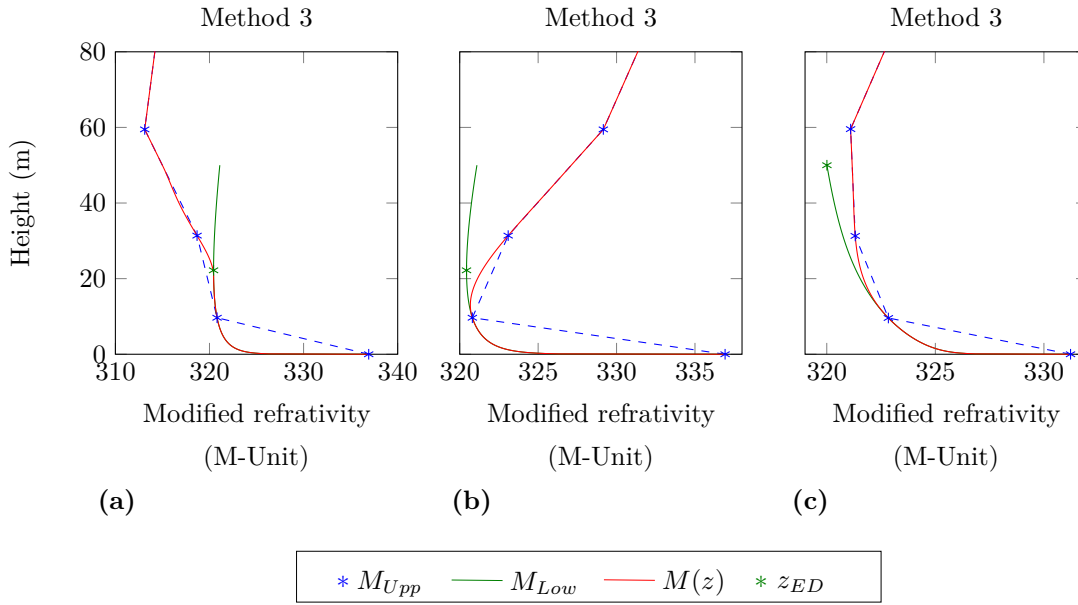


Figure 5-10: Blending lower and upper refractivity profiles with a evaporation duct height greater than z_{20} : $z_{20} < z_{ED} \leq z_2$ (a), $z_{20} < z_{ED} \leq z_2$ (b) and $z_2 < 50 \text{ m} \leq z_{ED}$ (c).

humidity transfer is generally well understood in the boundary layer. This may provide a more solid basis for the definition of deterministic blending algorithms than the rather more intuitive approach adopted above. For instance, blending decisions need not be based on characteristics of the evaporation duct profile which is generally, but not always, present. Secondly, rather than blending the three parameters at once in the form of a modified refractivity profile, focusing separately on the temperature, humidity and pressure profiles is likely to yield, over all, more accurate results.

The Naval Surface Warfare Center, Dahlgren Division (NSWCDD) developed a blending technique that blends in the physical domain [52]. In this technique the lower and upper profiles of potential virtual temperature, specific humidity and pressure are blended within a defined blending interval using a simple α -filter, similar to the blending method, Method 1, discussed above. As with the blending algorithm developed above, the resulting potential virtual temperature, specific humidity and pressure profiles are equal to their corresponding lower profiles below the blending interval and equal to their corresponding upper profiles above the blending interval.

The blending interval used in this technique extends from $z_s - l_m/2$ to $z_s + l_m/2$ where z_s is the height of the surface layer and l_m the mixing length. The height of the surface layer is defined as the lowest height at which wind, temperature and humidity fluxes are constant to within 10% of their surface value. The mixing length is the distance a turbulent eddy travels before mixing completely with the surrounding environment. The mixing length can be determined using: $1/l_m = 1/(kz_s) + 1/150$, where k is the Karman constant and equal to $k = 0.4$.

As with the blending approach of Frederickson and the one developed within this thesis, the technique developed by NSWCDD is designed to blend upper profiles provided by a NWP model and the lower profile provided by a MOST based evaporation duct model where the

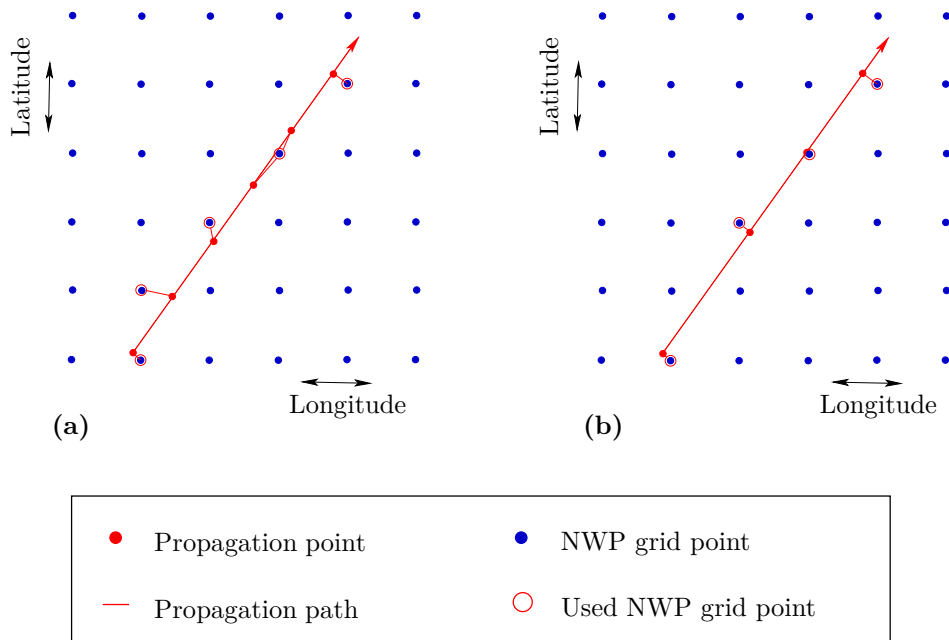


Figure 5-11: Two simple approaches for obtaining the refractivity profile along the propagation path from the NWP model grid.

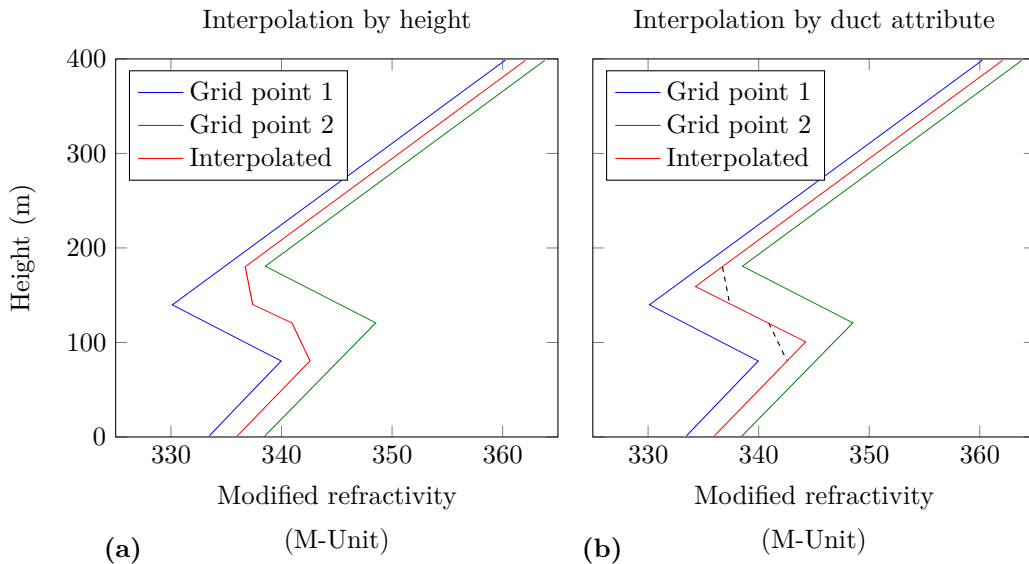


Figure 5-12: Interpolating vertical modified refractivity profiles between grid points by NWP model levels (a) and by duct attributes (b) [55].

bulk parameters are profiled by the lowest NWP model level. Whilst still being validated, the blending technique by NSWCCD shows promising results. For more information on this blending method see [52] or contact NSWCCD.

For this thesis the proposed blending technique in the modified refractivity domain described earlier is adopted, and not blending in the physical domain, merely because sufficiently detailed information on the latter approach became available late in the study.

It is recommended (to the RNLN and to other interested parties) to undertake further research into the field of blending (e.g. developing new methods and the validation of methods). Currently there is little research and information on this topic available, while it is important for accurate radar assessment.

5-3 Horizontal interpolation of vertical profiles

The last topic considered in modelling the environment is obtaining the modified refractivity profiles along the propagation path from the horizontal NWP model grid. A simple approach is to assume the refractivity profile to be identical to that of the closest NWP grid point at fixed intervals along the propagation path, as shown in Fig. 5-11(a). Another approach is to select grid profiles from NWP grid points within a specified distance threshold and project those profiles onto the nearest points along the propagation path, as shown in Fig. 5-11(b) [55]. These approaches will be sufficient as long as the horizontal grid resolution is high. However, with coarser resolutions they become increasingly problematic: as the distance between the profile along the propagation path and the profile of the nearest NWP grid point increases, the assumption that the two are identical becomes increasingly unrealistic.

Interpolation of the refractivity profile is also an option. In early versions of AREPS¹⁶ the vertical modified refractivity profiles at specific intervals along the propagation path are obtained by linear interpolation of the nearest four NWP model modified refractivity grid profiles at all model heights [55]. This approach, however, can have the undesirable effect of 'smoothing' trapping layers as shown in Fig. 5-12(a), which can adversely affect the accuracy of radar assessments.

The 'smoothing' of trapping layers can be avoided by interpolating duct attributes (i.e. duct height, trapping layer thickness, etc.) as shown in Fig. 5-12(b) rather than interpolating at model heights [55]. The latest version of AREPS adopts this approach to interpolate between the profiles at two points along the propagation path which are obtained using the method shown in Fig. 5-11(b).

Within this thesis, rather than in the refractivity domain as in approaches above, interpolation is carried out in the physical domain. The advantages of this are similar to the advantages of blending in the physical domain, as identified above. From the radar outwards along the propagation path, every 2.5 km vertical temperature, specific humidity, pressure, wind speed and height profiles are obtained by linear interpolation between the corresponding vertical profiles at the four nearest NWP model grid points. The required profiles are acquired using:

$$P(z) = w_3 (w_1 P_{NWP1}(z) + w_2 P_{NWP2}(z)) + w_4 (w_1 P_{NWP3}(z) + w_2 P_{NWP4}(z)), \quad (5-29)$$

¹⁶Including the version (3.6) used in this thesis.

where $P(z)$ is the interpolated profile at point P , P_{NWP1} , P_{NWP2} , P_{NWP3} and P_{NWP4} are the profiles at the four nearest NWP model grid points and w_1 , w_2 , w_3 and w_4 are the weighing factors. The weighing factors are equal to:

$$\begin{aligned} w_1 &= \frac{d_2}{d_1 + d_2}, \\ w_2 &= 1 - w_1, \\ w_3 &= \frac{d_4}{d_3 + d_4}, \\ w_4 &= 1 - w_3, \end{aligned} \tag{5-30}$$

where the distances d_1 , d_2 , d_3 and d_4 are shown in Fig. 5-13. An example of this approach is shown in Fig. 5-14. The figure shows the resulting interpolated upper modified refractivity profile at point P and the profiles at the nearest NWP grid points P_{NWP1} , P_{NWP2} , P_{NWP3} and P_{NWP4} . The distances where d_1 , d_2 , d_3 and d_4 are respectively: 53 m, 2506 m, 1444 m and 1100 m. Note that the position of P (see Fig. 5-13) lies almost directly in between P_{NWP1} and P_{NWP3} . In other words the profile at P is best described by the profiles at P_{NWP1} and P_{NWP3} . This corresponds with the results in Fig. 5-14, where the profile of P lies between the profiles of P_{NWP1} and P_{NWP3} .

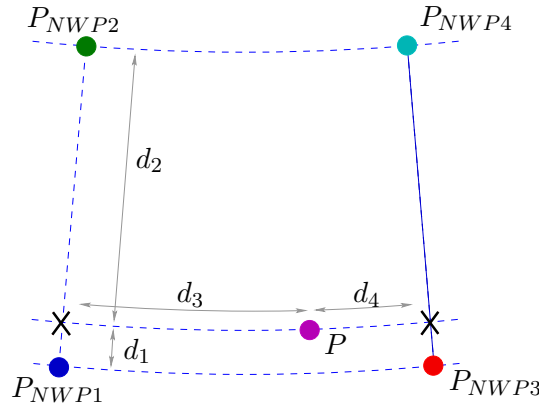


Figure 5-13: Illustration of how vertical profiles on the NWP model grid are interpolated.

While more sophisticated interpolation schemes are most likely possible, for example non-linear interpolation schemes that also take field gradients into account, the proposed scheme yields profiles that are sufficiently realistic for studying horizontal and temporal resolution requirements. As with the models and methods discussed above, this interpolation approach should be validated prior to its consideration for operational use.

5-4 The environment model

Within this thesis the new proposed environment model is based on the models and methods discussed above. From the radar outwards the vertical temperature, specific humidity, pressure, wind speed and height profiles from NWP model HARMONIE will be interpolated

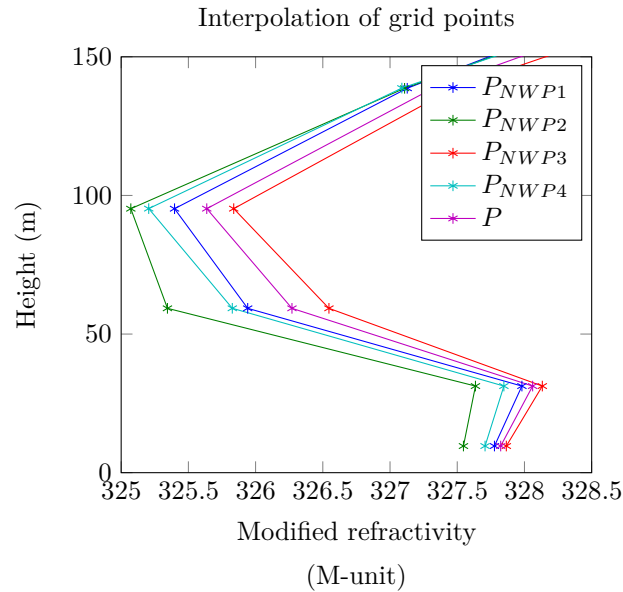


Figure 5-14: Interpolation of modified refractivity profiles in the physical domain.

along the propagation path with a resolution of 2.5 km, which is approximately the initial horizontal grid resolution of HARMONIE. From these interpolated profiles the upper modified refractivity profiles are determined using Eq. 5-7. After computing the upper profiles, the lower profile for each point along the propagation path will be computed using the NPS evaporation duct model that is implemented for this thesis (see Appendix C). The required bulk parameters temperature, specific humidity, pressure and wind speed are taken from the lowest data point above the surface of the corresponding interpolated vertical profile. The required sea surface temperatures are also provided by interpolated NWP model data. Next the upper and lower profiles will be blended together using the developed blending technique described above. Thus full modified refractivity profiles are obtained along the propagation path with a resolution of 2.5 km which can be used for radar assessment. Note that this technique yields a 2.5 km resolution along the propagation path, independent of the grid size.

In its entirety, the described model provides modified refractivity profiles that are under the prevailing weather conditions sufficiently realistic for the purpose of this thesis: examining the performance assessment accuracy sensitivity to the horizontal and temporal atmospheric input data resolution. The model is not validated and its profiles may not be sufficiently accurate for operational radar assessment. Note that for the purpose of this thesis, a very high accuracy is not required.

Approach to assessing accuracy sensitivity to resolution

The main goal of this thesis is to examine the sensitivity of radar performance assessment accuracy to input data resolution. Both the resolution of the horizontal grid and the temporal resolution of atmospheric data are considered, for varying weather conditions over the North Sea. The current chapter describes the method used to assess how radar performance assessment accuracy is affected by the resolution of the atmospheric data on which the prediction is based.

The first section describes the general approach of the sensitivity study used. To evaluate how well radar assessments based on a reduced resolution compare with a certain "ground truth", measures of accuracy need to be defined. Three such measures are presented in Section 6-2. Because radar performance is dependent on the radar system itself, the target and the environment, the scenarios examined in this thesis are discussed briefly in the last section of this chapter.

6-1 General approach

6-1-1 Ground truth

To assess the sensitivity of radar performance assessment accuracy to the horizontal resolution of atmospheric data, it is required that radar performance assessment accuracy can be measured in the first place. For this, a "ground truth" which represents the actual radar performance under the prevailing conditions is required. The performance of a radar can be represented, for example, by propagation losses versus range and height, by coverage versus range and height, or by maximum detection ranges. Ideally such ground truth is based on real life accurate measurements so that the ground truth wholly and truly represents reality. Any performance prediction can then be assessed against real life performance to determine

its accuracy. Sadly, near complete measurement of the environment and actual radar performance is prohibitively elaborate. Consequently, for the purpose of this thesis, a surrogate ground truth must be compiled.

For the ground truth it is important that the compiled radar performance closely resembles the actual radar performance under the prevailing weather conditions. Research has shown that parabolic equation based models can accurately assess radar performance for any practical environment when sufficient environmental data is available [4]. In this thesis the TDA AREPS (version 3.6 [2]) is used to compile ground truth radar performance. As discussed in Section 4-5, AREPS uses a parabolic equation based hybrid propagation model to assess radar performance.

The atmospheric data¹ used for obtaining the ground truth is HARMONIE² numerical weather prediction (NWP) data provided by the Royal Netherlands Meteorological Institute (KNMI). As discussed in Section 5-2-1 mesoscale NWP models, such as HARMONIE, produce data which is sufficiently detailed for AREPS to provide an indication of radar performance which is accurate enough for operational use [12]. It is then also sufficiently accurate to serve as ground truth data for the purpose of this thesis, which does not examine actual prediction accuracy, but merely how accuracy is affected by reducing atmospheric data resolution. It can therefore be assumed that AREPS computes actual radar performance when provided with NWP data: AREPS outputs can be taken as the ground truth. Of importance is that the initial horizontal resolution is small enough to model mesoscale phenomena. According to [13] such a resolution must be at least 5 km. HARMONIE has a grid resolution of approximately 2.5 km.

As AREPS requires modified refractivity profiles for input, the atmospheric HARMONIE data is converted to full vertical modified refractivity profiles along the propagation path by means of the method described in the previous chapter. For the establishment of ground truth, HARMONIE's maximal grid resolution is used (2.5 km).

For this study the two-way propagation loss versus range and height, as computed by AREPS, is taken as the root ground truth. From this and the use of AREPS's integrated radar model, detection probabilities³ versus height and range can be computed, and this will be used as the derived ground truths. The derived detection probabilities allow the determination of the radar's coverage and its maximum detection ranges; both of which will be used a lot within this study. Examples of the propagation loss ground truth and the coverage ground truth are shown in Fig. 6-2(a) and (d). Note that the coverage ground truth also provides the radar's maximum detection ranges.

6-1-2 Sensitivity study of horizontal grid resolution

After the ground truth for a specific scenario is established, the grid resolution of the atmospheric HARMONIE data is systematically reduced in steps of 2.5 km to a minimum resolution of 50 km. For each resolution reduction step radar propagation is modelled using AREPS. As was done for determining the ground truth, the reduced HARMONIE data

¹In this thesis only atmospheric effects are considered. Hence, for this thesis terrain data is not needed.

²Hirham Aladin research on mesoscale operational NWP in Euromed (HARMONIE).

³With a probability of false alarm equal to $P_{FA} = 10^{-6}$.

is converted to modified refractivity profiles along the propagation path using the method described in the previous chapter. The radar performance assessments based on reduced HARMONIE data, from now on referred to as the "spoiled" assessments⁴, are then compared to the ground truth using several measures of accuracy which are described in the following section. Comparison of the changes in accuracy at each resolution step, makes it possible to assess how the accuracy of radar assessment is affected by reducing horizontal grid resolution of the atmospheric input data.

Initially, comparison of spoiled assessments showed that the accuracy did not monotonically decrease with decreasing resolution, contrary to what was expected. For nearly all scenarios considered, some spoiled assessments based on relatively low resolution grid data, surprisingly produced more accurate results than some assessments based on higher resolution data. These non-monotonic accuracy anomalies can be explained by the relative position of the reduced HARMONIE data grid. It is not difficult to see that it is possible for an assessment based on a coarser resolution grid to have a higher accuracy than an assessment based on a finer resolution grid if the propagation path coincidentally hits or nearly hits many of the grid points of the reduced grid.

The accuracy anomalies described above make it difficult to assess the overall effect of reducing the resolution on the accuracies of the spoiled assessments. To get an overall measure for the accuracy of results that are based on a particular level of data resolution reduction, the accuracies for all possible offsets of the reduced grid were considered. Fig. 6-1 for example shows all possible grid offsets for a grid resolution of approximately 7.5 km. The 7.5 km resolution grid has a total of $(7.5/2.5)^2 = 9$ possible offsets. Averaging the accuracies of the individual spoiled assessments over all possible grid offsets at a specific resolution resulted in an overall monotonically decreasing accuracy with decreasing resolution.

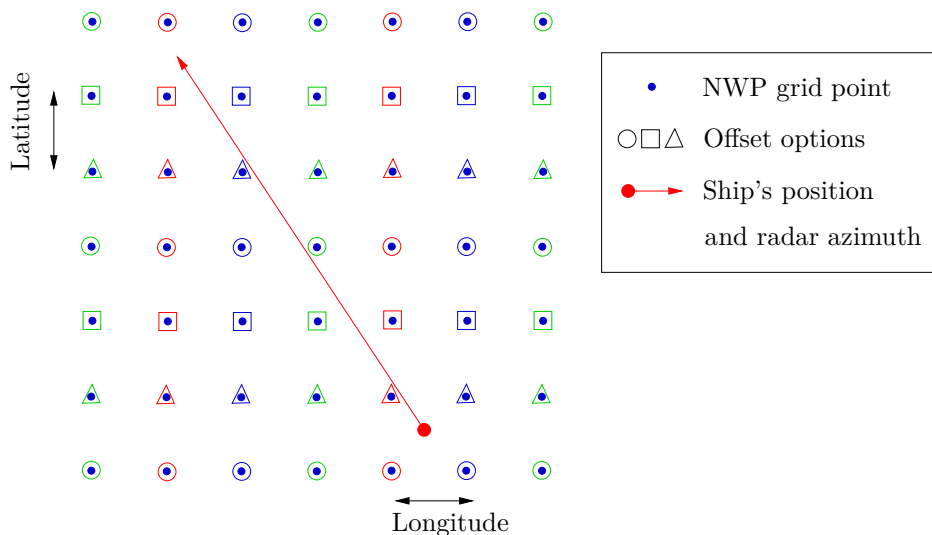


Figure 6-1: Possible offsets for a grid resolution equal to 1/3 of the initial NWP grid resolution.

Although the described process of averaging over all propagation prediction accuracies for all

⁴The word "spoiled" in "spoiled assessments" indicates that these assessments are based on artificially reduced resolution data, as is often done in similar studies (e.g. [4]).

possible grid offsets for each data reduction step for every scenario is relatively straightforward, its execution proved challenging, laborious and time consuming. A major problem was the large number of spoiled predictions that had to be computed. Including the ground truth, AREPS had to compute $\sum_{n=1}^{50/2.5=20} n^2 = 2870$ radar assessments for each of the 41 scenarios considered. Hence, the use of computer resources had to be thought of carefully. Another problem was the data transfer between all programs/models. The HARMONIE data was provided in GRIB format. Before the atmospheric data could be import into MATLAB (version 2013b), the GRIB files had to be converted to netCDF using a free converter available online [56]. After importing the atmospheric data into MATLAB, the data had to be processed to produce full vertical modified refractivity profiles using the environmental model discussed in the previous chapter. Next these modified refractivity profiles were exported into an ASCII file specifically formatted to be suitable as AREPS input data [2]. After automatically running AREPS (version 3.6 [2]) from MATLAB, the propagation loss data had to be imported into MATLAB from an ASCII file generated by AREPS. The imported data had to then be processed to produce radar coverage diagrams using AREPS's radar threshold model. Batch execution of these subsequent processes required approximately 2 days continuous processing for a single scenario. As the conversions and calculations are memory intensive, special care had to be taken to avoid crashes due to memory errors.

In addition to radar performance assessments based on reduced grid resolutions, assessments based on a single vertical profile as well as a standard atmosphere were compared to the ground truth. The latter comparisons show how accurate radar performance assessments are when based on a single radio sonde measurement, assuming a horizontally homogeneous atmosphere, or on the assumption of a standard atmosphere.

6-1-3 Sensitivity study of temporal resolution

Besides examining the sensitivity of radar performance assessment accuracy to the horizontal grid resolution of atmospheric data; the sensitivity to temporal resolution of atmospheric data is also considered. The required temporal resolution is the time interval with which the radar performance assessments needs to be updated with up to date atmospheric data to ensure that assessments remain accurate. In the case of radio sonde balloons, for example, temporal resolution is the time interval with which balloons need to be deployed to keep accurate radar performance assessments.

The sensitivity to temporal resolution is examined by comparing the ground truth to radar performance assessments based on maximal resolution NWP HARMONIE data of the hours before and after the HARMONIE data on which the ground truth is based. For example, if the ground truth is the truth at 14:00, the ground truth will be compared to the assessments based on HARMONIE data from 01:00 - 13:00 and 15:00 - 24:00⁵ with one hour⁶ intervals.

⁵In total 24 hour HARMONIE data sets are used with earliest and latest data times as provided by the KNMI.

⁶Highest temporal resolution of HARMONIE.

6-2 Measures of accuracy

To examine how resolution effects radar assessment accuracy a method must be defined to compare spoiled assessments to the ground truth. For this several measures of accuracy may be taken into account. For the purpose of this thesis three measures of accuracy are used: propagation loss error, radar coverage error and absolute detection range error. The first measure is chosen as it is a measure that is used widely in radar studies, the two other measures are chosen because these are of particular relevance to military users in operational scenarios.

6-2-1 Propagation loss errors

The first measure of accuracy considers the percentage of area where the absolute propagation loss error exceeds 5 dB, in which the propagation loss error is the difference in propagation loss between the ground truth and the spoiled propagation loss prediction. A threshold of 5 dB is used because in the radar propagation community predictions that are accurate within 5 dB are generally considered good [4]. The total area examined extends from 0-150 m in height and 0 to 100 km in range. A maximum height of 150 m is chosen because below this altitude the refractive effects on propagation are most severe [4]. This allows for the assumption that when the resolution is sufficient for modelling the radar propagation below 150 m accurately, it also allows accurate propagation modelling at higher altitudes [4]. The maximum range of 100 km allows to account for propagation far beyond the radar horizon, while accuracies of 5 dB remain realistic. Note that a change of the total area will result in a change of percentages. This must be considered when interpreting this measure. Because for a single grid resolution several offsets are possible, yielding differing accuracy results, the mean and maximum area percentage over all offsets per resolution are determined as an overall measure of accuracy for each resolution. The maximum value considers the worst case and relative to the mean is a measure of the error distribution.

An example is shown in Fig. 6-2. Figures 6-2(a) and (b) show respectively the propagation loss of the ground truth and the propagation loss assessment based on HARMONIE data that has a reduced resolution of approximately $R_{Hor} = 25$ km. Figure 6-2(c) shows the propagation loss error in discrete steps of 5 dB. The percentage of area where the absolute propagation loss error exceeds the 5 dB threshold (the non-white area) is approximately 20.5%. Considering all 10^2 offsets at a resolution of 25 km the mean and maximum percentage of area where the absolute propagation loss error exceeds 5 dB are respectively 15.5% and 25.8% (not shown in Fig. 6-2): it is clear that the grid offset significantly influences the accuracy of the propagation loss assessment.

6-2-2 Coverage errors

The next measure of accuracy considers radar coverage. For the Navy, an ability to predict where targets can or cannot be detected is highly beneficial. At the same time, errors in the modelled coverage can have dramatic consequences. For example, if it is expected that targets in a specific area will be detected while this is in fact not the case, enemy fighters can come as a big surprise. On the other hand, unrealistic low expectation of detection

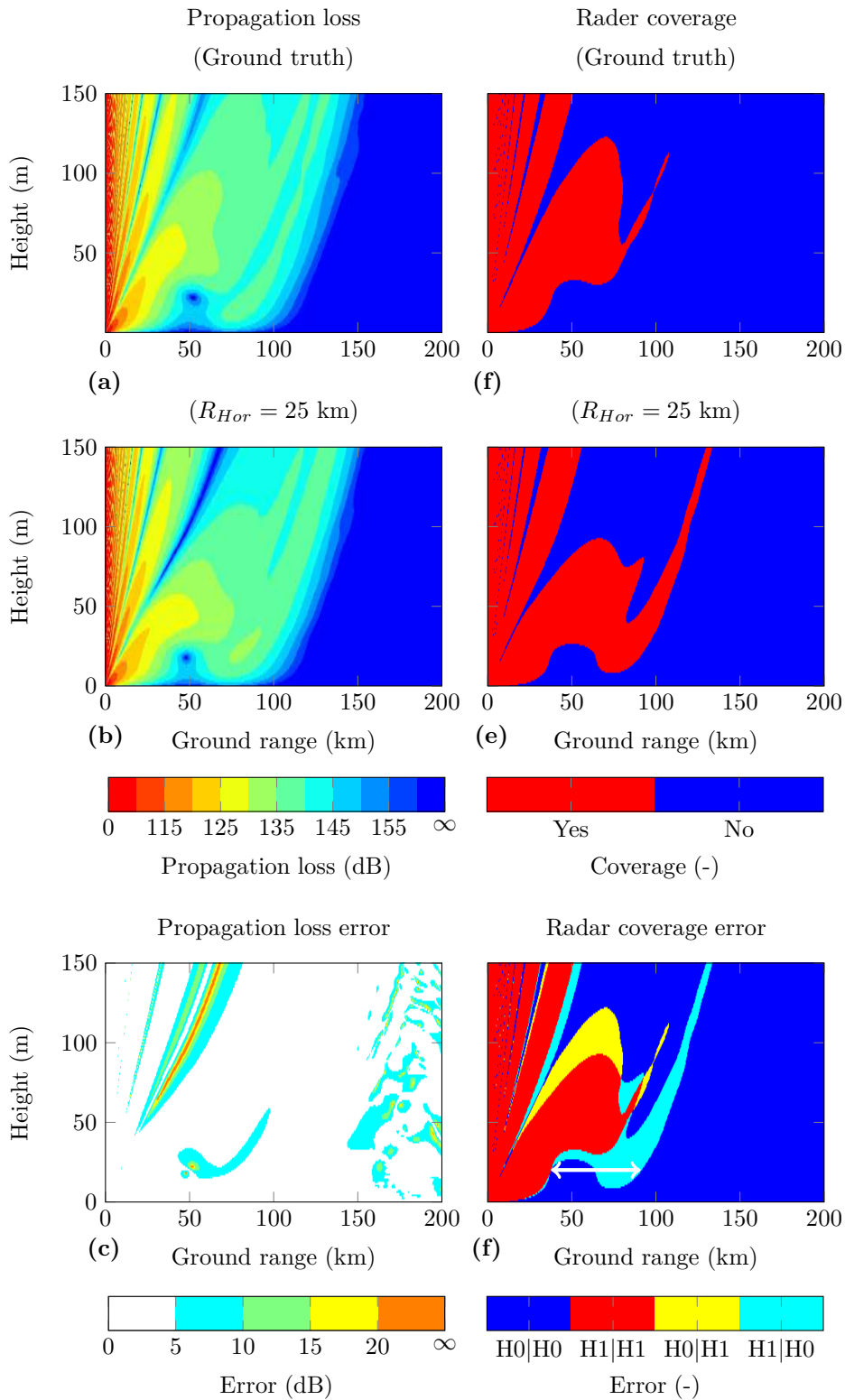


Figure 6-2: Illustration of the three measures of accuracy used in this thesis: propagation loss ground truth (a), propagation loss spoiled assessment (b), propagation loss error (c), coverage ground truth (d), coverage spoiled assessment (e) and coverage error (f).

probability is dangerous as the chance of counter detection by opposing forces with electronic support measures (ESM) is higher than expected. For this, accurate knowledge of the coverage prediction error is very important.

As for the measure of accuracy concerning propagation loss, the measure concerning coverage is defined as the percentage of area where the coverage is in error. Coverage is defined as the area where the detection probability exceeds $P_D = 0.95$ with a false alarm probability of $P_{FA} = 10^{-6}$. These probabilities are representative for naval ship borne radars [57]. Again, both the mean and maximum area percentage over all possible grid offsets are determined. The area considered extends, as with the propagation loss error measure, from 0-150 m in height in 0-100 km in range.

An example is provided in Fig. 6-2(d-f). Figures 6-2(d) and (e) show respectively the ground truth coverage and the coverage assessment based on HARMONIE data with a reduced resolution of 25 km. Figure 6-2(f) shows the coverage error. The area in red shows where coverage is predicted correctly, the area in blue shows where no coverage is predicted correctly, the areas in light blue and yellow present respectively where coverage or the absence thereof is predicted erroneously.

In the example, for 8.1% of the area no coverage is predicted while according to ground truth there is and for 5.8% coverage is predicted where there is none. Hence, for in total 13.9% of the area the coverage prediction is in error. The mean and maximum coverage errors over all possible offsets at the 25 km resolution are 14.8% and 22.0% respectively.

6-2-3 Maximum detection range errors

The last measure of accuracy considers the maximum detection range. The maximum detection range is very important as it determines the reaction time against e.g. incoming enemy fighters. The (absolute) detection range error is defined as the difference between the predicted maximum detection range and the ground truth maximum detection range. The maximum detection range at a specific height is the longest ground range where coverage is predicted⁷. The mean overall absolute detection range error for a particular resolution is determined by averaging over all heights (0-150 m) and all possible offsets. The maximum overall detection range error is the worst case over all heights and offsets.

In Fig. 6-2 (f) the detection range error is shown at height 20 m and is equal to 53.2 km (see double white arrow). The mean and maximum detection range errors over all heights and offsets are 13.8 km and 82.7 km respectively. See how the predicted maximum detection range can be highly inaccurate.

6-2-4 Other possible measures

Besides the measures of accuracy defined above, many more are possible. The above measures may be considered as general as they consider "absolute" errors. For specific purposes, more

⁷In this thesis a modelling domain of 150 m high and 200 km long is used. Hence detection ranges extending beyond 200 km are evaluated as a maximum detection range of 200 km. A larger domain can be used, however, because larger domains require longer computation time the maximum range is kept to 200 km.

specific measures may be appropriate: in a non-ESM scenario, for instance, it may be considered important only to determine the range within which no hostile target will be missed. An error where the actual detection range is better than predicted may then be dismissed and omitted from the measure of accuracy. As a consequence, a coarser data grid resolution may suffice than would be the case in general.

Another possible measure of accuracy can be defined to also take the target position error due to anomalous propagation that was discussed in Section 3-3-3 into account. While target position accuracy is obviously of importance, it is not considered within the scope of this thesis.

6-3 Scenarios

Radar performance is dependent on the radar system itself, the target and the environment. Hence, resolution requirements for environmental data depend not only on the type of environment but also on which specific radar is deployed for the detection of what specific targets. The analysis of this thesis applies to a specific radar system and target as detailed in Sections 6-3-1 and 6-3-2 respectively. The varying environmental weather conditions that are considered for this radar-target-combination are listed in Section 6-3-3.

6-3-1 Radar system parameters

The radar considered in this thesis is a generic 3.3 GHz medium range surveillance radar [58]. The specifications of the 3.3 GHz radar are provided in Table 6-1. The same specifications detail the radar that is modelled in AREPS. The radar is positioned at 20 m above sea level, which is representative of many ship borne long range surveillance radars [4].

6-3-2 Target parameters

The parameters for the target that this thesis is based on are listed in Table 6-2. AREPS uses these same parameters. The radar cross section is representative of a small fighter [25], as is the Swerling case [2], which is a measure for the fluctuation of the radar cross section (RCS) with the angle of incidence. For Swerling case 1, the fluctuation is negligible from pulse to pulse and uncorrelated from scan to scan.

6-3-3 Weather conditions

The performance of the radar against the type of target detailed above is evaluated for a total of 41 scenarios. These scenarios are based on HARMONIE weather data⁸ that spans 17 periods of 24 hours and is fairly representative of conditions over the North Sea throughout the year. The radar position and azimuth are varied relative to the environment. Short descriptions of the scenarios are provided below. More details are included in Appendix D.

⁸Provided by the KNML.

Table 6-1: Radar parameters used for modelling the radar in AREPS.

Parameter	value
Function	Medium range surveillance radar
Radar type	Integrated - coherent
Frequency	3.3 GHz
Peak power	100 kW
Pulse length	5 μ s
Compressed pulse length	1 μ s
Receiver noise figure	3 dB
Assumed system loss	5 dB
Beam pattern	Cosecant squared
Polarisation	Horizontal
Maximum antenna gain	30 dBi
Horizontal beam width	2°
Vertical beam width	30°
Antenna elevation angle	0°
Antenna height	20 m

Table 6-2: Target parameters used for modelling the target in AREPS.

Parameter	value
Target type	Small fighter
Radar cross section	2 m ² at 3300 MHz
Swerling case	1

Weather conditions were selected in consultation with a meteorological officer of the RNLN and with the KNMI. The selection was determined such that the chosen conditions would give rise to the occurrence of all forms of refraction: various types of ducts, super-refraction, normal-refraction and sub-refraction. Analysis of the many computed radar performance assessments showed that this was indeed the case. As will be explained later, it is desirable to analyse more scenarios: both similar and different in conditions. Analysing more scenarios will allow a more general conclusion. For this thesis it was decided to study only 41 scenarios due to the limited availability of time and HARMONIE data.

The assessment accuracy sensitivity was examined for the following weather conditions:

- 8 scenarios consider radar propagation near 4 different cold weather fronts. In 4 cases the radar is deployed towards the cold air mass. For the other 4 scenarios the radar is deployed towards the warm air mass. Ducting due to an evaporation duct is common under these conditions.
- 8 scenarios consider the propagation near 4 different warm weather fronts. In 4 cases the radar is deployed towards the warm air mass. For the other 4 scenarios the radar is deployed towards the cold air mass. Sub-refraction is common under these conditions.
- 1 scenario considers radar propagation in a warm sector. Sub-refraction is common under these conditions.
- 9 scenarios consider radar propagation in regions where there is land-sea advection of warm dry air. The scenarios are spread over 3 days. Ducting due to surface-ducts or elevated ducts is common under these conditions.
- 8 scenarios consider radar propagation near 3 different high pressure system. Ducting due to surface-ducts or elevated ducts is common under these conditions.
- 7 scenarios consider radar propagation in calm weather. Standard propagation is common under these conditions.

Whilst in this thesis the above scenarios are used for analysing radar performance assessment accuracy sensitivity to the resolution of atmospheric input data, the scenarios can also be considered for other studies in the (near) future. For example, Bruin [59] is currently researching⁹ how North Sea weather conditions affect detection ranges of automatic identification systems (AISs) and coastal radar systems (X-band). Bruin is using some of the same NWP HARMONIE data that was used within this study.

⁹The study takes place at the Knowledge, Innovation, eXperimentation and Simulation (KIXS) centre of the Dutch Armed Forces under the supervision of dr. A.V. van Leijen.

Accuracy sensitivity to resolution: results, analysis and discussion

The main goal of this thesis was to examine the sensitivity of radar performance assessment accuracy to input data resolution as well as the error as a result of using a single profile for radar assessment (upon assumption of a lateral homogenous atmosphere). As radar coverage and detection ranges are of particular relevance to military users in operational scenarios, the main focus lies on these two measures of accuracy. However, the error in propagation loss is also shown for the scenarios discussed.

In the first section the sensitivity to horizontal resolution is evaluated for the scenario categories listed in the previous section. For brevity, not all of the 41 scenarios are discussed in detail. The first section also covers the assessment error which would result if a single modified refractivity profile is used. For each scenario, it is determined if a single profile suffices for accurate radar assessment¹ or if three dimensional (3D) modified refractivity data is required. Depending on the required accuracy a minimum required horizontal grid resolution can then be chosen. Because this thesis examines only a small set of scenarios a general minimal resolution requirement for operational use cannot be inferred. Nonetheless, the analysis results clearly show the effect of reducing horizontal atmospheric data resolution on accuracy and the errors as a result of using a single profile. At the end of the first section the overall average error is given as well as general drawn conclusions.

In the second section of this chapter the temporal resolution will be examined briefly. This section clearly shows that a single data set per 24 hours does not suffice for accurate radar propagation prediction throughout the day. This is a significant result as the RNLN routinely bases their radar performance assessment on a single daily (or even older) radiosonde measurement.

¹In this thesis it is assumed that a single profile suffices if the coverage area in error does not exceed 5% of the total area and if the maximum detection range error is no more than 5 km. These maximum error values are chosen, as for the purpose of this thesis, it is assumed that errors below these values are operationally insignificant. Depending on the application and the operational circumstances different thresholds may be appropriate.

Besides examining the accuracy sensitivity to resolution, other findings will also be discussed throughout this chapter. For most of the results discussed an explanation is given, however in some cases no satisfactory explanation could be found. At the end an short overall discussion will be presented.

7-1 Horizontal resolution

This section examines the accuracy sensitivity to horizontal resolution. First the results considering weather front scenarios (cold front, warm front and warm sector) are discussed. Analysis will show that in these cases a single profile suffices for accurate radar assessment. Then results considering cases of warm dry air advection, high pressure systems and calm conditions are discussed; analysis will show that for these cases resolution requirements are more stringent.

7-1-1 Cold weather fronts

In this thesis 8 scenarios were considered in which the ship is positioned near a cold weather front and where the radar was deployed either towards or away from the cold air mass. Refractive conditions near a cold front are generally characterised by an evaporation duct. In the cold air mass behind the front the evaporation duct is generally developed most strongly. The duct weakens, decreases in height, towards the warm air mass in front of the cold front because warmer air can hold more water vapour than cold air. This leads to a less rapid decrease of water vapour from the surface and hence a weaker evaporation duct.

In Scenario 6 the ship is positioned in the cold air mass with the radar deployed towards the warm air mass. As expected the evaporation duct height decreases when the air becomes warmer. Figure 7-1 (a) shows the modified refractivity gradient along the propagation path; the evaporation duct height is the height at which the gradient changes from trapping to super-refractive conditions. The duct height decreases from approximately 9 to 4 m.

Even though the vertical refractivity profile varies along the propagation path, comparing the radar coverage assessment based on a single profile to the ground truth coverage showed that a single profile still suffices to accurately predict radar coverage and detection ranges in this scenario. In other words, the atmosphere can be assumed lateral homogeneous. The difference between the radar coverage assessment based on a single profile and the ground truth is shown in Fig. 7-1 (b). Using a single profile will result in a falsely predicted coverage area of merely 1.0% of the total area (100 km x 150 m) as shown by the measure of accuracy in Fig. 7-2 (b)). Predicted maximum detection range errors do not exceed 0.9 km and have a mean of 0.6 km. Hence, for this scenario 3D atmospheric data, in this case HARMONIE data, does not significantly improve the accuracy of the predicted coverage and detection ranges as shown in Fig. 7-2 (b) and (c) respectively. As is to be expected, Fig. 7-2 also shows that with increasing resolution of HARMONIE data, the prediction accuracy also increases. This is a general finding that is true for all scenario's that were investigated in this thesis.

The reason why a single profile suffices for this scenario is that the evaporation duct in this scenario is relatively weak and therefore has little effect on radar propagation. Comparing the ground truth coverage with the standard coverage shows that the evaporation duct does

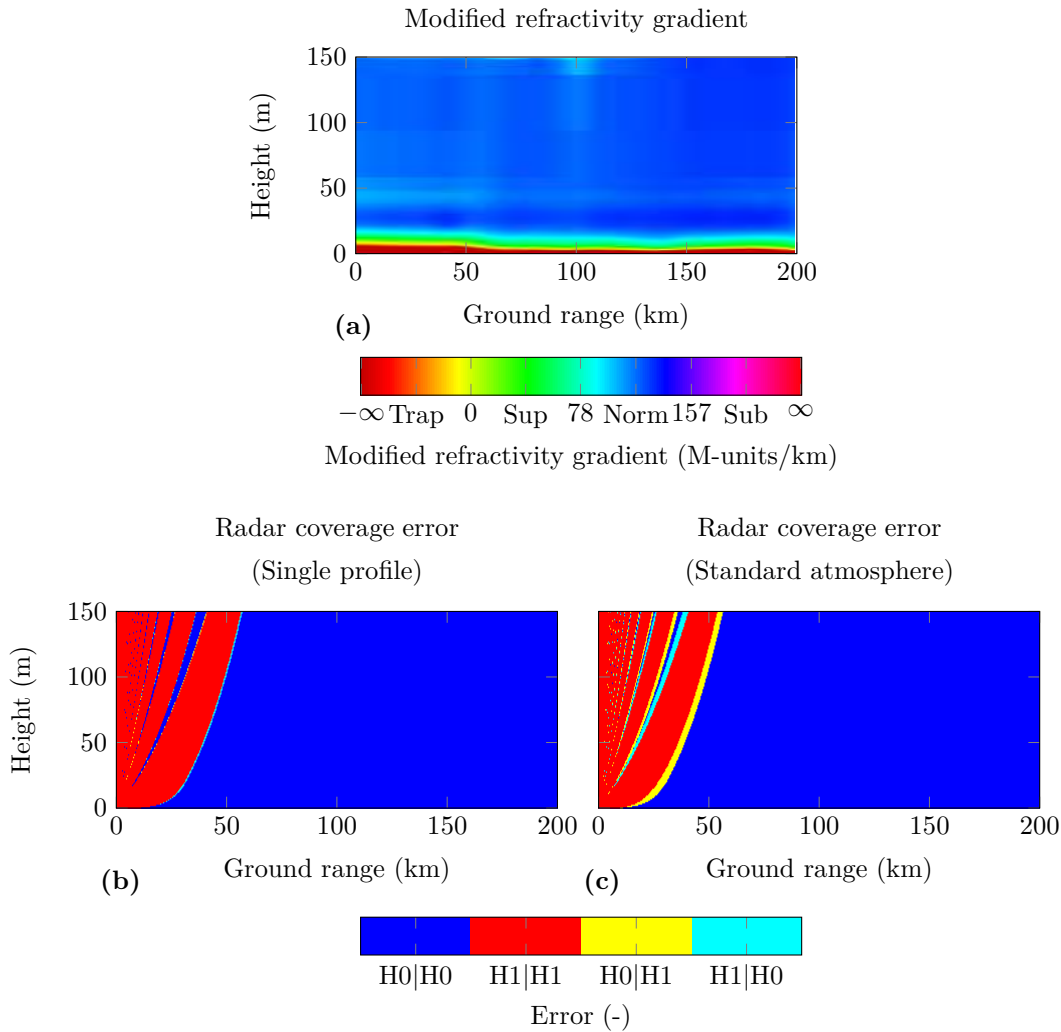


Figure 7-1: Modified refractivity gradients (a) for a ship positioned behind a cold front deploying its radar towards the warm air mass (Scenario 6) and the corresponding radar coverage error when using a single (b) and standard (c) vertical profile.

extend the maximum detection range a little (see Fig. 7-1 (c)), but there is no duct formed as in Fig. 3-12(b). The main reason behind this is that for the duct to trap significant energy at a radar operating frequency of 3.3 GHz the duct height must be at least approximately 23 m according to Eq. 3-2. Hence, because the effect of the evaporation duct in this scenario is small, errors due to variations in the vertical refractivity profile along the propagation path will also be small. In fact, radar assessments based on a single measured profile might even be more accurate than a HARMONIE based assessment as it is a direct measurement of the conditions and not a modelled prediction of the weather conditions.

In this scenario, if for some reason a single profile can't be obtained, depending on the required accuracy of the prediction, even a radar assessment based on a standard atmosphere might suffice. The false predicted coverage area of a standard atmosphere based assessment is 7.0%. The maximum detection range error is 4.1 km and has a mean of 2.9 km.

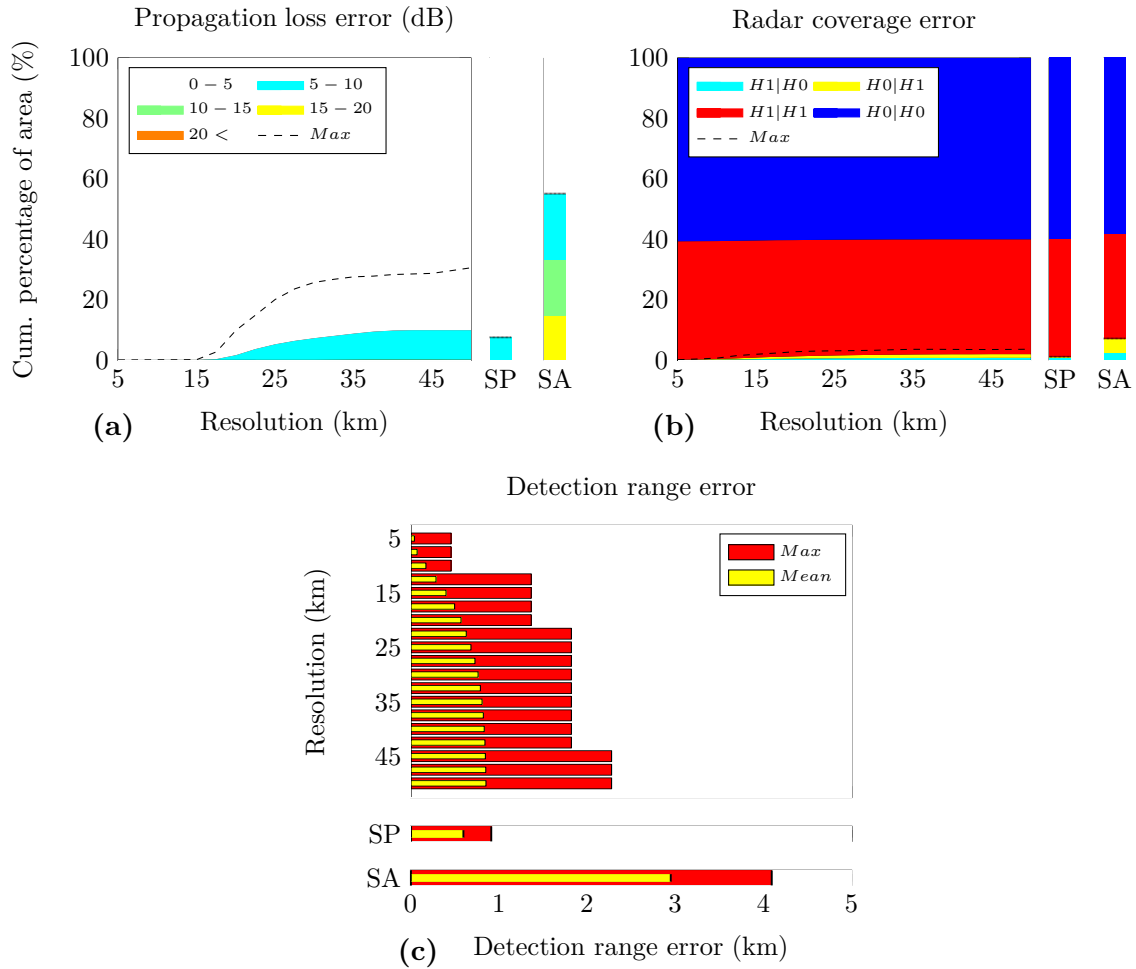


Figure 7-2: Measures of accuracy for Scenario 6 (cold weather front): propagation loss error (a), coverage error (b) detection range error (c). Propagation loss errors are in decibel.

To accurately predict propagation losses for e.g. communication applications, depending on the required accuracy, 3D HARMONIE data may be required. 7.4% of the total area is in error greater than 5 dB when assessing propagation loss using a single profile. This area can be reduced to, for example, a maximum area of 2.6% and an average of 0.2% if HARMONIE grid data with a horizontal grid resolution of 17.5 km is used (see Fig. 7-2 (a)). A standard profile should definitely not be used as 55.0% of the area has an error of 5 dB or greater. In general for propagation loss prediction requires higher data resolution than predicting coverage and ranges. This is because at any range propagation loss is a continuous phenomenon while coverage is discrete.

Comparing the accuracy sensitivity to horizontal grid resolution for all cold front scenarios considered, shows that sensitivity is the strongest in Scenario 6. Hence for all cold fronts scenarios a single profile suffices for predicting radar coverage and detection ranges. For all scenarios the percentage of the area where coverage prediction is in error, remained under 1% as is shown in Fig. 7-3, which shows for all cold front scenarios considered the mean and maximum area percentages where coverage prediction is erroneous.

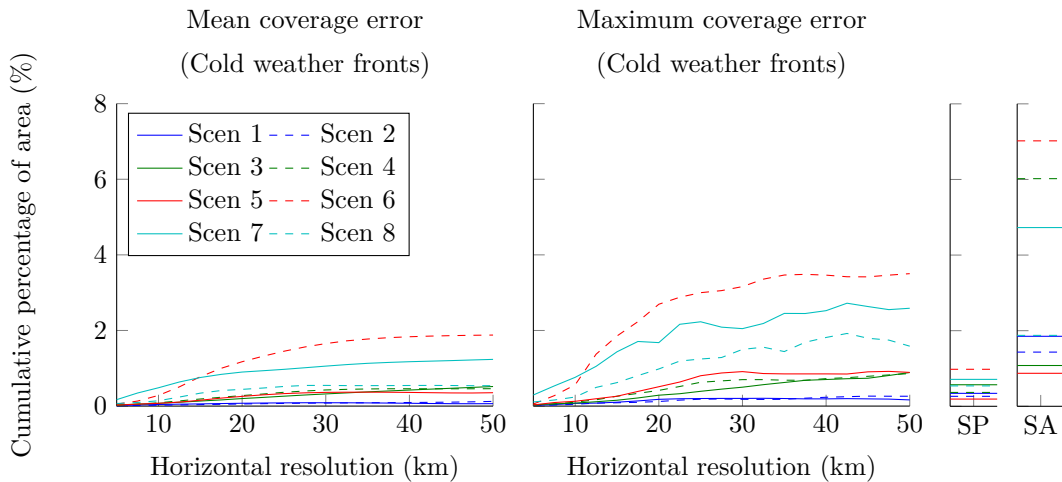


Figure 7-3: Mean and maximum radar coverage error near cold weather fronts (Scenarios 1-8).

In hindsight it could have been expected that a single profile suffices for radar coverage assessments in North Sea cold front scenarios. This because over the North Sea evaporation ducts have an average height of 14 m and seldom reach heights above 20 m. A couple of points must however be acknowledged. For higher frequencies, the above conclusions might not be valid as higher frequencies are more strongly affected by evaporation ducts. For example, at 10 GHz an evaporation duct of approximately 11 m significantly traps energy. Secondly, these conclusions are only valid for conditions similar to North Sea conditions. In areas where the cold fronts and the evaporation ducts are more strongly developed, or where other refractivity conditions are at play, accurate radar performance assessment may require 3D atmospheric data, e.g. HARMONIE data. The fact that a single profile does not suffice for these other conditions is in agreement with literature which states that the assumption of lateral homogeneous may not be valid near weather fronts [4, 9]. The above points are also applicable to the other weather scenarios discussed below.

7-1-2 Warm weather fronts

Compared to the vertical modified refractivity profile in cold weather front scenarios, in the warm front scenarios the vertical modified refractivity profile varied much more along the propagation path. This is because, unlike near cold fronts, propagation conditions other than the evaporation duct may occur. For example, Fig. 7-4 (a) and (b) show the modified refractivity gradient along the propagation path for respectively Scenarios 11 and 16. The elevated trapping layer in Fig. 7-4 (a) is most likely due to the temperature inversion in front of the warm weather front where the warm air mass slides over the cold air. The sub-refractive regions in Fig 7-4 (b) are characteristic for the warm air mass behind a warm front. As warm air moves over a relative cold surface it cools. Because cold air can hold less water vapour than the warmer air a loft, the vapour content will increase with height giving rise to sub-refractive conditions.

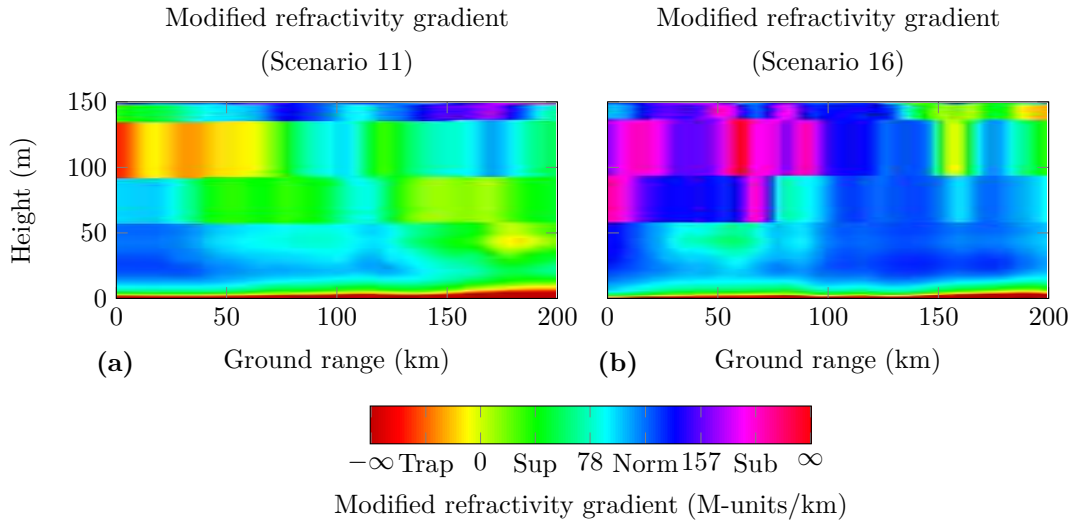


Figure 7-4: Modified refractivity gradients for a ship positioned in front (Scenario 11)(a) and behind (Scenario 16)(b) a warm weather front deploying its radar toward the warm and cold air mass respectively.

This said, even though the modified refractivity can vary horizontally much more than in a cold front, the predicted coverage and detection range errors as a result of coarse horizontal resolution remain small as can be seen in Fig. 7-5, which shows the measures of accuracy for Scenario 16². Using a single profile for radar coverage assessment results in an area of 4.0% in which radar coverage prediction is erroneous. The maximum detection range error of the single profile assessment is 3.6 km and has a mean of 2.3 km. Because the errors are so small, for this scenario it can be assumed that the atmosphere is horizontal homogeneous and thus a single profile is sufficient for radar coverage assessment.

The errors are so small because, as in the case of weak evaporation ducts near cold fronts, the non-standard refractive conditions near the warm front in this scenario are weak. Hence, variations in the vertical refractivity profiles along the propagation path will not significantly affect propagation.

Another interesting observation is that the coverage and detection errors of the assessment based on a standard atmosphere are smaller than the errors of the assessment based on a single profile. This contradicts results generally found in literature. However, because the errors of the single and standard profile based assessments for this warm weather front scenario are in itself small, it does not matter much which profile is used. This said, for scenarios other than weather front scenarios the errors as well as the difference between the single and standard profile based assessment can become quite large (e.g. Scenario 18, see Fig. 7-9), making it important to use the profile which results in the most accurate assessment. Since no method is available to determine which profile will result in the best assessment without prior knowledge of the vertical profile changes along the propagation path, 3D atmospheric data is generally to be preferred for cases other than weather front scenarios.

Assessing radar coverage in Scenario 16 using a single profile resulted in the largest error for all warm weather front scenarios considered. Because in this scenario a single modified

²The measures of accuracy for Scenario 11 are not shown within this thesis.

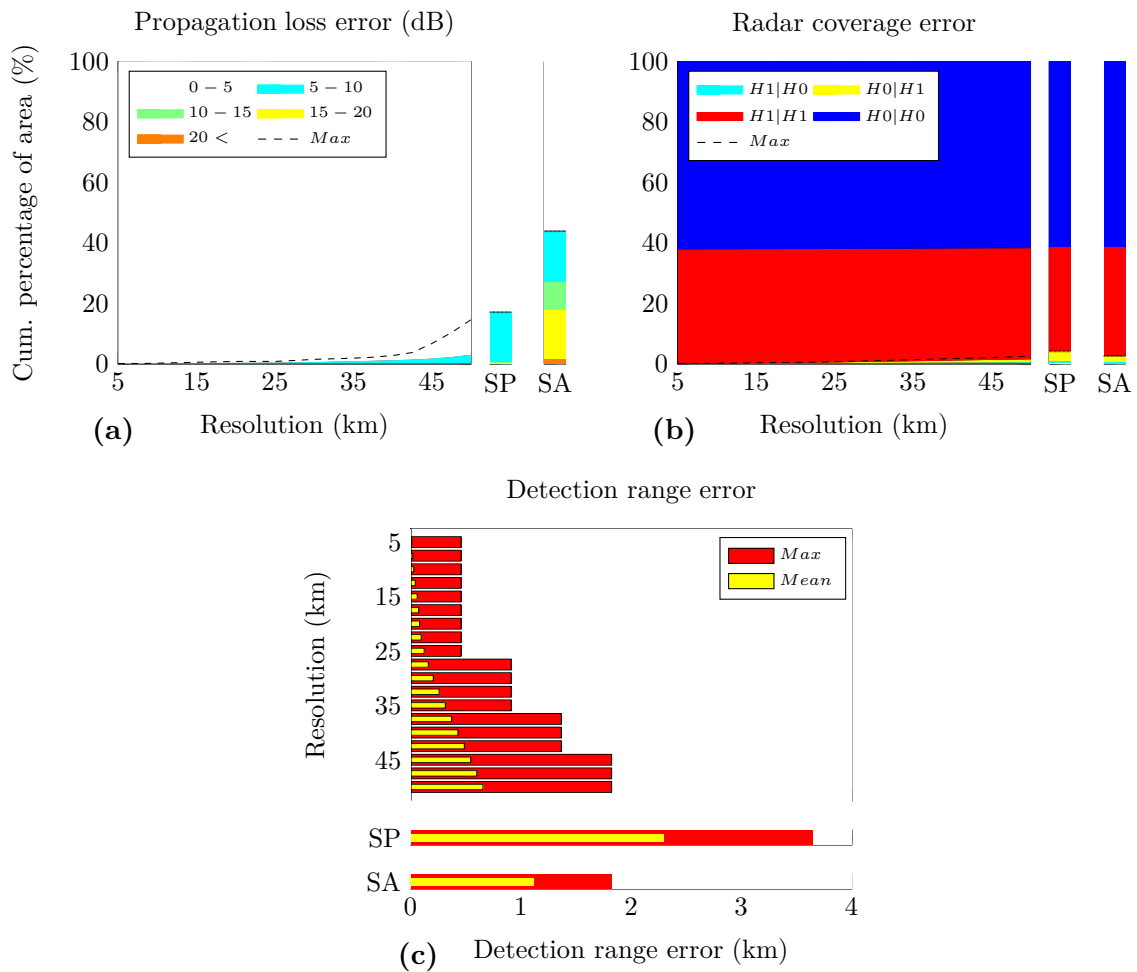


Figure 7-5: Measures of accuracy for Scenario 16 (warm weather front): propagation loss error (a), coverage error (b) detection range error (c). Propagation loss errors are in decibel.

refractivity profile is sufficient for accurate radar coverage assessment it may be concluded that a single profile suffices for all warm weather front conditions. Note however that, as for the cold front case, this conclusion is based on 8 scenarios only and it is only valid for conditions similar to those over the North Sea. As mentioned in literature sources, 3D modified refractivity data may be required for accurate radar assessment near stronger developed weather fronts where the vertical profiles vary significantly along the propagation path and where refractive conditions (e.g. strong trapping layers) affect propagation more significantly. For all warm weather front scenarios considered (9-16), the mean and maximum percentages of area in which radar coverage prediction is erroneous is shown in Fig. 7-6 as a function of resolution.

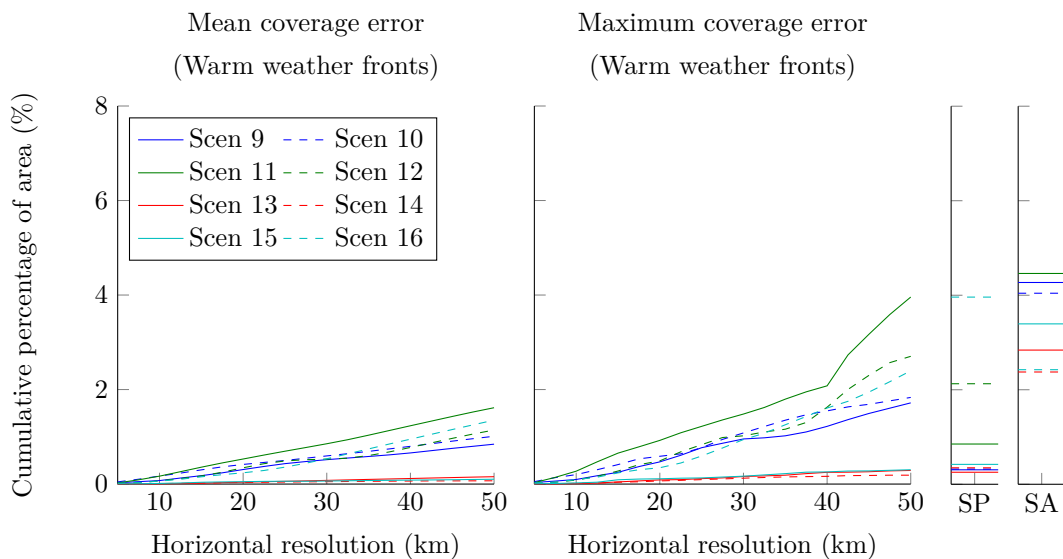


Figure 7-6: Mean and maximum radar coverage error near warm weather fronts (Scenarios 9-16).

7-1-3 Warm sectors

In this thesis a single scenario in which the ship is positioned far into a warm sector³ is considered. As mentioned in Section 3-2-1 sub-refractive conditions are characteristic for warm sectors. In the warm sector of Scenario 17 there are indeed regions of sub-refractive conditions (see Fig. 7-7). Notice that the sub-refractive layer extends all the way along the propagation path. The sub-refractive layer does increase in thickness beyond approximately 100 km, but this will not affect the coverage as this region lays beyond the horizon. Looking at just the first 100 km it can be assumed that the atmosphere is lateral homogeneous. The measures of accuracy concerning radar coverage error and detection range error indeed show this, as the errors as a result of using a single profile remain small (see Fig. 7-8). The falsely predicted coverage area is only 1.2% and the maximum detection range error is a mere 0.9 km. Using a standard atmosphere results in errors of 9.7% and 5.9 km respectively, which can still be acceptable depending on the operational circumstances.

As only one warm sector is considered in this thesis, it cannot be concluded that a single profile always suffices in warm sectors. One can well imagine that results will be different if the ship were positioned where the sub-refractive layer increases in thickness (see Fig. 7-7). Such a scenario was not considered for time constraints. Hence propagation in a warm sector must be examined further.

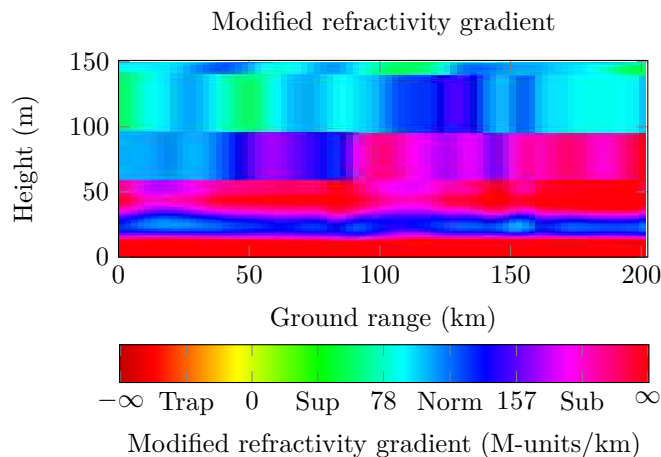


Figure 7-7: Modified refractivity gradients for a ship positioned far into a warm sector (Scenario 17).

³A warm sector is the region between a warm and cold weather front.

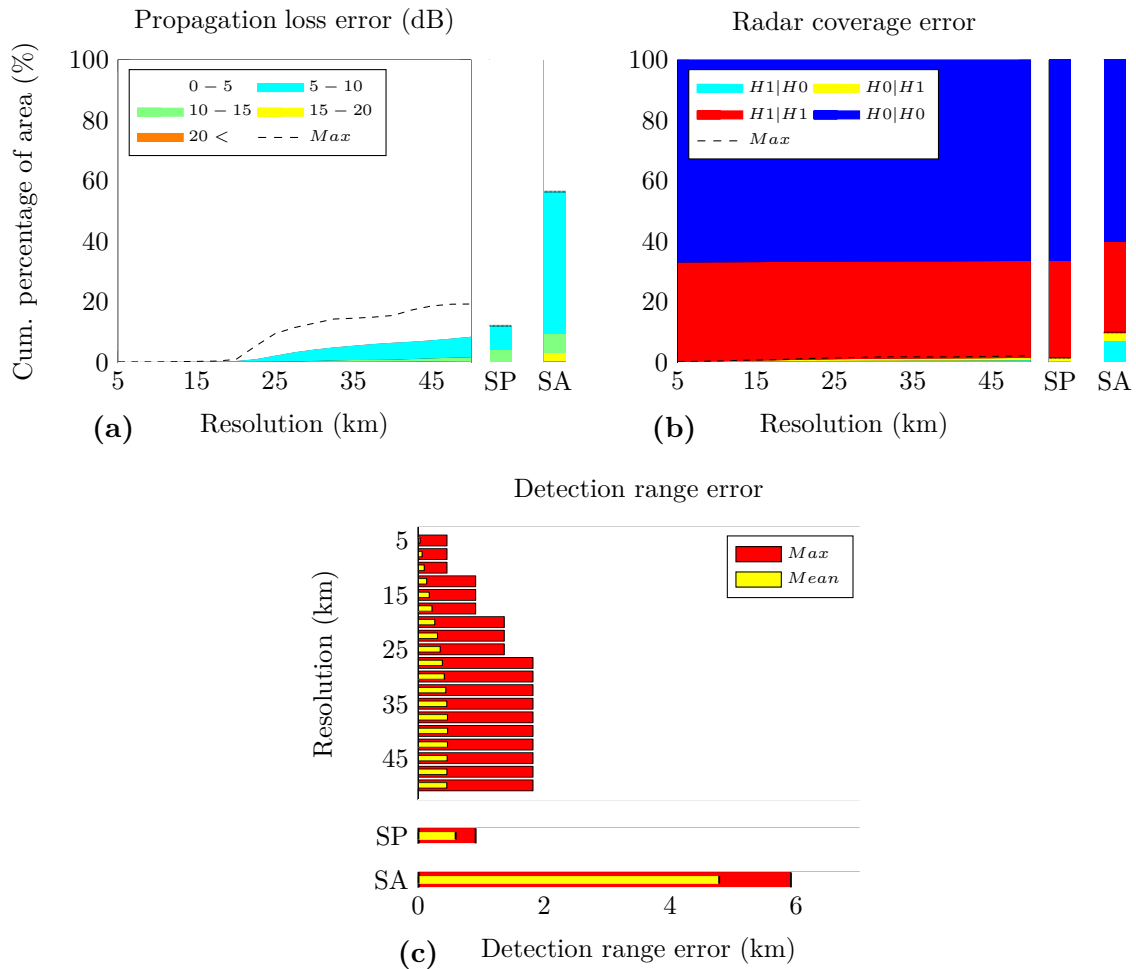


Figure 7-8: Measures of accuracy for Scenario 17 (warm weather sector): propagation loss error (a), coverage error (b) detection range error (c). Propagation loss errors are in decibel.

7-1-4 Warm dry air advection

Warm dry air blowing over the sea surface can significantly influence propagation due to the decrease of water vapour and the increase in temperature with height. The modified refractivity gradient along the propagation path of Scenario 18 in Figure 7-9 (a) shows strong elevated trapping regions as a result of this warm dry air advection. Figure 7-9 (c) illustrates how strongly propagation is affected by this advection. See that detection ranges, compared to a standard atmosphere, significantly increase at specific heights.

Figure 7-9 (b) shows the error as a result of using a single profile for radar coverage assessment. Clearly, a single profile is not sufficient to accurately assess radar performance. For example, using only a single modified refractivity profile will result in extreme erroneous detection ranges. By the false assumption of lateral homogeneity it is expected that detection ranges extend beyond 200 km while this is truly not the case. The falsely predicted coverage area is 36.1% of the total area and the mean detection range error is 62.5 km and has a maximum error of 161.8 km. The errors are so extreme because when a single profile is used, it is assumed that the atmosphere is horizontal homogenous and hence the elevated trapping layer

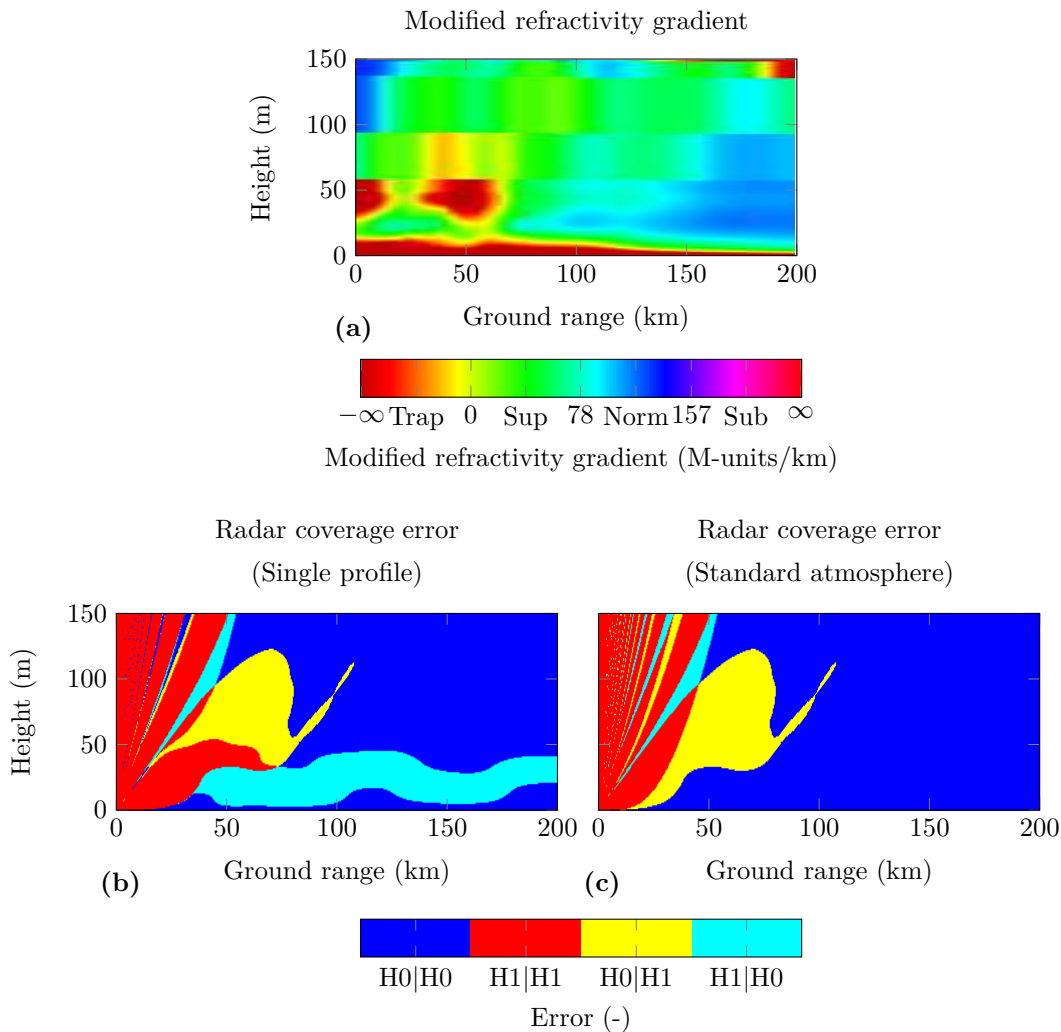


Figure 7-9: Modified refractivity gradients (a) for a ship positioned in weather conditions with warm dry air advecting over relatively cold water (Scenario 18) and the corresponding radar coverage error when using a single (b) and standard (c) vertical profile.

seemingly extends along the entire propagation path. As shown in Fig 7-9(a) this is not the case as the duct abruptly disappears at approximately 20 km to reappear and disappear again at ranges of approximately 30 and 65 km respectively. Hence, for accurate radar performance assessment 3D atmospheric data, in this case HARMONIE data, must be used. The required resolution depends on the required accuracy which depends on the operational circumstances and can be selected using the measures of accuracy in Fig. 7-10.

As shown in Fig. 7-10, the accuracy of the assessment is highly dependent on the horizontal grid resolution of the atmospheric data. For example, at a horizontal grid resolution of 5 km the average coverage area error is 2.9%, while decreasing the resolution to 10 km or 20 km results in an average area error of 8.1% or 13.2% respectively. Note that for this scenario the accuracy sensitivity to resolution does reduce at coarser resolution, but this is not always the case.

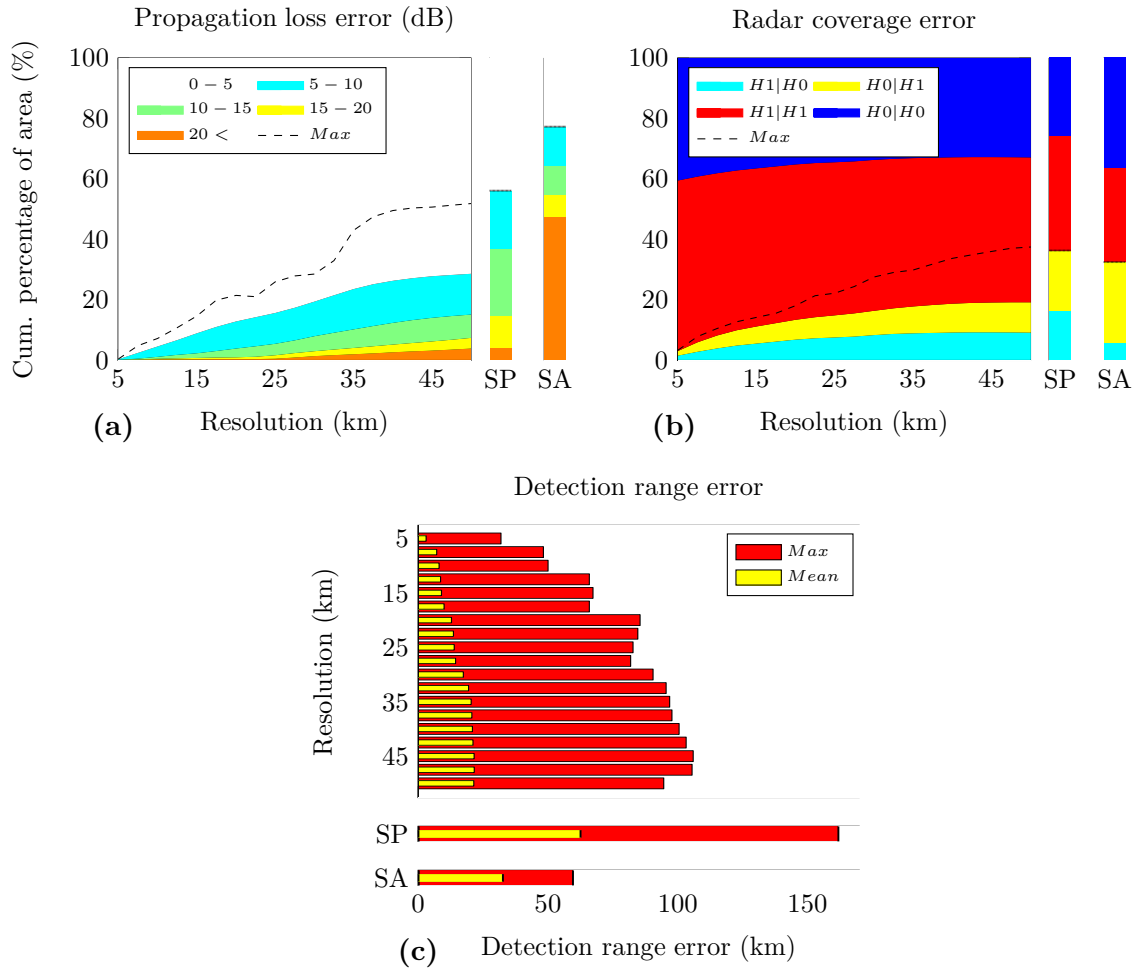


Figure 7-10: Measures of accuracy for Scenario 18 (warm dry air advection): propagation loss error (a), coverage error (b) detection range error (c). Propagation loss errors are in decibel.

The error in predicted detection ranges also increases with decreased resolution. For example at a resolution of 5 km the average⁴ error is 3 km, at a 10 km resolution the average error is 8 km.

Also notice that the radar assessment based on a standard atmosphere yields a more accurate prediction of the ground truth coverage and detection ranges than the assessment based on a single profile. Hence it is not always better to use a profile rather than none. This said however, both assessments are insufficient accurate for military applications. It is interesting to note that for some cases the coverage assessment based on a standard atmosphere was more accurate than the coverage assessment based on a single profile, while for predicting propagation losses the assessments based on a single profile were better for all cases considered.

⁴When considering the maximum detection range errors it must be noted that these may well be outliers and therefore may not accurately represent the overall accuracy of the detection range prediction. This is especially the case at high resolutions. Additional consideration of error variance may be helpful in this respect but was not undertaken within the scope of this thesis.

Figures 7-11(a) and (b) show the coverage error for respectively Scenarios 19 and 20. Scenarios 19 and 20 occur on the same day as Scenario 18 (Fig. 7-10) but three hours earlier and at different positions. Notice that again for these conditions, still warm dry air advecting over water, requires three dimensional atmospheric data for accurate radar performance assessment. Unlike in Scenario 18, in Scenario 19 the accuracy sensitivity to resolution does not decrease at coarser resolutions. It is also interesting that the resolution requirement is not reciprocal. This means that the resolution requirement for Scenario 19 which covers radar coverage between points 'A' and 'B' differs from the resolution requirement for 'B' to 'A' (Scenario 20). This is due to the fact that atmospheric conditions close to the radar have far more effect on overall performance than conditions further on. If prominent non-standard features are present in the atmosphere close to point 'A', while the atmosphere at 'B' is more standard, then accurate prediction for looking from 'A' to 'B' would likely require higher resolution 3D data than prediction for looking the other way. It has even been observed that for some cases an accurate prediction for looking from 'A' to 'B' requires 3D atmospheric refractivity data while a single profile suffices when looking from 'B' to 'A'.

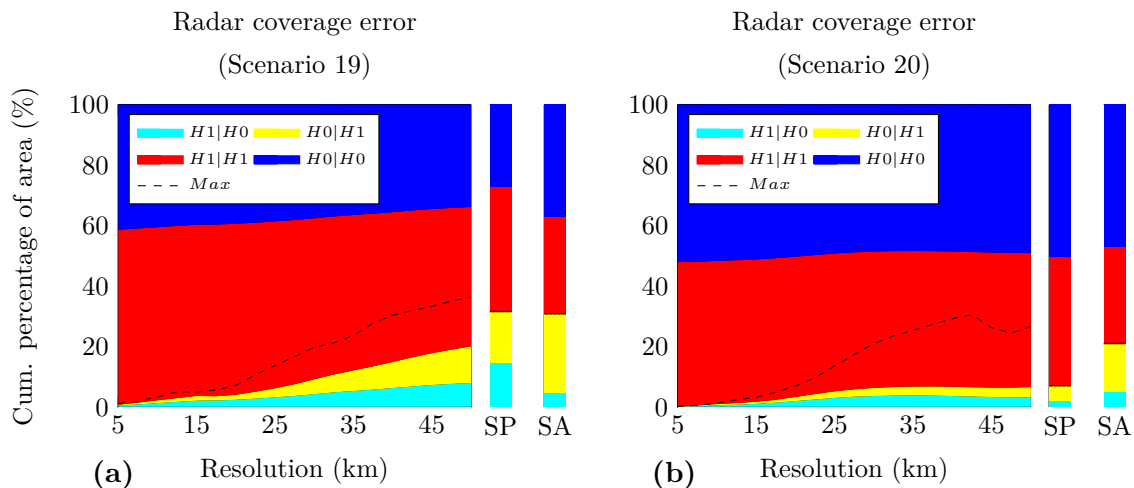


Figure 7-11: Coverage error for Scenarios 19 (a) and 20 (b) (warm dry air advection).

All scenarios (18-26) considering warm dry air advecting over water, with the exception of Scenario 23, require 3D atmospheric data to accurately predict radar coverage and detection ranges. For Scenario 23 a single profile suffices. For propagation loss prediction all scenarios considered required 3D data.

Another example of how horizontal grid resolution affects the prediction accuracy for a scenario considering warm dry air advection is presented in Fig. 7-12 (Scenario 17). Note that the assessment accuracy, measured by the different measures of accuracy, significantly declines when the atmospheric input data resolution becomes coarser.

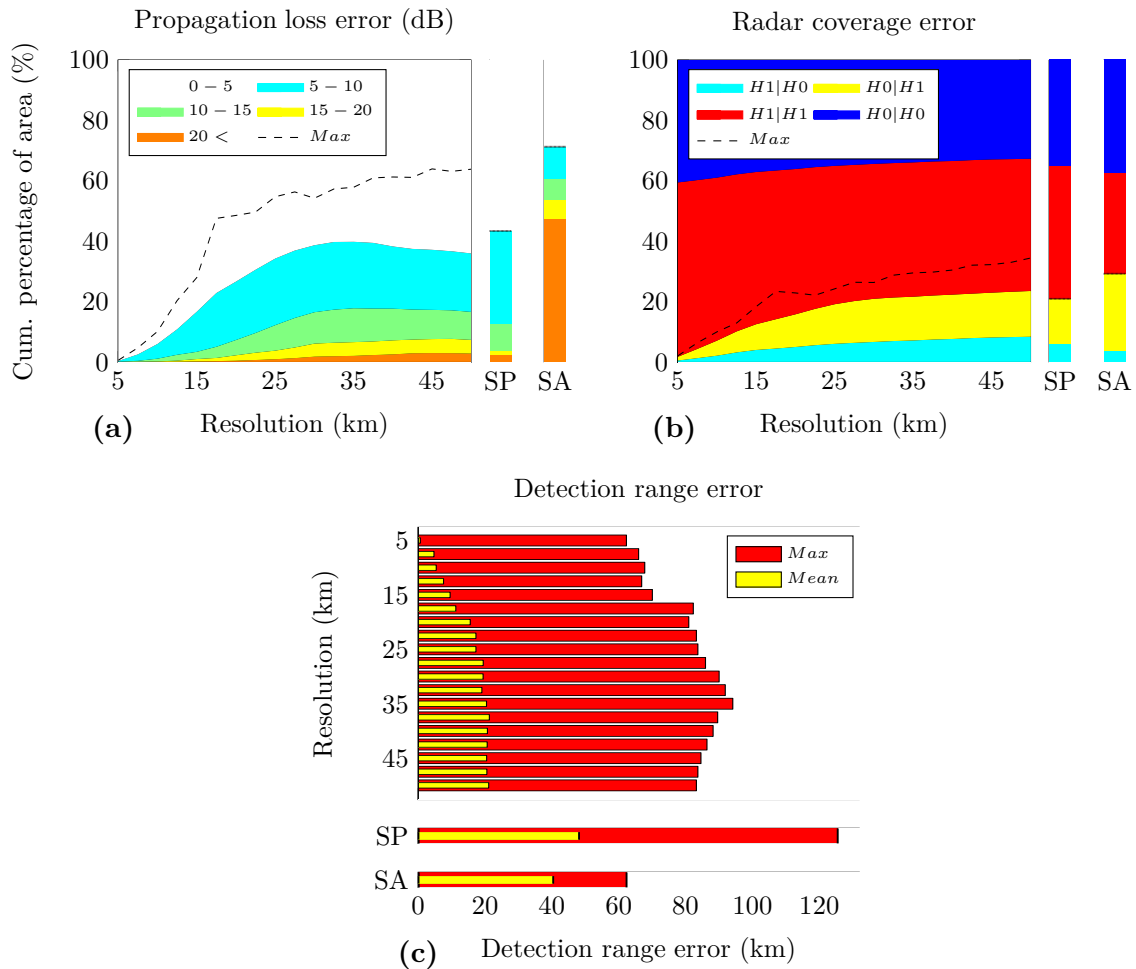


Figure 7-12: Measures of accuracy for Scenario 17 (warm dry air advection): propagation loss error (a), coverage error (b) detection range error (c). Propagation loss errors are in decibel.

7-1-5 High pressure systems

As mentioned in Section 3-2-4, elevated trapping layers can also develop in the vicinity of a high pressure system. A trapping layer due to subsidence near a high pressure system is clearly visible in Fig. 7-13(a). From analysing only the variation of the modified refractivity along the propagation path it already becomes clear that 3D atmospheric data must be used for accurate assessment of radar propagation. This is because the strong trapping layer dissolves abruptly at approximately 100 km. Hence, lateral homogeneity cannot be assumed. As with the condition in which warm dry air advects of water, using a single profile for modelling radar performance may result in large errors and lead to erroneous situational awareness with dramatic consequences (see the measures of accuracy of Scenario 29 in Fig. 7-14).

The required resolution of the atmospheric data depends on the accuracy requirement for the radar performance assessment. It is however clear that in high pressure systems, for most cases considered in this thesis, 3D atmospheric data is required. As shown in Fig. 7-14 and 7-15, the use of a single profile or a standard atmosphere results in significant errors.

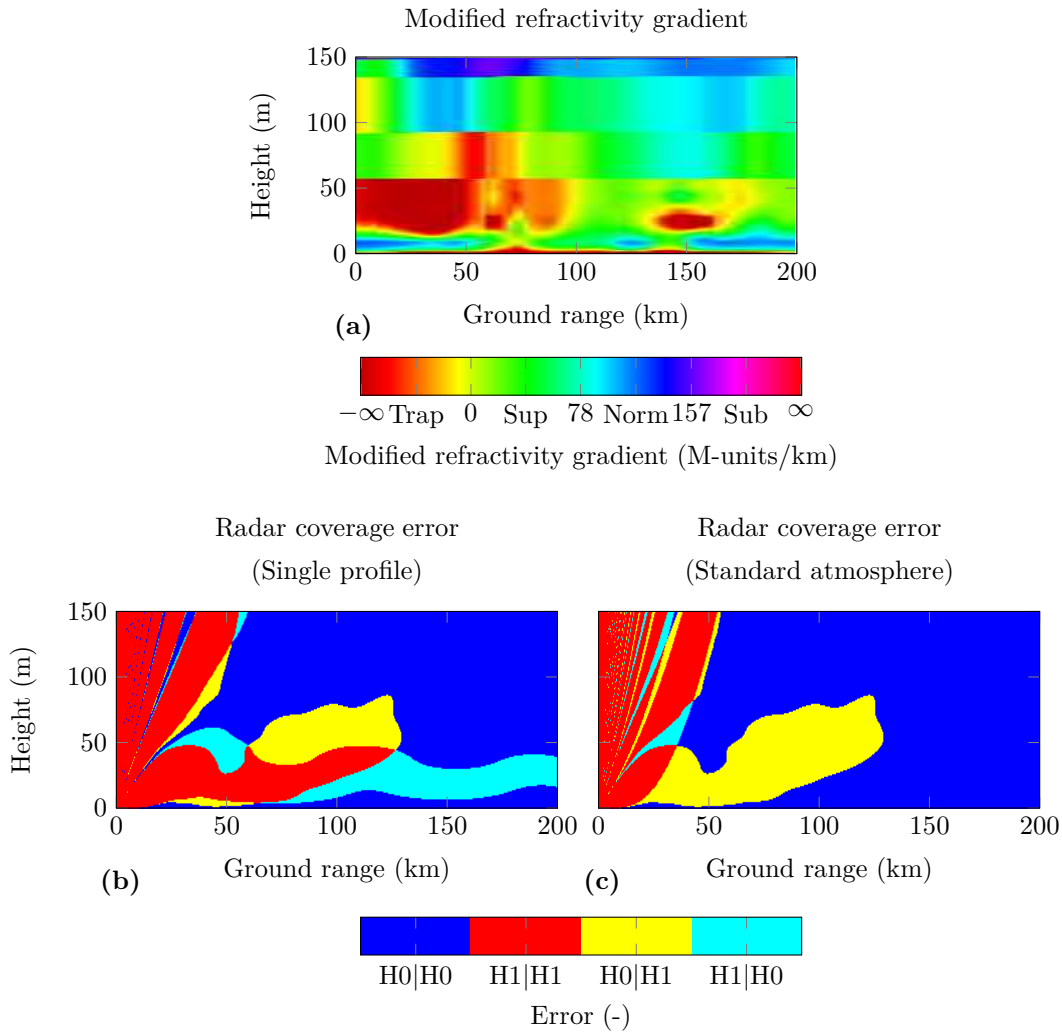


Figure 7-13: Modified refractivity gradients (a) for a ship positioned near a high pressure system (Scenario 29) and the corresponding radar coverage error when using a single (b) and standard (c) vertical profile.

Especially in Scenario 30 (Fig. 7-15), near ground truth resolution (2.5 km) is required to avoid unacceptable errors. Of all high pressure system scenarios considered (eight in total) in only two scenarios (31 and 33) a single profile is sufficient to model radar performance accurately. The measures of accuracy of Scenario 31 are shown in Fig. 7-16.

Note that Scenario 30 (Fig. 7-15), which requires high resolution data, and Scenario 31 (Fig. 7-16), in which a single profile suffices, are based on conditions at the same time but at different ship positions. This clearly demonstrates that the resolution requirement is depended on the ship's position as well as the general weather conditions; making it difficult to arrive at general resolution requirements.

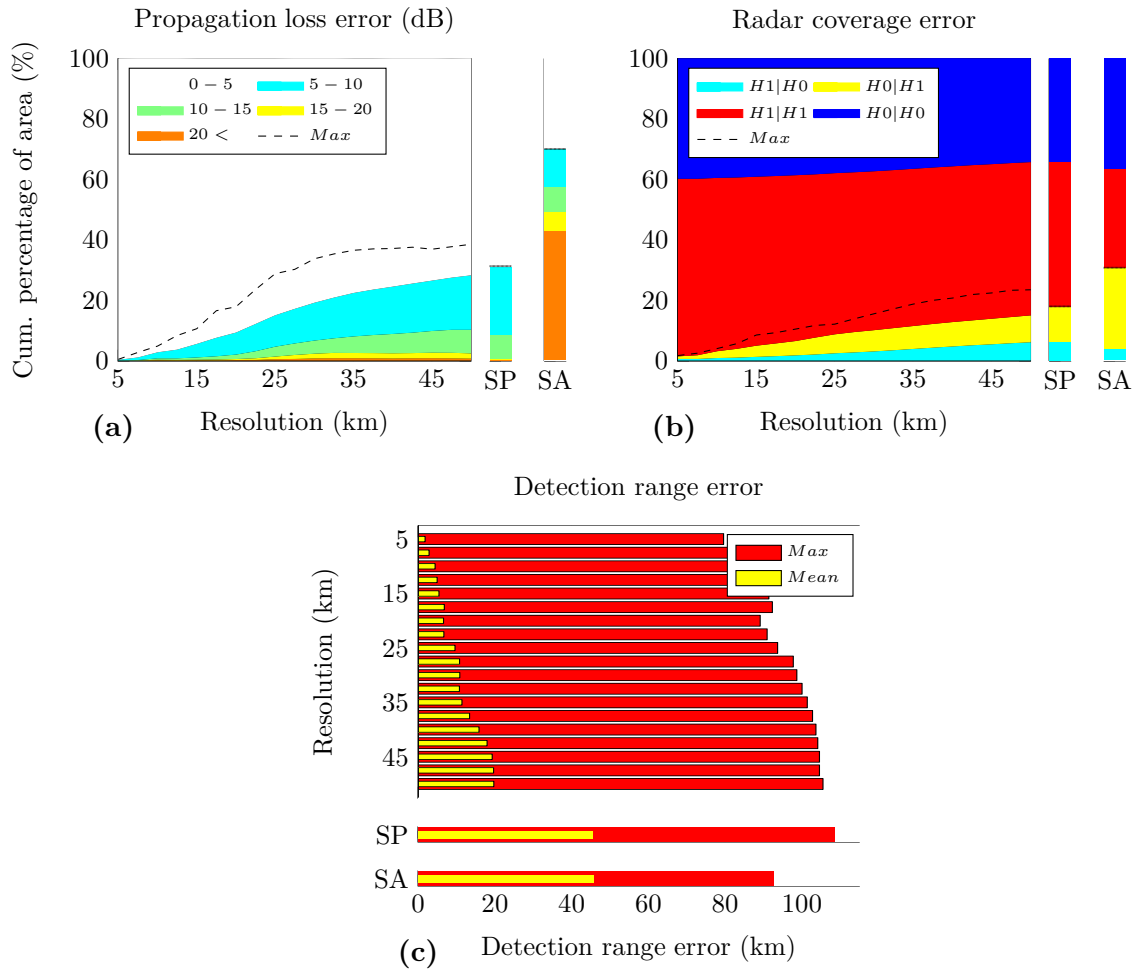


Figure 7-14: Measures of accuracy for Scenario 29 (high pressure system): propagation loss error (a), coverage error (b) detection range error (c). Propagation loss errors are in decibel.

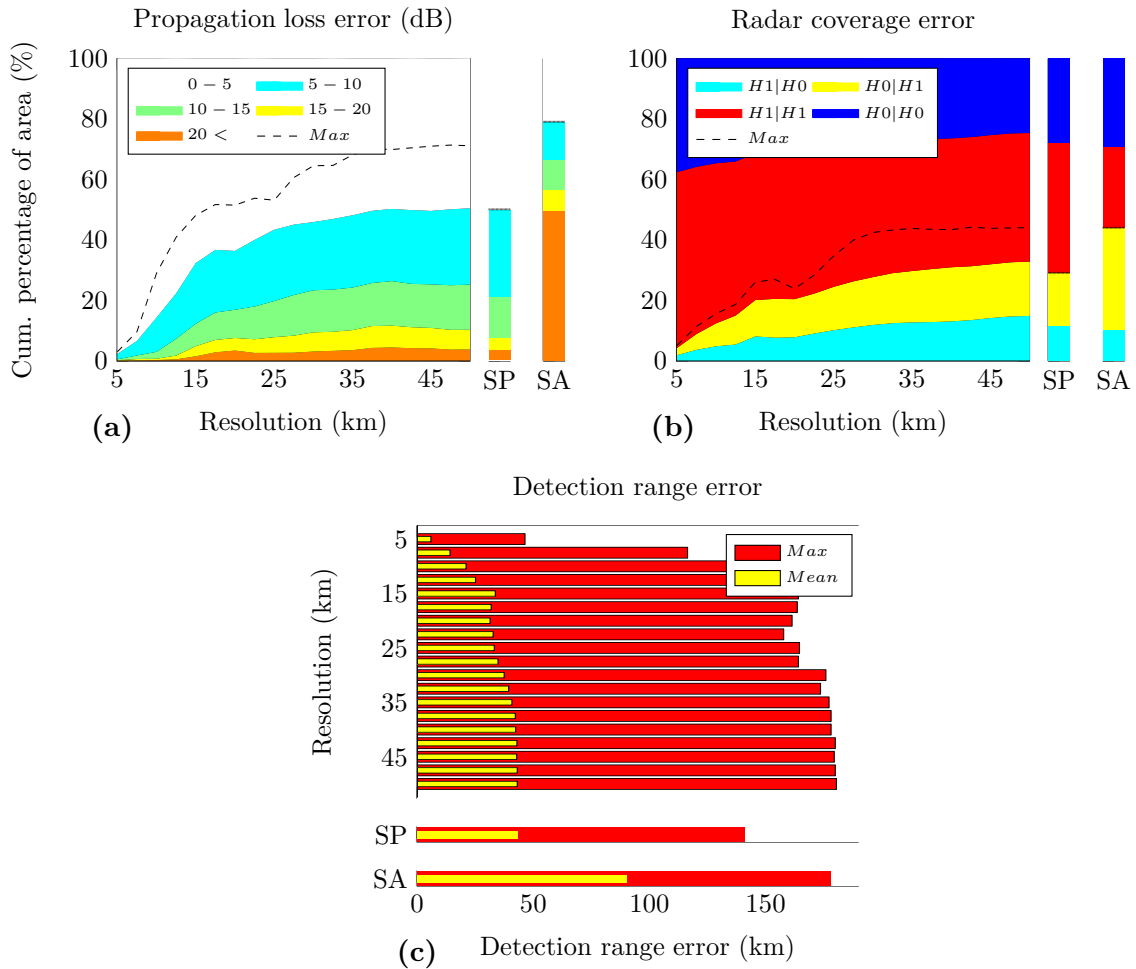


Figure 7-15: Measures of accuracy for Scenario 30 (high pressure system): propagation loss error (a), coverage error (b) detection range error (c). Propagation loss errors are in decibel.

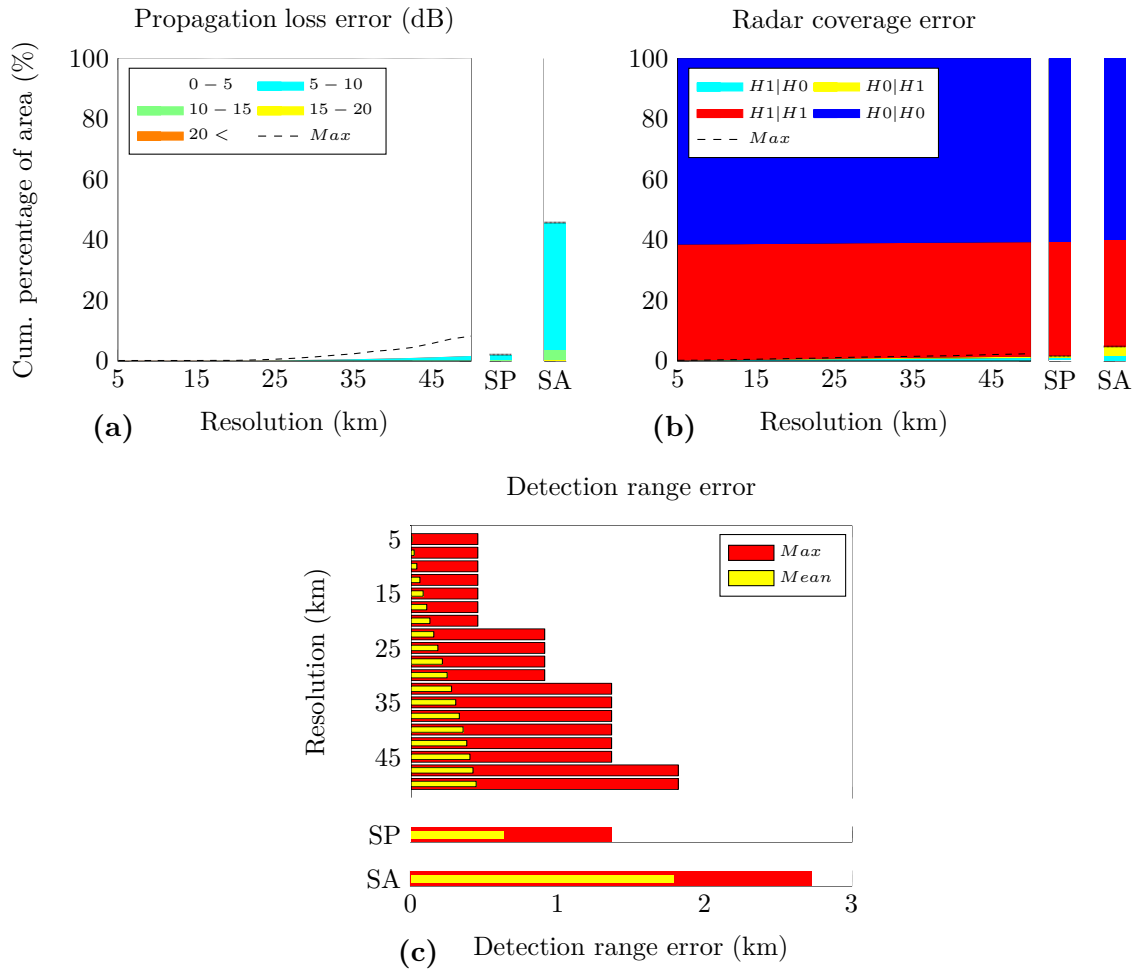


Figure 7-16: Measures of accuracy for Scenario 31 (high pressure system): propagation loss error (a), coverage error (b) detection range error (c). Propagation loss errors are in decibel.

7-1-6 Calm standard conditions

In seven scenarios examined (Scenarios 35-41) the weather conditions were calm. Based on the weather charts from the KNMI it was expected that refractive conditions would be normal with the exception of an evaporation duct. For five of the scenarios this was indeed the case and radar performance could be assessed using a single modified refractivity profile (Scenarios 35, 36, 37, 40 and 41) and in some cases even by assuming a standard atmosphere (Scenarios 35, 37 and 41). Figure 7-17 shows the measures of accuracy for Scenario 40. Notice how coverage and detection ranges can be predicted using a single profile.

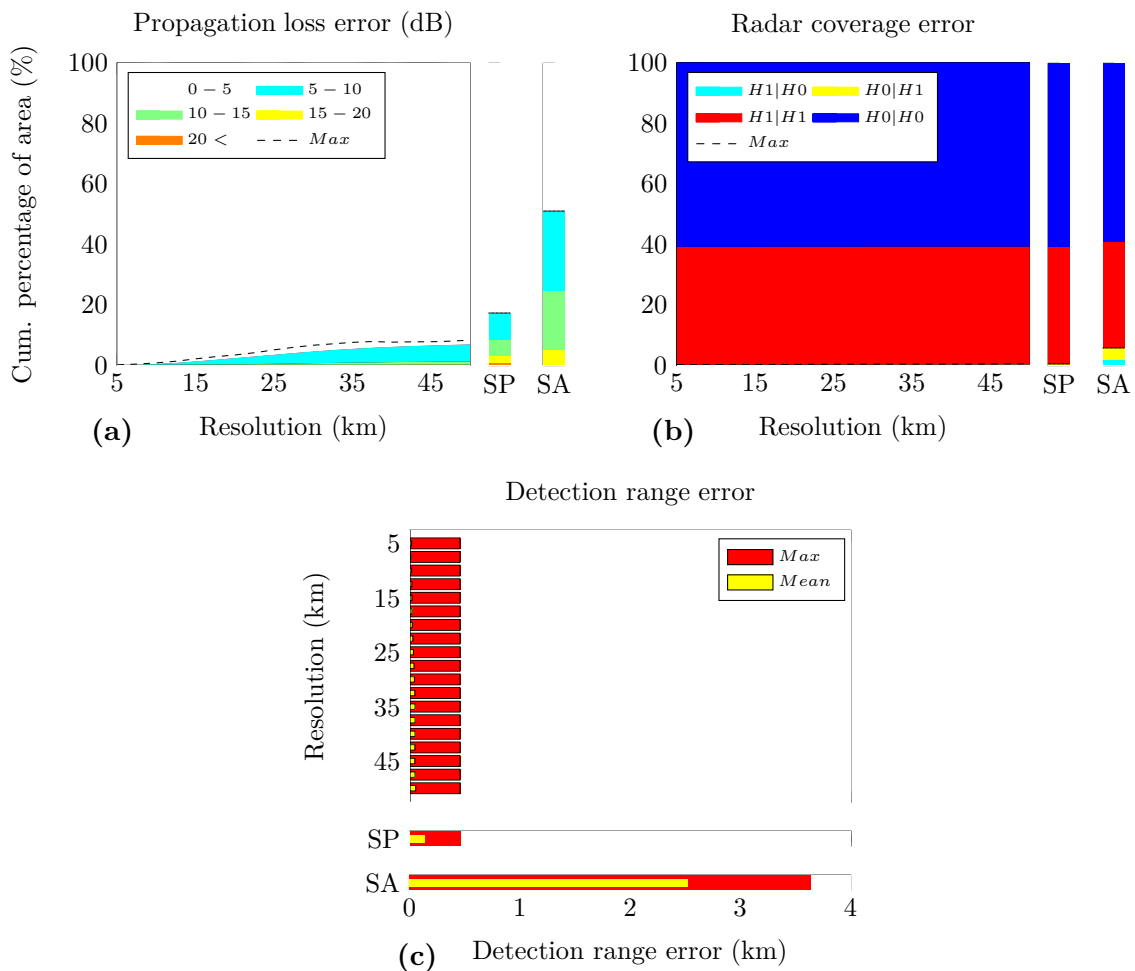


Figure 7-17: Measures of accuracy for Scenario 40 (calm conditions): propagation loss error (a), coverage error (b) detection range error (c). Propagation loss errors are in decibel.

In Scenarios 38 and 39 a single profile cannot be used. The measures of accuracy for Scenario 38 are given in Fig. 7-18. The large error is a result of the unexpected elevated trapping layer. It is clear that one cannot dependably predict if a single profile will suffice merely by looking at weather charts.

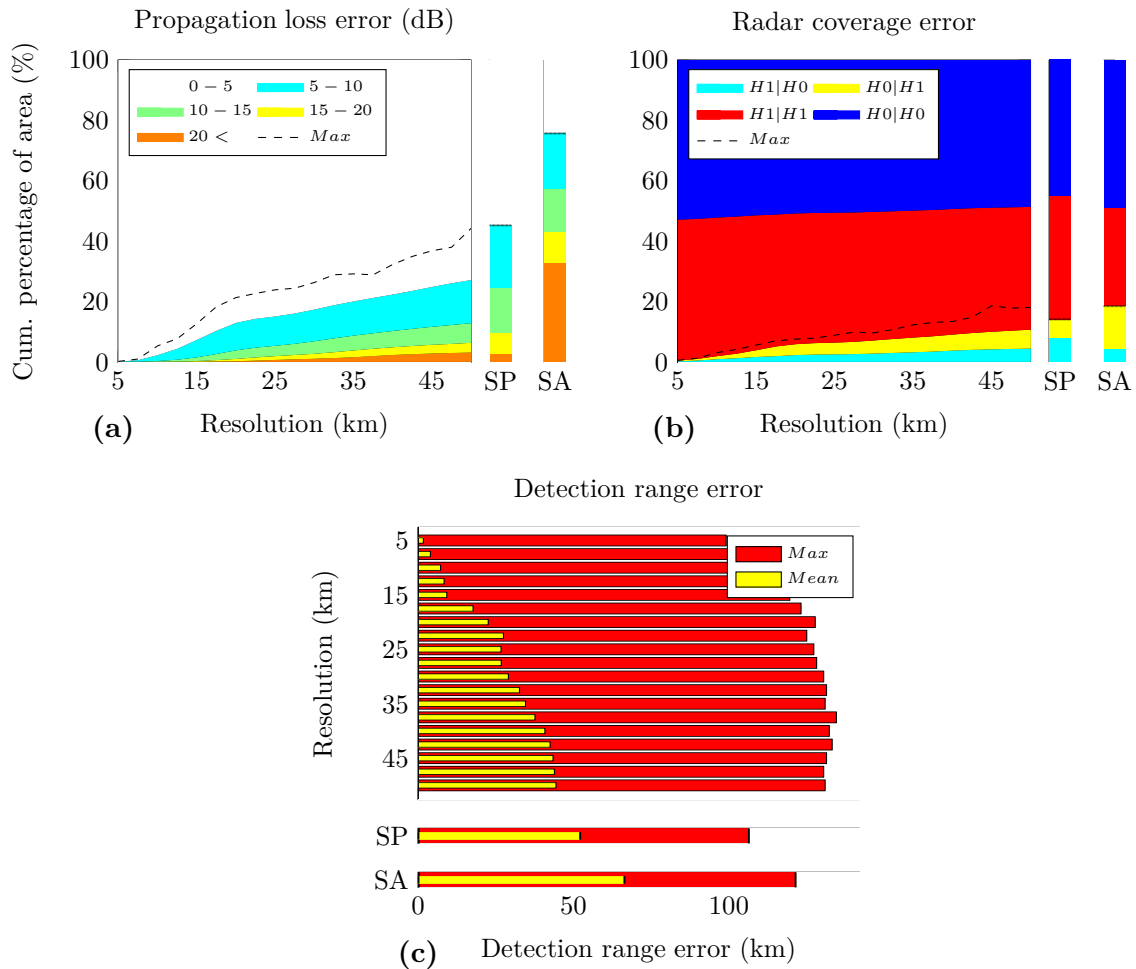


Figure 7-18: Measures of accuracy for Scenario 38 (calm conditions): propagation loss error (a), coverage error (b) detection range error (c). Propagation loss errors are in decibel.

7-1-7 General conclusions

In the above it is shown that while in some cases a single profile suffices⁵ for accurate radar prediction, in other cases single profile assessments contain operationally unacceptable errors. The scenarios for which a single and/or standard atmosphere suffices are summarised in Table 7-1. In 25 of the 41 scenarios (61%) a single profile is sufficient to accurately assess radar coverage and detection ranges. Of course, 3D data can be used for all scenarios. Where a single profile does not suffice, 3D atmospheric data must be used.

The required resolution depends on multiple factors. Firstly the required accuracy. It has been shown that on average the accuracy decreases with a decrease of resolution. Secondly the required resolution depends on the prevailing weather conditions at the position of the

⁵In this thesis it is assumed that a single profile suffices if the coverage area in error does not exceed 5% of the total area and if the maximum detection range error is no more than 5 km. These maximum error values are chosen, as for the purpose of this thesis, it is assumed that errors below these values are operationally insignificant. Depending on the application and the operational circumstances different thresholds may be appropriate.

Table 7-1: Overview of scenarios where a single profile and/or the standard atmosphere profile suffices for accurate radar performance assessment.

Weather conditions, Scenarios (total)	Single profile suffices (total)	Standard atmosphere suffices (total)
Cold weather front, Scenarios 1-8 (8)	Scenarios 1-8 (8)	Scenarios 1-3, 5, 7 and 8 (6)
Warm weather front, Scenarios 9-16 (8)	Scenarios 9-16 (8)	Scenarios 9-11 and 13-16 (7)
Warm sector, Scenario 17 (1)	Scenario 17 (1)	-
Advection warm dry air, Scenarios 18-26 (9)	Scenario 23 (1)	Scenario 23 (1)
High pressure systems, Scenarios 27-34 (8)	Scenarios 31 and 33 (2)	Scenarios 31 (1)
Calm conditions, Scenarios 35-41 (7)	Scenarios 35-37, 40 and 41 (5)	Scenarios 35, 37 and 41 (3)

ship and the azimuth of the radar. Because of these dependencies no general resolution requirement can be defined for any of the different weather categories.

This said, it is shown that for the cold front, warm front and warm sector scenarios considered a single profile suffices. It must be noted however, that it cannot be concluded that this is true for all cold front, warm front and warm sector scenarios. In the first place all conclusions are valid for North Sea conditions only. Secondly, the results will depend on radar parameters (and to some extent target parameters) such as the operating frequency. In this thesis a radar frequency of 3.3 GHz was considered (see also Section 6-3). And thirdly, too few scenarios are considered to allow conclusions with a general validity.

For all other scenarios (warm dry air advection, high pressure systems or calm conditions) it is recommended to always use 3D atmospheric data.

To get a more general idea of the overall accuracy sensitivity to horizontal grid resolution, the accuracy measures of the scenarios are averaged. Figures 7-19(a-c) show the average accuracies over the scenarios⁶ in which lateral homogeneity can safely be assumed, i.e. in which a single profile provides accurate performance assessments. Figures 7-19(d-f) show the average accuracies over the scenarios⁷ in which the atmosphere varies significantly along the propagation path and for which consequently 3D atmospheric data, i.e. HARMONIE data, is required. As expected, the average accuracy increases with horizontal grid resolution.

The average accuracies over all scenarios are shown in Fig. 7-19(g-i). These errors are indicative of assessment errors that are to be expected on average when an arbitrary pre-set resolution, or a single profile, is used regardless of the environmental atmospheric conditions.

On average, assessments based on a single profile yield better results than assessments based on a standard profile. However, in conditions where lateral homogeneity cannot be assumed, the accuracy of the coverage and detection range assessments based on a single profile is only (on average) marginally better than when a standard atmosphere is assumed. In other

⁶Scenarios 1-17, 23, 31, 33, 35-37, 40 and 41.

⁷Scenarios 18-22, 24-30, 32, 34, 38 and 39.

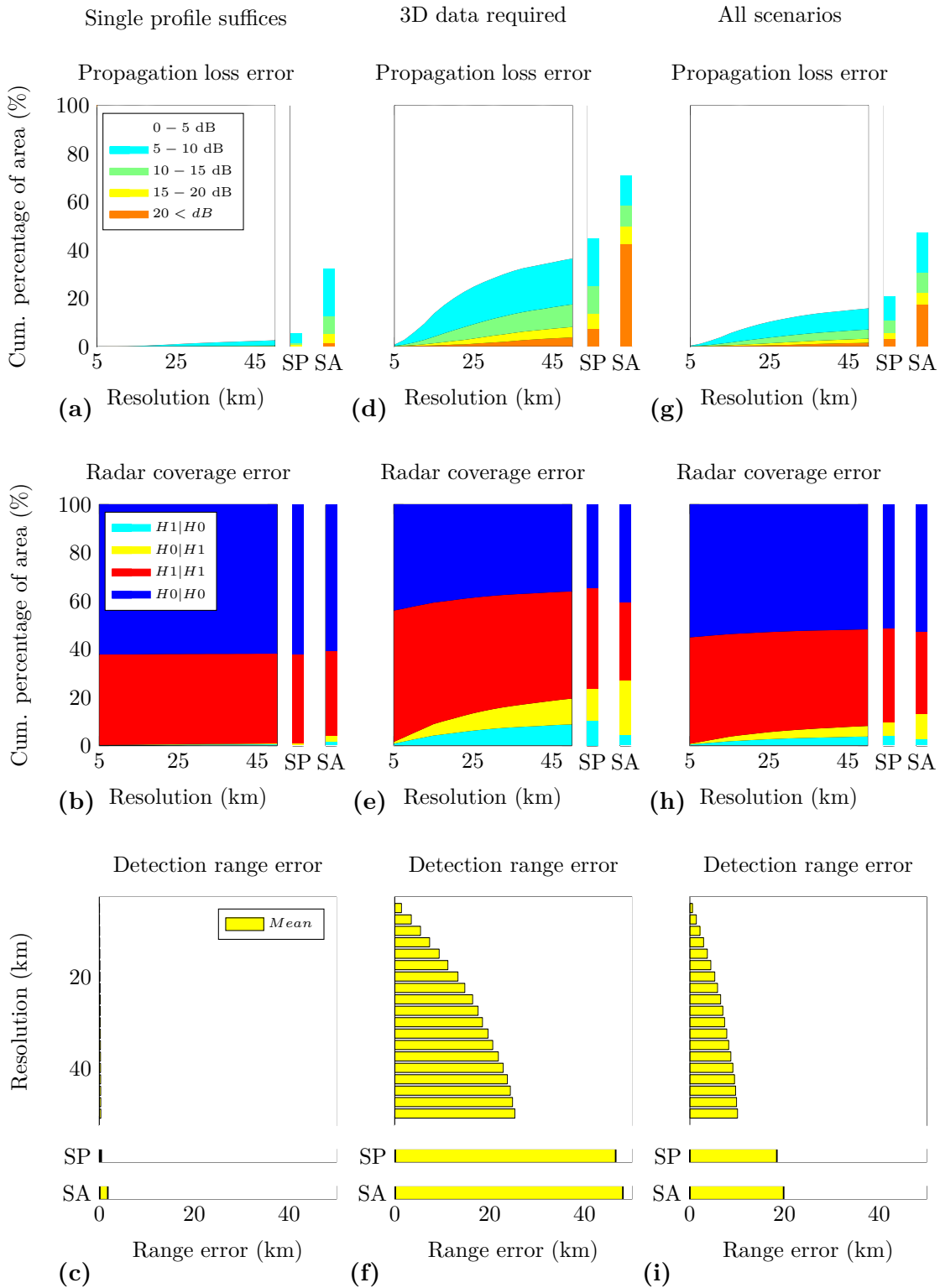


Figure 7-19: Averages of the different measures of accuracy: for scenarios in which a single profile suffices (a-c), for scenarios in which 3D atmospheric input data is required (d-f) and for all scenarios (g-i).

words, under these conditions deploying a weather balloon for radar performance assessments is hardly worth the effort.

This said, analysis of the measured single profile allows, to some extent, estimation of whether or not the atmosphere can be assumed lateral homogeneous. Analysis of the different scenarios showed that, in most cases, when the single profile shows no sign of strong trapping layers, other than the evaporation duct, the assumption of lateral homogeneity is generally valid. This because if a trapping layer, which is the main cause for stringent resolution requirements, should start not at the position of the radar itself but at some distance along the propagation path, the trapping layer generally will have little effect on propagation and hence on coverage. The reason for this is that the elevation angles increase with distance which according to Eq. 2-6 results in a large curvature radius. Therefore no trapping will occur.

Note that while assessments based on a single profile are generally better than assessments based on the standard atmosphere, some of the scenarios, contrary to literature, clearly show the opposite. While this is operationally highly relevant, it is of little practical use since, in the absence of 3D data, on board operators cannot tell when this will be the case.

Finally note that resolution requirements for the purpose of propagation loss determination are more stringent than for determination of coverage and detection ranges. This is because at any range propagation loss is a continuous phenomenon while coverage is discrete. Furthermore, analysis of the scenarios considered has shown that propagation loss assessments based on a single profile are always better than assessments based on a standard atmosphere, unlike coverage and detection range assessments.

7-2 Temporal resolution

Because the atmosphere continuously changes, radar performance assessments must be updated periodically with new atmospheric data to ensure that they remain accurate. The refresh rate of course depends on the rate at which the atmosphere changes. Currently, the RNLN measures the atmosphere's upper profile (generally) every 24 hours using weather balloon soundings. However, as will be shown below, a temporal resolution of 24 hours clearly doesn't always suffice.

In the case of lateral homogeneity one can expect that a coarse temporal resolution, like 24 hours, may more readily suffice than in the case of inhomogeneity. In other words, if a single profile suffices to accurately assess radar performance (which is the case if the atmosphere may be assumed to be lateral homogeneous), it may well be the case that the temporal resolution of HARMONIE data (1 hour) may be reduced significantly. Figure 7-20 shows two examples of the measures of accuracy concerning temporal resolution: Scenario 8 (cold weather front, 7-20 (a-c)) and Scenario 41 (calm weather conditions, 7-20 (d-e)). The figure shows that, if it is the case that performance prediction where the falsely predicted coverage area does not exceed 5% and the detection range error does not exceed 5 km is considered sufficiently accurate⁸, for these scenarios 24 hour resolution is likely to be sufficient. "Likely to be sufficient" rather than merely "sufficient" because, while the measures of accuracy span in total 24 hours, the maximum time difference between the radar performance assessment at

⁸The same thresholds are used for accepting assessments based on a single profile.

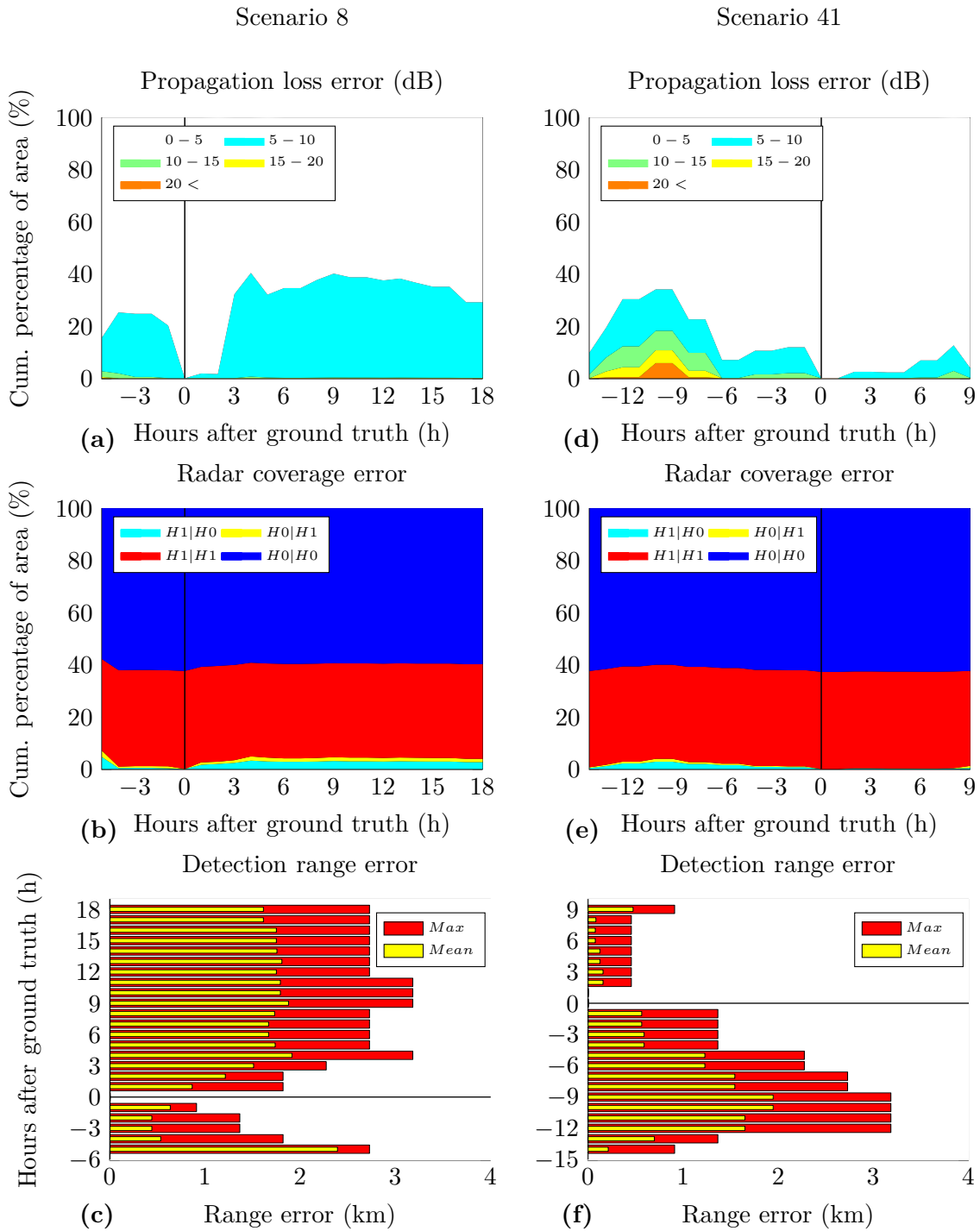


Figure 7-20: Measures of accuracy for Scenario 8 (cold weather front): propagation loss error (a), coverage error (b) and detection range error (c). Measures of accuracy for Scenario 41 (calm conditions): propagation loss error (a), coverage error (b) and detection range error (c). Propagation loss errors are in decibel.

time $T = 0$ and the ground truths is less than 24 hours. Nonetheless, because the differences between the assessment at $T = 0$ and all ground truths remain small at either side of $T = 0$, it seems likely that a single measurement over the 24 hour period suffices, regardless of which point in time is chosen as $T = 0$.

As can be seen in Fig. 7-20(a) and (d), propagation loss assessment accuracy is much more sensitive to temporal resolution than assessment of coverage and detection ranges, as was the case for horizontal resolution. Therefore higher resolution is required for accurate propagation loss prediction than is required for coverage and range assessment. This was determined to be the case for all scenarios considered.

In the previous section it was shown that for the cold front and warm front scenarios a single profile sufficed for accurate radar assessment. As demonstrated above, for many of these scenarios a temporal resolution of 24 hours suffices, suggesting that under the condition of lateral homogeneity a single profile per 24 hours generally enables sufficiently accurate radar assessment. That this is not always the case is shown in the examples of Fig. 7-21. Figure 7-21(a-c) and (d-f) show respectively the measures of accuracy for Scenario 6 and Scenario 16; the same cold and warm front scenarios discussed in the corresponding sections above (Sections 7-1-1 and 7-1-2). See how the errors become operationally unacceptable within the 24 hours span. Applying the thresholds discussed above yields in a temporal resolution requirement of 4 hours for Scenario 6. See how in Fig. 7-21(b-c) at 4 hours after $T = 0$, the falsely predicted coverage area exceeds 5% and the detection range error exceeds 5 km. For Scenario 16 the resolution requirement is even stricter: 2 hours from $T = 0$ (at $T = -2$), the error thresholds for coverage and detection range are exceeded.

In scenarios where a single profile does not suffice, for example where warm dry air advects over cold water or near high pressure systems, analysis of the results shows that high temporal resolution is required to keep the radar performance assessment sufficiently accurate for operational use. The need for high resolution is to be expected because in these scenarios the atmosphere cannot be assumed lateral homogenous and hence the atmosphere will change in time. Figure 7-22 shows the measures of accuracy for Scenarios 18 (advection of warm dry air) and 29 (high pressure system). Allowing the same accuracy thresholds as above yields a required temporal resolutions of one hour or less.

While it was shown that in the case of spatial resolution the error increases steadily with a decrease of horizontal resolution, in the temporal domain all measures of accuracy show that the error does not necessarily increase with time. In other words, radar performance assessment based on, for example, one hour old atmospheric data may be less accurate than assessment based on data which is five hours old. Such was the case in Scenario 18 (Fig. 7-22 (a-c)). It is not unthinkable that an atmosphere can change and subsequently change back to a state that is very similar to an earlier state.

Because the change in atmosphere is so dynamic, defining a minimum required temporal resolution is difficult, especially with the limited number of scenarios considered in this thesis. However, it has been shown that the atmosphere can change fast resulting in erroneous performance assessments when old atmospheric data is used. For example in Scenario 18 the area for which the coverage is predicted falsely exceeds 32% and the mean detection range error exceeds 43 km in a single hour; both errors are clearly too large for operational use. In the scenarios considered, the maximum error that was seen within 24 hours for

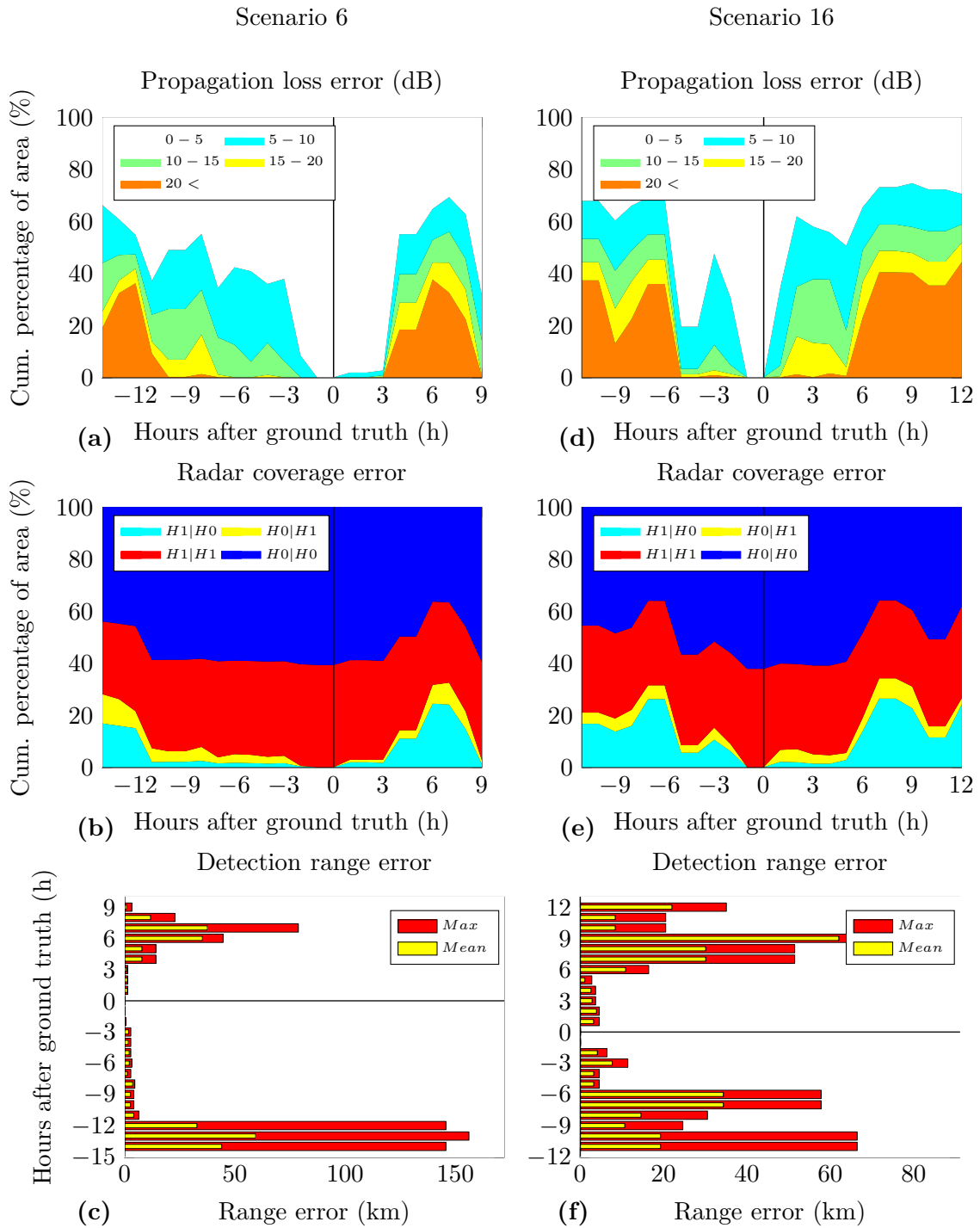


Figure 7-21: Measures of accuracy for Scenario 6 (cold weather front): propagation loss error (a), coverage error (b) and detection range error (c). Measures of accuracy for Scenario 16 (warm weather front): propagation loss error (a), coverage error (b) and detection range error (c). Propagation loss errors are in decibel.

the area for which coverage is predicted falsely was 46%, and the mean and max detection range errors were respectively 93 and 166 km.

Clearly, measuring the atmosphere every 24 hours, as the RNLN does, is not enough. It is recommended that in cases such as Scenario 18 a temporal resolution of at least one hour is used. However, in this thesis the problem of determining when high temporal resolution is required has not been solved. As discussed above, in cases where a single profile is sufficient for radar performance assessments it does not necessarily follow that temporal resolution requirements can be lax. It is therefore, for now, recommended to always use one hour temporal resolution when assessing radar performance.

7-3 General discussion

The above results show that resolution requirements, both horizontal and temporal, are highly dependent on the prevailing weather conditions and how these change over time. When considering horizontal resolution, the measures of accuracy show that in cases of warm dry air advection, high pressure systems and calm conditions, the accuracy of the performance assessment is generally highly sensitive to resolution. By using the measures of accuracy shown above the required resolution for achieving a specific accuracy can be determined.

It must be noted that the errors analysed in this thesis are not true errors as they are not relative to real propagation measurements but instead to a ground truth which is defined as the performance prediction based on HARMONIE data with a horizontal resolution of approximately 2.5 km. Hence, the true error may differ from the errors derived in this thesis as a result of:

1. inaccuracy of the propagation, radar and target model used in AREPS;
2. atmospheric data values obtained from the NWP system HARMONIE differing from the actual values of the atmosphere;
3. errors due to the limited spatial resolution of HARMONIE data which may accurately represent the actual atmosphere;
4. errors as a result of the used environment model, including the evaporation duct model, and blending techniques as developed in Chapter 5.

While the results above may be inappropriate for determining the actual accuracy for any specific assessment, it does show that the accuracy is sensitive to the horizontal grid resolution and that a single profile does not always suffice. In the cases where a single profile does not suffice, an assessment based on a single profile can have dramatic consequences. It is therefore recommended to the RNLN and others to not use a single profile in atmospheres where lateral homogeneity cannot be assumed. Depending on the required accuracy and weather conditions, the resolution of the 3D atmospheric (NWP) data can be relaxed to resolutions coarser than 2.5 km. This said, in the absence general and dependable minimal resolution requirements it is prudent to use 2.5 km or finer resolution atmospheric data always.

In this thesis it was shown that for scenarios considering cold fronts, warm fronts and warm sectors that a single profile sufficed. Note that, as with all results, including the results of cases where a single profile sufficed, the conclusions are not conclusive as they are based on

a limited set of scenarios. Furthermore, the results may not apply to weather conditions other than those that are similar to the conditions above the North Sea, to different radar parameters (e.g. frequency and height) and to different target parameters. In other words, for e.g. a 10 GHz (X-band) radar, a single profile may not suffice near cold weather fronts while it does for 3.3 GHz (S-band) radar.

The same applies for temporal resolution. In the results shown above it is clear that a single measurement of the atmosphere every 24 hours is in most cases insufficient for accurate radar assessments, even in those cases where a single profile suffices and lateral homogeneity can be assumed. It is recommended to refresh atmospheric data every hour.

Conclusions and recommendations

Radio detection and ranging systems (radars) are of great importance for naval operations as they are the primary sensors for detection, tracking and sometimes classification of friendly and hostile targets. These sensors are essential for creating the operational picture of the surroundings which is the foundation of situational awareness (SA). Because radar systems are so important, it is highly beneficial, if not essential, to have knowledge of their performance and coverage under the prevailing circumstances.

The propagation medium can significantly influence radar performance and coverage. Especially the refraction of electromagnetic energy¹ as a result of change of tropospheric refractivity along the wave's propagation path, can have a significant impact on radar performance and coverage. Under certain weather conditions radar performance and coverage can significantly differ from standard as, for example, ducts and skipping zones form. While little can be done to prevent these effects, awareness of these phenomena is of great importance to e.g. achieving sound SA. Ignorance of these propagation effects may cause uncertainty and confusion and lead to unexpected missed detections and avoidable counter detections².

Besides disadvantages, environmental conditions and their effects also carry operational advantages. A surface duct, for example, can be exploited to detect low flying targets like incoming sea-skimming missiles at extended ranges, far beyond the horizon. An attack aircraft can use knowledge of environmental effects on radar performance to penetrate the enemy's surveillance radar by flying in the radar hole just above a surface duct (see Fig. 3-13). For more examples of the importance and benefits of knowing real time radar performance and coverage see Sections 1-1 and 3-3.

Over the years, propagation models have matured to the point that propagation losses can be predicted with an accuracy of 5 dB for ranges up to 75 km. Especially propagation models based on the parabolic equation method yield very accurate results, even in complex environments. Since the 1980's propagation models have been embedded in tactical decision

¹Radars typically operate within the microwave-domain (300 MHz - 300 GHz).

²Counter detection is the detection of deployed radar systems by (passive) electronic support measures (ESM).

aids (TDAs), allowing the operational user to assess radar performance and coverage near real time and to mitigate and exploit atmospheric propagation effects, whenever the prevailing atmospheric conditions are known. A well-known, robust and accurate TDA is the Advanced Refractive Effects Predictions System (AREPS) developed by the Space and Naval Warfare Systems Command (SPAWAR). The Royal Netherlands Navy (RNLN) currently uses AREPS for radar performance assessment, in combination with the Computer-Aided Radar Performance Evaluation Tool (CARPET) from the Netherlands Organisation for Applied Scientific Research (TNO).

With the successful development of accurate propagation models, the challenge has shifted to obtaining adequate in situ atmospheric data as input to the propagation model. This is because the accuracy of performance prediction is highly depended on how well the input data accurately reflects the prevailing atmosphere.

For accurate radar performance prediction the refractivity along the propagation path must be known sufficiently well. In 86% of the cases (generally over the open ocean) the atmosphere can be assumed lateral homogeneous, which allows the use of a single vertical refractivity profile for accurate radar performance assessment [9]. The vertical profile can be determined by deploying e.g. a radiosonde that measures temperature, humidity and pressure along its ascend. Using the refractivity equation from Smith and Weintraub (see Section 5-1) the refractivity can be computed from these radiosonde measurements.

In coastal waters, where the atmosphere is generally more dynamic and complex, a single profile may not suffice. As shown in this thesis, using a single profile for radar assessment may even result in dramatic consequences. For example, an assessment based on a single profile may indicate detection ranges far beyond the horizon due to a duct which extends along the entire propagation path while, in reality, the duct disappears at some distance before the horizon, resulting in smaller detection ranges.

In cases where a single profile does not suffice, two dimensional (2D) or three dimensional (3D) refractivity data along the propagation path is required. The minimum required resolution of the refractivity data depends on the prevailing weather conditions, radar and target system parameters as well as the required radar assessment accuracy for the specific radar application.

Obtaining in situ refractivity data is challenged by logistic and/or technical limitations. Potential solutions for obtaining range- and azimuth-dependent vertical refractivity profiles include frequent flights by manned or unmanned aircraft equipped with atmospheric sensors or dropsondes, and 3D remote sensing techniques. Another approach, which is currently adopted by several navies around the world — but not (until now) by the RNLN, is to use numerical weather prediction (NWP) systems. However, NWP data files are notoriously large, which hinders or precludes their transmission to the navy vessel requiring the atmospheric data. For both methods of obtaining atmospheric data it is important to determine the minimum resolution which is required for accurate radar performance assessment. For in situ measurements it is important to establish the minimum resolution, as it is particularly difficult to acquire 3D in situ atmospheric data. For the use of NWP data, reducing the data resolution as much as possible is preferable for transmission purposes. Above consideration yielded the question:

what is the minimal required horizontal grid and temporal atmospheric data resolution to assess radar coverage with sufficient accuracy, under specific environmental conditions?

Answering this question conclusively is beyond the scope of this thesis. However, three goals were set to make a beginning to give a "partial answer" and to provide the RNLN with knowledge and recommendations concerning radar propagation through a range- and azimuth-dependent inhomogeneous atmosphere. These three goals, in which the second goal is the main goal, are the following.

1. To reach a better understanding of the mechanisms by which microwaves propagate through the (inhomogeneous) troposphere³, of how these mechanisms determine radar performance/coverage, of electromagnetic propagation models and of the atmospheric data that is required for radar performance assessment. This goal includes providing clear and understandable documentation on the above listed topics and on the findings of this study.
2. To examine the sensitivity of radar performance assessment accuracy to the horizontal and temporal resolution of input data for different weather conditions over the North Sea, as well as the error as a result of assuming the atmosphere to be laterally homogeneous and using a single refractivity profile for radar performance assessment. Note that vertical resolution is not investigated as obtaining data with sufficient vertical resolution is less problematic.
3. To advise the RNLN on the use of radar propagation models which are facilitated by NWP systems for the assessment of radar performance in an inhomogeneous atmosphere, and on further research.

How these goals were achieved and what was discovered is summarised in the subsections below (Sections 8-1-1 to 8-1-3). The question of the minimal required resolution will also be discussed. In the second section of this chapter, Section 8-2, recommendations will be presented.

8-1 Conclusions

8-1-1 Goal 1 - reaching an understanding and providing documentation

The first goal of reaching an understanding of radar propagation⁴ and the modelling of radar propagation through an inhomogeneous atmosphere, was achieved through extensive literature research. Achieving this goal was necessary to gain general knowledge of the importance and the fundamental topics of modelling radar performance in an azimuth- and range-dependent environment, and — most importantly — to acquire the tools required for developing an environmental model suitable for computing radar performance assessments. The acquired knowledge is summarised below.

In Chapter 2, all propagation mechanisms that affect radar waves propagating through the troposphere were discussed, including how they can be modelled in normal atmospheric con-

³In this thesis only propagation through the troposphere is discussed. The troposphere has the most impact on microwave propagation (frequency band: 300 MHz - 300 GHz).

⁴As in many literary sources, "radar propagation" stands for the propagation of radio/microwaves (300 MHz - 300 GHz) through the atmosphere; it does not portray an actual radar system propagating over the earth's surface.

ditions. Radar waves propagating through the troposphere spread, refract, reflect, diverge, interfere, diffract, scatter and are attenuated.

In Chapter 3, the combined effects of the propagation mechanisms were discussed. It was clearly shown that refraction can significantly alter radar performance and coverage. In cases where the refractive index decreases with height more rapidly than under normal conditions, tropospheric ducts may develop, resulting in extended (and elsewhere reduced) detection ranges at specific altitudes. On the other hand, an increase of the refractivity sub-refraction will always result in reduced detection ranges. The alteration in coverage yields tactical disadvantages and advantages as discussed above and in Section 3-3.

The effects of lateral inhomogeneity, where the refractivity is dependent on range and azimuth as well as on height, were also discussed in Chapter 3. Refractivity data with insufficient horizontal resolution, with the extreme case of a single profile, can result in erroneous radar performance assessments.

The methods of modelling radar propagation were evaluated in Chapter 4: the geometric optics method, the mode theory method and the parabolic equation method. The parabolic equation method is generally the preferred method as it is robust and provides accurate results before, on and beyond the radar horizon, even in complex range- and azimuth dependent environments. The disadvantage of the parabolic equation method is that it demands large computational resources. This is overcome by combining the parabolic equation method with other methods, leveraging the strengths of each method. For example the Advanced Propagation Model (APM) integrated in the TDA AREPS is a propagation model that combines the parabolic equation method with the geometric optics method.

In Chapter 5 the methods of acquiring 3D atmospheric data were discussed, as well as methods for modelling (range-dependent) vertical profiles that are suitable for AREPS. Currently the only way to obtain multiple upper vertical refractivity profiles that is operationally realistic, is through the use of NWP systems. While radar performance assessments based on NWP data are not exact, the assessment results are sufficiently accurate to provide a useful indication of radar performance under the prevailing weather conditions, and can thereby e.g. significantly increase the situational awareness on board.

The lower profile, also known as the evaporation duct profile, must be modelled as opposed to measured, because measurement of the lower profile is challenging. While there are various ways of modelling the lower profile, Monin-Obukhov similarity theory (MOST) is the most widely used. In Chapter 5 different MOST based models were implemented and compared. In many cases the resulting profiles of the different models were similar, the results diverged more under stable conditions.

Once the upper and lower refractivity profiles were acquired, they needed to be blended realistically such that the transition between the profiles was smooth and continuous, that no blending artifacts were introduced and that salient features were not distorted. While blending the profiles is important for obtaining accurate radar performance assessments, it is a relatively new topic for which there is currently little literature/research available. It is therefore recommended to research the blending of profiles further. For this study a new blending algorithm was developed, which shall be discussed further under Goal 2 in Section 8-1-2.

The first goal also includes the production of clear and understandable documentation on

radar propagation through an inhomogeneous atmosphere and providing it to the RNLN. This was achieved by documenting a selection of the reviewed literature (Chapters 1-5), the developed environmental model (Chapter 5) and the discoveries made while researching the accuracy sensitivity to atmospheric data resolution (Chapters 6 and 7, see also Section 8-1-2). It was attempted to write in a way that makes it suitable as a general overview of, or an introduction to, radar propagation and performance modelling for educational purposes within e.g. the Netherlands Defence Academy (NLDA). It can also be used to identify topics for further research. For example, Bruin [59] is currently researching⁵ how North Sea weather conditions affect detection ranges of automatic identification systems (AISs) and coastal radar systems (X-band). Bruin is using some of the same NWP HARMONIE (Hirlam Aladin research on mesoscale operational NWP in Euromed) data that was used within this study. He is also using the MATLAB scripts developed for this study to import HARMONIE data into AREPS and to export AREPS results into MATLAB for further analysis.

8-1-2 Goal 2 - accuracy sensitivity to input data resolution

The second goal, which was the main goal of this thesis, was achieved by comparing "ground truths" with radar performance assessments based on reduced resolution atmospheric data (referred to as "spoiled" assessments as is often done in similar studies (e.g. [4])). In this thesis the ground truth was taken to be the radar performance assessment computed by AREPS using the environment model discussed in Chapter 5 with NWP HARMONIE data at the highest resolution (2.5 km) as input. Hence the ground truth is not an actual truth. Therefore the errors found when comparing the ground truth to the spoiled assessment are not actual errors. Nonetheless, the defined ground truth is suitable for use in an accuracy sensitivity study, as it does realistically represent radar performance under the prevailing conditions.

The horizontal resolution of the HARMONIE data was reduced from 5 to 50 km in steps of 2.5 km. The assessments were primarily compared using measures of accuracy concerning radar coverage⁶ and maximum detection ranges. These measures are of particular relevance to military users in operational scenarios. The third measure of accuracy considered propagation losses. Besides comparing the ground truth to assessments based on reduced resolution data, the ground truth was also compared to the radar assessment based on a single profile and a standard atmosphere.

Before computing the needed ground truths and spoiled performance assessments, the atmospheric data provided by the NWP system HARMONIE, needed to be made suitable for accurate radar performance assessment. For this the lower vertical profiles needed to be computed⁷ and blended into the upper profiles obtained from the HARMONIE data. As mentioned there is yet little literature/research available on blending. Therefore, for this study, a new blending algorithm was developed for blending the upper and lower modified

⁵The study takes place at the Knowledge, Innovation, eXperimentation and Simulation (KIXS) centre of the Dutch Armed Forces under the supervision of dr. A.V. van Leijen.

⁶Radar coverage is for the purpose of this thesis defined as the area where the probability of detection is 0.95 or higher with a false alarm probability of 10^{-6} .

⁷The model used for computing the lower refractivity profiles is based on MOST and uses the similarity functions of the Naval Postgraduate School (NPS). The algorithm of this model can be found in Appendix C and was implemented by the author of this thesis.

refractivity profiles. The algorithm was specifically designed for blending profiles for North Sea conditions that are based on HARMONIE NWP data. The algorithm uses one of three different methods to blend the profiles together. These methods employ an alpha (α) filter, a third degree polynomial and a fourth degree polynomial respectively (see Section 5-2-3). The method used, together with its blending interval, depends on several characteristics of the upper and lower modified refractivity profiles. The most appropriate method for a set of profiles was determined by analysing a large amount of cases and visual determination of which method best achieved the blending goals. The resulting algorithm provides realistic blended profiles under prevailing conditions. It must be noted that the algorithm is not yet validated and therefore it is not ready for operational use. This said, because the produced profiles are realistic, the algorithm can be used for analysing the accuracy sensitivity to input data resolution and provides a good basis for further research. For the complete environmental model used in this thesis see Chapter 5. Besides blending the upper and lower refractivity profiles together the environmental model also interpolates vertical profiles between grid points.

In total forty-one scenarios were considered in this study. The weather conditions varied between cold weather fronts (8x), warm weather fronts (8x), a warm sector, advection of relatively warm dry air over water, high pressure systems and calm standard weather. Besides differing in weather conditions the scenarios differed in ship position and radar azimuth. For all scenarios the radar considered was a generic 3.3 GHz medium range surveillance radar positioned 20 m above sea level, which is a representative height for many ship borne surveillance radars. For all scenarios a small fighter with a radar cross section (RCS) of 2 m² was used as a target.

In this thesis it was found that in all considered scenarios near a weather front or in a warm sector⁸, a single vertical modified refractivity profile suffices for accurate radar performance assessment. Hence, under these conditions 3D atmospheric data, e.g. HARMONIE data is not required. This discovery contradicts many literature sources that state that 3D data is generally required in coastal environments and near weather fronts. However, the above conclusion is based on only eight cold front scenarios, eight warm front scenarios and one warm sector. It may be that 3D data is required for stronger developed fronts with a more varied troposphere. Or 3D data may be required for scenarios in which the radar parameters differ, e.g. frequency, or in which other targets are to be detected. Note also that all scenarios considered are based on North Sea conditions (or similar). Results may differ in other regions, e.g. near the equator where the evaporation duct is generally much stronger developed. These limitative considerations apply of course to most results and conclusions of this thesis that are based on the limited number of scenarios that were examined.

In some weather front or warm sector scenarios 3D atmospheric data was required for predicting propagation losses. These results are relevant for e.g. communication performance prediction. For all scenarios considered, prediction of propagation losses required higher resolution data than prediction of coverage and detection ranges.

In the scenarios where warm dry air advected over water and in scenarios near high pressure systems, 3D atmospheric data was required for most cases⁹ to accurately predict radar performance. What resolution is required depends on the required accuracy and can be de-

⁸Note, only a single warm sector scenario was examined in this study.

⁹Eight out of nine advection scenarios required 3D atmospheric data for accurate radar performance prediction; seven out of eight high pressure system scenarios required 3D atmospheric data.

terminated using the measures of accuracy found in Chapter 7: higher accuracy requires higher resolution data. The relationship between accuracy and resolution is highly dependent on the local prevailing weather conditions. Nonetheless, it is shown that use of a single profile where 3D data is required, yields erroneous assessments with a potential for dramatic operational consequences.

Comparing the results of the advection and high pressure systems scenarios to the results of the scenarios considering weather fronts, showed that when the single profile contains no trapping features a single profile is most likely to suffice, while 3D data is generally required when the profile does contain a trapping layer. This feature can be used to assess whether e.g. 3D HARMONIE data may be required. However, it cannot be concluded that this is always the case; for more general conclusions more scenarios, both similar and different, should be examined (see also Section 8-1-4).

Seven scenarios where the weather was calm were examined. From the weather charts it was expected that the conditions would result in normal propagation and that a single profile should suffice to accurately assess radar coverage. It appeared however, that in two out of the seven scenarios a single profile did not suffice because significant ducting occurred. From this it is clear that propagation and radar performance cannot be directly deduced from mere observation of weather charts.

At the end of Section 7-1 errors were averaged. Figure 7-19 clearly shows that the overall accuracy of the radar performance assessment is very sensitive to horizontal data resolution when a single profile does not suffice. Figure 7-19 also shows that a single profile should only be used if a single profile suffices. Whether this is the case, can only be determined with 3D dimensional data. In other words, to avoid unexpected erroneous assessments 3D atmospheric data is always required. On average, using a single profile will result in performance assessments with a predicted coverage area in error of approximately 10% and a predicted detection range error of approximately 20 km.

For temporal resolution it was shown that in some scenarios a resolution of 24 hours sufficed while in other scenarios a temporal resolution of one hour or less was required. Which resolution is required under which condition could not be determined, as the results varied significant under similar conditions. It is therefore, for now, recommended to always use one hour temporal resolution when assessing radar performance. Note however, as could be expected, temporal resolution can generally be coarser when a single profile suffices: temporal and spatial resolution requirements are broadly linked¹⁰.

8-1-3 Goal 3 - providing recommendations

Pursuit of the third goal of advising the RNLN on the use of radar propagation models yielded insights that are described as conclusions here and that led to the recommendations in the following section. As mentioned, currently the RNLN uses a single profile for radar performance assessments. It was clearly shown that the use of a single profile, in other words assuming that the atmosphere is horizontally homogeneous, can yield erroneous radar performance predictions and lead to dramatic operational consequences when the assumption of homogeneity

¹⁰A relationship between temporal and spatial resolution requirements is to be expected as spatial inhomogeneity naturally induces temporal change.

is actually false. For example¹¹, a single profile based assessment may yield a maximum detection range exceeding 200 km at a certain height, while in truth the detection range at that height is limited to a mere 40 km. Such erroneous analysis of the radar performance results in false situational awareness and can lead to confusion on board. It is therefore recommended to start using 3D atmospheric data for radar performance assessments. As measuring 3D atmospheric data is still logistically and technologically difficult it is recommended to use mesoscale NWP data. Because NWP data does not represent the atmosphere perfectly, it is also recommended to continue the deployment of balloon radiosondes and use both the NWP data and the measured profile for radar performance assessment. The measured in situ profile can also be used to validate the NWP data by comparing the measured profile with the corresponding profile computed by the NWP system. It is however recommended that the comparison is done by a meteorologist or someone who is experienced in the field of anomalous radar propagation. Also, it is expected that in the near future NWP systems will incorporate in situ measurement results to improve the computed atmospheric prediction accuracy.

Because no minimum resolution requirement for 3D data is yet determined, it is recommended that in azimuth- and range-dependent atmospheres, the maximum horizontal grid (2.5 km) and temporal (1 hour) resolution of HARMONIE is used. This regardless of the complications of transmitting large HARMONIE data files by satellite to His Majesties ships of the RNLN¹². Because there is currently no dependable method for determining when 3D atmospheric data is required as opposed to a single profile, it is also recommended to always use HARMONIE data whenever accurate radar performance assessment is required.

8-1-4 Minimum resolution requirements

The determination of a general minimal requirement for the horizontal grid resolution and temporal resolution of atmospheric data that is necessary to assess radar coverage with sufficient accuracy, given specific environmental conditions, lies beyond the scope of this thesis. First of all, in Chapter 7 it was shown that resolution requirements may vary significantly, even under similar weather conditions. Secondly, to arrive at general conclusions more scenarios must be considered. And lastly the results presented in Chapter 7 are specific to a generic 3.3 GHz medium range surveillance radar and a small fighter as target. Changing for example the operating frequency of the radar, or the radar cross section of the target, may have a significant impact on the resolution requirement.

It must also be noted that the resolution requirement depends on the radar's application and the required (measures of) accuracy. For example, if the goal is to determine the position of a target for fire control purposes, the measure of accuracy must reflect target position accuracy in addition to coverage accuracy (e.g. altitude error, see Section 3-3), which will lead to higher resolution requirements.

While the question of a minimum resolution requirement is not decisively answered in this thesis, much was accomplished. The three goals of this thesis as set in the introduction have been achieved to a significant extent. Still, there is much yet to be discovered.

¹¹Such an example was provided in Figure 7-9 (b).

¹²The use of appropriate data reduction techniques to reduce file size can partially help overcome the complications of transmitting large NWP files by satellite.

8-1-5 Summary

As mentioned in the introduction (Section 1-5), this thesis is larger than master theses generally are. This is mostly driven by the aim that this thesis should provide a comprehensive overview of topics concerning radar propagation and performance modelling in an inhomogeneous atmosphere, so that it can be used for educational purposes and/or as introduction to further research. Additionally, this study covers much that is new, academically or practically, or both. The following is, to the knowledge of the author of this thesis, new. If not entirely than at least to a certain extend.

- A new comparison of evaporation duct models LKB, NPS, NWA, NRL, BYC and the model integrated in AREPS.
- A new implementation of a MOST based evaporation duct model that uses the similarity functions from the evaporation duct models LKB, NPS, NWA, NRL en BYC. The implementation is written in MATLAB and provided in Appendix C.
- A new blending algorithm which blends upper and lower refractivity profiles together in the modified refractivity domain.
- The first time HARMONIE data is used for radar performance assessment as well as the first time HARMONIE data is used to run AREPS.
- A new method for investigating assessment accuracy sensitivity to resolution, including new measures of accuracy to consider.
- A new way of showing how important three dimensional data is for accurate radar performance assessment and how erroneous single profile assessments can be.
- A new sense of how sensitive assessment accuracy is to the horizontal and temporal resolution of atmospheric data under different prevailing weather conditions.
- The first study concerning radar performance in inhomogenous atmospheres above the North Sea.
- New recommendations for the RNLN concerning radar performance assessments in inhomogenous atmospheres.

8-2 Recommendations

This section consist of two subsections. The first subsection gives recommendations for further research while the second subsection gives recommendations for the RNLN. This said, some recommendations of the first subsection also apply to the second subsection and vice versa.

8-2-1 Recommended further research

In this thesis an environmental model suitable for radar performance assessment was developed (see Chapter 5). In this model profiles are interpolated between grid points and upper and lower profiles are blended together. Even though incorrect environmental models can yield erroneous assessments, there is currently little knowledge on how e.g. the profiles can best be interpolated and blended. The models that do exist are loosely validated, as validation is difficult and expensive. The model developed in this thesis is also not validated.

It is recommended that further research be carried out on methods of modelling the atmosphere for accurate radar performance assessment. Especially interpolation schemes and blending techniques should be researched, for example methods that achieve blending in the physical domain. Besides the development of new methods/models, existing methods and models should be validated.

The accuracy of radar assessment is highly dependent on the accuracy of the evaporation duct model. In Chapter 5 different models were implemented and compared. Under unstable atmospheric conditions all models showed similar results, but model output varied significantly for stable conditions. It is therefore recommended to further develop and validate evaporation duct models.

This study covers the preliminary steps into an enquiry of atmospheric data requirements for accurate radar assessment. The "main" question concerning the minimum required horizontal and temporal resolution is yet far from answered and therefore further research is recommended. The analysis of more and better defined scenarios, with the use of different measures of accuracy including statistical measures, for other radar (e.g. frequency) and target parameters will be an other significant step towards acquiring general atmospheric data requirements such as resolution requirements. An analysis of the accuracy sensitivity to vertical resolution in different conditions is an other topic to consider researching. It is recommendable to also perform a similar study with regard to communication systems.

As mentioned, this study was the first to use HARMONIE NWP data for radar performance assessment. Whether HARMONIE data is sufficient for this purpose, however, has not yet been determined. It is therefore recommended to validate the use of HARMONIE data for radar assessment. Also, the HARMONIE model itself may be improved to better facilitate radar propagation models, e.g. by using in situ measured data to improve NWP data.

8-2-2 Recommendations for the Royal Netherlands Navy

First of all, as mentioned above, it is recommended to the RNLN to start using NWP data for radar performance assessment, especially in coastal environments where the atmosphere is azimuth and range-dependent. Falsely assuming lateral homogeneity may yield erroneous radar performance assessments. Note that it is therefore also recommended to rely less on CARPET¹³ in these environments, as CARPET assumes lateral homogeneity, it cannot predict radar performance in complex environments.

Secondly, the RNLN should determine what assessment accuracy is required for specific operational scenarios. For example, under the threat of incoming fighters higher radar performance assessment accuracy is required than under transit conditions. But what accuracy suffices when? This must first be determined before minimum resolution requirements can be determined.

Thirdly, the RNLN should look into other possible applications provided by radar propagation models; other than that of determining radar performance and coverage. For example, if the assessments are sufficiently accurate, radar propagation assessments can be used to tune sensor systems to enhance performance and exploit and mitigate environmental effects. For

¹³CARPET is integrated into the combat management system (CMS) of His Netherlands Majesty's (HNLM) naval ships and is currently the primary TDA for radar performance assessment in the RNLN.

example, to tune frequency and phase shifts in broad band active phased array radars to allow detection in specific regions that would otherwise not be covered. Or, when the assessments are sufficiently accurate, these can be used to reduce target position errors that are a result of anomalous propagation (see Section 3-3-3). Both ideas, to use radar assessments for tuning radar parameters and to use radar assessments to reduce target position errors, are definitely new to the RNLN and likely to many navies around the world.

Lastly, the RNLN should further investigate how NWP data can be used for naval applications other than radar performance assessment. For weather prediction, for example, but also for performance assessment of electrical optical and infra-red systems or for improving weapon accuracy. Weapon accuracy can be improved by using prevailing atmospheric data to estimate, for example, the ballistic trajectory of naval gun fire¹⁴.

¹⁴Weapon accuracy can be improved also by determining the target's position more accurately as discussed above.

Chapter 9

Operational advice for the Royal Netherlands Navy

This chapter discusses several shortcomings in the way the Royal Netherlands Navy (RNLN) currently operates with regard to radar performance assessment in inhomogeneous atmospheres. It subsequently discusses what steps can be taken, in the author's opinion, to eliminate these flaws and hence improve the overall accuracy of radar performance assessment on board His Netherlands Majesty's (HNLN) naval ships.

Governed by current disclosure policies, this chapter is excluded from this general publication of the thesis. To obtain the chapter, please contact either the author or one of the following supervisors of this thesis: dr. A.V. van Leijen at the Knowledge, Innovation, eXperimentation and Simulation (KIXS) center of the Dutch Armed Forces or KTZ (TD) dr. ir. F. Bolderheij at the Netherlands Defence Academy (NLDA).

Appendix A

Radar assessment projections

Radar propagation and performance assessment figures can display ray traces, propagation losses and/or coverages versus range and height. The computed results can be projected either over a spherical or flat earth. Projecting the results over a spherical earth is far more intuitive than projecting the results over a flat earth. However, in certain cases it is preferable to project the results over a flat earth nonetheless, because ranges and heights can be read directly from such projection, for example. Also, most programs output results as X and Y values over a flat earth projection, which is neatly rectangular and thus easy to display both on screen and in print.

In this thesis all assessment figures project computed results over a flat earth. A downside is that flat earth projections are easily misinterpreted by readers who are inexperienced in interpreting these figures. Perhaps the most confusing aspect is that electromagnetic energy that is shown to curve away from the earth in a flat earth projection may actually curve towards the round earth, albeit at a larger radius than the earth surface and consequently away from the surface. To aid correct interpretation, this aspect is clarified below, by the use of two examples.

For each example, six figures show ray traces, propagation losses and coverages over both a flat earth on the left and a spherical earth on the right hand side. The images are screen shots of results computed by the programs MIRAT¹ [20] and AREPS² [2].

The first example considers a standard atmosphere. As mentioned in Chapters 2 and 3, in a standard atmosphere electromagnetic energy will curve slightly towards the earth which is visible in (d - f) of Fig. A-1. Note however that whilst the energy curves towards the earth it still propagates away from the earth's surface as the surface curves stronger than the energy.

In projecting results over a flat the distance between the earth's surface and the energy must be shown correctly. As the earth is flattened, energy that propagates away from the earth surface is displayed as curving upward, i.e. away from the earth, while in actuality, it may

¹Microwave ray tracing (MIRAT) is a ray tracing propagation program developed by the author of this thesis [20].

²Advanced Refractive Effects Predictions System (AREPS).

still curve down into the direction of the earth (see Fig. A-1 (a - b)). Note that between Fig. A-1(b) and (e) the distance between the propagating energy and the earth's surface is the same at any range.

Figure A-2 gives another example. This time the atmospheric conditions are that of a surface-based duct.

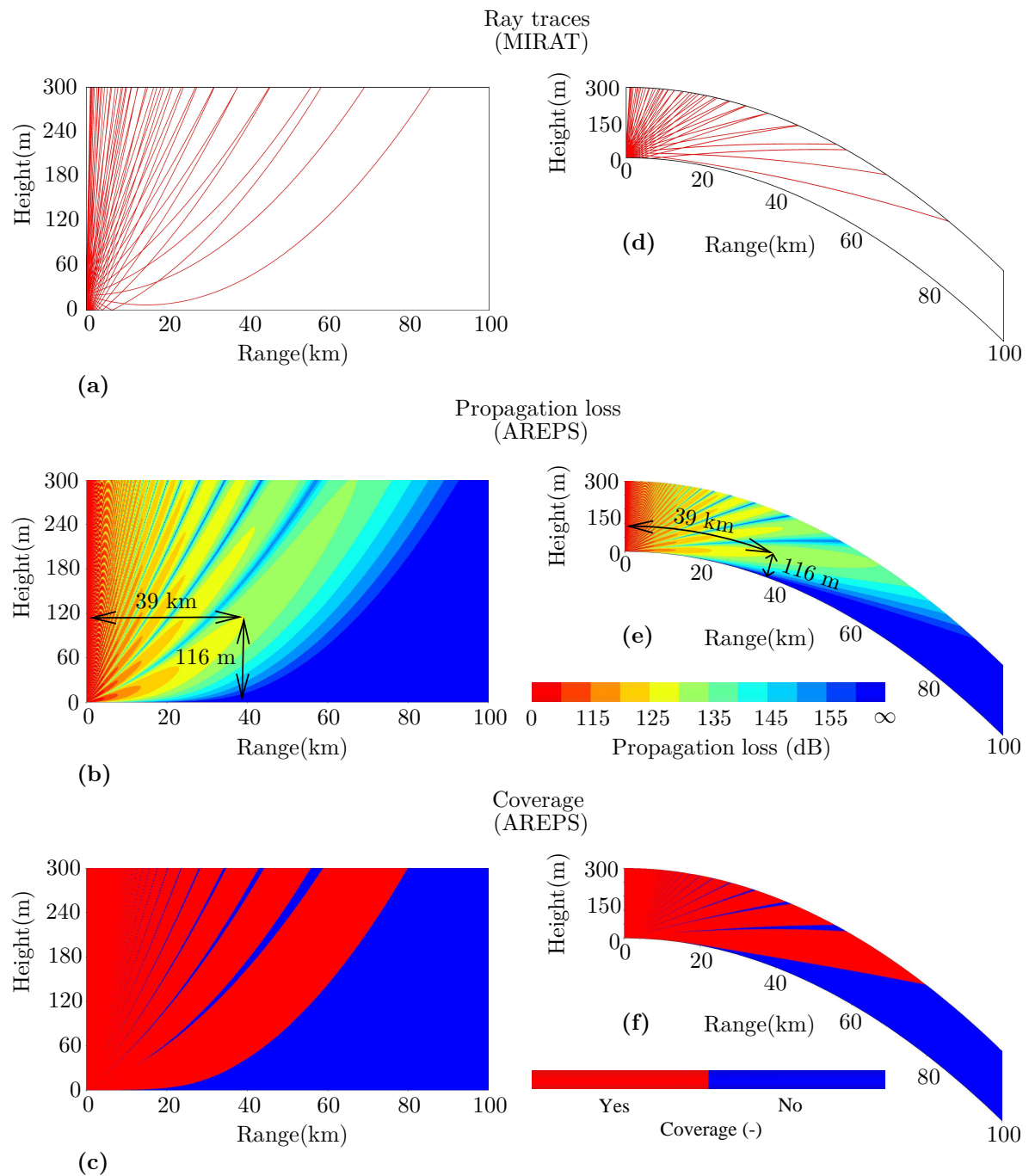


Figure A-1: Radar performance assessments for a standard atmosphere projected above a flat earth (a - c) and a spherical earth (d - e). The ray traces (a & d) are computed using MIRAT [20]. The propagation loss assessment (b & e) and the coverage assessment (c & f) are computed using AREPS [2].

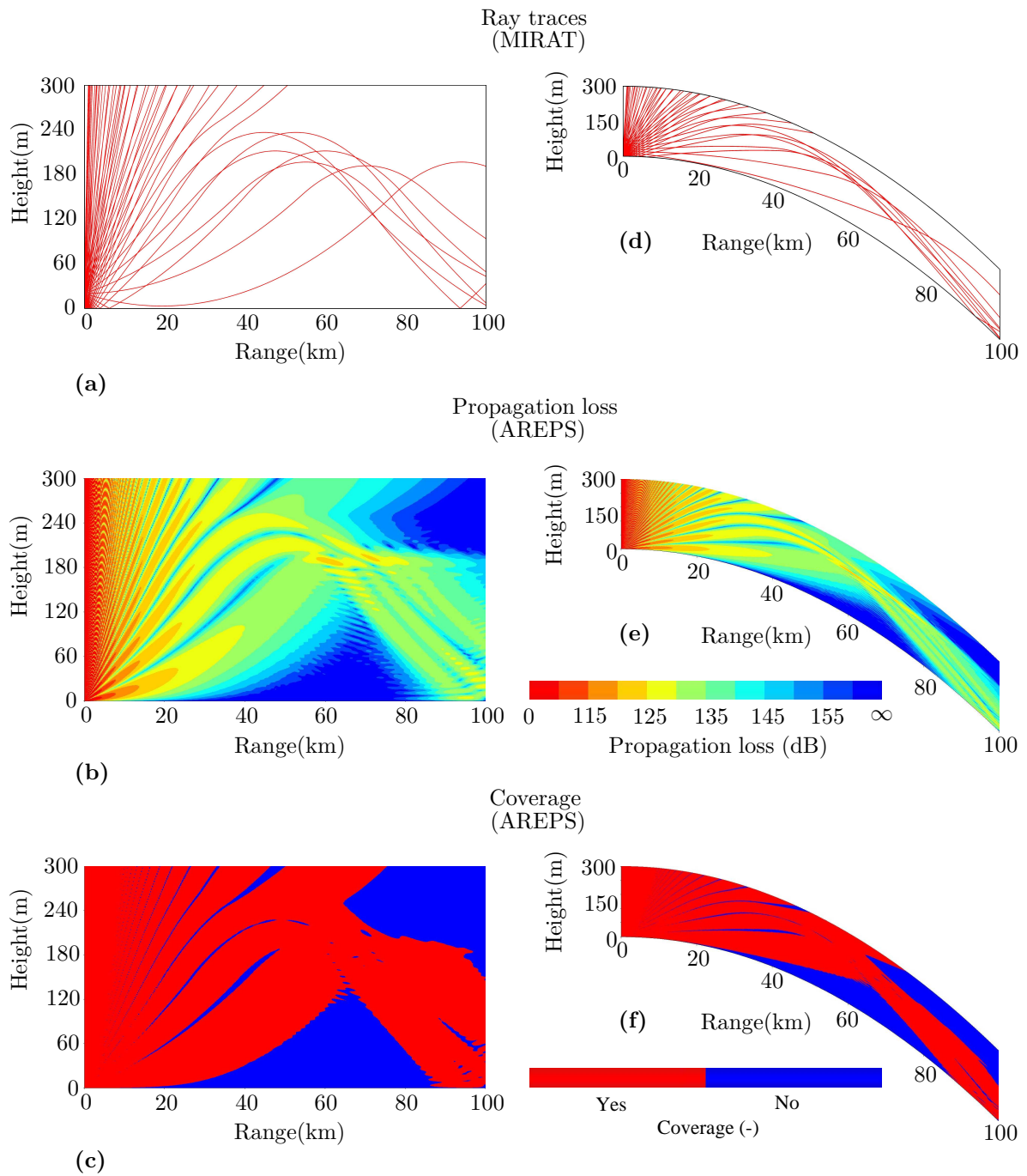


Figure A-2: Radar performance assessments for a surface-based duct projected above a flat earth (a - c) and a spherical earth (d - e). The ray traces (a & d) are computed using MIRAT [20]. The propagation loss assessment (b & e) and the coverage assessment (c & f) are computed using AREPS [2].

Appendix B

Similarity functions

Over the years researchers have derived several sets of similarity functions $\psi(\zeta)$ (with $\zeta = z/L$, where z is the altitude and L the Monin Obukhov length) or their integral representation $\Psi(\zeta)$ based on specifically organised experiments. This appendix lists five sets of similarity functions in integral form ($\Psi(\zeta)$) which are used in different evaporation duct models:

- The model developed by Liu, Katsaros and Businger (LKB)(1979) [51],
- The Naval Warfare Assessment station in Corona (NWA) model developed by Liu and Blanc (1984) [53],
- The Naval Research Lab (NRL) model developed by Cook (1991) [53],
- The model developed by Babin, Young and Carton (BYC) (1996) [53],
- The Naval Postgraduate School (NPS) model developed by Frederickson, Davidson and Goroeh (2000) [53],

All sets of similarity functions have been implemented in the evaporation duct model discussed in Section 5-2-2 using Matrix Laboratory (MATLAB) 2013b. The MATLAB script can be found in Appendix C. Results of the model are shown in Section 5-2-2. For more information on these similarity functions refer to [51, 53].

B-1 The LKB similarity functions

Probably the most widely used model is the model developed by Liu, Katsaros and Businger (LKB); many models developed later are based on the LKB model. The wind similarity function in integral form for unstable ($\zeta < 0$) and stable conditions ($\zeta > 0$) is equal to:

$$\Psi_u(\zeta) = \begin{cases} 2 \ln\left(\frac{1+x}{2}\right) + \ln\left(\frac{1+x^2}{2}\right) - 2 \arctan(x) + \frac{\pi}{2} & \text{for } \zeta \leq 0, \\ -\gamma\zeta & \text{for } \zeta > 0, \end{cases} \quad (\text{B-1})$$

where x is a auxiliary constant equal to $x = (1 - \beta\zeta)^{1/4}$. The numerical constants β and γ are determined experimentally and equal to: $\beta = 16$ and $\gamma = 5$. The universal function for temperature and humidity is:

$$\Psi_h(\zeta) = \begin{cases} \ln\left(\frac{1+x^2}{2}\right) & \text{for } \zeta \leq 0, \\ -\gamma\zeta & \text{for } \zeta > 0. \end{cases} \quad (\text{B-2})$$

B-2 The NWA similarity functions

In the NWA model the wind similarity function in integral form is given by:

$$\Psi_u(\zeta) = \begin{cases} 2\ln\left(\frac{1+x}{2}\right) + \ln\left(\frac{1+x^2}{2}\right) - 2\arctan(x) + \frac{\pi}{2} & \text{for } \zeta < 0, \\ -6\ln(1+\zeta) & \text{for } \zeta \geq 0, \end{cases} \quad (\text{B-3})$$

where $x = (1 - 16\zeta)^{1/4}$. Note that the wind similarity function under unstable conditions is equal to the wind similarity function under unstable conditions of the LKB model. The universal function for temperature and humidity is:

$$\Psi_h(\zeta) = \begin{cases} \ln\left(\frac{1+x^2}{2}\right) & \text{for } \zeta < 0, \\ -6\ln(1+\zeta) & \text{for } \zeta \geq 0. \end{cases} \quad (\text{B-4})$$

Note again that the similarity function under unstable condition is the same as that of the LKB model.

B-3 The NRL similarity functions

For unstable conditions, the NRL model uses the same similarity functions (Ψ_u and Ψ_h) as the NWA model. For stable and neutral conditions ($\zeta \geq 0$):

$$\Psi_u = \Psi_h = -7\zeta. \quad (\text{B-5})$$

B-4 The BYC similarity functions

In the BYC model the wind similarity function in integral form is given by:

$$\Psi_u(\zeta) = \begin{cases} \frac{\Psi_{uk} - \zeta^2 \Psi_k}{1 + \zeta^2} & \text{for } \zeta < 0, \\ -5\zeta & \text{for } \zeta \geq 0, \end{cases} \quad (\text{B-6})$$

where

$$\begin{aligned}\Psi_{uk} &= 2 \ln \left[\frac{1 + z_{pu}}{2} \right] + \ln \left[\frac{1 + z_{pu}^2}{2} \right] - 2 \arctan(z_{pu}) + \left(\frac{\pi}{2} \right), \\ \Psi_k &= 1.5 \ln \left[\frac{z_{pg}^2 + z_{pg} + 1}{3} \right] - \sqrt{3} \arctan \left[\frac{2z_{pg} + 1}{\sqrt{3}} \right] + \left(\frac{\pi}{\sqrt{3}} \right), \\ z_{pu} &= x = (1 - 16\zeta)^{0.25},\end{aligned}\tag{B-7}$$

and

$$z_{pg} = x = (1 - 12.87\zeta)^{0.333}.\tag{B-8}$$

The universal function for temperature and humidity is the same as the function for wind except that Ψ_{tk} replaces Ψ_{uk} :

$$\Psi_{tk} = 2 \ln \left[\frac{1 + z_{pt}}{2} \right],$$

where

$$z_{pt} = x = (1 - 16\zeta)^{0.5}.$$

B-5 The NPS similarity functions

In the NPS model, for unstable conditions $\zeta < 0$, the same functions are used as the BYC model except that z_{pg} for the wind similarity function is equal to:

$$z_{pg} = (1 - 10\zeta)^{0.333}.$$

And for the temperature and humidity function equal to:

$$z_{pg} = (1 - 34\zeta)^{0.333}.$$

The wind similarity function and the temperature and humidity similarity function in integral form under stable and neutral conditions are given respectively by:

$$\Psi_u = -\zeta - \frac{2}{3} \left[\zeta - \frac{5}{0.35} \right] \exp(-0.35\zeta) - \left(\frac{2}{3} \right) \left(\frac{5}{0.35} \right),\tag{B-9}$$

and

$$\Psi_h = 1 - \left[1 + \frac{2\zeta}{3} \right]^{1.5} - \frac{2}{3} \left[\zeta - \frac{5}{0.35} \right] \exp(-0.35\zeta) - \left(\frac{2}{3} \right) \left(\frac{5}{0.35} \right).\tag{B-10}$$

Implementation of Monin-Obukhov similarity theory in MATLAB

The implementation of the similarity functions in Appendix B in a Monin-Obukhov similarity theory (MOST) based evaporation duct model is presented below. The implementation is written in Matrix Laboratory (MATLAB) 2013b. The similarity functions of the evaporation duct model developed by the Russian State Hydrometeorological University (RSHMU) and the model developed by the Centre for Oceanic Awareness, Research and Education (COARE) are also implemented (see [51]). However, these are not considered within this thesis as they frequently produced unexpected evaporation duct profiles. The unexpected profiles are most likely the result of an implementation error.

The implementation below is an adaptation of the evaporation duct model developed and used¹ by the Royal Netherlands Navy (RNLN). In reviewing the implementation of the RNLN a number of implementation errors were discovered. These errors were pointed out to the Defence Materiel Organisation (DMO) of the Dutch Armed Forces. The errors have been corrected in the implementation below.

¹The evaporation duct model developed by the RNLN is integrated into the combat management systems (CMSs) of His Netherlands Majesty's (HNLN) naval ships and is the navy's primary model used to acquire the lower refractivity profile for radar performance assessment.

```

1 function [M, z, L, dataAtm, dataStar] = getEvapProf(T_r, p_r, q_r, ...
2     u_r, T_0, z_r, varargin)
3 % getEvapProf evaluates the evaporation duct profile based on 7 different
4 % models. All models are based on Monin-Oboukhov Similarity Theory and
5 % differ only in the Universal Functions each model uses. The literature
6 % used creating this function can be found below. At the end of the main
7 % function the assumptions and uncertainties are listed. The assumptions
8 % are referenced using {} in the main function. The uncertainties are
9 % referenced using "". The equations used are referenced using []. The
10 % validation of this function has been done by comparing results with the
11 % NPS model implemented in AREPS (version 3.6) from SPAWAR. Results compare
12 % nicely in most cases.
13 %
14 % Input:      T_r      : Reference (measured) temperature in
15 %              degrees Kelvin (default) at height z_r
16 %              p_r      : Reference (measured) pressure in hPa or mBar at
17 %              height z_r
18 %              q_r      : Reference (measured) specific humidity in kg/kg
19 %              (default) at height z_r
20 %              u_r      : Reference (measured) wind velocity in m/s
21 %              (default) at height z_r
22 %              T_0      : Reference (measured) sea temperature in degrees
23 %              Kelvin
24 %              z_r      : Reference (measuring) height in metres
25 %
26 % Output      M        : Modified refractivity profile in M-Units
27 %              z        : Height vector (max 50 m) in metres
28 %              L        : Monin Obukhov length in metres
29 %              dataATM  : Data matrix consist of the pressure profile in
30 %              hPa (column 1), the temperature profile in
31 %              degrees Celsius (column 2), the relative
32 %              humidity in percentages (column 3), the partial
33 %              vapour pressure in hPa (column 4), the wind
34 %              velocity in m/s (column 5) and the specific
35 %              humidity in kg/kg (column 6)
36 %              dataStar: Data matrix containing the values of the wind
37 %              velocity scale (column 1), the potential
38 %              virtual temperature scale (column 2) and the
39 %              specific humidity scale (column 3) during the
40 %              iterations. With this the convergence can be
41 %              checked.
42 %
43 % Properties  Model    : Defines the model used: LKB [1], RSHMU [1],
44 %              COARE [1], NPS [4], NWA [4], NRL [4] and BYC
45 %              [4] (string)
46 %              TemperatureUnits : Units of T_r and T_0 'Kelvin'
47 %              (default) or 'Celsius' (string)
48 %              WindUnits       : Units of u_0 'm/s' (default)
49 %              or 'kts' (knots) (string)
50 %              Humidity        : Value of q_r 'Specific' (default)
51 %              or 'Relative' (string)
52 %
53 % Example:
54 %     T_r = 17.8;           % Air temperature (degrees Celsius)
55 %     p_r = 1018;          % Air pressure (hPa)
56 %     RH = 80;             % Relative humidity (%)
57 %     u_r = 10;           % Wind velocity (knots)

```

```

58 %     T_0 = 18;           % Sea temperature (degrees Celsius)
59 %     z_r = 6;           % Measureing height (m)
60 %     [M_NPS, z, dataAtm_NPS, dataStar_NPS] = getEvapProf(T_r, p_r, RH,...
61 %     u_r, T_0, z_r, 'Humidity','Relative','TemperatureUnits','Celsius',...
62 %     'WindUnits','kts','Model','NPS');
63 %
64 % USED LITERATURE
65 % [1] Ivanov, V. Shalyapin, V. & Levadnyi, Y.
66 %     Determination of the evaporation duct height from standard
67 %     meteorological data, Izvestiya, Atmospheric and Oceanic Physics,
68 %     Nauka/Interperiodica, 2007, 43, 36-44
69 % [2] Jacobson, M.
70 %     Fundamentals of atmospheric modeling,
71 %     Cambridge university press, 2005
72 % [3] Babin, S.; Young, G. & J.A., C.
73 %     A new model of the oceanic evaporation duct Journal of applied
74 %     meteorology, 1997, 36, 193-204
75 % [4] Babin, S. & Dockery, G.
76 %     LKB-based evaporation duct model comparison with buoy data,
77 %     Journal of applied meteorology, 2002, 401, 434-446
78 %
79 % Author      :   Joris Derksen
80 % Date        :   2 April 2014
81 % Version     :   1
82 % -----
83
84 %% Main Function -----
85
86 % SET PROPERTIES -----
87 properties = {'Model'...
88               'TemperatureUnits',...
89               'WindUnits',...
90               'Humidity'};
91
92 values.Model = 'NPS';
93 values.TemperatureUnits = 'Kelvin';
94 values.WindUnits = 'm/s';
95 values.Humidity = 'Specific';
96
97 given_property = varargin(1:2:end);
98 propertyValue = varargin(2:2:end);
99
100 % Determine used properties
101 for i=1:size(given_property, 2)
102 validInput = sum(cell2mat(strfind(properties, given_property{i})));
103
104     if validInput
105         values.(sprintf('%s',given_property{i})) = propertyValue{i};
106     end
107 end
108
109 % CONVERT INPUT TO PROPER UNITS -----
110
111 if strcmpi(values.TemperatureUnits, 'Celsius')
112 % Conversion temperature
113     T_r = T_r + 273.15;           % Converse Celsius into Kelvin
114     T_0 = T_0 + 273.15;           % Converse Celsius into Kelvin

```

```

115 end
116
117 if strcmpi(values.WindUnits, 'kts')
118 % Conversion wind velocity
119     u_r = u_r * 1852/(60*60); % Converse knots into m/s
120 end
121
122 if strcmpi(values.Humidity, 'Relative')
123 % Conversion humidity
124     p_vs_temp = 6.112*exp(6816*(1/273.15-1/T_r) + 5.1309*log(273.15/T_r));
125 % Determine the saturated vapour
126 % pressure (hPa) at height h_r
127 % [2, eq 2.61]
128     p_v_temp = q_r/100 * p_vs_temp; % Determine vapour pressure (aka e) at
129 % height h_r [2, eq 2.66]
130
131     q_r = (0.62197*p_v_temp) / (p_r - (1 - 0.62197) * p_v_temp);
132 % Conversion relative humidity (%)
133 % into specific humidity (kg/kg)
134 % [3, eq 4]
135 end
136
137
138
139 % USED CONSTANTS -----
140 Karman = 0.4; % Von Karman constant (-) [1, pg 37]
141 g = 9.80665; % Nominal average acceleration of
142 % gravity (m/s^2) [http://en.wikipedia
143 % .org/wiki/Gravity_of_Earth]
144 alpha = 0.018; % Charnock constant [1, pg 39-40]
145 v = 1.5 * 10^-5; % Dynamic viscosity of air (m^2/s)
146 % [1, pg 39]
147 eps = 0.62197; % The ratio of the individual
148 % gasconstant for dry air to that of
149 % water vapour (-) [3, pg 197] [2,
150 % pg 31]
151 k = 1.3806488 * 10^-23; % Boltzmann's constant (J/K)
152 % [http://en.wikipedia.org/wiki/
153 % Boltzmann_constant]
154 K = 0.286; % Ratio (-) of individual gasconstant for dry air
155 % to the specific heat of dry air [2, eq 2.93]
156 M_av = 4.8096*10^-26.0; % average mass of one air molecule
157
158 % PARAMETER TRANSFORMATION -----
159 Tv_r = T_r*(1+0.608*q_r); % Reference virtual temperature (K) at reference
160 % height z_r. [2, eq 2.38]
161 Theta_r = Tv_r * (1000/p_r)^K; % Reference potential virtual
162 % temperature (K) at height z_r.
163 % [2, eq 2.97]
164
165 H_r = (k*Tv_r) / (M_av*g); % Scale height (-) at height z_r.
166 % [2, eq 2.47] {1} "1"
167 p_0 = p_r*exp(-(0-z_r)/H_r); % Estimated total pressure (hPa) at
168 % height 0 [2, eq 2.48] {1} "1"
169
170 p_vs_temp = 6.112*exp(6816*(1/273.15-1/T_0) + 5.1309*log(273.15/T_0));
171 % Saturated vapour pressure (hPa) at

```

```

172                                     % height 0 [2, eq 2.61]
173 RH_0 = 98;                          % Assume a relative humidity of RH_0
174                                     % at height 0 {2}
175 p_v0 = (RH_0/100) * p_vs_temp;       % Vapour pressure (aka e) (hPa) at
176                                     % height 0. [2, eq 2.66]
177 q_0 = (eps*p_v0)/(p_0-(1-eps)*p_v0); % Specific humidity (kg/kg) at height
178                                     % 0. [3, eq 4] [2, eq 2.32]
179
180 Tv_0 = T_0*(1+0.608*q_0);            % Reference virtual temperature (K) at height 0.
181                                     % [2, eq 2.38]
182 Theta_0 = Tv_0 * (1000/p_0)^K;       % Reference potential virtual
183                                     % temperature (K) at height 0.
184                                     % [2, eq 2.97]
185
186 u_0 = 0;                              % Wind velocity (m/s) at height 0 {2}
187
188 % INITIALISATION -----
189 u_star = (u_r-u_0)*Karman / (log(z_r/0.00015)-0);
190                                     % Wind velocity scale (m) [1, eq 8]
191                                     % {2}, {3}
192 Theta_star = (Theta_r-Theta_0)*Karman / (log(z_r/0.00015)-0);
193                                     % Potential virtual temperature scale
194                                     % (m) [1, eq 9] {2}, {3}
195 q_star = (q_r-q_0)*Karman / (log(z_r/0.00015)-0);
196                                     % Specific humidity scale (m)
197                                     % [1, eq 10] {2}, {3}
198
199 % ITERATIONS -----
200 % The unknown scales u_star, Theta_star and q_star are contained through
201 % successive iterations. According to literature convergence should be
202 % reached within 50 iterations.
203
204 % If the user defines 5 outputs the fourth output will give a matrix
205 % containing the values of the wind velocity scale (column 1), the
206 % potential virtual temperature scale (column 2) and the specific humidity
207 % scale (column 3) during the iterations. With this the convergence can be
208 % checked.
209 if nargout > 4
210     dataStar = zeros(51,3);           % Prelocate memory
211     dataStar(1,1) = u_star;           % Wind velocity scale in m (column 1)
212     dataStar(1,2) = Theta_star;      % Potential virtual temperature scale
213                                     % in m (column 2)
214     dataStar(1,3) = q_star;          % Specific humidity scale in m
215                                     % (column 3)
216 end
217
218 for i = 1:50;
219
220     L = (u_star^2*Theta_0) / (Karman*g*Theta_star);
221                                     % Monin Obukhov length (m) [1, eq 5]
222                                     % "2"
223     z_0u = (alpha*u_star^2)/g + (0.11*v)/u_star;
224                                     % Wind velocity roughness height (m)
225                                     % [1, eq 21] "3"
226     z_0Theta = 0.40 * v/u_star;      % Potential virtual temperature
227                                     % roughness height (m) [1, eq 23] {4}
228     z_0q = 0.62 * v/u_star;         % Specific humidity roughness height

```

```

229             % (m) [1, eq 23] {4}
230
231
232     Psi_u = getPsi_u(z_r,L,values.Model);    % Get universal function for
233                                               % wind transfer according to
234                                               % model
235     Psi_h = getPsi_h(z_r,L,values.Model);    % Get universal function for
236                                               % heat transfer according to
237                                               % model
238
239     u_star = (u_r-u_0)*Karman / (log(z_r/z_0u)-Psi_u);
240                                               % Wind velocity scale (m) [1, eq 8]
241                                               % {2}
242     Theta_star = (Theta_r-Theta_0)*Karman / (log(z_r/z_0Theta)-Psi_h);
243                                               % Potential virtual temperatrue scale
244                                               % (m) [1, eq 9] {2}
245     q_star = (q_r-q_0)*Karman / (log(z_r/z_0q)-Psi_h);
246                                               % Specific humidity scale (m)
247                                               % [1, eq 10] {2}
248
249     if nargin > 4
250     % Save scale data to matrix if varargin > 4
251         dataStar(i+1,1) = u_star;           % Wind velocity scale in m (column 1)
252         dataStar(i+1,2) = Theta_star;      % Potential virtual temperature scale
253                                               % in m (column 2)
254         dataStar(i+1,3) = q_star;         % Specific humidity scale in m
255     end                                     % (column 3)
256
257 end
258
259 % GET PROFILES -----
260 z = [0.00001; (0.1:0.1:50)'];           % Height intervals (m). For z = 0 the
261                                           % profiles can't be determined. It is
262                                           % assumed that z = 0.00001 will give
263                                           % a close value to the value at z = 0.
264
265 L = (u_star^2*Theta_0) / (Karman*g*Theta_star);
266                                           % Monin Obukhov length (m) [1, eq 5]
267                                           % "2"
268
269 Psi_u = getPsi_u(z,L,values.Model);    % Get universal function for wind
270                                           % transfer according to model
271 Psi_h = getPsi_h(z,L,values.Model);    % Get universal function for heat
272                                           % transfer according to model
273
274 u = u_0 + (u_star / Karman) .* (log(z./z_0u) - Psi_u);
275                                           % Get wind velocity profile (m/s)
276                                           % [1, eq 8]
277 Theta = Theta_0 + (Theta_star / Karman) .* (log(z./z_0Theta) - Psi_h);
278                                           % Get potential virtual temperature
279                                           % profile (K) [1, eq 9]
280 q = q_0 + (q_star / Karman) .* (log(z./z_0q) - Psi_h);
281                                           % Get specific humidity profile
282                                           % (kg/kg) [1, eq 10]
283
284 z(1) = 0;                               % Change values of z=0.00001 to z=0
285 u(1) = 0;

```

```

286 Theta(1) = Theta_0;
287 q(1) = q_0;
288
289
290 p = p_r*exp(-(z-z_r)/H_r);           % Get total pressure profile (hPa)
291                                     % [2, eq 2.48] {1} "1"
292
293 % Converse potential virtual temperature (Theta) into temperature (T)
294 Tv = Theta ./ (1000 ./ p).^K;       % Virtual temperature profile (K)
295                                     % [2, eq 2.96]
296 T = Tv ./ (1 + 0.608.*q);          % Temperature profile (K) [2, eq 2.38]
297
298 e = (q.*p) ./ (eps + (1 - eps)*q); % Vapour pressure (aka p_v) profile
299                                     % (hPa) [4, eq 3]
300
301 N = (77.6 ./ T) .* (p + (4810 * e ./ T));
302                                     % Refractivity profile (N-Units)
303                                     % [4, eq 1]
304 M = N + 0.157*z;                   % Modified refractivity profile
305                                     % (M-units) [4, eq 2]
306
307
308 if nargout > 3
309 % If user defines 4 (or more) outputs the third output will be a data
310 % matrix which consist of the pressure profile in hPa (column 1), the
311 % temperature profile in degrees Celsius (column 2), the relative humidity
312 % in percentages (column 3), the partial vapour pressure in hPa (column
313 % 4) and the wind velocit in m/s (column 5)
314
315     p_vs = 6.112*exp(6816*(1/273.15 - (1./T)) + 5.1309*log(273.15 ./ T));
316                                     % Determine the saturated vapour
317                                     % pressure (hPa) [2, eq 2.61]
318     RH = 100 * e./p_vs;              % Relative humidity (%) [2, eq 2.66]
319
320     dataAtm(:,1) = p;                % Pressure profile in hPa (column 1)
321     dataAtm(:,2) = T - 273.15;      % Temperature profile in degrees
322                                     % Celsius (column 2)
323     dataAtm(:,3) = RH;              % Relative humidity in percentages
324                                     % (column 3)
325     dataAtm(:,4) = e;                % Vapour pressure (aka p_v) in hPa
326                                     % (column 4)
327     dataAtm(:,5) = u;                % Wind velocity in m/s (column 5)
328     dataAtm(:,6) = q;                % Specific humidity in kg/kg
329                                     % (column 6)
330 end
331
332 end
333
334
335 %% Get universal function
336 function Psi_h = getPsi_h(z,L,model)
337 % This function returns Psi_h computed by the user defined model: LKB [1],
338 % RSHMU [1], COARE [1], NPS [4], NWA [4], NRL [4] or BYC [4].
339 % Input:      z      : height [m]
340 %            L      : Monin-Oboukhov length
341 %            model   : Defined model by user (string)
342 % Output:     Psi_h  : Result universal function

```

```

343
344 switch model
345     case 'LKB'
346         Psi_h = Psi_h_LKB(z,L);
347     case 'RSHMU'
348         Psi_h = Psi_h_RSHMU(z,L);
349     case 'COARE'
350         Psi_h = Psi_h_COARE(z,L);
351     case 'NPS'
352         Psi_h = Psi_h_NPS(z,L);
353     case 'NWA'
354         Psi_h = Psi_h_NWA(z,L);
355     case 'NRL'
356         Psi_h = Psi_h_NRL(z,L);
357     case 'BYC'
358         Psi_h = Psi_h_BYC(z,L);
359     otherwise
360         error(['Incorrect model is defined. Choose between: '...
361             ' LKB, RSHMU, COARE, NPS, NWA, NRL or BYC'])
362 end
363 end
364
365 function Psi_u = getPsi_u(z,L,model)
366 % This function returns Psi_u computed by the user defined model: LKB [1],
367 % RSHMU [1], COARE [1], NPS [4], NWA [4], NRL [4] or BYC [4].
368 % Input:      z      : height [m]
369 %            L      : Monin-Oboukhov length
370 %            model   : Defined model by user (string)
371 % Output:     Psi_u  : Result universal function
372
373 switch model
374     case 'LKB'
375         Psi_u = Psi_u_LKB(z,L);
376     case 'RSHMU'
377         Psi_u = Psi_u_RSHMU(z,L);
378     case 'COARE'
379         Psi_u = Psi_u_COARE(z,L);
380     case 'NPS'
381         Psi_u = Psi_u_NPS(z,L);
382     case 'NWA'
383         Psi_u = Psi_u_NWA(z,L);
384     case 'NRL'
385         Psi_u = Psi_u_NRL(z,L);
386     case 'BYC'
387         Psi_u = Psi_u_BYC(z,L);
388     otherwise
389         error(['Incorrect model is defined. Choose between: '...
390             ' LKB, RSHMU, COARE, NPS, NWA, NRL or BYC'])
391 end
392 end
393
394 %% LKB universal function
395
396 function Psi_h = Psi_h_LKB(z,L)
397 % This function gives the universal function for heat transfer
398 % according to the LKB model and is described in [1, pg 38].
399 % Input:      z      : height [m]

```

```

400 %           L      :   Monin-Oboukhov length
401 % Output:      Psi_h  :   Result universal function
402
403     zeta = z/L;           % dimensionless stability parameter
404                       % (-) [1, pg 37]
405     if L <= 0           % Stating L <= 0 gives the same result
406                       % as zeta <= 0
407     % Unstable and neutral atmospheric conditions
408         beta = 16;       % Numerical constant [1, pg 38]
409         x = (1 - beta*zeta).^(1/4); % Intermediat function [1, pg 38]
410         Psi_h = 2*log((1+x).^2)./2); % Universal function for heat transfer
411                       % [1, eq 14]
412     else
413     % Stable atmospheric conditions
414         gamma = 5;       % Numerical constant [1, pg 38]
415         Psi_h = -gamma*zeta; % Universal function for heat transfer
416                       % [1, eq 14]
417     end
418 end
419
420 function Psi_u = Psi_u_LKB(z,L)
421 % This function gives the universal function for wind transfer
422 % according to the LKB model and is described in [1, pg 38].
423 % Input:      z      :   height [m]
424 %           L      :   Monin-Oboukhov length
425 % Output:      Psi_h  :   Result universal function
426
427     zeta = z/L;           % dimensionless stability parameter
428                       % (-) [1, pg 37]
429     if L <= 0           % Stating L <= 0 gives the same result
430                       % as zeta <= 0
431     % Unstable and neutral atmospheric conditions
432         beta = 16;       % Numerical constant [1, pg 38]
433         x = (1 - beta*zeta).^(1/4); % Intermediat function [1, pg 38]
434         Psi_u = 2*log((1+x).^2)+log((1+x.^2)./2)-2*atan(x)+(pi/2);
435                       % Universal function for wind transfer
436                       % [1, eq 12]
437     else
438     % Stable atmospheric conditions
439         gamma = 5;       % Numerical constant [1, pg 38]
440         Psi_u = -gamma*zeta; % Universal function for wind transfer
441                       % [1, eq 12]
442     end
443 end
444
445 %% RSHMU universal functions
446
447 function Psi_h = Psi_h_RSHMU(z,L)
448 % This function gives the universal function for heat transfer
449 % according to the RSHMU model and is described in [1, pg 38-39].
450 % Input:      z      :   height [m]
451 %           L      :   Monin-Oboukhov length
452 % Output:      Psi_h  :   Result universal function
453
454     zeta = z/L;           % Dimensionless stability parameter
455                       % (-) [1, pg 37]
456     if L <= 0           % Stating L <= 0 gives the same result

```

```

457                                     % as zeta <= 0
458     % Unstable and neutral atmospheric conditions
459         beta1 = 8;                       % Constant [1, pg 39]
460         beta2 = 35;                      % Constant [1, pg 39]
461         y1 = (1-beta2*zeta).^(1/3);      % Intermediat function [1, pg 39]
462         Psi_h = (3/2)*log(1+beta1*zeta.^2)+...
463             0.7*((3/2)*log((1+y1+y1.^2)./3)-sqrt(3)*...
464             (atan((2*y1+1)./sqrt(3))-(pi/3)));
465                                     % Universal function for heat transfer
466                                     % [1, eq 18]
467     else
468     % Stable atmospheric conditions
469         gamma2 = 6;                      % Constant [1, pg 39]
470         Psi_h = -gamma2*zeta;            % Universal function for heat transfer
471                                     % [1, eq 18]
472     end
473 end
474
475 function Psi_u = Psi_u_RSHMU(z,L)
476 % This function gives the universal function for wind transfer
477 % according to the RSHMU model and is described in [1, pg 38-39].
478 % Input:          z          : height [m]
479 %                L          : Monin-Oboukhov length
480 % Output:         Psi_u     : Result universal function
481
482     zeta = z/L;                          % dimensionless stability parameter
483                                     % (-) [1, pg 37]
484     if L <= 0
485                                     % Stating L <= 0 gives the same result
486                                     % as zeta <= 0
487     % Unstable and neutral atmospheric conditions
488         beta1 = 8;                       % Constant [1, pg 39]
489         x1 = (1-beta1*zeta).^(1/3);      % Intermediat function [1, pg 39]
490         Psi_u = (3/2)*log((1+x1+x1.^2)./3) ...
491             -sqrt(3)*(atan((2*x1+1)./sqrt(3))-(pi/3));
492                                     % Universal function for wind transfer
493                                     % [1, eq 17]
494     else
495     % Stable atmospheric conditions
496         gamma1 = 5.4;                    % Constant [1, pg 39]
497         Psi_u = -gamma1*zeta;            % Universal function for wind transfer
498                                     % [1, eq 17]
499     end
500 end
501
502 %% COARE universal function
503
504 function Psi_h = Psi_h_COARE(z,L)
505 % This function gives the universal function for heat transfer
506 % according to the COARE model and is described in [1, pg 39].
507 % Input:          z          : height [m]
508 %                L          : Monin-Oboukhov length
509 % Output:         Psi_h     : Result universal function
510
511     zeta = z/L;                          % dimensionless stability parameter
512                                     % (-) [1, pg 37]
513     if L < 0
514                                     % Stating L < 0 gives the same result

```

```

514                                     % as zeta < 0
515 % Unstable atmospheric conditions
516     x2 = (1-16*zeta).^(1/4);           % Intermediat function [1, pg 39]
517     y2 = (1-10*zeta).^(1/3);         % Intermediat function [1, pg 39]
518     Psi_h = (1./(1+zeta.^2)).*2.*log((1+x2)./2)+(1-1./(1+zeta.^2))...
519             +(1.5.*log((1+y2+y2.^2)./3)-sqrt(3).*atan((2.*y2+1)./sqrt(3))...
520             +(pi./sqrt(3)));         % Universal function for heat transfer
521                                     % [1, eq 20]
522 else
523 % Stable and neutral atmospheric conditions
524     a=1;                               % Constant [1, pg 39]
525     b=2/3;                             % Constant [1, pg 39]
526     c = 5;                             % Constant [1, pg 39]
527     d = 0.35;                          % Constant [1, pg 39]
528     z2 = d*zeta;                       % Constant (z2 = z) [1, pg 39]
529     Psi_h = 1 - (1+2*a/3.*zeta).^(3.2) - b*(zeta-c/d).*exp(-z2) - b*c/d;
530                                     % Universal function for heat transfer
531                                     % [1, eq 20]
532 end
533 end
534
535 function Psi_u = Psi_u_COARE(z,L)
536 % This function gives the universal function for wind transfer
537 % according to the COARE model and is described in [1, pg 39].
538 % Input:      z      : height [m]
539 %             L      : Monin-Oboukhov length
540 % Output:     Psi_u   : Result universal function
541
542     zeta = z/L;                       % dimensionless stability parameter
543                                     % (-) [1, pg 37]
544     if L < 0
545                                     % Stating L < 0 gives the same result
546                                     % as zeta < 0
547     % Unstable atmospheric conditions
548     x2 = (1-16*zeta).^(1/4);           % Intermediat function [1, pg 39]
549     y2 = (1-10*zeta).^(1/3);         % Intermediat function [1, pg 39]
550     Psi_u = (1./(1+zeta.^2)) ...
551             *(2.*log((1+x2)./2)+log((1+x2.^2)./2)-2.*atan(x2)+(pi/2))...
552             + (1-(1./(1+zeta.^2))).*(1.5.*log((1+y2+y2.^2)./3) ...
553             - sqrt(3).*atan((2*y2+1)./sqrt(3))+(pi/sqrt(3)));
554                                     % Universal function for wind transfer
555                                     % [1, eq 19]
556 else
557 % Stable and neutral atmospheric conditions
558     a=1;                               % Constant [1, pg 39]
559     b=2/3;                             % Constant [1, pg 39]
560     c = 5;                             % Constant [1, pg 39]
561     d = 0.35;                          % Constant [1, pg 39]
562     z2 = d*zeta;                       % Constant [1, pg 39]
563     Psi_u = -a*zeta-b.*(zeta-c/d).*exp(-z2)-b*c/d;
564                                     % Universal function for wind transfer
565                                     % [1, eq 19]
566 end
567 end
568 %% NPS universal functions
569
570 function Psi_h = Psi_h_NPS(z,L)

```

```

571 % This function is gives the universal function for heat transfer
572 % according to the NPS model and is described in [4, pg 438].
573 % Input:      z      : height [m]
574 %            L      : Monin-Oboukhov length
575 % Output:     Psi_h   : Result universal function
576
577     zeta = z/L;                % dimensionless stability parameter
578                                % (-) [4, pg 438]
579     if L < 0                    % Stating L < 0 gives the same result
580                                % as zeta < 0
581     % Unstable atmospheric conditions
582
583         z_pt = (1-16*zeta).^0.5; % Intermediat function [4, pg 438]
584         z_pg = (1 - 34*zeta).^0.333; % Intermediat function [4, pg 438]
585
586         Psi_tk = 2*log((1+z_pt)/2); % Intermediat function [4, pg 438]
587         Psi_k = 1.5*log((z_pg.^2 + z_pg + 1)/3) ...
588             - sqrt(3)*atan((2*z_pg + 1)/sqrt(3)) + (pi/sqrt(3));
589                                % Intermediat function [4, pg 438]
590
591         Psi_h = (Psi_tk + zeta.^2.*Psi_k) ./ (1 + zeta.^2);
592                                % NPS Universal function for heat
593                                % under unstable condntions [4, eq 5]
594     else
595     % Stable and neutral atmospheric conditions
596
597         Psi_h = 1 - (1 + (2*zeta/3)).^1.5 ...
598             - (2/3)*(zeta - (5/0.35)).*exp(-0.35*zeta) ...
599             - (2/3)*(5/0.35);
600                                % NPS Universal function for heat
601                                % under stable and neutral condntions
602                                % [4, eq 6]
603     end
604 end
605 function Psi_u = Psi_u_NPS(z,L)
606 % This function is gives the universal function for wind transfer
607 % according to the NPS model and is described in [4]. In this function
608 % Psi_u is Psi_m in [4].
609 % Input:      z      : height [m]
610 %            L      : Monin-Oboukhov length
611 % Output:     Psi_u   : Result universal function
612
613     zeta = z/L;                % dimensionless stability parameter
614                                % (-) [4, pg 438]
615     if L < 0                    % Stating L < 0 gives the same result
616                                % as zeta < 0
617     % Unstable atmospheric conditions
618
619         z_pu = (1-16*zeta).^0.25; % Intermediat function [4, pg 438]
620         z_pg = (1 - 10*zeta).^0.333; % Intermediat function [4, pg 438]
621
622         Psi_uk = 2*log((1+z_pu)/2) + log((1+z_pu.^2)/2) ...
623             - 2*atan(z_pu) + (pi/2); % Intermediat function [4, pg 438]
624         Psi_k = 1.5*log((z_pg.^2 + z_pg + 1)/3) ...
625             - sqrt(3)*atan((2*z_pg + 1)/sqrt(3)) + (pi/sqrt(3));
626                                % Intermediat function [4, pg 438]
627

```

```

628     Psi_u = (Psi_uk + zeta.^2.*Psi_k) ./ (1 + zeta.^2);
629                                     % NPS Universal function for wind
630                                     % under unstable condtions [4, eq 5]
631                                     % (see line under eq 5!)
632 else
633     % Stable and neutral atmospheric conditions
634
635     Psi_u = -zeta - (2/3)*(zeta-(5/0.35)).*exp(-0.35*zeta) ...
636           - (2/3)*(5/0.35);          % NPS Universal function for heat
637                                     % under stable and neutral condtions
638                                     % [4, eq 7]
639 end
640 end
641
642 %% NWA universal functions
643
644 function Psi_h = Psi_h_NWA(z,L)
645 % This function is gives the universal function for heat transfer
646 % according to the NWA model and is described in [4, pg 438].
647 % Input:      z      : height [m]
648 %            L      : Monin-Oboukhov length
649 % Output:     Psi_u   : Result universal function
650
651     zeta = z/L;          % dimensionless stability parameter
652                       % (-) [4, pg 438]
653     if L < 0            % Stating L < 0 gives the same result
654                       % as zeta < 0
655     % Unstable atmospheric conditions
656
657     z_pu = (1-16*zeta).^0.25; % Intermediat function [4, pg 438]
658     Psi_h = 2*log((1+z_pu.^2)/2);
659                                     % Universal function for heat transfer
660                                     % [4, eq 8]
661
662 else
663     % Stable and neutral atmospheric conditions
664     Psi_h = -6*log(1+zeta);          % Universal function for heat transfer
665                                     % [4, eq 10]
666 end
667 end
668
669 function Psi_u = Psi_u_NWA(z,L)
670 % This function is gives the universal function for wind transfer
671 % accorinding to the NWA model and is described in [4, pg 438]. In this
672 % function Psi_u is Psi_m in [4].
673 % Input:      z      : height [m]
674 %            L      : Monin-Oboukhov length
675 % Output:     Psi_h   : Result universal function
676
677     zeta = z/L;          % dimensionless stability parameter
678                       % (-) [4, pg 438]
679     if L < 0            % Stating L < 0 gives the same result
680                       % as zeta < 0
681     % Unstable atmospheric conditions
682
683     z_pu = (1-16*zeta).^0.25; % Intermediat function
684     Psi_u = 2*log((1+z_pu).^2)+log((1+z_pu.^2)/2)...

```

```

685         -2*atan(z_pu)+(pi/2); % Universal function for heat transfer
686                                     % [4, eq 9]
687
688     else
689         % Stable and neutral atmospheric conditions
690         Psi_u = -6*log(1+zeta); % Universal function for heat transfer
691                                     % [4, eq 10]
692     end
693 end
694
695 %% NRL universal functions
696
697 function Psi_h = Psi_h_NRL(z,L)
698 % This function is gives the universal function for heat transfer
699 % according to the NRL model and is described in [4, pg 438-439].
700 % Input:      z      : height [m]
701 %            L      : Monin-Oboukhov length
702 % Output:     Psi_u  : Result universal function
703
704     zeta = z/L; % dimensionless stability parameter
705                 % (-) [4, pg 438]
706     if L < 0 % Stating L < 0 gives the same result
707                 % as zeta < 0
708         % Unstable atmospheric conditions
709
710         z_pu = (1-16*zeta).^0.25; % Intermediat function [4, pg 438]
711         Psi_h = 2*log((1+z_pu.^2)/2); % Universal function for heat transfer
712                                     % [4, eq 8]
713
714     else
715         % Stable and neutral atmospheric conditions
716         Psi_h = -7*zeta; % Universal function for heat transfer
717                                     % [4, pg 439]
718     end
719 end
720
721
722 function Psi_u = Psi_u_NRL(z,L)
723 % This function is gives the universal function for wind transfer
724 % according to the NRL model and is described in [4, pg 438-439]. In this
725 % function Psi_u is Psi_m in [4].
726 % Input:      z      : height [m]
727 %            L      : Monin-Oboukhov length
728 % Output:     Psi_h  : Result universal function
729
730     zeta = z/L; % dimensionless stability parameter
731                 % (-) [4, pg 438]
732     if L < 0 % Stating L < 0 gives the same result
733                 % as zeta < 0
734         % Unstable atmospheric conditions
735
736         z_pu = (1-16*zeta).^0.25; % Intermediat function
737         Psi_u = 2*log((1+z_pu)./2)+log((1+z_pu.^2)/2)...
738             -2*atan(z_pu)+(pi/2); % Universal function for heat transfer
739                                     % [4, eq 9]
740
741     else

```

```

742     % Stable and neutral atmospheric conditions
743     Psi_u = -7*zeta;           % Universal function for wind transfer
744                                 % [4, pg 439]
745     end
746 end
747
748 %% BYC universal functions
749
750 function Psi_h = Psi_h_BYC(z,L)
751 % This function is gives the universal function for heat transfer
752 % accorinding to the BYC model and is described in [4].
753 % Input:      z      :   height [m]
754 %            L      :   Monin-Oboukhov length
755 % Output:     Psi_h  :   Result universal function
756
757     zeta = z/L;                % dimensionless stability parameter
758                                 % (-) [4, pg 438]
759     if L < 0                    % Stating L < 0 gives the same result
760                                 % as zeta < 0
761     % Unstable atmospheric conditions
762
763     z_pt = (1-16*zeta).^0.5;    % Intermediat function [4, pg 438]
764     z_pg = (1 - 12.87*zeta).^0.333; % Intermediat function [4, pg 439]
765
766     Psi_tk = 2*log((1+z_pt)/2); % Intermediat function [4, pg 438]
767     Psi_k = 1.5*log((z_pg.^2 + z_pg + 1)/3) ...
768           - sqrt(3)*atan((2*z_pg + 1)/sqrt(3)) + (pi/sqrt(3));
769                                 % Intermediat function [4, pg 438]
770
771     Psi_h = (Psi_tk + zeta.^2.*Psi_k) ./ (1 + zeta.^2);
772                                 % Universal function for heat transfer
773                                 % [4, eq 5] (see also page 439)
774
775     else
776     % Stable and neutral atmospheric conditions
777     Psi_h = -5*zeta;           % Universal function for heat transfer
778                                 % [4, pg 439]
779     end
780 end
781
782 function Psi_u = Psi_u_BYC(z,L)
783 % This function is gives the universal function for wind transfer
784 % accorinding to the BYC model and is described in [4]. In this function
785 % Psi_u is Psi_m in [4].
786 % Input:      z      :   height [m]
787 %            L      :   Monin-Oboukhov length
788 % Output:     Psi_u  :   Result universal function
789
790     zeta = z/L;                % dimensionless stability parameter
791                                 % (-) [4, pg 438]
792     if L < 0                    % Stating L < 0 gives the same result
793                                 % as zeta < 0
794     % Unstable atmospheric conditions
795
796     z_pu = (1-16*zeta).^0.25;   % Intermediat function [4, pg 438]
797     z_pg = (1 - 12.87*zeta).^0.333; % Intermediat function [4, pg 439]
798

```

```

799     Psi_uk = 2*log((1+z_pu)/2) + log((1+z_pu.^2)/2) ...
800         - 2*atan(z_pu) + (pi/2); % Intermediat function [4, pg 438]
801     Psi_k = 1.5*log((z_pg.^2 + z_pg + 1)/3) ...
802         - sqrt(3)*atan((2*z_pg + 1)/sqrt(3)) + (pi/sqrt(3));
803         % Intermediat function [4, pg 438]
804
805     Psi_u = (Psi_uk + zeta.^2.*Psi_k) ./ (1 + zeta.^2);
806         % Universal function for heat transfer
807         % [4, eq 5] % (see line under eq 5!
808         % and on pg 439)
809     else
810     % Stable and neutral atmospheric conditions
811     Psi_u = -5*zeta; % Universal function for heat transfer
812         % [4, pg 439]
813     end
814 end
815
816 %% ASSUMPTIONS AND UNCERTANTIES -----
817
818 % ASSUMPTIONS -----
819 % {1} By determining the total pressure at height 0, it is assumed that the
820 % air temperature in the surface layer (z_r - 0) is constant and that the
821 % scale height H_r at height z_r is equal to the scale height H_0 at height
822 % 0.
823 % {2} By determining the specific humidity at height 0, it is assumed that
824 % the air adjacent to the water surface is (almost) fully saturated. Some
825 % sources (e.g. [1, pg 36]) state that the air is fully saturated (hence
826 % relative humidity of 100%). Other sources state (e.g. [5, pg. 16 and
827 % KNMI) that a relative humidity of 98% is a beter approximation. This due
828 % to the saltinity of the water. In determining the temperature and wind
829 % velocity at height zero, it is assumed that the temperature is equal to
830 % the sea temperature and that the wind velocity is zero. (See
831 % [1, pg 36]).
832 % {3} By the initialisation it is assumed that the integral representation
833 % of the universal function Psi(z/L) is 0. This occures when the
834 % dimensionless stability parameter zeta = z/L becomes very small. Hence
835 % stable conditions. It is also assumed that the initial values of the
836 % rougness heights z_0u, z_0Theta, z_0q kan be estimated with the values
837 % 0.00015, 0.00015 and 0.00015 respectivly. These estimations can be found
838 % in literature.
839 % {4} Rougness length recommended by the ECMWF. Many other options can be
840 % found in literature.
841
842
843 % UNCERTAINTIES -----
844 % "1" Can the pressure at height 0 be estimated accuratly through [2, eq
845 % 2.47 and eq 2.48]? The question concernes mainly the use of the scale
846 % height H_r and not H_0, which can't be determined easily.
847 % "2" The potential virtual temperature used in [1, eq 5] is unclear.
848 % Because it is assumed that L is a fixed value, Theta must be a
849 % temperature at a constant height, e.g. 0. However, maybe it is wise to
850 % use Theta_r? No litterature is yet found for clarification.
851 % "3" [2, pg 232] states that the left part of [1, eq 21] is the roughness
852 % height above rough seas. The right part is the scale height over smooth
853 % seas. Should it be better not to combine them? Or is the left part
854 % neglectable at smooth seas and the right part neglectable at rough seas?

```

Appendix D

Scenarios

The results presented in Chapter 7 are based on 41 scenarios that differ in atmospheric conditions (i.e. the weather), ship position, and/or radar azimuth. This appendix provides a general and brief overview of each scenario considered in this study. The atmospheric data used for this study was computed by the NWP model HARMONIE (Hirlam Aladin research on mesoscale operational NWP in Euromed) and provided by the Royal Netherlands Meteorological Institute (KNMI). The radar and target parameters were constant for all scenarios and can be found in Section 6-3.

For each scenario the following is given:

- the time and date of the scenario (atmospheric conditions);
- the ship's position;
- the radar's azimuth;
- a general description of the prevailing atmospheric conditions (weather) during the scenario;
- the minimum, maximum and mean wind speeds at the lowest model level above the surface (circa 10 m), over the entire area¹ as well as just over the water;
- the minimum, maximum and mean air temperatures at the lowest model level over the entire area and just over the water;
- the minimum, maximum and mean (sea) surface temperatures of the entire surface and just of the water;
- the minimum, maximum and mean air-surface temperature differences ($T_{air} - T_{surf}$) over the entire area and just over the water;
- the minimum, maximum and mean specific humidities at the lowest model level over the entire area and just over the water;
- a general description of the expected refractive conditions according to weather charts provided by the KNMI [60].

¹The entire area is defined as the area between approximately 49°N - 56 °N and 0 °E - 11°E (also see the charts on the following pages).

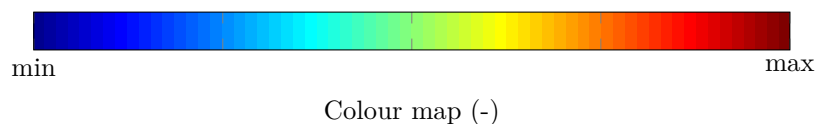
Seven or eight charts are also added. From left to right and from top to bottom the first six charts display:

- the ship's position and radar azimuth; the blue circle represents the ship's position and the red line represents the radar azimuth and a distance of 200 km;
- the wind speed and direction;
- the air temperature at the lowest model level;
- the (sea) surface temperature;
- the air-surface temperature difference;
- the specific humidity.

The seventh chart is the weather chart corresponding with the time and date of the scenario. The weather charts are provided by the KNMI and can also be found on the internet [60]. If no chart was available for the specific time of the scenario, the charts closest before and after the specific time are given².

In the chart displaying the wind speed and direction, the wind speed is represented by the length of the arrow where the shortest arrow has the value of the minimum wind speed over the entire area listed in the table and the longest arrow the maximum wind speed. The direction of the wind is represented by the direction of the arrow.

The colour map of the other charts is given in the colour bar below. The blue colour represents the minimum value listed in the table (over the entire area) of the corresponding chart and the red colour represents the maximum value.



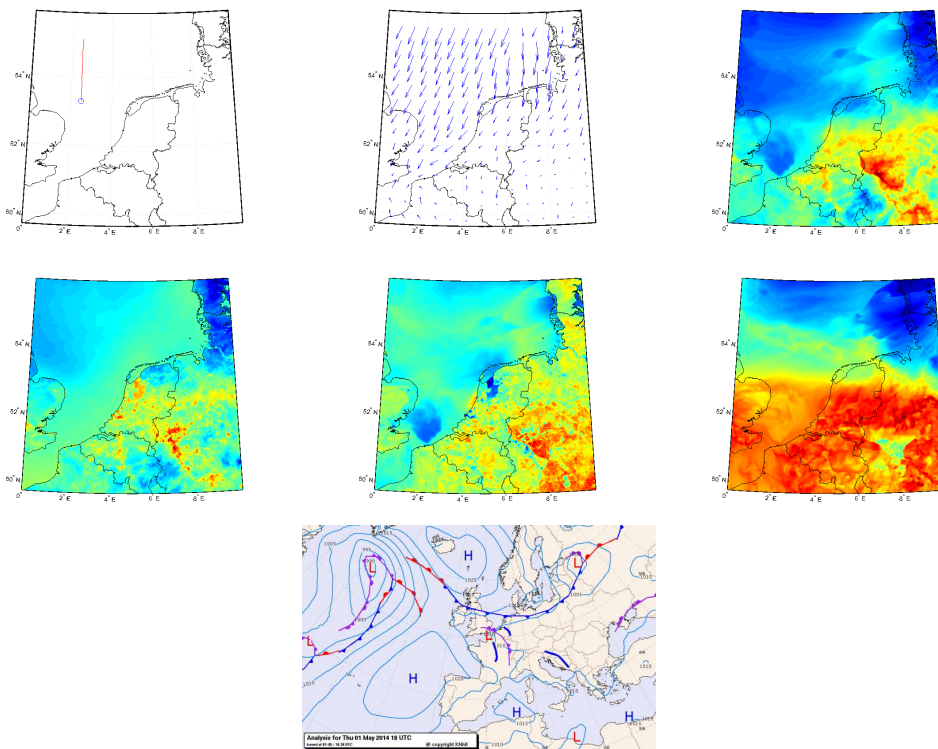
²Charts are made by the KNMI every six hours.

Scenario 1

Time, date	18:00, 01-05-2014 Z
Ship position, remarks	53.3 N - 2.5 E, near the cold weather front
Radar azimuth, remarks	000, towards the cold air mass
Weather conditions	Cold weather front passage from the north, northerly wind, on average unstable conditions over water

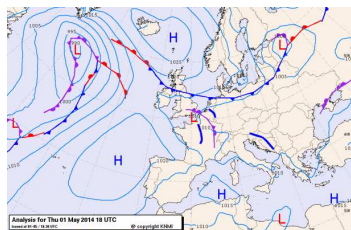
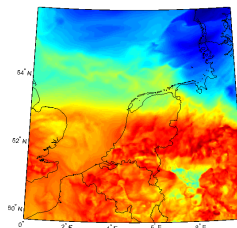
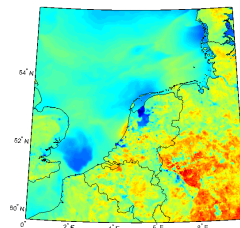
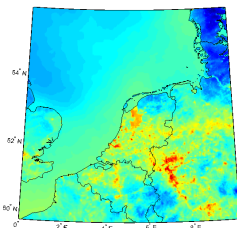
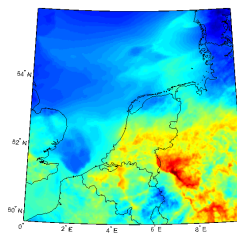
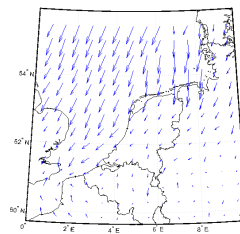
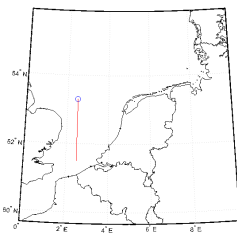
	Overall (min/max/mean)	Over water (min/max/mean)
Wind speed (kts)	0.01/23.00/9.59	0.43/23.00/16.21
Temperature (°C)	6.34/18.14/10.93	7.96/13.39/9.61
Sea surface temp. (°C)	4.64/18.99/10.60	8.78/12.24/10.23
Air-surface temp. difference (°C)	-4.32/4.92/0.33	-3.23/2.07/-0.62
Specific humidity ($\times 10^{-3}$ kg/kg)	2.25/9.03/6.18	2.50/8.14/5.20

General refractive conditions	Evaporation duct with heights increasing from 5-10 m
--------------------------------------	--



Scenario 2

Time, date	18:00, 01-05-2014 Z	
Ship position, remarks	53.3 N - 2.5 E, near the cold weather front, same as Scenario 1	
Radar azimuth, remarks	180, towards the warm air mass	
Weather conditions	Cold weather front passage from the north, northerly wind, on average unstable conditions over water	
	Overall	Over water
	(min/max/mean)	(min/max/mean)
Wind speed (kts)	0.01/23.00/9.59	0.43/23.00/16.21
Temperature (°C)	6.34/18.14/10.93	7.96/13.39/9.61
Sea surface temp. (°C)	4.64/18.99/10.60	8.78/12.24/10.23
Air-surface temp. difference (°C)	-4.32/4.92/0.33	-3.23/2.07/-0.62
Specific humidity ($\times 10^{-3}$ kg/kg)	2.25/9.03/6.18	2.50/8.14/5.20
General refractive conditions	Evaporation duct with heights decreasing from 5-3 m	

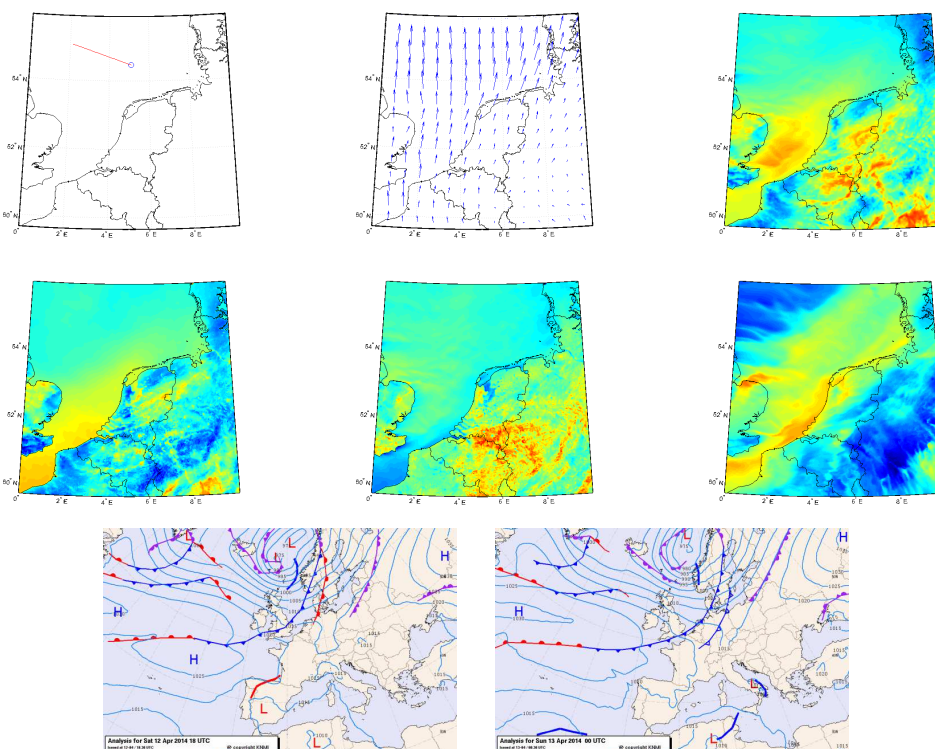


Scenario 3

Time, date	21:00, 12-04-2014 Z
Ship position, remarks	54.5 N - 5.1 E, in front of the cold weather front
Radar azimuth, remarks	290, towards the cold air mass
Weather conditions	Cold weather front passage from the north west, southerly wind, on average stable conditions

	Overall	Over water
	(min/max/mean)	(min/max/mean)
Wind speed (kts)	0.04/29.95/11.57	8.10/29.95/19.51
Temperature (°C)	4.70/14.52/9.47	7.30/11.79/9.35
Sea surface temp. (°C)	2.74/14.81/7.92	6.79/11.19/8.41
Air-surface temp. difference (°C)	-2.91/6.45/1.55	-1.64/3.21/0.94
Specific humidity ($\times 10^{-3}$ kg/kg)	4.03/7.83/5.58	4.60/6.77/5.81

General refractive conditions	Evaporation duct with heights increasing from 3-6 m
--------------------------------------	---

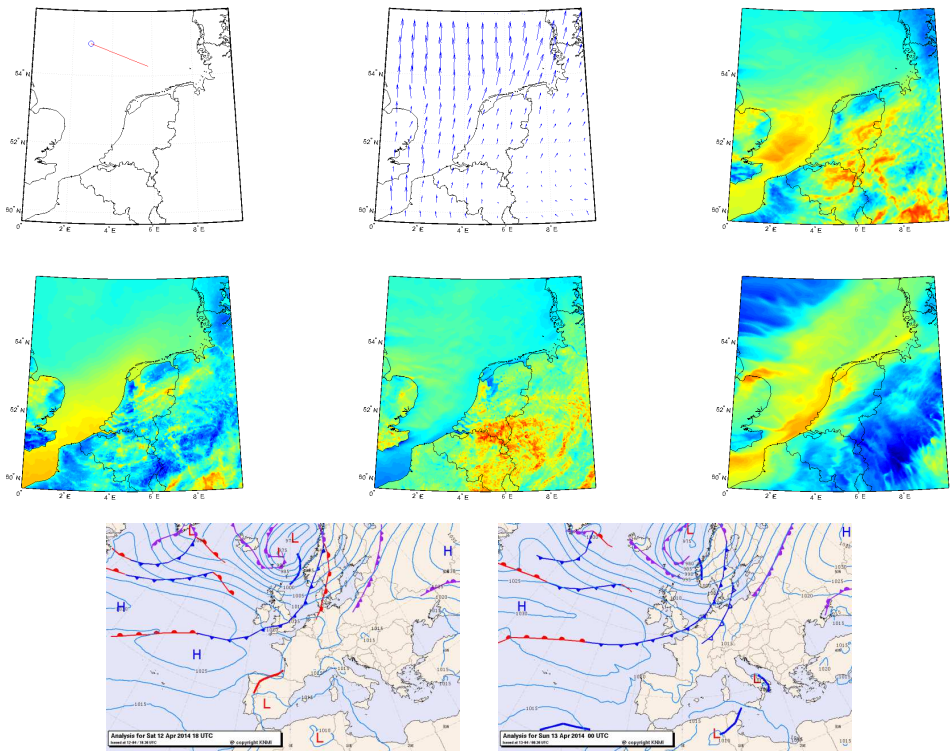


Scenario 4

Time, date	21:00, 12-04-2014 Z
Ship position, remarks	54.9 N - 2.9 E, behind the cold weather front
Radar azimuth, remarks	110, towards the warm air mass
Weather conditions	Cold weather front passage from the north west, southerly wind, on average stable conditions

	Overall (min/max/mean)	Over water (min/max/mean)
Wind speed (kts)	0.04/29.95/11.57	8.10/29.95/19.51
Temperature (°C)	4.70/14.52/9.47	7.30/11.79/9.35
Sea surface temp. (°C)	2.74/14.81/7.92	6.79/11.19/8.41
Air-surface temp. difference (°C)	-2.91/6.45/1.55	-1.64/3.21/0.94
Specific humidity ($\times 10^{-3}$ kg/kg)	4.03/7.83/5.58	4.60/6.77/5.81

General refractive conditions Evaporation duct with heights varying between 2-5 m

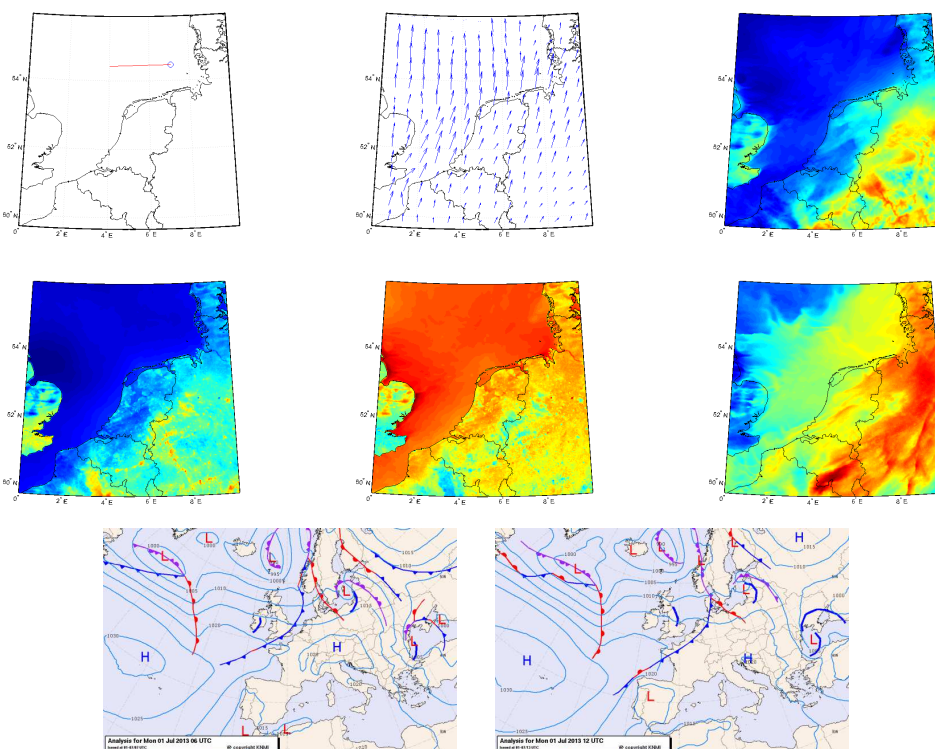


Scenario 5

Time, date	09:00, 01-07-2013 Z
Ship position, remarks	54.5 N - 7.1 E, far in front of the cold weather front
Radar azimuth, remarks	270, towards the cold air mass
Weather conditions	Cold weather front passage from the west, southerly wind, on average stable conditions over water

	Overall (min/max/mean)	Over water (min/max/mean)
Wind speed (kts)	0.15/20.87/9.36	0.91/20.87/12.53
Temperature (°C)	11.47/22.93/15.25	11.74/17.45/12.99
Sea surface temp. (°C)	10.90/34.59/17.59	10.90/20.59/12.89
Air-surface temp. difference (°C)	-16.22/4.28/-2.34	-3.49/4.28/0.10
Specific humidity ($\times 10^{-3}$ kg/kg)	5.21/11.14/8.49	5.38/9.78/7.88

General refractive conditions	Evaporation duct with heights increasing from 2-4 m
--------------------------------------	---

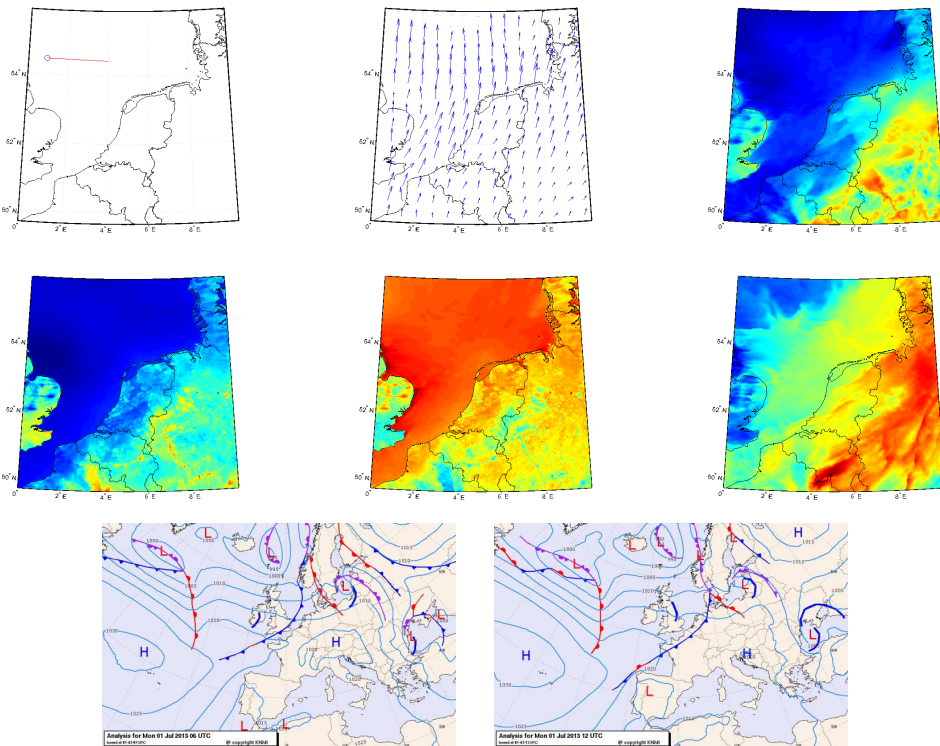


Scenario 6

Time, date	09:00, 01-07-2013 Z
Ship position, remarks	54.5 N - 0.9 E, far behind the cold weather front
Radar azimuth, remarks	090, towards the warm air mass
Weather conditions	Cold weather front passage from the west, southerly wind, on average stable conditions over water

	Overall (min/max/mean)	Over water (min/max/mean)
Wind speed (kts)	0.15/20.87/9.36	0.91/20.87/12.53
Temperature (°C)	11.47/22.93/15.25	11.74/17.45/12.99
Sea surface temp. (°C)	10.90/34.59/17.59	10.90/20.59/12.89
Air-surface temp. difference (°C)	-16.22/4.28/-2.34	-3.49/4.28/0.10
Specific humidity ($\times 10^{-3}$ kg/kg)	5.21/11.14/8.49	5.38/9.78/7.88

General refractive conditions	Evaporation duct with heights decreasing from 9-4 m
--------------------------------------	---

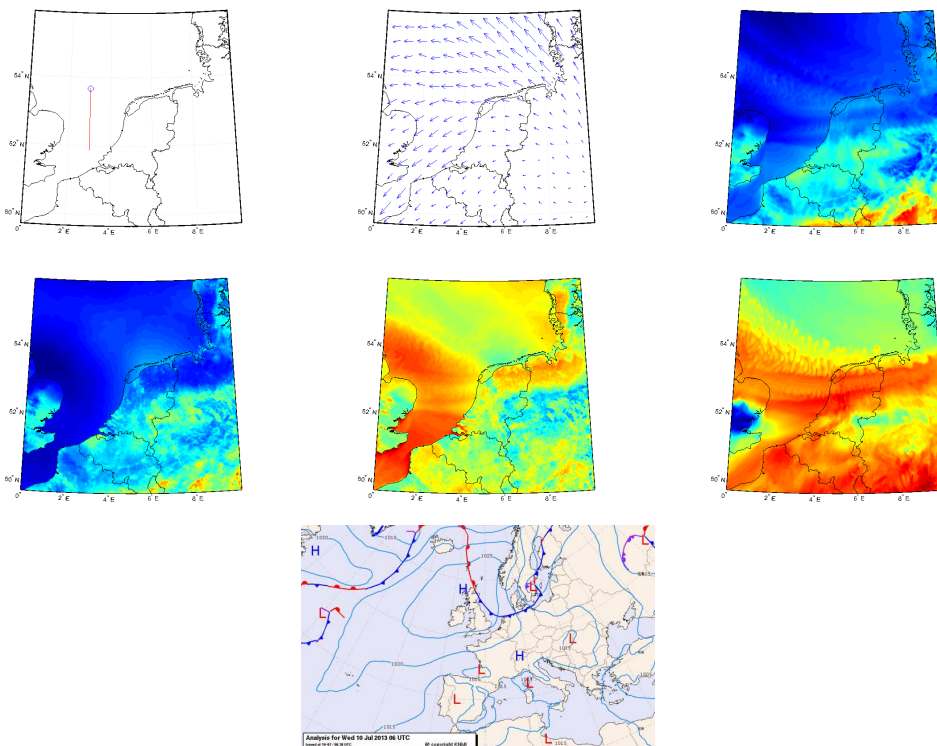


Scenario 7

Time, date	06:00, 10-07-2013 Z
Ship position, remarks	53.7 N - 3.0 E, behind the cold weather front
Radar azimuth, remarks	180, towards the warm air mass
Weather conditions	Cold weather front passage from the north, easterly wind, on average unstable conditions

	Overall (min/max/mean)	Over water (min/max/mean)
Wind speed (kts)	0.09/25.28/11.20	3.87/25.28/17.71
Temperature (°C)	12.18/22.92/15.45	12.18/16.97/13.78
Sea surface temp. (°C)	13.04/30.43/17.80	13.04/18.92/15.33
Air-surface temp. difference (°C)	-8.78/2.44/-2.35	-3.90/2.44/-1.55
Specific humidity ($\times 10^{-3}$ kg/kg)	3.38/10.88/8.29	4.59/9.87/7.81

General refractive conditions	Evaporation duct with heights decreasing from 8-2 m
--------------------------------------	---

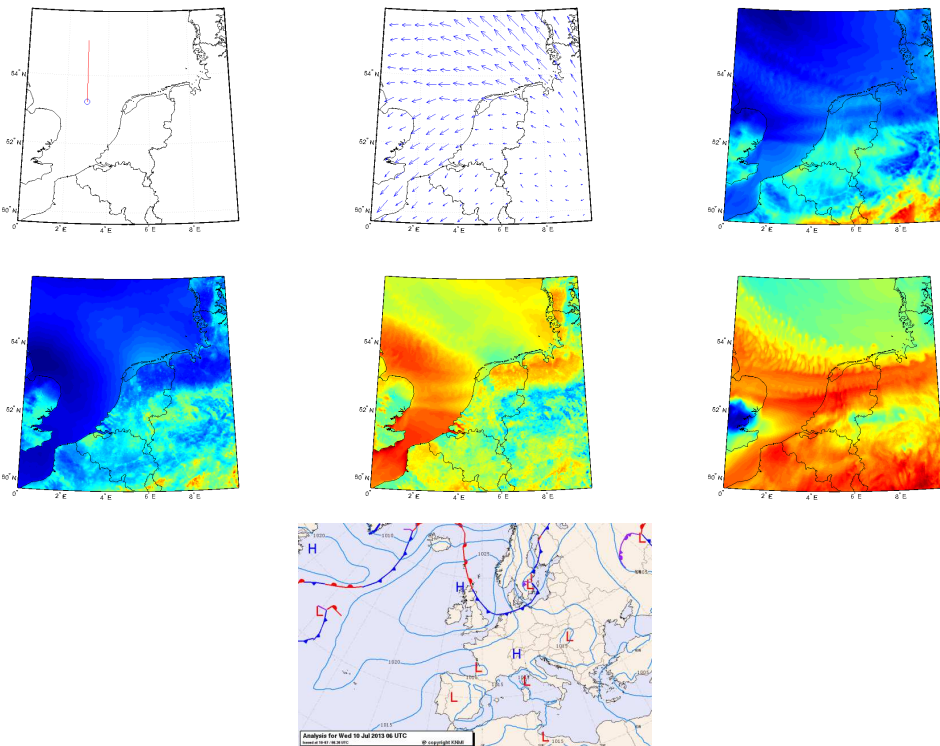


Scenario 8

Time, date	06:00, 10-07-2013 Z
Ship position, remarks	53.2 N - 3.0 E, in front of the cold weather front
Radar azimuth, remarks	000, towards the cold air mass
Weather conditions	Cold weather front passage from the northerly, easterly wind, on average unstable conditions

	Overall (min/max/mean)	Over water (min/max/mean)
Wind speed (kts)	0.09/25.28/11.20	3.87/25.28/17.71
Temperature (°C)	12.18/22.92/15.45	12.18/16.97/13.78
Sea surface temp. (°C)	13.04/30.43/17.80	13.04/18.92/15.33
Air-surface temp. difference (°C)	-8.78/2.44/-2.35	-3.90/2.44/-1.55
Specific humidity ($\times 10^{-3}$ kg/kg)	3.38/10.88/8.29	4.59/9.87/7.81

General refractive conditions Evaporation duct with heights increasing from 5-9 m

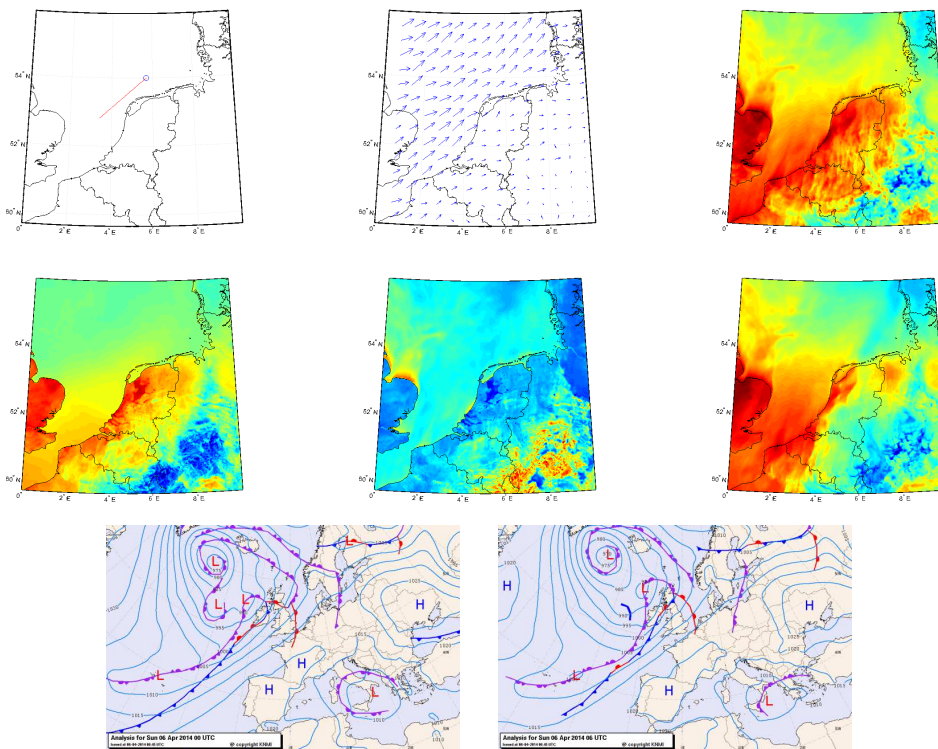


Scenario 9

Time, date	03:00, 06-04-2014 Z
Ship position, remarks	54.0 N - 5.7 E, near the warm weather front
Radar azimuth, remarks	230, towards the warm air mass
Weather conditions	Warm weather front passage from the west, south-westerly wind, on average stable conditions

	Overall (min/max/mean)	Over water (min/max/mean)
Wind speed (kts)	0.04/24.78/9.91	3.65/24.78/16.38
Temperature (°C)	2.51/13.91/9.57	6.20/13.65/9.55
Sea surface temp. (°C)	-0.43/15.27/8.07	5.89/10.89/7.82
Air-surface temp. difference (°C)	-2.38/7.99/1.50	-0.99/5.80/1.73
Specific humidity ($\times 10^{-3}$ kg/kg)	4.70/8.52/6.90	5.82/8.36/6.98

General refractive conditions	Sub-refractive layer near the surface up to about 50 m, most likely due to fog
--------------------------------------	--

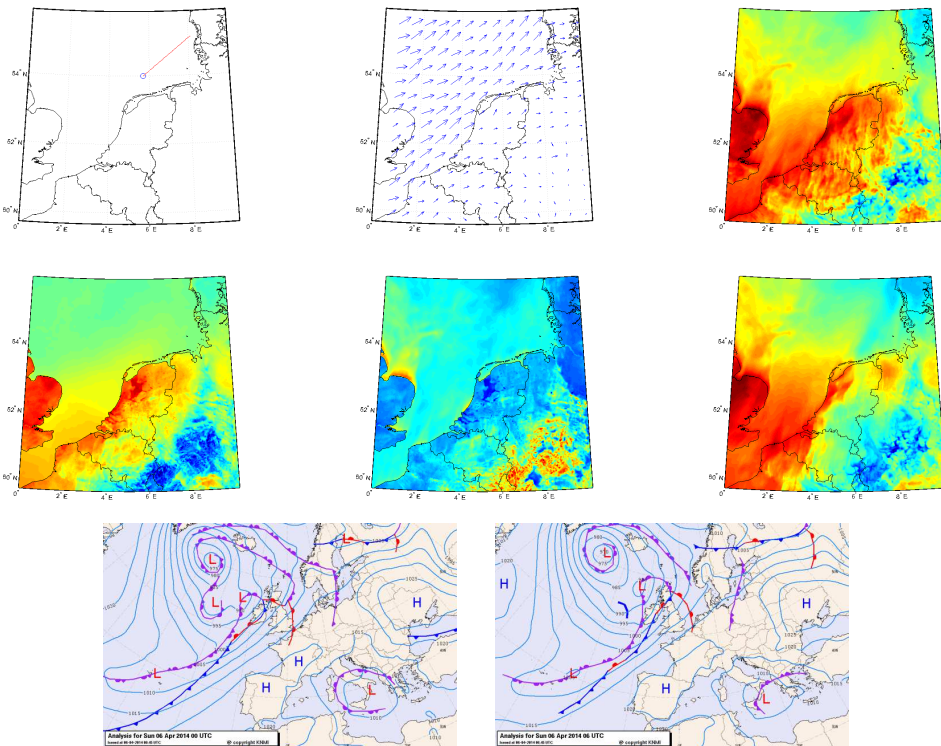


Scenario 10

Time, date	03:00, 06-04-2014 Z
Ship position, remarks	54.0 N - 5.7 E, near the warm weather front, same as Scenario 9
Radar azimuth, remarks	050, towards the cold air mass
Weather conditions	Warm weather front passage from the west, south-westerly wind, on average stable conditions

	Overall (min/max/mean)	Over water (min/max/mean)
Wind speed (kts)	0.04/24.78/9.91	3.65/24.78/16.38
Temperature (°C)	2.51/13.91/9.57	6.20/13.65/9.55
Sea surface temp. (°C)	-0.43/15.27/8.07	5.89/10.89/7.82
Air-surface temp. difference (°C)	-2.38/7.99/1.50	-0.99/5.80/1.73
Specific humidity ($\times 10^{-3}$ kg/kg)	4.70/8.52/6.90	5.82/8.36/6.98

General refractive conditions A relative standard atmosphere with some weak high sub-refractive layers

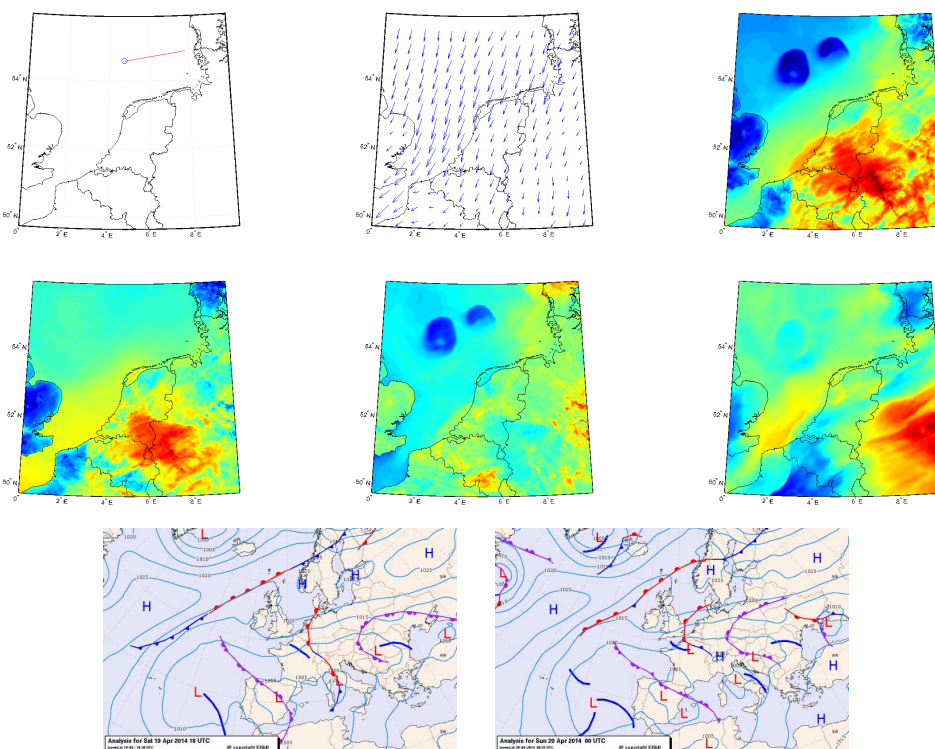


Scenario 11

Time, date	21:00, 19-04-2014 Z
Ship position, remarks	54.6 N - 4.8 E, in front of the warm weather front
Radar azimuth, remarks	080, towards the warm air mass
Weather conditions	Warm weather front passage from the east, northerly wind, on average stable conditions

	Overall (min/max/mean)	Over water (min/max/mean)
Wind speed (kts)	0.08/26.09/11.79	6.03/26.09/16.28
Temperature (°C)	5.31/15.20/10.22	5.31/12.92/9.08
Sea surface temp. (°C)	2.74/15.60/9.02	7.62/11.61/8.81
Air-surface temp. difference (°C)	-4.51/7.82/1.21	-3.15/3.51/0.27
Specific humidity ($\times 10^{-3}$ kg/kg)	3.87/8.11/6.00	4.72/6.73/5.91

General refractive conditions	Evaporation duct with heights increasing from 3-9 m, weak trapping, super refractive and some sub-refractive layers
--------------------------------------	---

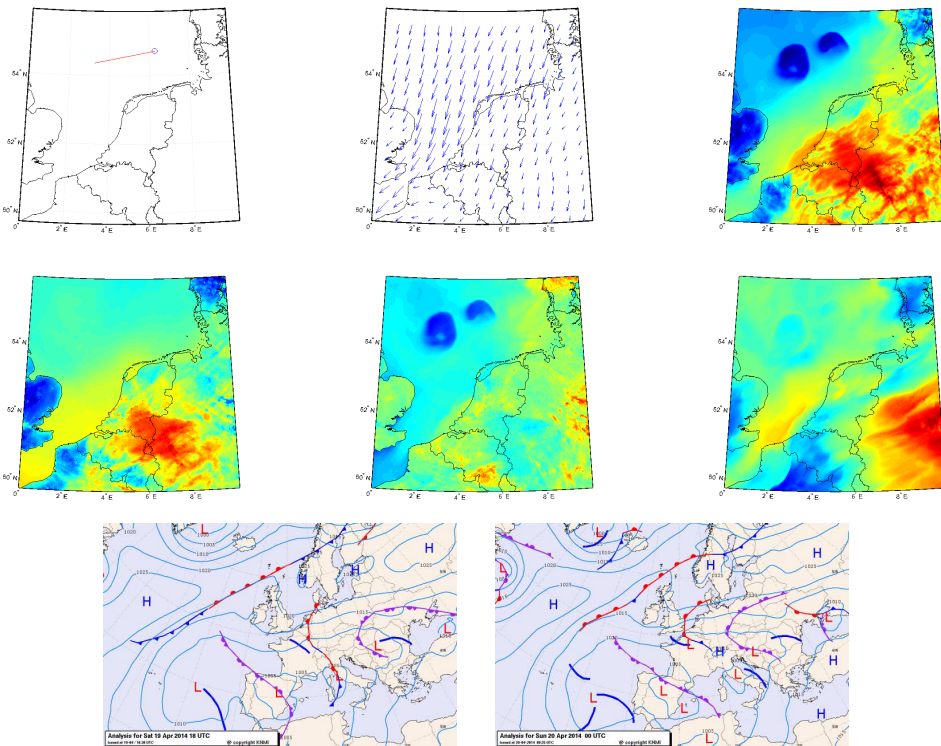


Scenario 12

Time, date	21:00, 19-04-2014 Z
Ship position, remarks	54.7 N - 6.3 E, behind the warm weather front
Radar azimuth, remarks	260, towards the cold air mass
Weather conditions	Warm weather front passage from the east, northerly wind, on average stable conditions

	Overall (min/max/mean)	Over water (min/max/mean)
Wind speed (kts)	0.08/26.09/11.79	6.03/26.09/16.28
Temperature (°C)	5.31/15.20/10.22	5.31/12.92/9.08
Sea surface temp. (°C)	2.74/15.60/9.02	7.62/11.61/8.81
Air-surface temp. difference (°C)	-4.51/7.82/1.21	-3.15/3.51/0.27
Specific humidity ($\times 10^{-3}$ kg/kg)	3.87/8.11/6.00	4.72/6.73/5.91

General refractive conditions	Evaporation duct with a height of approximately 5 m, trapping layers closer to the warm weather front
--------------------------------------	---

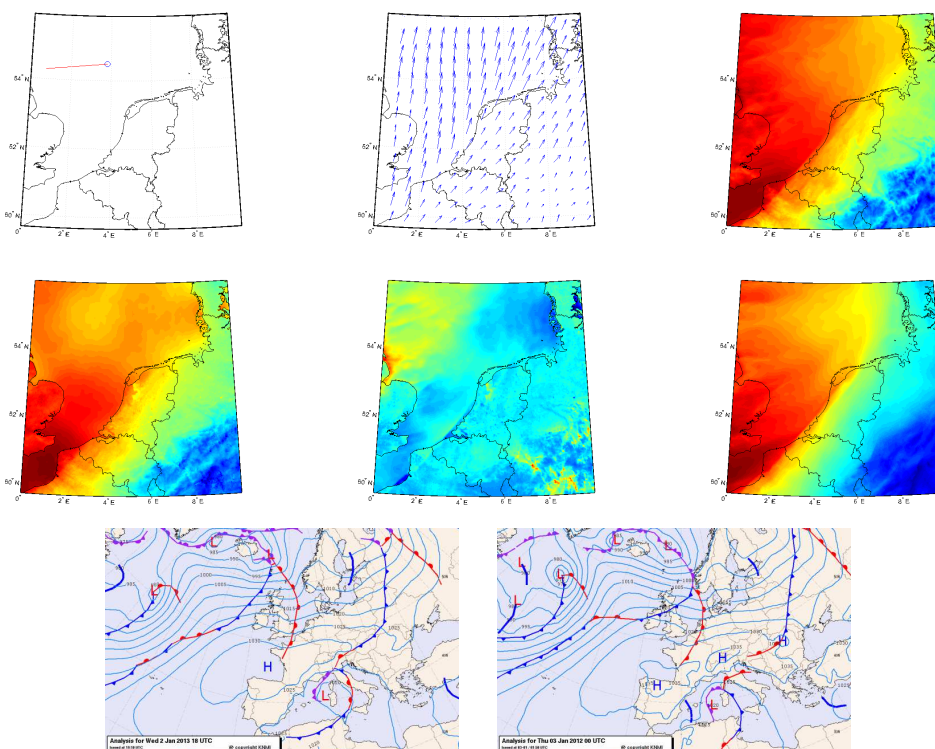


Scenario 13

Time, date	23:00, 02-01-2013 Z
Ship position, remarks	54.5 N - 3.8 E, near the warm weather front
Radar azimuth, remarks	265, towards the warm air mass
Weather conditions	Warm weather front passage from the west, southerly wind, on average stable conditions

	Overall	Over water
	(min/max/mean)	(min/max/mean)
Wind speed (kts)	0.96/29.46/15.41	10.26/29.46/22.16
Temperature (°C)	-1.83/11.29/6.27	4.66/11.28/8.50
Sea surface temp. (°C)	-2.50/11.04/5.55	4.51/11.04/7.57
Air-surface temp. difference (°C)	-1.81/4.82/0.72	-1.75/4.29/0.92
Specific humidity ($\times 10^{-3}$ kg/kg)	3.45/7.53/5.53	4.62/7.53/6.33

General refractive conditions	Sub-refractive layer near the surface with heights varying between 0-10 m
--------------------------------------	---

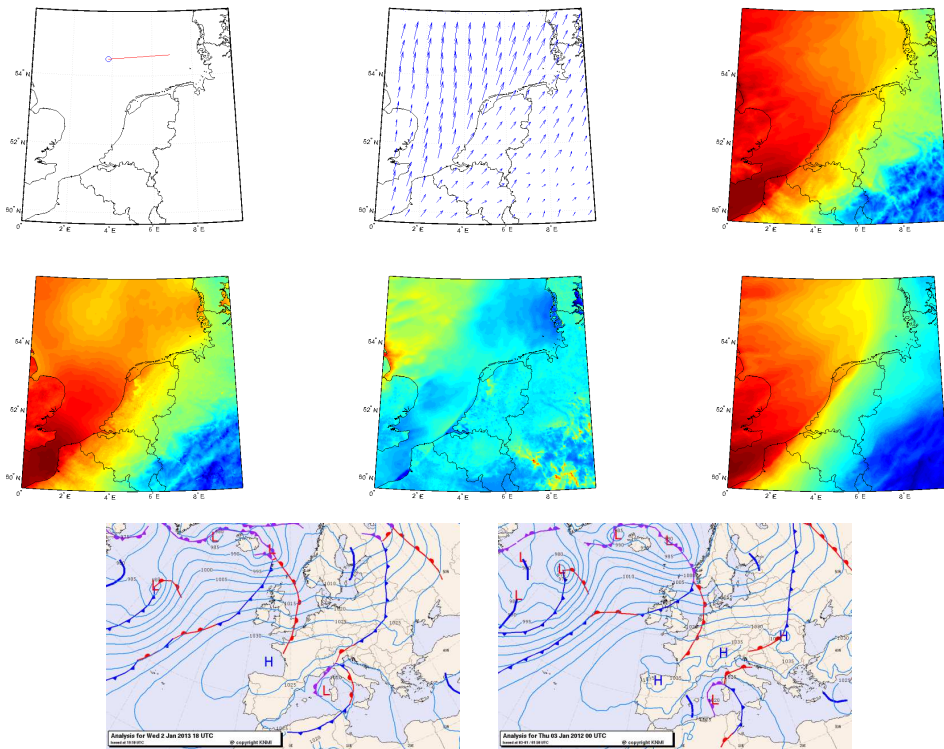


Scenario 14

Time, date	23:00, 02-01-2013 Z
Ship position, remarks	54.5 N - 3.8 E, near the warm weather front, same as Scenario 13
Radar azimuth, remarks	085, towards the cold air mass
Weather conditions	Warm weather front passage from the west, southerly wind, on average stable conditions

	Overall (min/max/mean)	Over water (min/max/mean)
Wind speed (kts)	0.96/29.46/15.41	10.26/29.46/22.16
Temperature (°C)	-1.83/11.29/6.27	4.66/11.28/8.50
Sea surface temp. (°C)	-2.50/11.04/5.55	4.51/11.04/7.57
Air-surface temp. difference (°C)	-1.81/4.82/0.72	-1.75/4.29/0.92
Specific humidity ($\times 10^{-3}$ kg/kg)	3.45/7.53/5.53	4.62/7.53/6.33

General refractive conditions	Evaporation duct with a height of approximately 1 m and sub-refractive regions
--------------------------------------	--

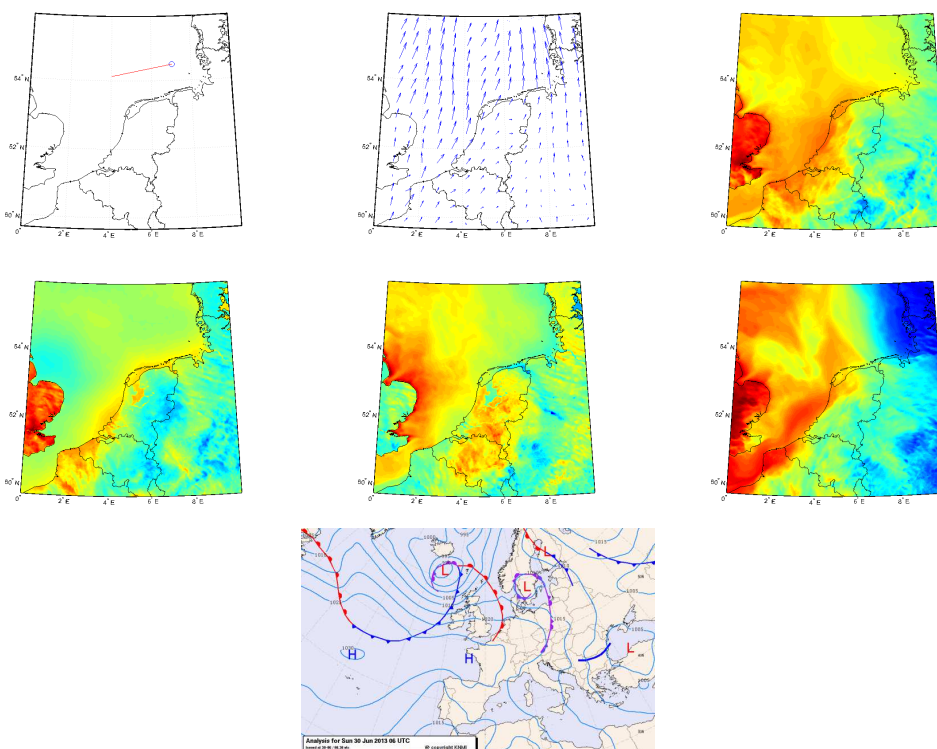


Scenario 15

Time, date	06:00, 30-06-2013 Z
Ship position, remarks	54.5 N - 7.0 E, far in front of the warm front
Radar azimuth, remarks	260, towards the warm air mass
Weather conditions	Warm weather front passage from the west, southerly wind, on average neutral conditions over water

	Overall (min/max/mean)	Over water (min/max/mean)
Wind speed (kts)	0.01/25.03/8.28	3.24/25.03/12.53
Temperature (°C)	4.68/17.22/11.93	10.79/15.55/12.74
Sea surface temp. (°C)	5.57/19.07/12.45	10.77/16.11/12.75
Air-surface temp. difference (°C)	-5.62/3.65/-0.52	-5.22/3.59/0.00
Specific humidity ($\times 10^{-3}$ kg/kg)	5.05/9.54/7.29	5.28/9.15/7.78

General refractive conditions	Evaporation duct with heights varying between 4-8 m, some super-refraction and trapping regions at higher altitude
--------------------------------------	--

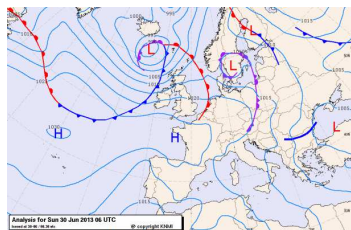
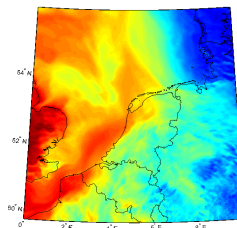
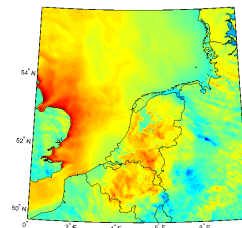
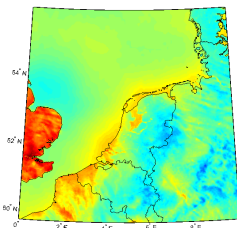
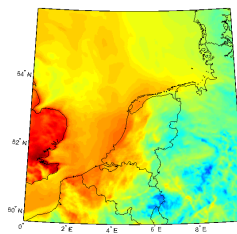
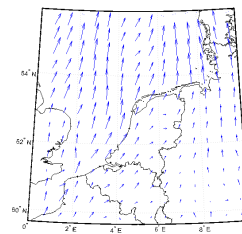
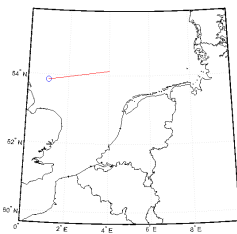


Scenario 16

Time, date	06:00, 30-06-2013 Z
Ship position, remarks	53.9 N - 1.0 E, far behind the warm front
Radar azimuth, remarks	080, towards the cold air mass
Weather conditions	Warm weather front passage from the west, southerly wind, on average neutral conditions over water

	Overall (min/max/mean)	Over water (min/max/mean)
Wind speed (kts)	0.01/25.03/8.28	3.24/25.03/12.53
Temperature (°C)	4.68/17.22/11.93	10.79/15.55/12.74
Sea surface temp. (°C)	5.57/19.07/12.45	10.77/16.11/12.75
Air-surface temp. difference (°C)	-5.62/3.65/-0.52	-5.22/3.59/0.00
Specific humidity ($\times 10^{-3}$ kg/kg)	5.05/9.54/7.29	5.28/9.15/7.78

General refractive conditions	Sub-refractive layers at higher altitudes with super-refractive layers closer to the weather front
--------------------------------------	--

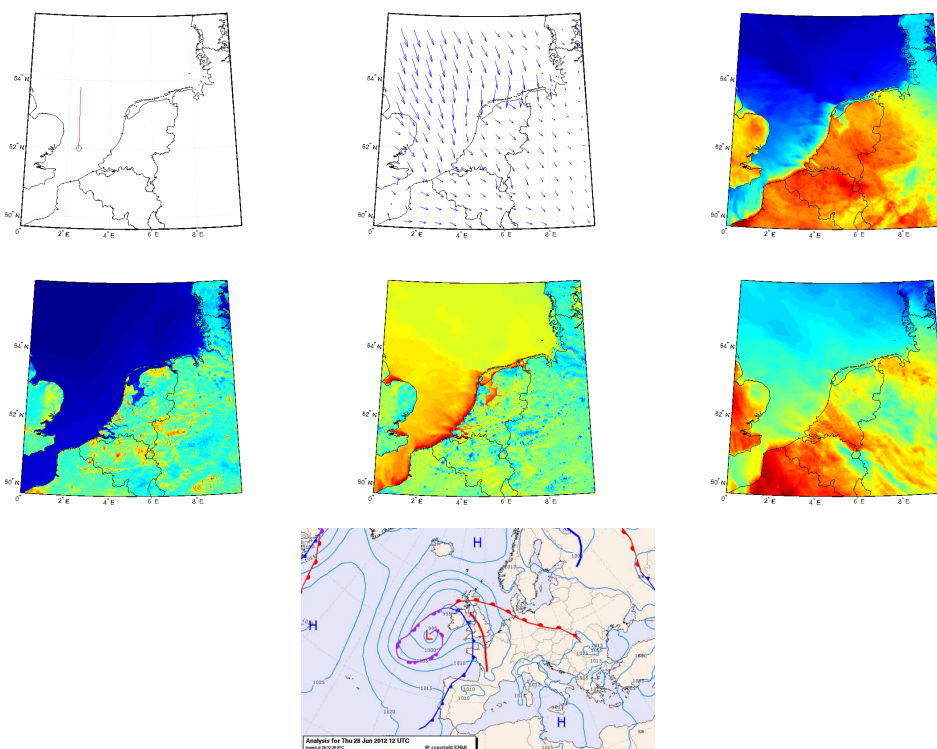


Scenario 17

Time, date	12:00, 28-06-2012 Z
Ship position, remarks	52.0 N - 2.5 E, -
Radar azimuth, remarks	000, -
Weather conditions	Warm sector, southerly wind, on average stable conditions over water

	Overall (min/max/mean)	Over water (min/max/mean)
Wind speed (kts)	0.01/25.58/9.46	0.12/25.58/13.37
Temperature (°C)	11.71/31.66/20.81	11.71/28.73/14.77
Sea surface temp. (°C)	11.79/48.56/22.25	11.79/29.34/13.16
Air-surface temp. difference (°C)	-20.69/15.16/-1.44	-10.75/13.97/1.60
Specific humidity ($\times 10^{-3}$ kg/kg)	5.26/16.39/11.18	6.68/14.46/9.62

General refractive conditions	Sub-refractive layers at surface and higher altitudes
--------------------------------------	---

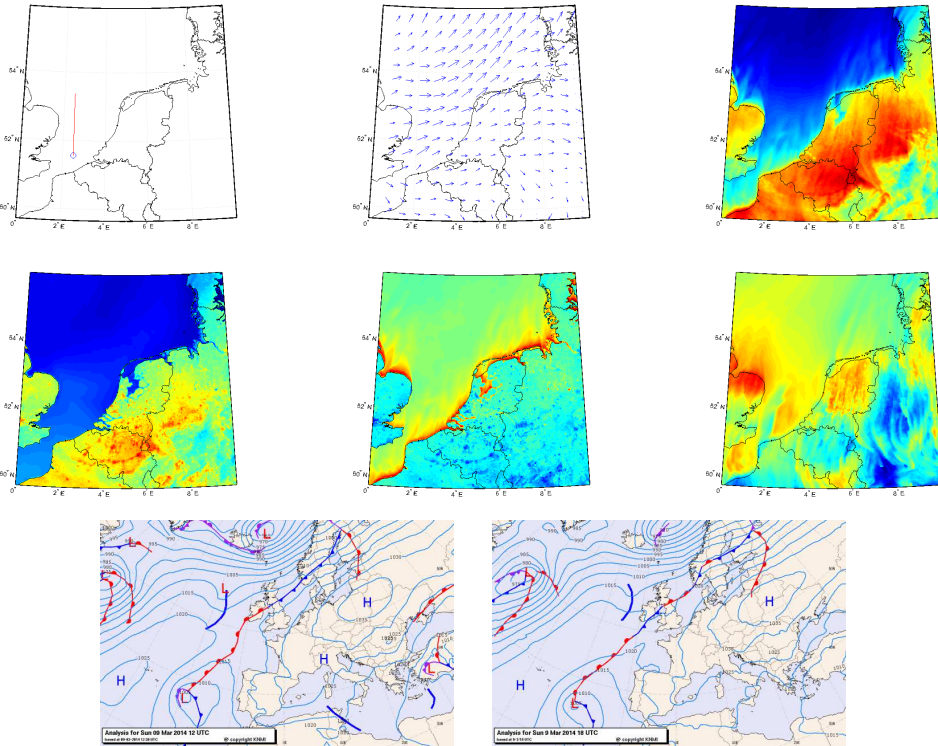


Scenario 18

Time, date	15:00, 09-03-2014 Z
Ship position, remarks	51.6 N - 2.5 E, north east of the English Channel
Radar azimuth, remarks	000, -
Weather conditions	Relatively warm dry air over a cold surface, southerly wind

	Overall (min/max/mean)	Over water (min/max/mean)
Wind speed (kts)	0.04/21.95/10.63	1.95/21.95/14.33
Temperature (°C)	6.65/22.02/13.68	6.76/20.19/9.31
Sea surface temp. (°C)	3.84/28.37/13.02	3.84/13.29/6.91
Air-surface temp. difference (°C)	-8.02/11.27/0.66	0.69/11.23/2.40
Specific humidity ($\times 10^{-3}$ kg/kg)	2.51/7.81/5.17	3.87/6.90/5.52

General refractive conditions Evaporation duct with heights decreasing from 15-5 m, multiple regions of strong ducting due to an elevated trapping layers, elevated trapping layer disappears abruptly

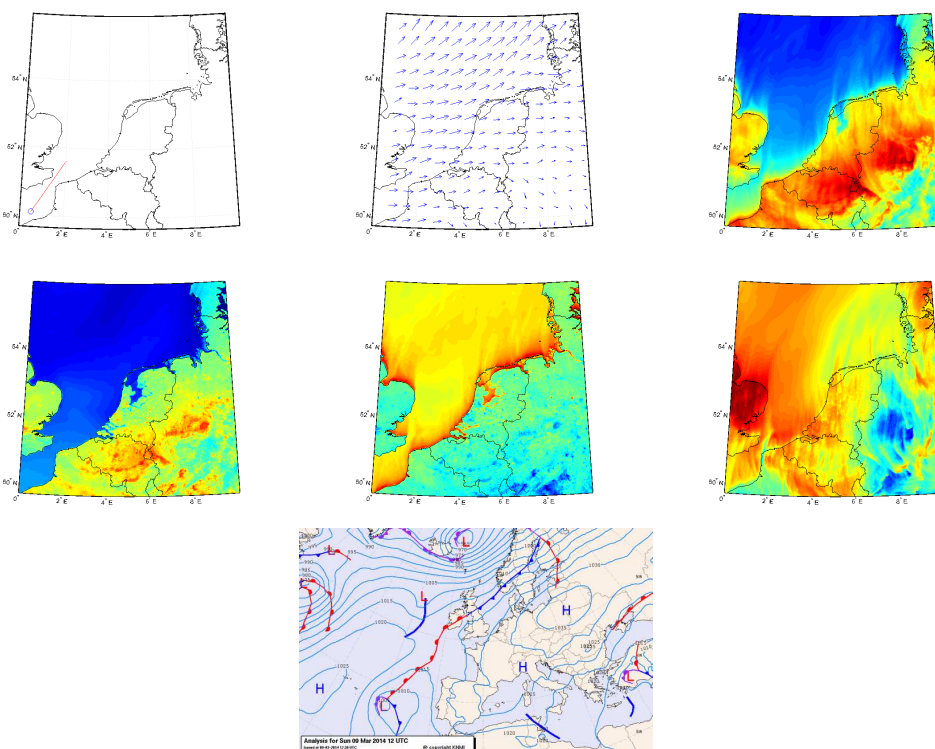


Scenario 19

Time, date	12:00, 09-03-2014 Z
Ship position, remarks	50.1 N - 0.5 E, in the English Channel
Radar azimuth, remarks	032, out of the channel
Weather conditions	Relatively warm dry air over a cold surface, westerly wind

	Overall (min/max/mean)	Over water (min/max/mean)
Wind speed (kts)	0.14/23.79/12.24	7.53/23.79/17.76
Temperature (°C)	5.47/19.54/12.23	5.47/16.85/8.89
Sea surface temp. (°C)	3.84/28.12/13.07	3.84/13.05/6.90
Air-surface temp. difference (°C)	-11.70/9.34/-0.83	0.46/8.96/1.99
Specific humidity ($\times 10^{-3}$ kg/kg)	2.14/6.80/4.97	4.00/6.52/5.30

General refractive conditions	Evaporation duct with heights decreasing from 20-10 m, ducting due to an elevated trapping layer at the beginning of the propagation path
--------------------------------------	---

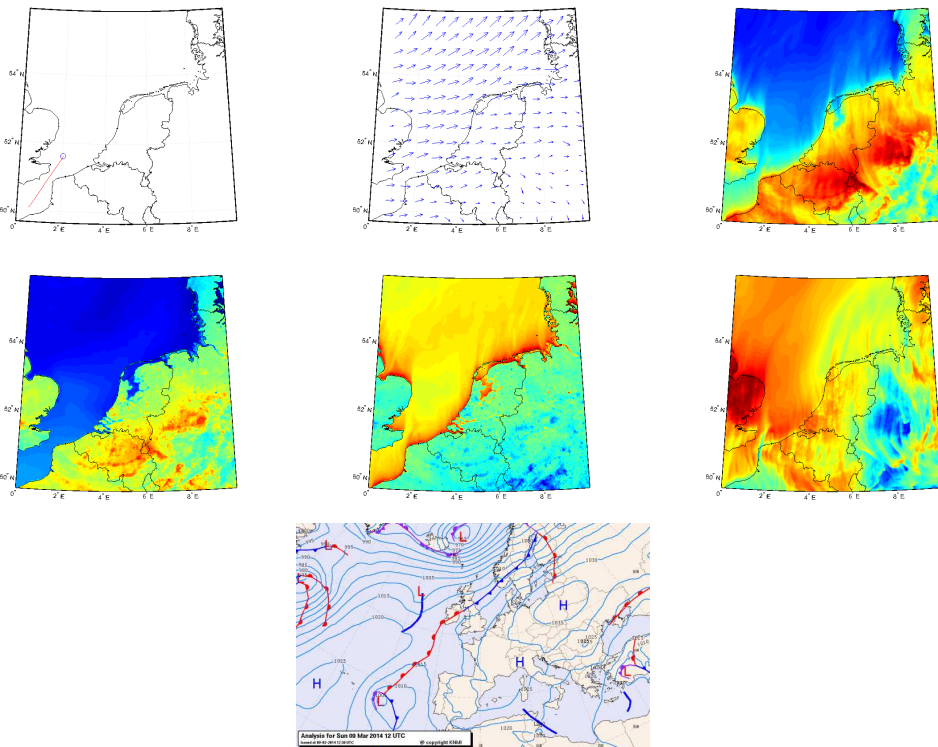


Scenario 20

Time, date	12:00, 09-03-2014 Z
Ship position, remarks	51.6 N - 2.0 E, north east of the English channel, 200 km north west of Scenario 19
Radar azimuth, remarks	212, into the channel, toward Scenario 19
Weather conditions	Relatively warm dry air over a cold surface, westerly wind

	Overall (min/max/mean)	Over water (min/max/mean)
Wind speed (kts)	0.14/23.79/12.24	7.53/23.79/17.76
Temperature (°C)	5.47/19.54/12.23	5.47/16.85/8.89
Sea surface temp. (°C)	3.84/28.12/13.07	3.84/13.05/6.90
Air-surface temp. difference (°C)	-11.70/9.34/-0.83	0.46/8.96/1.99
Specific humidity ($\times 10^{-3}$ kg/kg)	2.14/6.80/4.97	4.00/6.52/5.30

General refractive conditions Evaporation duct with heights increasing from 10-20 m, ducting due to an elevated trapping layer at the end of the propagation path



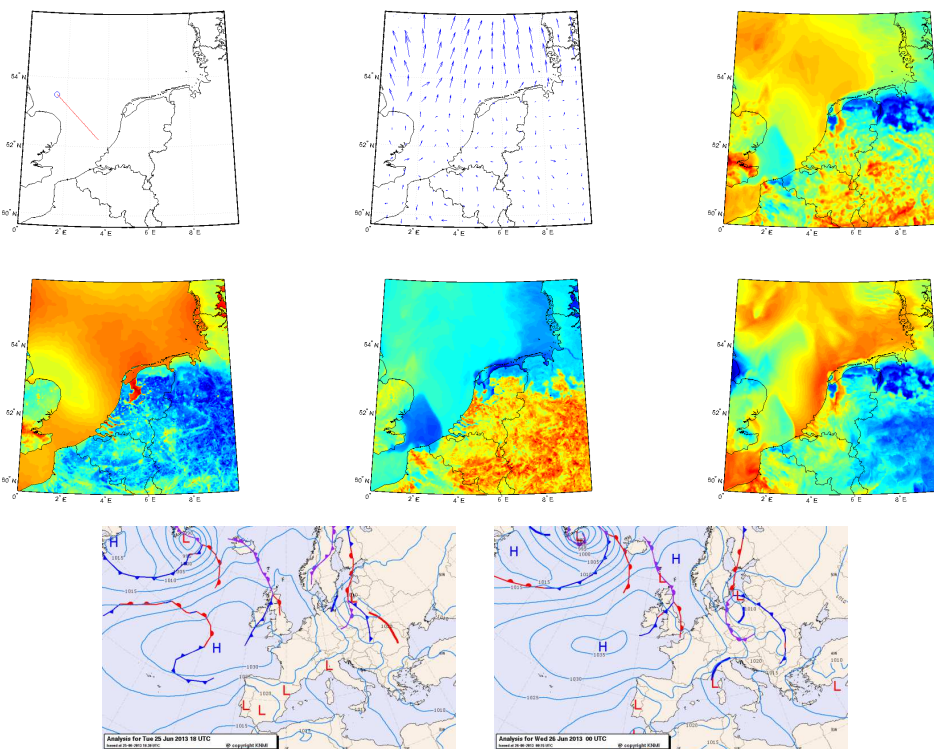
Scenario 21

Time, date	21:00, 25-06-2013 Z
Ship position, remarks	53.5 N - 1.5 E, near the east coast of England
Radar azimuth, remarks	135, -
Weather conditions	Relatively warm dry air over a cold surface, southerly wind

	Overall (min/max/mean)	Over water (min/max/mean)
Wind speed (kts)	0.01/17.84/4.52	0.03/17.84/7.31
Temperature (°C)	6.30/20.86/14.57	11.21/19.11/15.22
Sea surface temp. (°C)	4.75/19.99/12.66	13.57/19.58/15.48
Air-surface temp. difference (°C)	-6.76/10.91/1.91	-6.60/3.70/-0.26
Specific humidity ($\times 10^{-3}$ kg/kg)	5.84/11.48/8.71	6.70/10.74/9.44

General refractive conditions

Strong elevated trapping layer

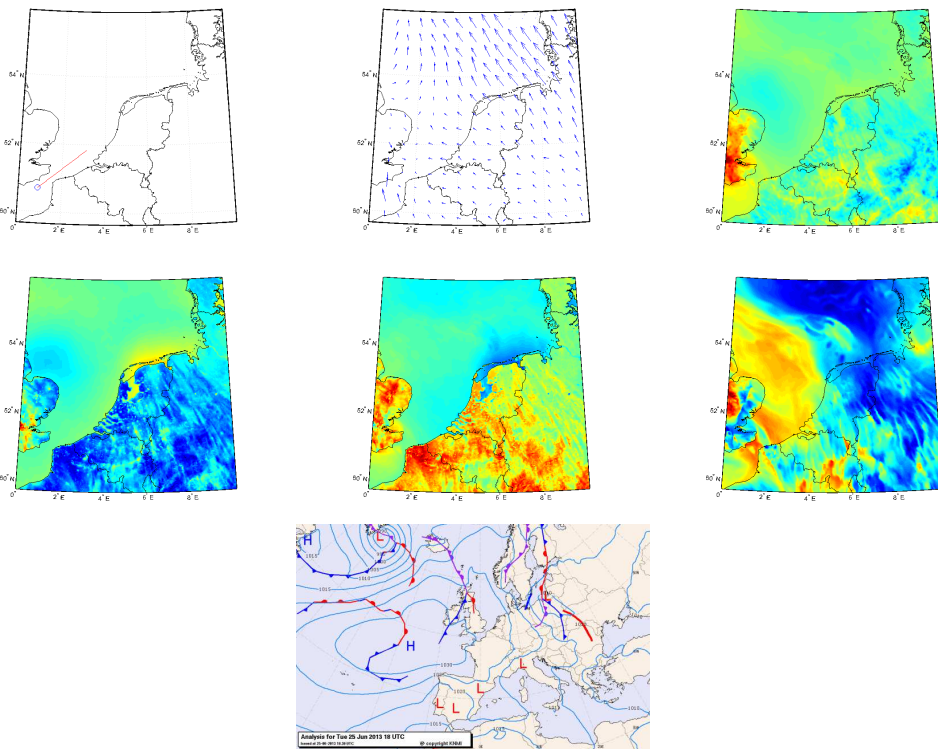


Scenario 22

Time, date	18:00, 25-06-2013 Z
Ship position, remarks	50.7 N - 0.9 E, in the English Channel
Radar azimuth, remarks	050, out of the channel
Weather conditions	Relatively warm dry air over a cold surface, south-easterly wind

	Overall (min/max/mean)	Over water (min/max/mean)
Wind speed (kts)	0.03/23.67/8.34	0.04/23.51/11.11
Temperature (°C)	5.46/18.89/11.91	10.65/15.83/11.98
Sea surface temp. (°C)	5.96/20.08/11.13	10.56/17.54/12.48
Air-surface temp. difference (°C)	-4.96/5.93/0.78	-4.04/3.71/-0.50
Specific humidity ($\times 10^{-3}$ kg/kg)	5.32/8.57/6.64	5.41/8.04/6.68

General refractive conditions Strong elevated trapping layer

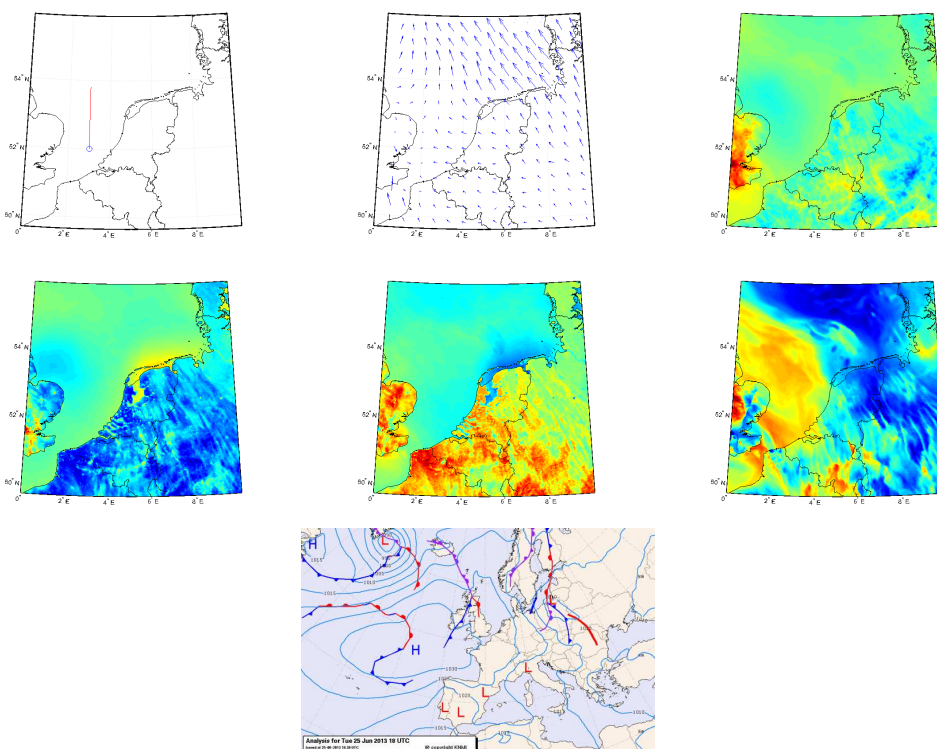


Scenario 23

Time, date	18:00, 25-06-2013 Z
Ship position, remarks	52.0 N - 3.0 E, north east of the English Channel
Radar azimuth, remarks	000, -
Weather conditions	Relatively warm dry air over a cold surface, south-easterly wind

	Overall (min/max/mean)	Over water (min/max/mean)
Wind speed (kts)	0.03/23.67/8.34	0.04/23.51/11.11
Temperature (°C)	5.46/18.89/11.91	10.65/15.83/11.98
Sea surface temp. (°C)	5.96/20.08/11.13	10.56/17.54/12.48
Air-surface temp. difference (°C)	-4.96/5.93/0.78	-4.04/3.71/-0.50
Specific humidity ($\times 10^{-3}$ kg/kg)	5.32/8.57/6.64	5.41/8.04/6.68

General refractive conditions	Evaporation duct with a height of approximately 3 m, at 75 km a strong elevated trapping layer appears
--------------------------------------	--

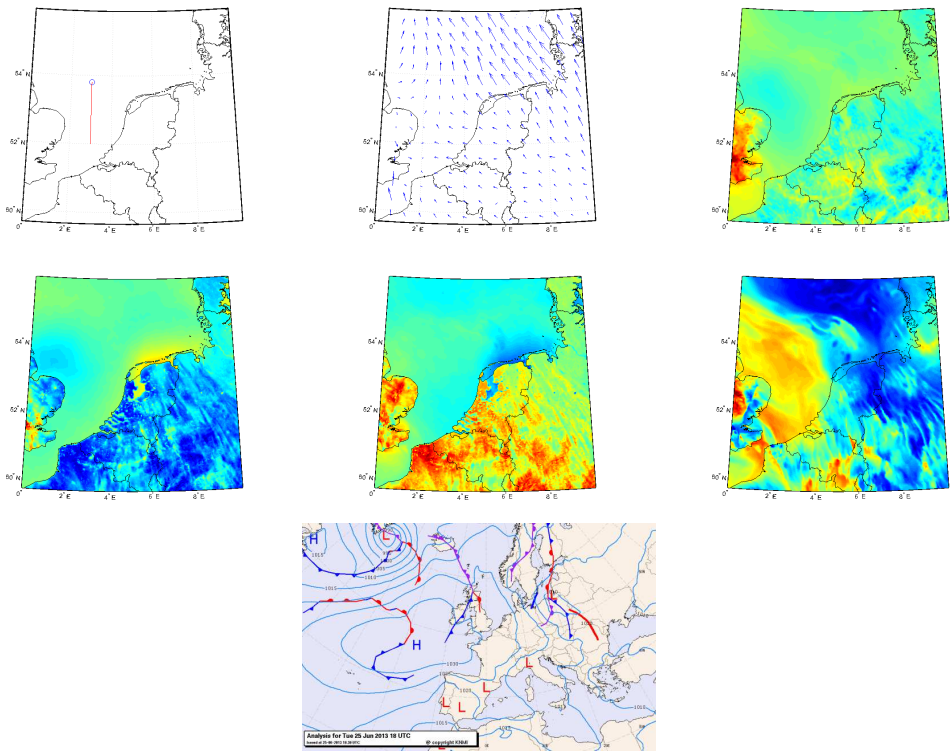


Scenario 24

Time, date	18:00, 25-06-2013 Z
Ship position, remarks	53.8 N - 3.0 E, north west of the Netherlands, 200 km north of Scenario 23
Radar azimuth, remarks	180, towards Scenario 23
Weather conditions	Relatively warm dry air over a cold surface, south-easterly wind

	Overall (min/max/mean)	Over water (min/max/mean)
Wind speed (kts)	0.03/23.67/8.34	0.04/23.51/11.11
Temperature (°C)	5.46/18.89/11.91	10.65/15.83/11.98
Sea surface temp. (°C)	5.96/20.08/11.13	10.56/17.54/12.48
Air-surface temp. difference (°C)	-4.96/5.93/0.78	-4.04/3.71/-0.50
Specific humidity ($\times 10^{-3}$ kg/kg)	5.32/8.57/6.64	5.41/8.04/6.68

General refractive conditions	Strong elevated trapping layer disappears at 125 km
--------------------------------------	---

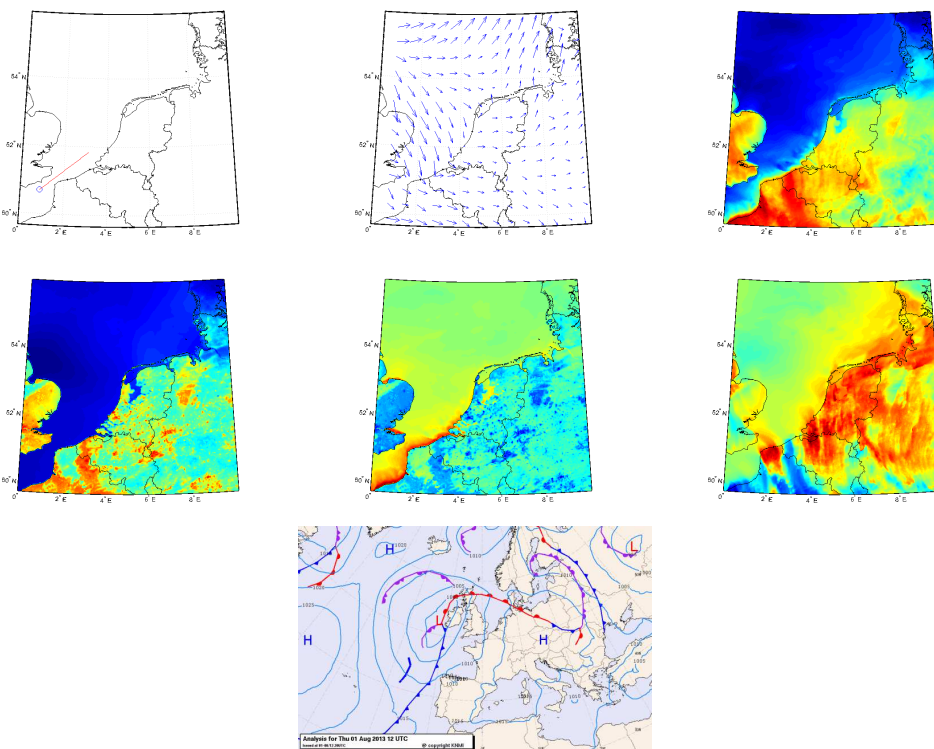


Scenario 25

Time, date	12:00, 01-08-2013 Z
Ship position, remarks	50.7 N - 0.9 E, in the English Channel
Radar azimuth, remarks	050, out of the channel
Weather conditions	Relatively warm dry air over a cold surface, easterly wind

	Overall (min/max/mean)	Over water (min/max/mean)
Wind speed (kts)	0.11/22.57/8.81	0.33/22.57/11.33
Temperature (°C)	15.44/34.92/23.28	15.44/33.16/18.28
Sea surface temp. (°C)	13.98/47.92/25.48	13.98/25.87/17.05
Air-surface temp. difference (°C)	-17.69/17.58/-2.20	-4.17/16.68/1.23
Specific humidity ($\times 10^{-3}$ kg/kg)	6.94/14.89/11.43	7.74/13.92/11.36

General refractive conditions	Strong elevated trapping regions
--------------------------------------	----------------------------------



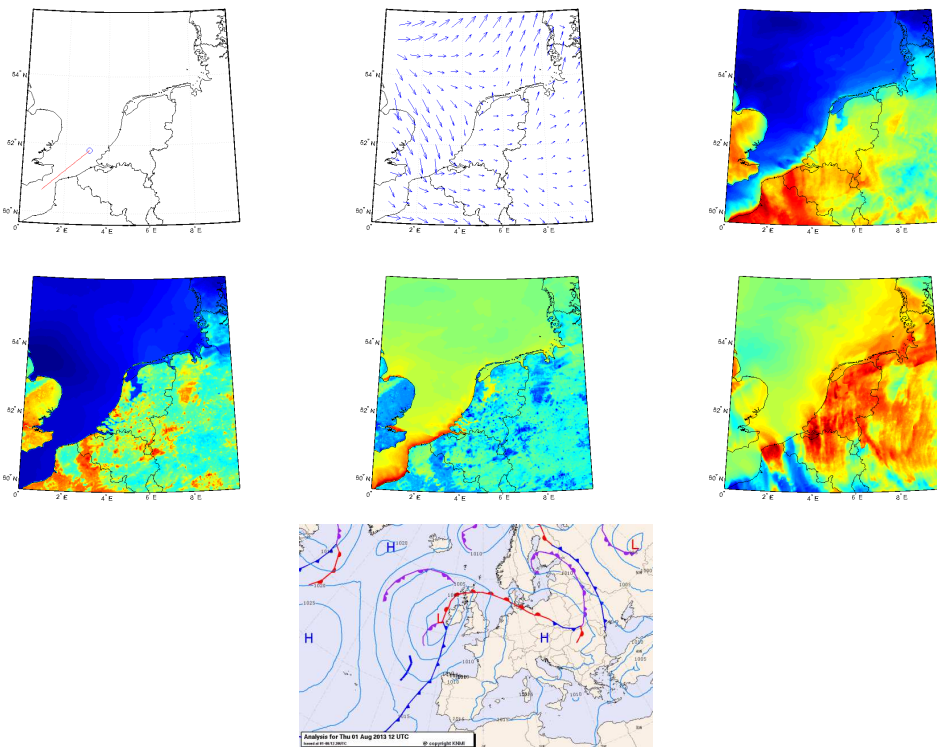
Scenario 26

Time, date	12:00, 01-08-2013 Z
Ship position, remarks	51.8 N - 3.1 E, north east of the English channel, 200 km north west of Scenario 25
Radar azimuth, remarks	230, into the channel, towards Scenario 25
Weather conditions	Relatively warm dry air over a cold surface, easterly wind

	Overall (min/max/mean)	Over water (min/max/mean)
Wind speed (kts)	0.11/22.57/8.81	0.33/22.57/11.33
Temperature (°C)	15.44/34.92/23.28	15.44/33.16/18.28
Sea surface temp. (°C)	13.98/47.92/25.48	13.98/25.87/17.05
Air-surface temp. difference (°C)	-17.69/17.58/-2.20	-4.17/16.68/1.23
Specific humidity ($\times 10^{-3}$ kg/kg)	6.94/14.89/11.43	7.74/13.92/11.36

General refractive conditions

Strong elevated trapping regions

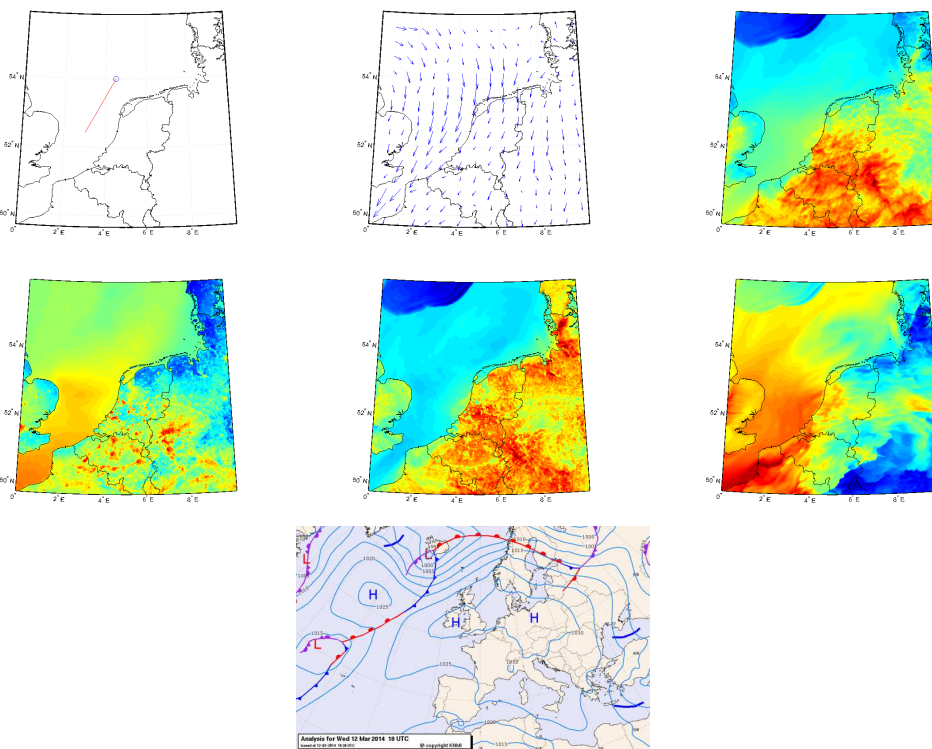


Scenario 27

Time, date	18:00, 12-03-2014 Z
Ship position, remarks	54.0 N - 4.5 E, -
Radar azimuth, remarks	210, -
Weather conditions	High pressure system, northerly wind, on average unstable conditions over water

	Overall (min/max/mean)	Over water (min/max/mean)
Wind speed (kts)	0.03/16.60/5.53	0.06/16.60/7.32
Temperature (°C)	0.60/17.56/9.33	0.60/14.06/6.97
Sea surface temp. (°C)	-1.28/14.03/6.49	4.42/10.35/7.21
Air-surface temp. difference (°C)	-5.49/10.05/2.84	-5.49/4.27/-0.24
Specific humidity ($\times 10^{-3}$ kg/kg)	2.37/7.21/4.81	3.36/7.06/5.29

General refractive conditions	Strong elevated trapping layer
--------------------------------------	--------------------------------

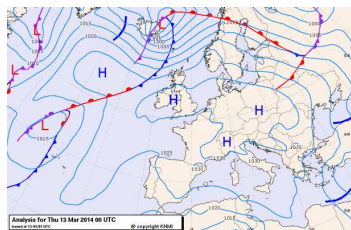
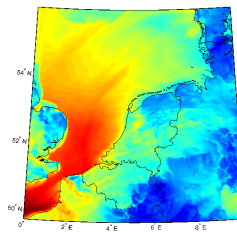
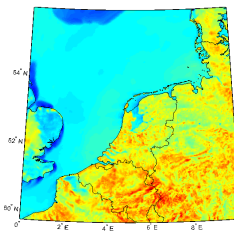
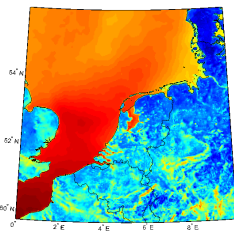
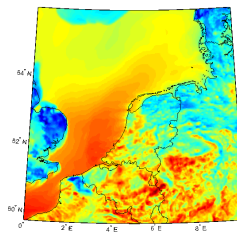
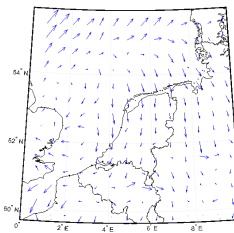
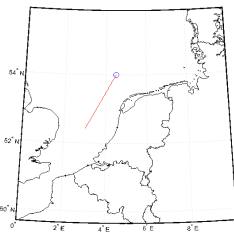


Scenario 28

Time, date	00:00, 13-03-2014 Z
Ship position, remarks	54.0 N - 4.5 E, same as Scenario 27
Radar azimuth, remarks	210, same as Scenario 27
Weather conditions	High pressure system, northerly wind, on average unstable conditions over water

	Overall (min/max/mean)	Over water (min/max/mean)
Wind speed (kts)	0.02/12.71/4.17	0.08/12.71/5.32
Temperature (°C)	-2.13/12.62/6.36	1.34/10.78/7.11
Sea surface temp. (°C)	-3.90/10.35/3.39	2.43/10.35/7.20
Air-surface temp. difference (°C)	-7.99/13.73/2.97	-6.36/2.51/-0.09
Specific humidity ($\times 10^{-3}$ kg/kg)	2.38/7.16/4.56	2.93/7.16/5.34

General refractive conditions Strong elevated trapping layer

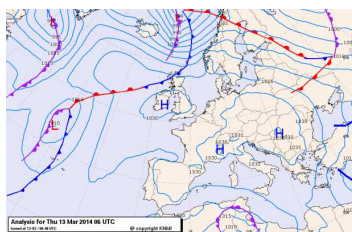
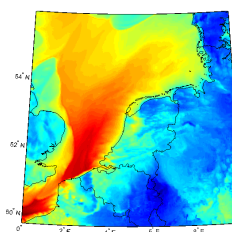
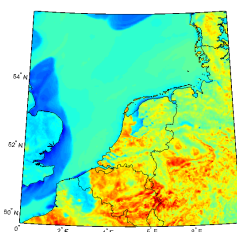
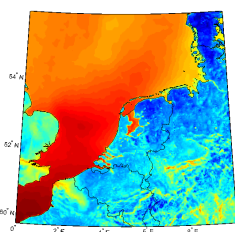
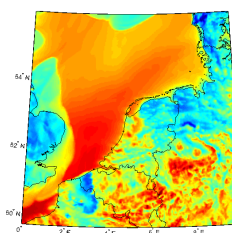
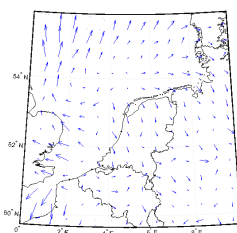
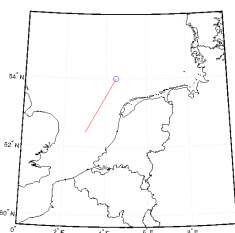


Scenario 29

Time, date	06:00, 13-03-2014 Z
Ship position, remarks	54.0 N - 4.5 E, same as Scenario 27
Radar azimuth, remarks	210, same as Scenario 27
Weather conditions	High pressure system, random wind, on average unstable conditions over water

	Overall (min/max/mean)	Over water (min/max/mean)
Wind speed (kts)	0.01/11.47/3.52	0.08/11.47/4.67
Temperature (°C)	-3.75/10.89/4.99	1.12/9.95/6.47
Sea surface temp. (°C)	-3.84/10.35/3.63	2.55/10.35/7.20
Air-surface temp. difference (°C)	-8.34/11.01/1.36	-6.37/1.98/-0.73
Specific humidity ($\times 10^{-3}$ kg/kg)	2.36/7.00/4.41	3.33/7.00/5.36

General refractive conditions	Strong elevated trapping layer
--------------------------------------	--------------------------------

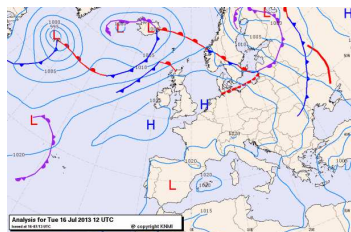
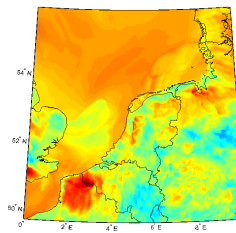
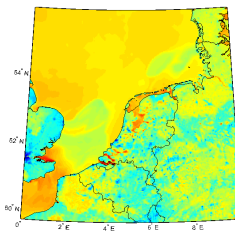
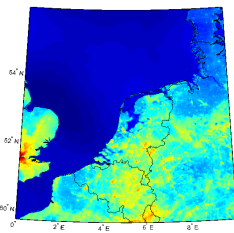
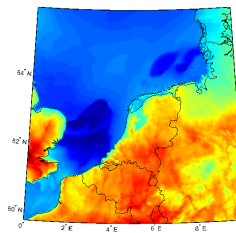
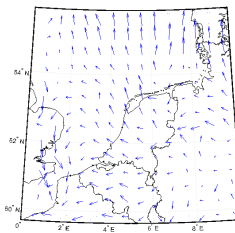
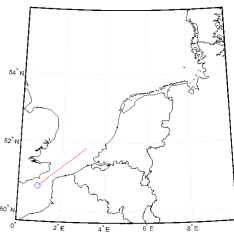


Scenario 30

Time, date	12:00, 16-07-2013 Z
Ship position, remarks	50.7 N - 0.9 E, in the English Channel
Radar azimuth, remarks	050, out of the channel
Weather conditions	High pressure system, random wind, on average stable conditions over water

	Overall (min/max/mean)	Over water (min/max/mean)
Wind speed (kts)	0.02/16.30/5.78	0.02/16.30/5.87
Temperature (°C)	11.50/31.44/21.17	11.50/25.49/15.61
Sea surface temp. (°C)	13.57/48.74/23.24	13.57/27.37/15.53
Air-surface temp. difference (°C)	-18.01/10.38/-2.08	-7.33/10.08/0.08
Specific humidity ($\times 10^{-3}$ kg/kg)	2.53/13.00/8.87	7.23/10.96/9.80

General refractive conditions	Strong elevated trapping layer
--------------------------------------	--------------------------------

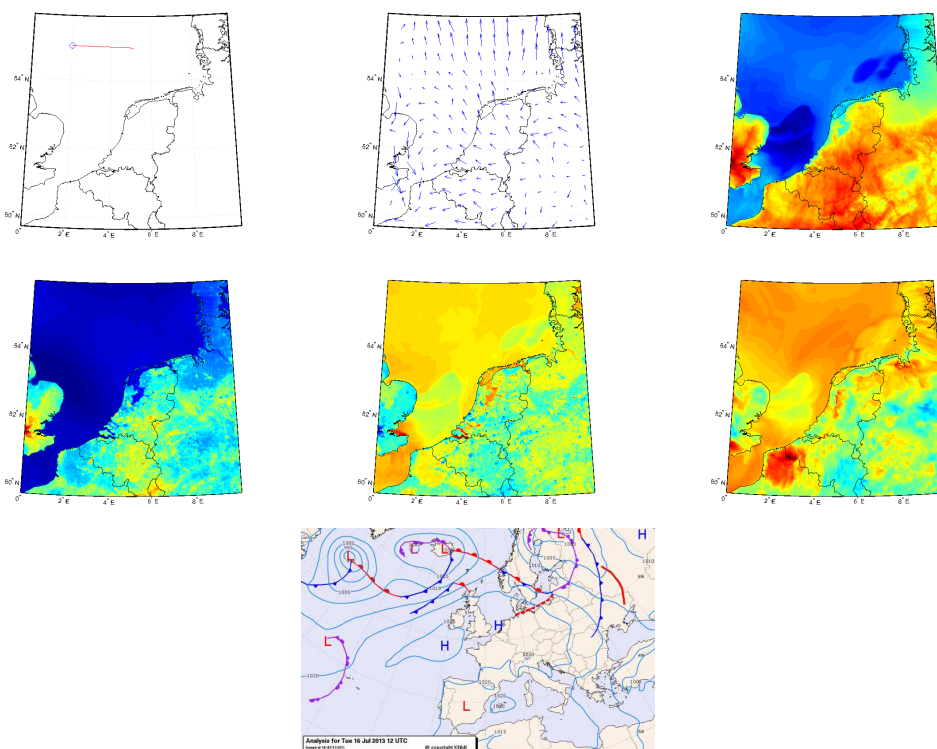


Scenario 31

Time, date	12:00, 16-07-2013 Z
Ship position, remarks	55.0 N - 2.0 E, -
Radar azimuth, remarks	090, -
Weather conditions	High pressure system, random wind, on average stable conditions over water

	Overall (min/max/mean)	Over water (min/max/mean)
Wind speed (kts)	0.02/16.30/5.78	0.02/16.30/5.87
Temperature (°C)	11.50/31.44/21.17	11.50/25.49/15.61
Sea surface temp. (°C)	13.57/48.74/23.24	13.57/27.37/15.53
Air-surface temp. difference (°C)	-18.01/10.38/-2.08	-7.33/10.08/0.08
Specific humidity ($\times 10^{-3}$ kg/kg)	2.53/13.00/8.87	7.23/10.96/9.80

General refractive conditions	Evaporation duct with a height of approximately 4 m
--------------------------------------	---

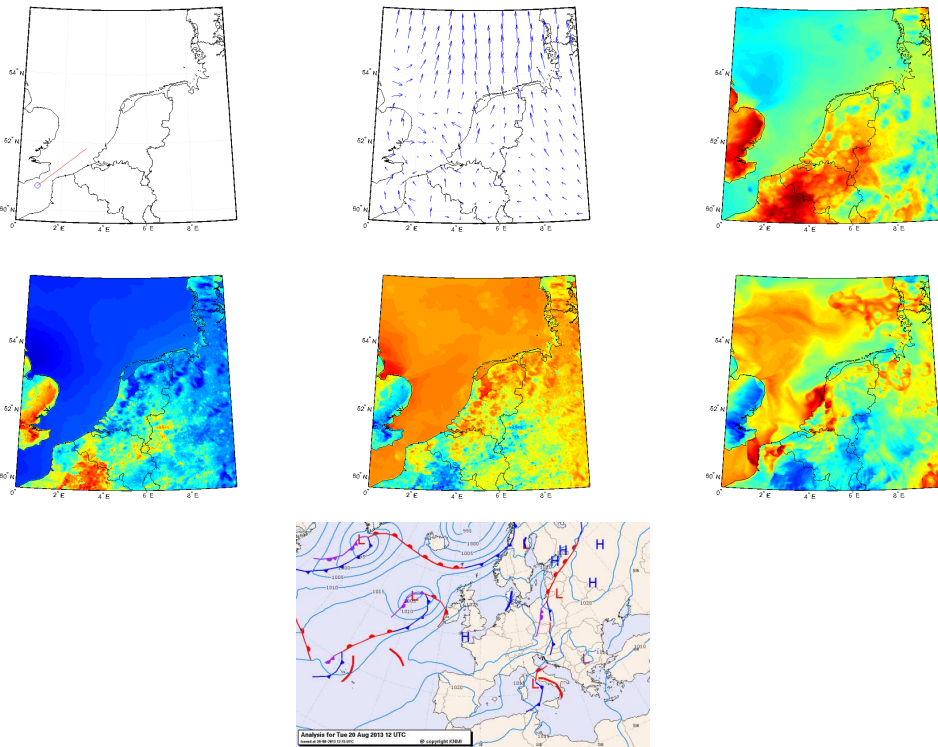


Scenario 32

Time, date	12:00, 20-08-2013 Z
Ship position, remarks	50.7 N - 0.9 E, in the English channel
Radar azimuth, remarks	050, out of the channel
Weather conditions	High pressure system, southerly wind, on average unstable conditions

	Overall (min/max/mean)	Over water (min/max/mean)
Wind speed (kts)	0.01/19.09/6.95	0.03/18.55/8.98
Temperature (°C)	10.98/23.60/17.92	14.08/21.14/16.47
Sea surface temp. (°C)	11.85/41.83/20.96	14.35/24.61/17.05
Air-surface temp. difference (°C)	-19.72/6.62/-3.04	-5.98/6.62/-0.58
Specific humidity ($\times 10^{-3}$ kg/kg)	4.54/10.52/7.86	5.92/10.40/8.37

General refractive conditions Strong elevated trapping layer

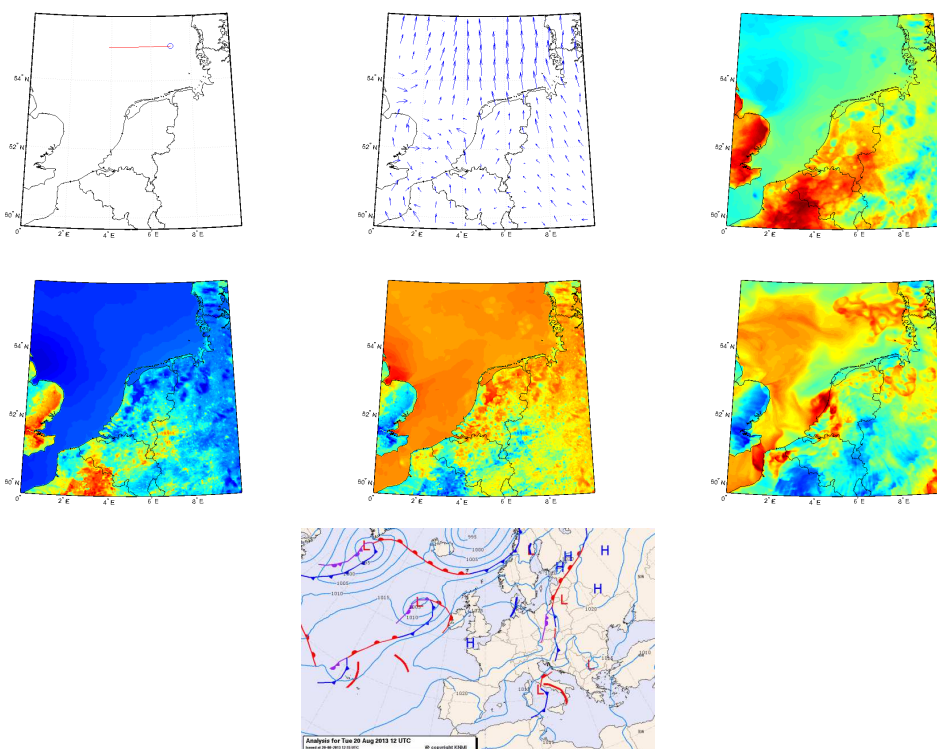


Scenario 33

Time, date	12:00, 20-08-2013 Z
Ship position, remarks	55.0 N - 7.0 E, -
Radar azimuth, remarks	270, -
Weather conditions	High pressure system, southerly wind, on average unstable conditions

	Overall (min/max/mean)	Over water (min/max/mean)
Wind speed (kts)	0.01/19.09/6.95	0.03/18.55/8.98
Temperature (°C)	10.98/23.60/17.92	14.08/21.14/16.47
Sea surface temp. (°C)	11.85/41.83/20.96	14.35/24.61/17.05
Air-surface temp. difference (°C)	-19.72/6.62/-3.04	-5.98/6.62/-0.58
Specific humidity ($\times 10^{-3}$ kg/kg)	4.54/10.52/7.86	5.92/10.40/8.37

General refractive conditions	Evaporation duct with heights varying between 5-12 m
--------------------------------------	--

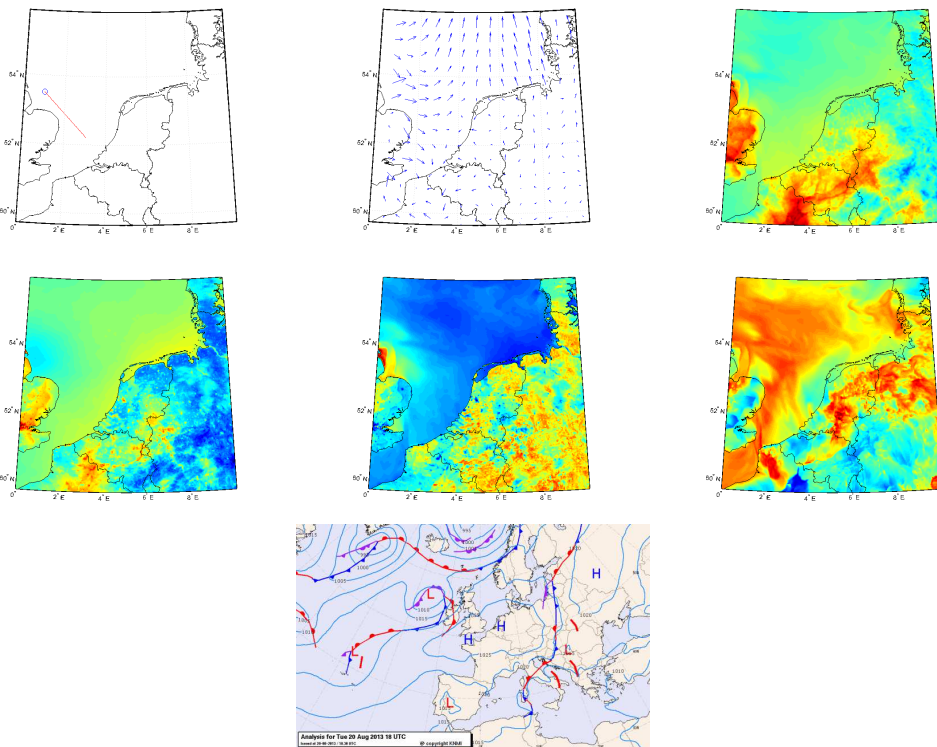


Scenario 34

Time, date	18:00, 20-08-2013 Z
Ship position, remarks	53.5 N - 1.0 E, close to the coast of England
Radar azimuth, remarks	135, -
Weather conditions	High pressure system, random wind, on average unstable conditions over water

	Overall (min/max/mean)	Over water (min/max/mean)
Wind speed (kts)	0.02/19.11/5.64	0.06/19.11/8.54
Temperature (°C)	10.30/23.47/17.12	15.51/21.14/16.60
Sea surface temp. (°C)	8.51/25.54/15.98	14.35/19.06/17.02
Air-surface temp. difference (°C)	-2.91/6.63/1.14	-2.39/6.63/-0.42
Specific humidity ($\times 10^{-3}$ kg/kg)	4.76/10.47/8.07	6.31/9.81/8.54

General refractive conditions	Strong elevated trapping layer
--------------------------------------	--------------------------------

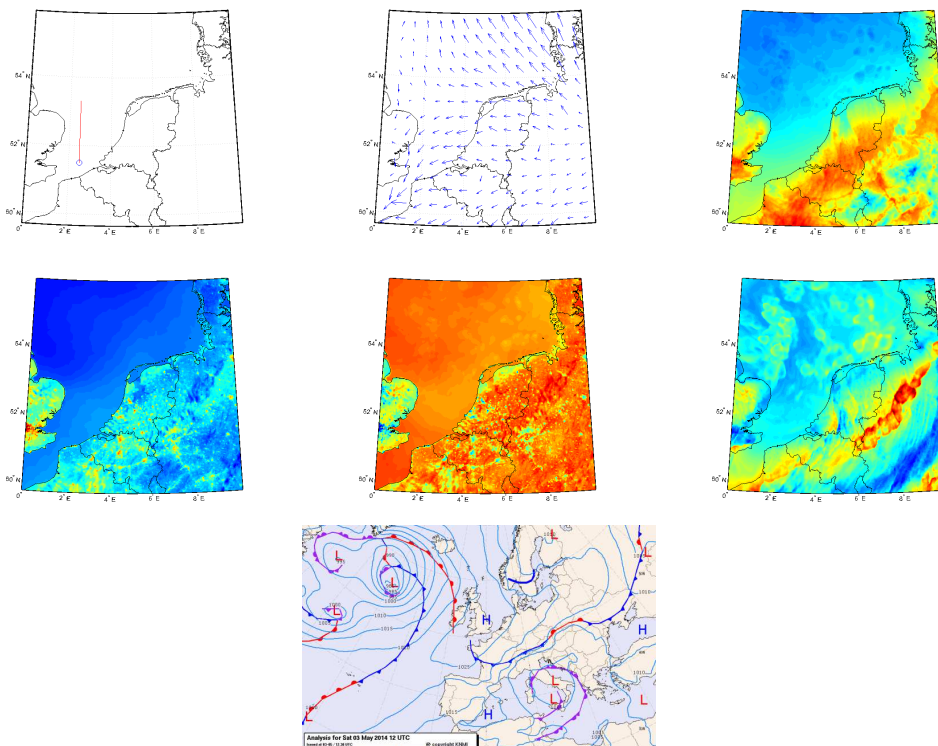


Scenario 35

Time, date	12:00, 03-05-2014 Z
Ship position, remarks	51.5 N - 2.5 E, -
Radar azimuth, remarks	000, -
Weather conditions	Relatively calm unstable conditions, high pressure system above England, easterly wind

	Overall (min/max/mean)	Over water (min/max/mean)
Wind speed (kts)	0.01/21.45/8.95	0.03/21.45/9.88
Temperature (°C)	4.12/15.01/9.56	6.47/12.31/7.75
Sea surface temp. (°C)	5.61/28.54/12.25	8.52/15.48/10.15
Air-surface temp. difference (°C)	-15.51/1.99/-2.69	-6.83/1.20/-2.40
Specific humidity ($\times 10^{-3}$ kg/kg)	2.58/6.24/4.15	3.45/5.23/3.99

General refractive conditions	Evaporation duct with heights decreasing from 8-5 m
--------------------------------------	---

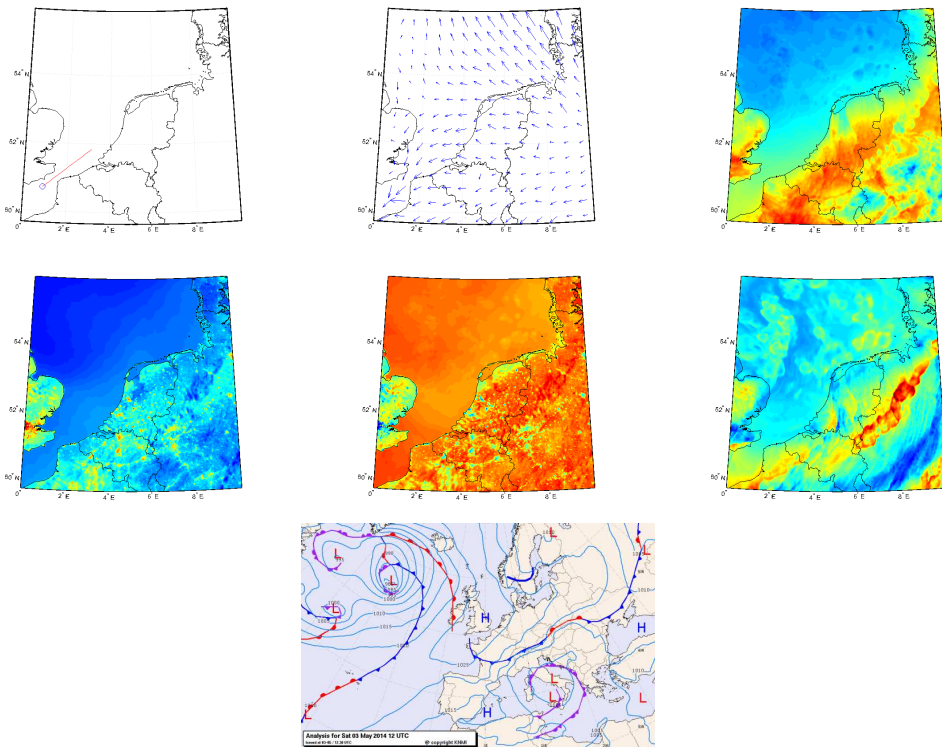


Scenario 36

Time, date	12:00, 03-05-2014 Z
Ship position, remarks	50.7 N - 0.9 E, -
Radar azimuth, remarks	050, -
Weather conditions	Relatively calm unstable conditions, high pressure system above England, easterly wind

	Overall (min/max/mean)	Over water (min/max/mean)
Wind speed (kts)	0.01/21.45/8.95	0.03/21.45/9.88
Temperature (°C)	4.12/15.01/9.56	6.47/12.31/7.75
Sea surface temp. (°C)	5.61/28.54/12.25	8.52/15.48/10.15
Air-surface temp. difference (°C)	-15.51/1.99/-2.69	-6.83/1.20/-2.40
Specific humidity ($\times 10^{-3}$ kg/kg)	2.58/6.24/4.15	3.45/5.23/3.99

General refractive conditions	Evaporation duct with a height of approximately 9 m
--------------------------------------	---

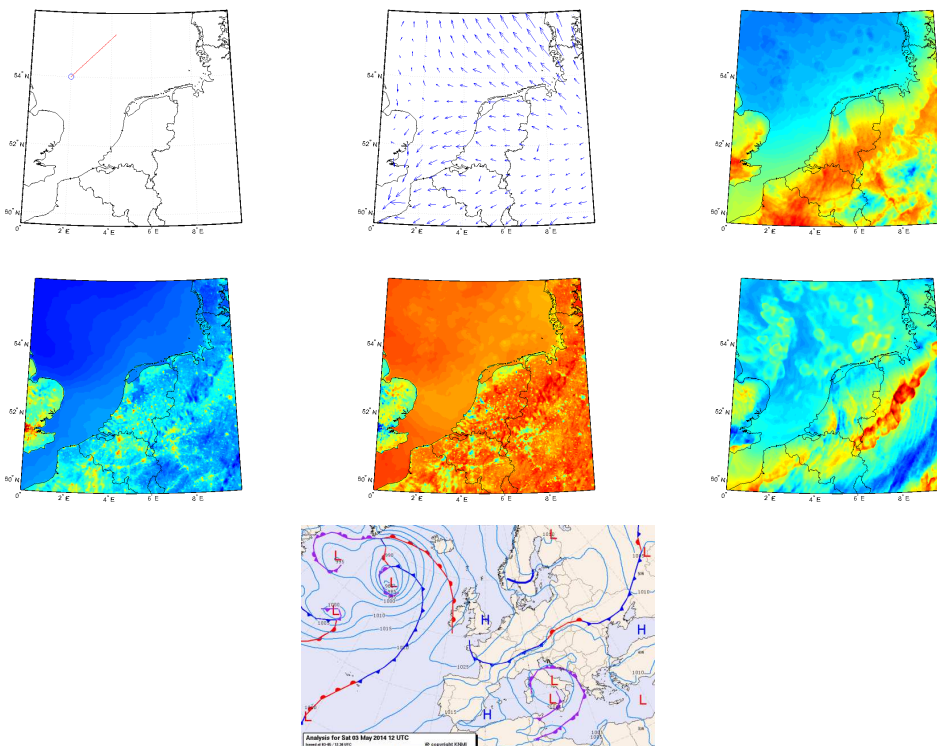


Scenario 37

Time, date	12:00, 03-05-2014 Z
Ship position, remarks	54.0 N - 2.0 E, -
Radar azimuth, remarks	045, -
Weather conditions	Relatively calm unstable conditions, high pressure system above England, easterly wind

	Overall (min/max/mean)	Over water (min/max/mean)
Wind speed (kts)	0.01/21.45/8.95	0.03/21.45/9.88
Temperature (°C)	4.12/15.01/9.56	6.47/12.31/7.75
Sea surface temp. (°C)	5.61/28.54/12.25	8.52/15.48/10.15
Air-surface temp. difference (°C)	-15.51/1.99/-2.69	-6.83/1.20/-2.40
Specific humidity ($\times 10^{-3}$ kg/kg)	2.58/6.24/4.15	3.45/5.23/3.99

General refractive conditions	Evaporation duct with a height increasing from 5-7 m
--------------------------------------	--

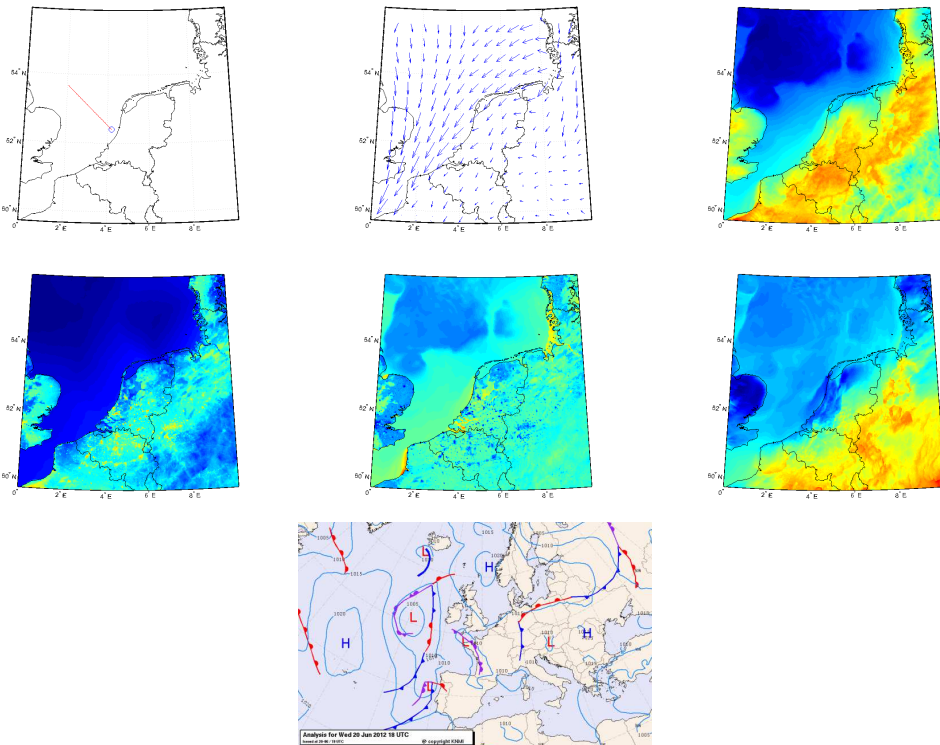


Scenario 38

Time, date	18:00, 20-06-2012 Z
Ship position, remarks	52.4 N - 4.2 E, close to the coast of the Netherlands
Radar azimuth, remarks	315, Pointed out to sea
Weather conditions	Relatively calm unstable conditions, north-easterly wind

	Overall (min/max/mean)	Over water (min/max/mean)
Wind speed (kts)	0.08/23.51/9.20	0.16/23.51/12.97
Temperature (°C)	8.58/26.48/16.29	8.58/22.22/12.17
Sea surface temp. (°C)	11.70/33.69/16.87	11.70/19.81/13.19
Air-surface temp. difference (°C)	-7.72/10.90/-0.58	-3.63/7.71/-1.02
Specific humidity ($\times 10^{-3}$ kg/kg)	4.43/15.12/9.00	5.17/10.58/7.56

General refractive conditions Strong surface based duct

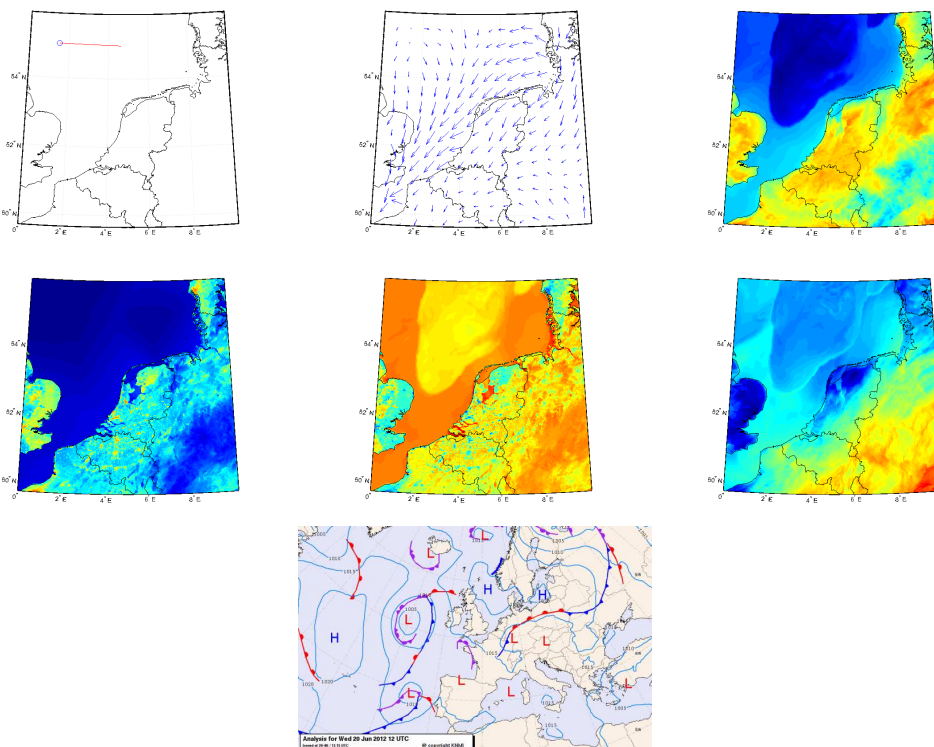


Scenario 39

Time, date	12:00, 20-06-2012 Z
Ship position, remarks	55.0 N - 1.5 E, -
Radar azimuth, remarks	090, -
Weather conditions	Relatively calm unstable conditions, north-easterly wind

	Overall (min/max/mean)	Over water (min/max/mean)
Wind speed (kts)	0.04/21.83/7.92	0.04/20.98/9.44
Temperature (°C)	8.83/26.39/16.42	8.83/20.27/12.20
Sea surface temp. (°C)	11.70/44.54/19.00	11.70/23.97/13.21
Air-surface temp. difference (°C)	-21.66/7.77/-2.57	-8.05/5.34/-1.01
Specific humidity ($\times 10^{-3}$ kg/kg)	4.60/14.75/8.92	4.87/9.33/7.76

General refractive conditions	Strong surface duct disappearing at approximately 75 km
--------------------------------------	---

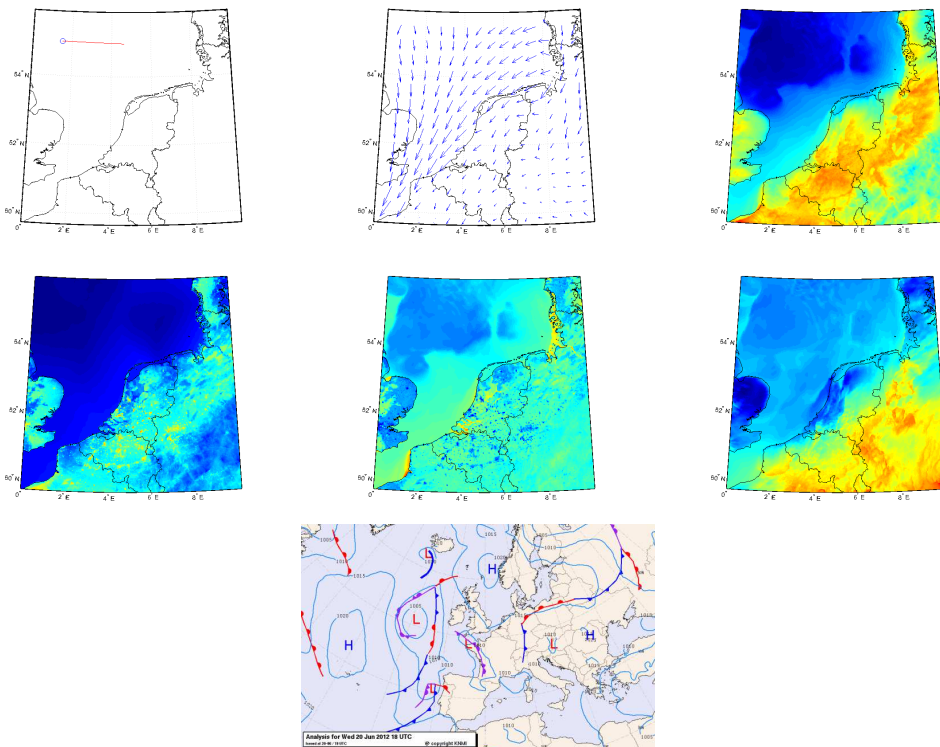


Scenario 40

Time, date	18:00, 20-06-2012 Z
Ship position, remarks	55.0 N - 1.5 E, same position as Scenario 31
Radar azimuth, remarks	090, same azimuth as Scenario 31
Weather conditions	Relatively calm unstable conditions, north-easterly wind

	Overall (min/max/mean)	Over water (min/max/mean)
Wind speed (kts)	0.08/23.51/9.20	0.16/23.51/12.97
Temperature (°C)	8.58/26.48/16.29	8.58/22.22/12.17
Sea surface temp. (°C)	11.70/33.69/16.87	11.70/19.81/13.19
Air-surface temp. difference (°C)	-7.72/10.90/-0.58	-3.63/7.71/-1.02
Specific humidity ($\times 10^{-3}$ kg/kg)	4.43/15.12/9.00	5.17/10.58/7.56

General refractive conditions	Evaporation duct with a height of approximately 3 m
--------------------------------------	---

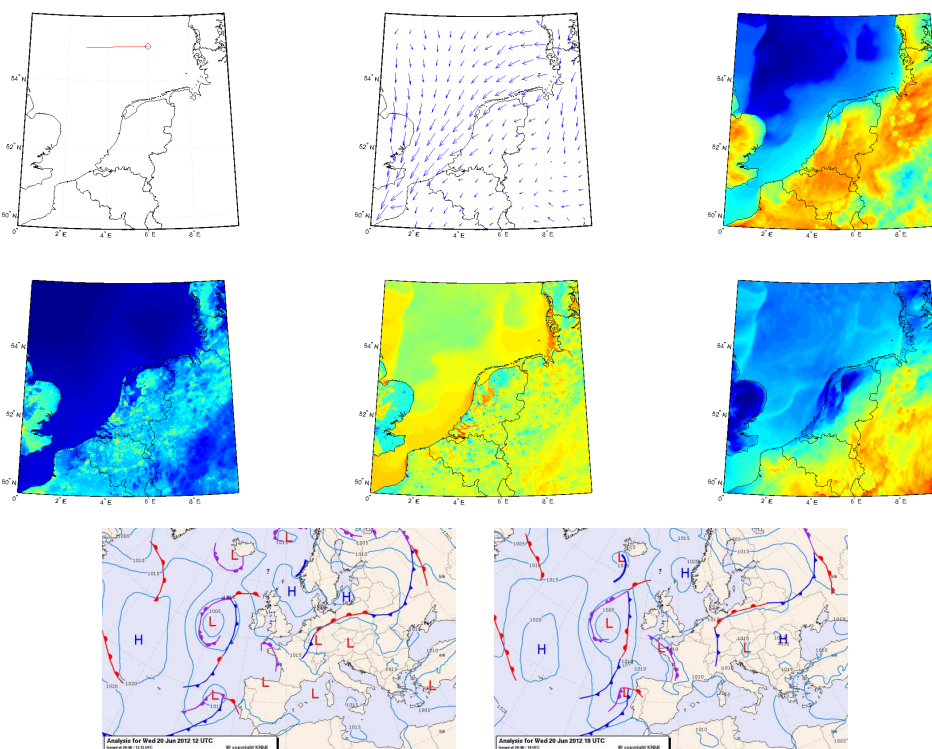


Scenario 41

Time, date	15:00, 20-06-2012 Z
Ship position, remarks	55.0 N - 6.0 E, -
Radar azimuth, remarks	270, -
Weather conditions	Relatively calm unstable conditions, north-easterly wind

	Overall (min/max/mean)	Over water (min/max/mean)
Wind speed (kts)	0.07/22.71/8.97	0.16/22.71/11.75
Temperature (°C)	8.56/26.59/16.68	8.56/21.82/12.19
Sea surface temp. (°C)	11.70/44.02/18.17	11.70/22.47/13.21
Air-surface temp. difference (°C)	-17.67/10.80/-1.49	-3.97/6.84/-1.02
Specific humidity ($\times 10^{-3}$ kg/kg)	4.73/14.86/8.99	5.14/9.58/7.61

General refractive conditions	Evaporation duct with a height of approximately 3 m
--------------------------------------	---



References

- [1] H. V. Hitney, "Refractive effects from VHF to EHF - part A: propagation mechanisms," *Advisory Group for Aerospace Research & Development*, vol. LS-196, pp. 4A-1 – 4A-13, 1994.
- [2] Space and Naval Warfare Systems Command (SPAWAR), *User's manual (UM) for Advanced Refractive Effects Predictions System (AREPS)*. Space and Naval Warfare Systems Command (SPAWAR), San Diego, 3.6 ed., December 2006.
- [3] W. F. Ford, "Atmospheric refraction: how electromagnetic waves bend in the atmosphere and why it matters." http://www.met.nps.edu/~psgust/EMEO_online/module4/Atmospheric_Refraction_of_EM_Waves.doc.
- [4] G. D. Dockery and J. Goldhirsh, "Atmospheric data resolution requirements for propagation assessment: case studies for range-dependent coastal environments," in *Propagation Assessment in Coastal Environments*, pp. 7-1 – 7-13, September 1994. Paper presented at the Sensor and Propagation Panel Symposium on "Propagation Assessment in Coastal Environments" held in Bremerhaven, Germany 19-22 September 1994.
- [5] G. D. Dockery, "Development and use of electromagnetic parabolic equation propagation models for U.S. navy applications," *Johns Hopkins APL Technical Digest*, vol. 19, no. 3, pp. 283-292, 1998.
- [6] H. V. Hitney, "Refractive effects from VHF to EHF - part B: propagation models," *Advisory Group for Aerospace Research & Development*, vol. LS-196, pp. 4A-1 – 4A-13, 1994.
- [7] I. Sirkova, "Brief review on PE method application to propagation channel modeling in sea environment," *Central European Journal of Engineering*, vol. 2, no. 1, pp. 19-38, 2012.
- [8] A. E. Barrios, "A terrain parabolic equation model for propagation in the troposphere," *IEEE Transactions on Antennas and Propagation*, vol. 42, pp. 90-98, Januari 1994.

- [9] H. V. Hitney, J. H. Richter, R. A. Pappert, K. D. Anderson, and G. B. Baumgartner, "Tropospheric radio propagation assessment," *Proceedings of the IEEE*, vol. 73, no. 2, pp. 265–283, 1985.
- [10] J. H. Richter, "Sensing of radio refractivity and aerosol extinction," *Advisory Group for Aerospace Research & Development*, vol. LS-196, pp. 3–1 – 3–16, 1994.
- [11] J. Goldhirsh and G. D. Dockery, "Measurement resolution criteria for assessment of coastal ducting," in *Antennas and Propagation*, vol. 2, pp. 317–322, 1995.
- [12] R. E. Marshall, W. D. Thornton, G. Lefurjah, and T. S. Casey, "Modeling and simulation of notional future radar in non/standard propagation environment facilitated by mesoscale numerical weather prediction modeling," *Naval engineers journal*, vol. 120, pp. 55–66, 2008.
- [13] T. Haack, C. Wang, S. Garrett, A. Glazer, J. Mailhot, and R. E. Marshall, "Mesoscale modeling of boundary layer refractivity and atmospheric ducting," tech. rep., Naval Research Laboratory, Monterey, California USA; Defence Technology Agency, Auckland, New Zealand; Environment Canada, Meteorological Service of Canada, Dorval, Qu'Ébec Canada; Naval Surface Warfare Center, Dahlgren, Virginia USA, March 2010.
- [14] Space and Naval Warfare Systems Command (SPAWAR), "Face to face discussions," September 2014.
- [15] C. Bailey, *Principles of modern radar - basis principles*, ch. 9, pp. 309–346. SciTech Publishing, 2010.
- [16] J. Griffiths, *Radio wave propagation and antennas - an introduction*. Prentice-Hall International LTD, London, 1987.
- [17] B. R. Bean and E. J. Dutton, *Radio meteorology*. Dover Publications, New York, March 1966.
- [18] E. K. Smith and S. Weintraub, "The constants in the equation for atmospheric refractive index at radio frequencies," *Proceedings of the IRE*, vol. 41, no. 8, pp. 1035–1037, 1953.
- [19] K. H. Craig, "Clear-air characteristics of the troposphere," in *Propagation of radiowaves* (L. Barclay, ed.), ch. 7, pp. 103–128, The Institution of Electrical Engineers, London, 2nd ed., 2003.
- [20] J. Derksen, "Microwave ray tracing - modelling the propagation of microwaves through a non-uniform atmosphere near the earth's surface," Master's thesis, Royal Netherlands Naval College, March 2012.
- [21] H. R. Reed and C. M. Russel, *Ultra high frequency propagation*. Chapman & Hall LTD, London, 2nd ed., 1965.
- [22] 527-3 Recommendation, "Electrical characteristics of the surface of the earth," tech. rep., ITU-R, March 1992.
- [23] A. G. Huizing and A. Theil, *Computer-Aided Radar Performance Evaluation Tool (CARPET) version 2.0 manual*. Netherlands Organisation for Applied Scientific Research (TNO) Physics and Electronic Laboratory, The Hague, 1.2 ed.

-
- [24] A. Picquenard, *Radio wave propagation*. The Macmillan Press LTD, London, 1979.
- [25] M. I. Skolnik, *Introduction to radar system*. McGraw-Hill Companies, Inc., New York, 3rd ed., 2001.
- [26] J. Saffold, *Principles of modern radar - basis principles*, ch. 4, pp. 112–164. SciTech Publishing, 2010.
- [27] 526-13 Recommendation, “Propagation by diffraction,” tech. rep., ITU-R, March 2013.
- [28] J. H. Whittaker, “Ground wave and diffraction - part A,” *Advisory Group for Aerospace Research & Development*, vol. LS-196, 1994.
- [29] J. H. Whittaker, “Ground wave and diffraction - part B,” *Advisory Group for Aerospace Research & Development*, vol. LS-196, 1994.
- [30] L. P. Yeh, “Simple methods for designing troposcatter circuits,” *IRE transactions on communications systems*, 1960.
- [31] 617-3 Recommendation, “Propagation prediction techniques and data required for the design of trans/horizon radio/relay systems,” tech. rep., ITU-R, March 2013.
- [32] 676-3 Recommendation, “Attenuation by atmospheric gases,” tech. rep., ITU-R, 1997.
- [33] 840-3 Recommendation, “Attenuation due to clouds and fog,” tech. rep., ITU-R, 1999.
- [34] T. Wilbrink, “Elektromagnetische propagatie.” Royal Netherlands Navy, August 2010.
- [35] K. L. Twigg, “A smart climatology of evaporation duct height and surface radar propagation in the indian ocean,” Master’s thesis, Naval Postgraduate School, 2007.
- [36] F. E. Nathanson, J. P. Reilly, and M. N. Cohen, *Radar design principles - signal processing and the environment*. McGraw-Hill Companies, Inc., New Jersey, 2nd ed., 1999.
- [37] J. Brandon, “Pilot friend - weather fronts.” <http://www.pilotfriend.com/index.htm>, October 2014.
- [38] J. Goldhirsh and G. D. Dockery, “Propagation factor errors due to the assumption of lateral homogeneity,” *Radio Science*, vol. 33, pp. 239–249, March-April 1998.
- [39] O. Ozgun, G. Apaydin, M. Kuzuoglu, and L. Sevgi, “PETOOL: MATLAB based one-way and two-way split-step parabolic equation tool for radiowave propagation over variable terrain,” *Computer Physics Communications*, 2011.
- [40] Y. K. Chuan, L. M. Kwong, J. S. R. Chen, and F. C. Liheng, “Ducting phenomena and their impact on a pulse doppler radar,” *Defence Science & Technology Agency - Horizons*, 2010.
- [41] E. L. Cairns-McFeeters, “Effects of surface-based ducts on electromagnetic systems,” Master’s thesis, Naval Postgraduate School, 1992.
- [42] M. Levy, *Parabolic equation methods for electromagnetic wave propagation*. The Institution of Electrical Engineers, London, 2000.

- [43] A. E. Barrios, "Considerations in the development of the Advanced Propagation Model (APM) for U.S. navy applications," in *Radar Conference, 2003. Proceedings of the International*, pp. 77–82, 2003.
- [44] M. Richards, J. A. Scheer, and W. A. Holm, eds., *Principles of modern radar - basic principles*. Scitech publishing, 2010.
- [45] C. C. Constantinou, "Numerically intensive propagation prediction methods," in *Propagation of radiowaves* (L. Barclay, ed.), ch. 10, pp. 163–183, The Institution of Electrical Engineers, London, 2nd ed., 2003.
- [46] J. R. Kuttler and G. D. Dockery, "Theoretical description of the parabolic approximation/Fourier split-step method of representing electromagnetic propagation in the troposphere," *Radio Science*, vol. 26, pp. 381–393, March-April 1991.
- [47] P. C. Etter, *Underwater acoustic modeling and simulation*. CRC Press, Florida, 2013.
- [48] H. V. Hitney, "Hybrid ray optics and parabolic equation methods for radar propagation modeling," in *Radar 92. International Conference*, pp. 58–61, 1992.
- [49] S. van der Tol, *Atmosfeermodellen - dictaat*. KNMI, 1st ed., 2004.
- [50] B. G. Reynolds, "Pic of the day - formation passing exercise." <http://charlesmccain.com/tag/uss-vicksburg-cg-69/>, March 2012.
- [51] V. K. Ivanov, V. N. Shalyapin, and Y. V. Levadnyi, "Determination of the evaporation duct height from standard meteorological data," *Izvestiya, Atmospheric and Oceanic Physics*, vol. 43, no. 1, pp. 36–44, 2007.
- [52] K. L. Horgan, W. D. Thornton, J. K. Stapleton, V. R. Wiss, and R. Marshall, "A validation study of a numerical weather prediction / surface layer refractivity blending technique based on Monin-Obukhov similarity theory." Presentation, Naval Surface Warfare Center, Dahlgren Division (NSWCDD), April 2010.
- [53] S. M. Babin and G. D. Dockery, "LKB-based evaporation duct model comparison with buoy data," *Journal of applied meteorology*, vol. 401, pp. 434–446, April 2002.
- [54] M. Z. Jacobson, *Fundamentals of atmospheric modeling*. Cambridge university press, 2nd ed., 2005.
- [55] P. A. Frederickson, "Improving the characterization of the environment for AREPS electromagnetic performance predictions." Presentation, Naval Postgraduate School (NPS), March 2012.
- [56] "Netcdf java library." <http://www.unidata.ucar.edu/software/thredds/current/netcdf-java/documentation.htm>, Sept 2014.
- [57] A. V. van Leijen, W. L. van Norden, and F. Bolderheij, "Unification of radar and sonar coverage modeling," in *Information Fusion, 2009. FUSION '09. 12th International Conference on*, pp. 1673–1678, July 2009.

- [58] J. J. A. Vlaar and R. Buschmann, “Radar/EW parameter harmonization - parameter sets for use with computer simulation programs,” tech. rep., Defence Materiel Organisation of the Royal Netherland’s Ministry of Defence, July 2007.
- [59] E. Bruin, “The edge of maritime situation awareness - modelling the impact on North Sea weather conditions on the performance of AIS and coastel radar systems,” Master’s thesis, Utrecht University, Januari 2016.
- [60] Royal Netherlands Meteorological Institute (KNMI), “Weerkaarten archief europa.” <https://www.knmi.nl/nederland-nu/klimatologie/daggegevens/weerkaarten>, 2016.